Development of hybrid photocathodes for solar hydrogen production

Thiphaine Bourgeteau

Thèse de doctorat de l'Ecole Polytechnique

Spécialité : Chimie

Présentée par Tiphaine Bourgeteau le 30 Septembre 2015

Development of hybrid photocathodes for solar hydrogen production

Développement de photocathodes hybrides pour la production de carburant solaire

Composition du jury :

Jean Roncali	CNRS – Université d'Angers	Rapporteur
Alain Deronzier	CNRS	Rapporteur
Pere Roca i Cabarrocas	Ecole Polytechnique	Examinateur
Bruno Jousselme	CEA	Directeur de thèse
Bernard Geffroy	CEA/Ecole Polytechnique	Co-encadrant

LICSEN - Laboratoire d'Innovation en Chimie des Surfaces et Nanosciences

CEA Saclay

Abstract

One of the challenges of the 21st century is to produce clean and inexpensive energy at the TW scale to face the increasing energy demand and the global climate change. Because renewable energies are intermittent, they must be converted and stored in order to use them at the same scale of fossil energies. Hydrogen appears to be an ideal energy carrier when it is produced from water and sunlight. This fuel can be stored, transported and use on-demand by its combination with oxygen, for example in a fuel cell. Photo-electrochemical (PEC) cells able to carry out the photo-electrolysis of water are not yet cost-effective, because most of the materials used for their fabrication are rare or expensive (platinum, crystalline semiconductors). Producing hydrogen in a PEC cell at industrial scale depends on the finding of readily-available and easily-processed materials.

In this thesis, the development of a noble-metal free hydrogen-evolving photocathode was undertaken, to reduce protons from light and acidic water. The photo-converting unit was based organic semiconductors organized in a polymer-fullerene bulk-heterojunction layer (P3HT:PCBM) coupled to amorphous molybdenum sulfide (MoS_3) as a catalyst. In the device, the P3HT:PCBM layer absorbs the photons and the photogenerated electrons are then transported to the interface with the catalyst, which uses the electrons to produce hydrogen.

After studying each material (catalyst and solar cell) separately and checking the alignment of their energy levels, the first assemblies were made by solution processes. The deposition methods were adapted depending on the nature of the materials. Spin-coating and spray were used for the deposition of the light-harvesting unit and the catalyst, respectively. With the photo-electrochemical characterization setup, a photocurrent of up to 100 µA cm^{-2} was obtained, corresponding to production of hydrogen, as analyzed by gas chromatography. These first results proved the viability of the concept of this hybrid noble-metal free photocathode.

In order to improve the photocathode performance, new configurations were designed. Firstly, interfacial materials placed between P3HT:PCBM and MoS_3 (electron-extracting layer, EEL) were studied to improve charge collection by the catalyst. Among studied materials, photocathodes with titanium-protected aluminum reached up to 10 mA cm^{-2} of photocurrent. The presence of aluminum induced instability in aqueous media, so that oxides (TiO_x) and organic materials (C_{60} fullerene and graphene) were considered. TiO_x brought only a slight improvement compared to photocathodes without EELs, while C_{60} allowed to reach 5 mA cm^{-2} but with a lower stability compared to metallic EELs. The origin of the increased performances with EELs was attributed to the burying of the photovoltaic junction, removing the influence of the electrolyte.

Secondly, the material between the transparent electrode and the photovoltaic part, i.e. the hole-extracting layer (HEL), was replaced by amorphous oxides (graphene oxide (GO), MoO_x, NiO_x). It led to the fabrication of performant photocathodes, stables for several hours, by process temperatures below 150 °C in the case of MoO_x and GO. The increase of the performance seemed to be related to the increase of the HEL work function, leading to the suggestion that the Fermi level difference between the HEL and the electrolyte has an impact on the capacity of the photocathode to separate the charges and use them for photocatalysis. The most performant photocathodes (several mA cm^{-2} and 0.6 V of photovoltage) were the one with MoO_x, i.e. the material with the largest work function, and had a much better stability than the photocathodes with metallic EELs.

Résumé

L'utilisation des énergies renouvelables, qui sont intermittentes, à l'égal des énergies fossiles (échelle du TW) doit passer par leur conversion et stockage en un vecteur transportable. L'hydrogène semble le vecteur énergétique idéal qui peut être produit à partir de l'eau et de l'énergie solaire. Ce carburant peut ainsi être stocké, transporté puis utilisé à la demande en le combinant avec l'oxygène dans une pile à combustible. Les cellules photo-électrochimiques (PEC) utilisées pour la conversion ne sont actuellement pas rentables car les matériaux majoritairement utilisés pour leur fabrication, tels que le platine et les semiconducteurs cristallins, sont rares ou chers. Le point clé est de trouver des matériaux qui soient disponibles en grande quantité et facilement mis en forme.

Ce travail de thèse concerne le développement d'une photocathode sans matériau rare pour la photoproduction de H_2 via la réduction des protons à partir de l'énergie solaire et de l'eau. Pour cela, une cellule solaire à hétérojonction polymère-fullerène (P3HT:PCBM) a été couplée directement à un catalyseur sans métal précieux, MoS_3. La cellule solaire absorbe les photons, et les électrons photogénérés sont ensuite acheminés jusqu'au catalyseur qui les utilise pour produire l'hydrogène.

Après avoir étudié chacun des matériaux (cellule solaire et catalyseur) séparément et vérifié le bon alignement des niveaux énergétiques, les premiers assemblages ont été faits par des procédés en solution. Les méthodes de dépôt ont dû être adaptées en fonction de la nature des matériaux. Ainsi, le spin-coating et le spray ont été utilisés respectivement pour déposer la partie photovoltaïque et le catalyseur. Les caractérisations photo-électrochimiques mises en place ont permis de mettre en évidence la présence d'un photo-courant (100 µA cm^{-2}) correspondant à la production d'hydrogène, qui a été analysé par chromatographie en phase gazeuse. Ces résultats ont permis de montrer la viabilité des photocathodes hybrides sans matériau noble.

Afin d'augmenter les performances des photocathodes, de nouvelles configurations ont été conçues. Dans un premier temps des matériaux d'interface entre la couche mince photovoltaïque et le catalyseur ont été étudié (couche extractrice d'électrons, CEE) pour améliorer la collection des électrons photogénérés par le catalyseur. Parmi les métaux étudiés, l'aluminium protégé par le titane a permis d'atteindre des photocourants de 10 mA cm^{-2}. Cependant la présence de l'aluminium induisait une instabilité en milieu aqueux, aussi des oxydes (TiO_x) et des matériaux organiques (fullerène C_{60} et graphène) ont été envisagés. Le TiO_x n'a permis qu'une légère amélioration par rapport aux photocathodes sans CEE, tandis que le C_{60} a permis d'atteindre 5 mA cm^{-2} mais avec une stabilité moindre par rapport aux CEE métalliques. L'origine de l'amélioration des performances a été attribuée à l'isolement de la jonction photovoltaïque par rapport à l'électrolyte.

Dans une deuxième approche, la couche extractrice de trous (CET) située entre l'électrode transparente et le P3HT:PCBM a été remplacée par des oxydes amorphes (oxyde de graphène (GO), MoO_x, NiO_x). Ce changement a permis la réalisation de photocathodes performantes et stables pendant plusieurs heures, avec des températures de dépôt ne dépassant pas 150 °C dans le cas du MoO_x et du GO. L'augmentation des performances semblant aller de pair avec l'augmentation du travail de sortie de la CET, il a été suggéré que la différence des niveaux de Fermi de la CET et de l'électrolyte avait un impact sur la capacité de la photocathode à séparer les charges et les utiliser pour la photocatalyse. Les photocathodes avec MoO_x (matériau testé avec le plus grand travail de sortie) ont les meilleurs rendements (plusieurs mA cm^{-2} et un photovoltage de 0.6 V), et présentent une plus grande stabilité par rapport aux photocathodes ayant une CTE métallique.

Remerciements

Merci à Bruno Jousselme de m'avoir permis de passer ces six mois de stage et trois ans de thèse au LICSEN. C'était un bonheur de venir chaque matin au labo, grâce à tous les collègues extraordinaires et l'ambiance chaleureuse entre tous. Merci d'avoir encadré ma thèse, pour toutes tes idées qui permettaient de voir un problème sous un nouveau jour, pour les discussions sur les résultats parfois étonnants, pour toutes les rencontres occasionnées par les collaborations. Merci également pour ta confiance, et de m'avoir incluse dans d'autres projets. J'espère que tu ne m'en veux pas trop d'avoir dépassé 80 pages de manuscrit. Ton enthousiasme à chaque nouvelle manip était communicatif, et promis, je vais faire tes photocathodes souples ! Je languis de voir.

Merci à Serge Palacin, directeur du NIMBE, et à Vincent Derycke, chef du LICSEN, pour m'avoir accueillie dans le laboratoire. Il paraît que dans d'autres laboratoires, les directeurs ne côtoient pas les thésards, et ce n'est pas votre cas. Merci pour votre gentillesse et l'aide que vous avez pu apporter durant ces trois années.

Merci à Bernard Geffroy et Denis Tondelier, pour leur accueil à Orgatech à l'Ecole Polytechnique. Avoir accès aux différentes machines a été très précieux pour mes dispositifs, et j'ai beaucoup apprécié de travailler avec vous, de discuter de mes résultats, de parler de la physique des semi-conducteurs organiques en contact avec un électrolyte … Merci à Bernard d'avoir suivi de près mes travaux, et merci à Denis pour tous les bons plans de Massy ;-). Je remercie également Pere Roca i Cabarrocas, directeur du LPICM, et à Yvan Bonnassieux et Jean-Charles Vanel, chef du groupe OLAE du LPICM à l'Ecole Polytechnique, de m'avoir permis de venir à Orgatech pour mes expériences, et pour leur aide pour mes projets au Japon.

Merci à Romain Brisse, on se suivra jusqu'à la retraite, partis comme on est ! Après Rhodia en Chine, le stage dans des bâtiments voisins, et trois ans de thèse à tes côtés, on ne va pas s'arrêter là. J'espère que tu continueras dans ta lancée, tu as toutes les qualités d'un chercheur : la persévérance, la volonté de comprendre tes résultats, les idées un peu farfelues, … Bon courage à toi, (presque) Docteur Brisse !

Merci également à Renaud, mon voisin de bureau depuis mon arrivée. Même si tu as bien squatté mon directeur de thèse, ton aide a été précieuse tout au long de la thèse, pour les préparations de conférences, pour le manuscrit, pour les articles, pour l'électrochimie. Ce fut un plaisir de partager le bureau avec toi. Je n'oublierai pas la société européenne des chevaux miniatures de sitôt. Eduque bien Sacha et Arthur dans la philosophie de l'électrochimie, continue à faire des canelés et de la course à pied, et profite bien de ces années au LICSEN aux côtés de la team Bruno-Stéphane-Vincent !

Merci à Laure pour toute ton aide et tes conseils, pour le soutien moral à certains moments, pour les pauses thé et les afters work au christ de saclay. Nous formions une paire diabolique pour régner sur le labo. Dommage que l'arrivée d'une petite Liora nous ait coupées dans notre élan, mais c'était peut-être mieux comme ça, on aurait tous fini en surpoids à cause de tous ces canelés, tartes au citron et électrochimiquement vôtre !

Merci à Catherine, sans qui rien ne serait possible. Tu es quelqu'un d'extraordinaire et je pense que j'ai de la chance de partir avant toi !

Merci aux collègues du premier étage autour de la machine à café. Cédric, toujours présent avant 7h15 avec la punto verte sur le parking, le café, les soirées jeux, des sbires plus ou moins efficaces, et surtout, une connaissance incroyable sur tellement de sujets ! Steven, maître de la RRDE, je crois qu'il va falloir que tu motives Renaud à aller courir ! Que dit un hydrogène en sortant du bar ? H^+ ! Guy, merci pour toutes les histoires que tu nous as racontées, pour ta joie de vivre et j'espère que tu vas continuer tes aventures à vélo. Claire, même si tu as rejoint le côté obscur de la force en allant au 462, merci d'être venue chez nous pour finir ta thèse. Au Laos ils écrivent des remerciements de thèse ? Merci à Xavier, ancien thésard de Bruno, pour tes conseils et ton dynamisme, Thibault et Guillaume, deux excellents collègues parmi les sbires de Cédric, les occupants du bureau maudit (Thomas, Hugolin, Dorris). Un grand merci à Cécile, pour ta gentillesse. Ton départ a laissé un grand vide au laboratoire.

Merci à Vincent Artero, du CEA Grenoble, pour m'avoir accueilli dans son laboratoire pour les mesures d'hydrogène, ainsi qu'à Nicolas Kaeffer et Adina Morozan.

Merci à la team foot, Hugo, Théo, Vincent, Stéphane (s'il y a un apéro après), Joël, Bruno, Renaud, Fabien et David du 462, Pascal, Tania et Jéléna lorsque l'on était en stage, Thomas Baubeau, et d'autres que j'oublie certainement. Merci à la team Pilates avec notre prof Valentina, Jocelyne, Rita, Romain, Nabila, Arianna et Brigitte (qui nous bat tous à la course à pied). Merci à tous les collègues du LICSEN et d'ailleurs : Gaëlle, Nathalie, Yu-Pu, Goeffrey, Andrea, Adrian, Michael, Géraldine, Aurélie, Thomas Berthelot, Fanny, Ludovic, Alexandre, Yohan, Caue, Julie, Ekaterina, Pascale, Elodie, Sérigne, Ludovic, Bruno Lectard, Sylvain, Thomas Aghavnian, Quentin, Qirong, Fabrice Charra et son groupe. Merci à tous pour les tous les souvenirs. Vive les Flying Sharks et Faux-Thons ! Merci à Jinwoo et Warda et tous les autres collègues du LPICM que j'ai pu croiser. Merci également à mes collègues thésards physiciens, Maxime, Patrick et Jelle, ainsi qu'à Lisa de l'infogérance, d'ailleurs on n'a pas fait notre Rotonde de l'automne ! Merci à tous ceux que j'ai pu oublier et qui se reconnaîtront.

Merci à ma famille pour leur soutien tout au long de ces trois ans, « même s'ils n'ont jamais été inquiets » ! Et un merci particulier à Tristan, pour beaucoup de choses…

Content

Introduction

Providing clean and unlimited energy to the humankind is one of the greatest challenges of the 21st century. It has been taken up by the scientific community some decades ago in response to the rising concern about environmental issues combined with world population growth. Richard E. Smalley, Nobel prize of chemistry in 1996, named it the "Terawatt" challenge"[1] and explained that solving the energy problem would impact the other problems that we face: water, food, environment, poverty, disease, education, and population. In 2014, 18 TW of energy were consumed by 7 billion people.[a] In addition to the 3 billion new inhabitants by 2050, 3 other billion people which are currently consuming very few energy will probably have rising standard of living. In 2050, the energy demand is projected to be 30-35 TW, in a scenario in which consuming societies will have slowed down their energy consumption rate, in other words, not the worst case scenario. Within decades, it is necessary to use sustainable and carbon-neutral energy sources to meet this demand without aggravating environmental but also geopolitical and economic crises. Among renewable energy sources, sunlight is by far the most abundant: each hour, the amount of sunlight energy that strikes the Earth would be enough to meet one year of energy demand.

One must however take into account the intermittence of this energy source. Efficient storage of sunlight but also of other energies from renewable resources is a crucial step to truly replace fossil fuels. Batteries are an interesting solution for storing the energy where it will be consumed. But the energy is not always consumed where it is produced. For transporting energy, batteries are not optimal solutions. Instead, fuels, which store the energy in chemical bonds, are energy carriers that are easily transported to a different place to be distributed and consumed. Hydrogen gas appears as an ideal fuel to store solar energy. When produced from water, hydrogen is part of a carbon-free energy cycle involving solar-powered water electrolysis to produce it, and a fuel cell to recover electricity on demand, with only water as byproduct. Photo-electrochemical cells (PEC) have been designed to perform both light harvesting and water splitting. Made of one or two photoelectrodes, their expected efficiency is higher than a system built from two separate devices (solar panel and electrolyzer).

However, the development of carbon-neutral energy at a scale of equal measure with fossil energy must be low cost. In the legacy world, where large-scaled and centralized energy plants are already available, the use of carbon neutral energy will benefit from the existing infrastructures. On the contrary, it will be cost prohibitive to build infrastructures where they do not currently exist to produce and distribute energy to the billions of new energy consumers. The need for low cost systems able to

[a] Enerdata yearbook, 2014. Available free of charge : https://yearbook.enerdata.net/

provide highly distributed energy around the world is a challenge that requires the use of earth-abundant and easily-processed materials.

The objective of this work was to develop a new type of hydrogen-evolving photocathode for PEC devices working in water, using low-cost materials and fabrication processes. We chose to assemble an organic solar cell (based on the bulk heterojunction P3HT:PCBM with an earth-abundant catalyst for hydrogen production, molybdenum trisulfide. In the device, the role of organic solar cell part is to fulfill the steps of visible light absorption, charge separation and electronic transfer. Then, the electrons are transmitted to the catalyst, which uses the photogenerated electrons to produce hydrogen.

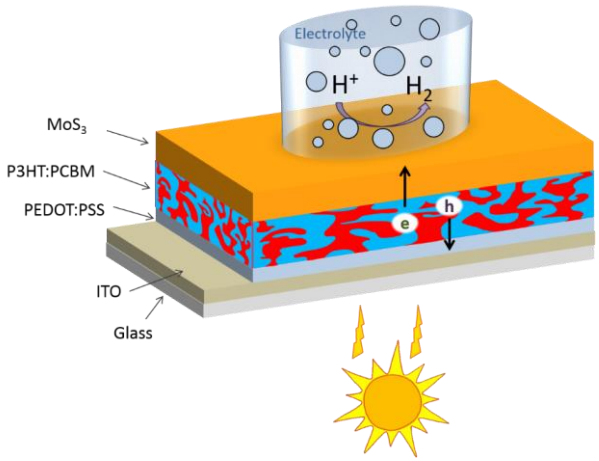

Fig. 1. Schematic illustration of the targeted photocathode

Chapter 2 presents the advantages of MoS_3 as hydrogen evolution reaction (HER) catalyst for the use on an organic photovoltaic junction. The synthesis, characterization and deposition of the MoS_3 catalyst are studied. The direct assembly on the P3HT:PCBM BHJ by successive deposition of the layers is then described.

In Chapter 3, electron-extracting layers are added at the interface between P3HT:PCBM and MoS_3 to enhance the photocurrent generation and protect the underlying organic layer from the acidic aqueous media. Two figures-of-merit are applied and discussed to compare the performance of the photocathodes.

In Chapter 4, the impact of the hole-extraction layer (placed between the transparent electrode and the P3HT:PCBM layer) on the performance of the photocathode is investigated. Different materials are tested to understand the energetics of the device towards the electrolyte, in particular the energy level alignment between the solar cell and the catalyst.

Finally, further development of these photocathodes and their potential integration in tandem PEC cells are discussed.

Chapter 1. State-of-the-art for clean hydrogen production from water and solar energy

1.1.Hydrogen solar fuel for a carbon-free energy economy

1.1.1. Hydrogen as energy carrier

Addressing the Terawatt challenge means that we have to face the shortage of fossil energy sources and the increase of energy demand while limiting environmental damages as much as possible. Sunlight is a highly interesting renewable source of energy, being an inexpensive, non-polluting, abundant and endlessly renewable source. In one hour, the Earth receives the equivalent of one year of energy consumption.[2] It is the only renewable energy source that scales to a sufficient level to replace fossil fuels[2] and the cost gap between solar-produced energy and traditional fuels is reducing. Taking into account sunlight intermittence, an area of solar panels the size of Spain would be enough to power the planet, and divided among the countries (and especially in places such as Sahara desert, whose unpopulated area is ten times as big as Spain), it would only represent 25 solar plants of 10 km a side in each country. At present, solar energy (photovoltaic and thermal conversion combined) represents approximately only 0.25 % of the total worldwide energy consumption.

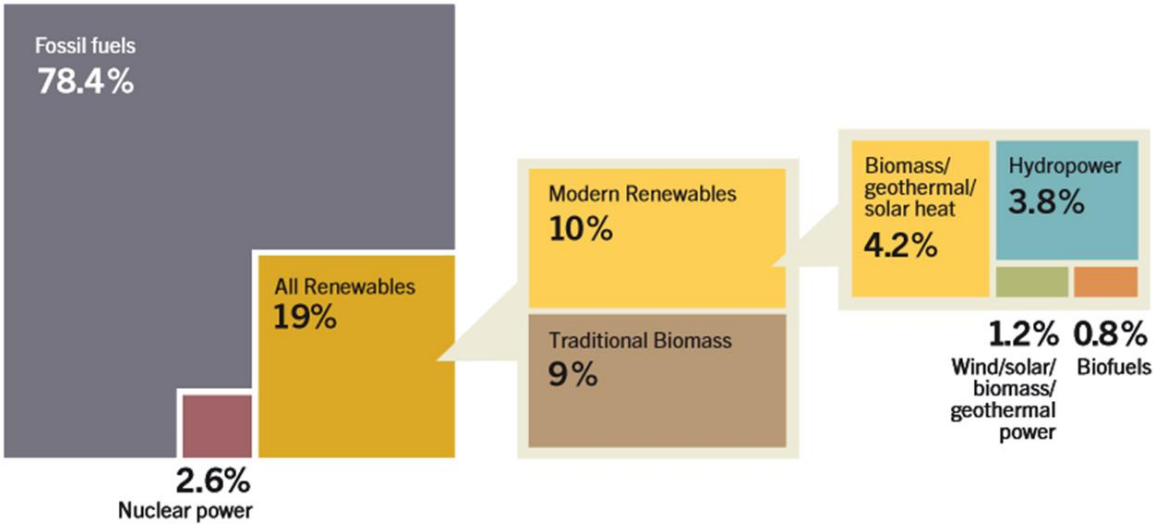

Fig. 2. Estimated renewable energy share of global final energy consumption in 2012. Reproduced from the Global Status Report "Renewable 2014" published by the Renewable Energy Policy Network REN21.

One of the main reasons why the part of solar energy in the energy mix (distribution of the different sources of primary energy in the global energy consumption, Fig. 2) is not rapidly expanding is, aside from the cost, that this source is intermittent (diurnal and dependent on weather condition) and dilute (it cannot directly power a standard car). Consequently, supplying solar energy day and night cannot happen without a storage mechanism, which should preferably be as inexpensive as the photo-converting unit. Indeed, D. Nocera pointed out that the cost of consumer goods that are neither hi-tech nor commodity will be low if the manufactured item is light in weight and is able to be produced at a

high volume.[3] Current energy technologies are at the opposite of this observation (centralized and large energy plants), so that disruptive energy technologies will be those that are light-weight and highly manufacturable while being robust and of low maintenance, in order to provide energy in a decentralized way.

Efficient energy harvesting, conversion and storage of solar energy for on-demand usage and transport still remain a main challenge.[1] To store photovoltaic electricity (or from others intermittent renewable sources), several methods exist, each with advantages and drawbacks, sometimes preventing their use for large-scale solar application. Among them, the pumped hydro-energy storage consists in using electricity when it is available to pump water in the reservoir of a hydraulic dam. It is highly efficient and has been largely developed but it is geographically limited and can be expensive if the hydraulic dam has to be built. Batteries are an efficient energy carrier, especially for mobile applications (cars) and for consumption of energy at the same place where it is produced. However, renewable energies are not always available at the same place to where they are consumed, and TWs of energy cannot be transported in batteries. This limitation in transport is actually present for other ways of energy storage (thermal energy storage, compressed air energy storage, …). On the contrary, fossil energy sources (oil, coal), widely used all over the world, are easily transported by pipelines or container ships. Molecular fuels (usually in a liquid phase) are storing energy in the form of chemical energy. The volume of electron storage is chemical bonds, so that they are high mass energy density (around 50 MJ kg^{-1}) energy carriers compared to batteries, which store electric energy (less than 1 MJ kg^{-1}, due to the mass of external components).[2-5] Traditional fuels are however carbonated and limited in amount. As a result, huge amounts of CO_2 are released in the atmosphere when they are burnt to retrieve energy as heat or electricity, with the consequences that we know. But if we are able to store solar energy into molecules, solar-derived fuels will likely prevail as an energy storage medium for solar energy, allowing their transport to the consumer. In fact, the most interesting solar fuels are those focusing on two raw materials: water and CO_2. The solar storage and release reactions are:

$$H_2O + \text{solar energy} \rightarrow H_2 + O_2$$
$$CO_{2\,(aq.)} + \text{solar energy} \rightarrow CO\ (\text{or other carbonated molecules}) + {}^{1}/_{2}\,O_2 \qquad \text{Storage}$$

$$H_2 + O_2 \rightarrow H_2O + \text{energy}$$
$$Carbonated\ fuel + O_2 \rightarrow CO_2 + \text{energy} \qquad \text{Release}$$

With water electrolysis, the energy carrier is hydrogen, which has a very high energy density (120 MJ kg^{-1}). Solar energy is used to re-arrange the bonds in the water molecules into the higher energy H–H and O–O bonds. When the sun no longer shines, at night, the energy stored into H_2 and O_2 is released by combining them, for example in a fuel cell to recover energy as electricity, with only water as a byproduct.[3, 5] In the meantime, hydrogen can be stored in high pressure cylinders or other means of

storage, and transported similarly to other gases. In fact, hydrogen pipelines already deliver main ammonia production and oil refining plants. The huge advantage of water compared to CO_2 as a raw material is that it does not involve carbonated molecules in the energy cycle (Fig. 3), a very important factor for the development of a carbon-free hydrogen energy economy.

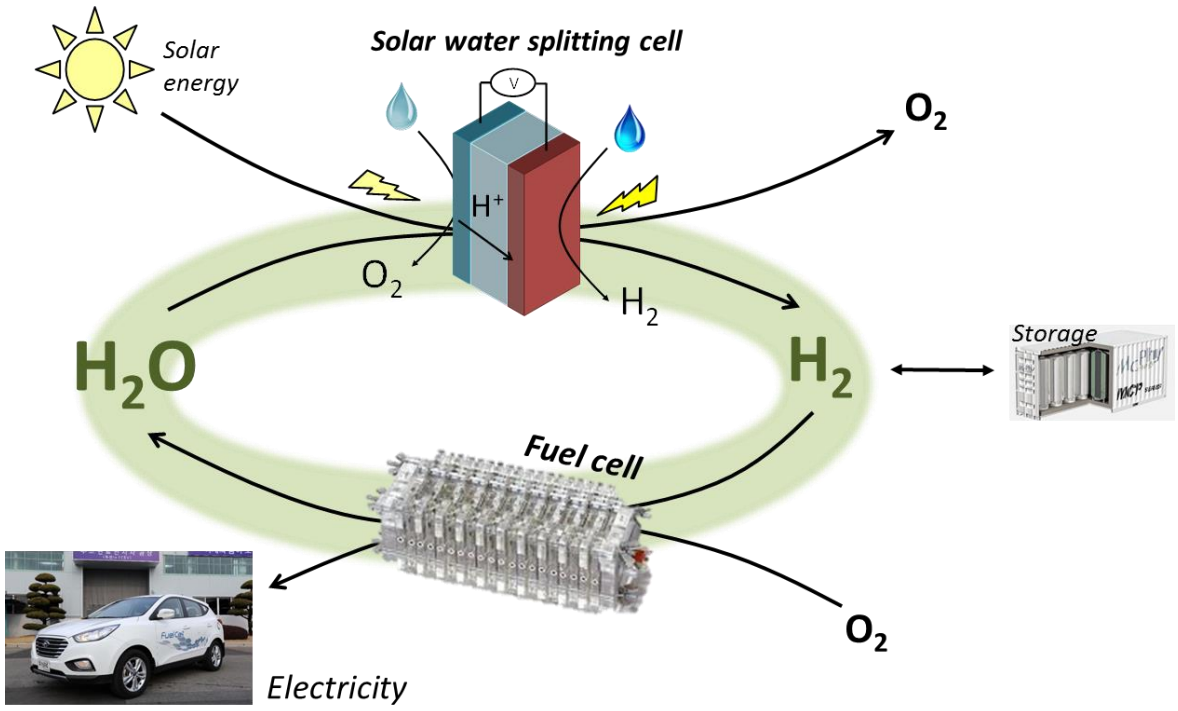

Fig. 3. Carbon-free energy cycle for the storage of solar energy in hydrogen from solar-powered water splitting. Hydrogen is an energy carrier which has a very high mass energy density, but it must be used under high pressures (700 bar) because hydrogen at atmospheric pressure has a low volume energy density compared to liquid fuels. Hydrogen can be stored and transported before being distributed in fuel stations to hydrogen cars, which uses hydrogen in a fuel cell to recover energy as electricity with only water as a byproduct.

Thus, hydrogen appears as an ideal energy carrier, provided that it is produced from water and renewable energies.

1.1.2. Clean hydrogen production

In the past years, companies have been increasingly interested in this alternative fuel. The automobile industry has produced hydrogen cars powered by a fuel cell: concept vehicles from Honda, Toyota or Mercedes demonstrated the feasibility in 2008-2014, and commercial vehicles were released in limited numbers by Hyundai in 2013 and Toyota in 2014. Energy or gas companies have been installing hydrogen fuel stations, around 600 worldwide, though only two in France. In the hydrogen energy cycle of Fig. 3 the less advanced part (commercially speaking) is the clean hydrogen production.

Indeed, 95 % of the hydrogen that is currently used is produced by steam reforming of methane,[b] a carbonated molecule, which yields to syngas ($CO + H_2$), with unavoidable release of CO_2 in the atmosphere. While the academic community has been searching actively for materials to build solar water splitting cells, only a few companies are investing in clean hydrogen production. The only potentially commercial setup is the assembly of a solar panel array with a water electrolyzer, both of which are mature technologies. But their combined use for hydrogen production is exceeding the cost of non-renewable fuels, partly because two separate devices must be fabricated.

In nature, the photosynthesis process is performed in many organisms such as plants, algae or cyanobacteria, which are storing solar energy into molecules. These organisms, called autotrophs, are able to convert water and CO_2 with sunlight into chemical bonds (carbohydrate molecules such as sugars) while releasing oxygen. In an attempt to artificially recreate photosynthesis, devices called photo-electrochemical (PEC) cells have been designed, performing in only one device light harvesting, photovoltaic conversion, and chemical transformation.[4] Splitting water into oxygen and hydrogen in such a system is a huge challenge but it would be an ideal long-term solution because high efficiencies are expected.[2] The US department of energy (DOE) has established a threshold cost goal of 2-4 $ per gge[c] delivered, dispensed and untaxed, to be cost-effective compared to fossil fuels. Different methods for hydrogen production (reforming of natural and bio-derived carbonated molecules, coal and biomass gasification, water electrolysis, solar thermochemical water hydrogen, photoelectrochemical, photobiological and fermentation processes) are compared to this target cost. While gas reforming is already cost-competitive, the estimated current price for hydrogen from solar-powered water electrolysis is 10-12 $ per kg H_2[c], and the cost target for photo-electrochemically produced hydrogen in 2020 is around 5 $ per kg H_2[c]. A report pointed out that producing hydrogen at a competitive cost is realistic but innovative breakthroughs are still needed, especially regarding the PV-critical materials which could hinder the wide-scale development of solar-powered water splitting.[5] It has also been pointed out that the lifetime of these solar hydrogen production devices should exceed 15-20 years to be economically competitive.[5,6] Presently, the lifetime of a solar cell is over 20 years and 10-20 years for a proton-exchange membrane (PEM) electrolyzer.[7] However, current PEC systems last from a few hours to a few months, at the laboratory scale. Thus, PEC cells still need to be improved, both in performance and in stability.

[b] Afhypac, « Mémento de l'Hydrogène – Production d'hydrogène à partir des procédés de reformage et d'oxydation partielle », 2011

[c] gge = gallon of gasoline equivalent. The energy content of a gallon of gasoline and a kg of hydrogen is approximately equal on a lower-heating-value basis.

Inset 1. Electrolysis of water

The electrolysis of water consists in the electrochemical decomposition of water into hydrogen and oxygen gases in which electrical energy is the driving force of chemical reactions. The two half-reactions of water splitting are termed as OER (oxygen evolution reaction, i.e. water oxidation into oxygen) and HER (hydrogen evolution reaction, i.e. water reduction into hydrogen).

$2\,H^+ + \ 2\,e^- \ \rightarrow \ H_2$	HER (acidic media)	$E^0_{H^+/\,H_2} = 0\,V\ vs\ NHE$
$2\,H_2O \ \rightarrow \ O_2 + 4\,H^+ + 4\,e^-$	OER (acidic media)	$E^0_{O_2/\,H_2O} = 1.23\,V\ vs\ NHE$
$H_2O \ \rightarrow \ H_2\,(g) + \frac{1}{2}O_2\,(g)$	Overall water splitting	$\Delta G = 237.2\ kJ\ mol^{-1}$

The HER takes place at the negatively charged cathode, and the OER takes place at the positively charged anode (Fig. 4).

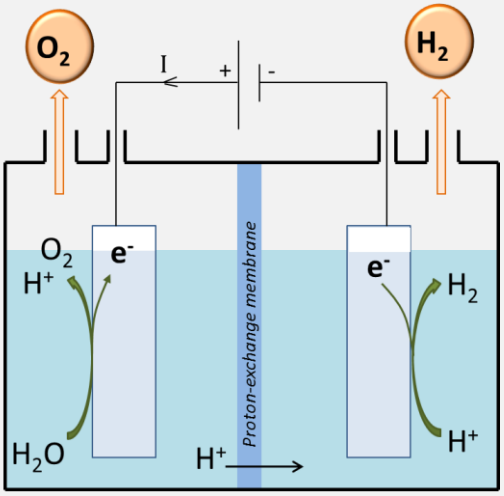

Fig. 4. Schematic representation of an electrolyzer in acidic media. The two electrodes are usually separated by a proton exchange membrane to evolve H_2 and O_2 in two different compartments.

At standard pressure and temperature conditions, the free energy of the reaction is + 237 kJ mol^{-1}, which, according to the Nernst equation, corresponds to 1.23 V per electron transferred: the reaction is not spontaneous and can only be driven forward if a sufficient voltage is applied, in other words, if electrical energy is provided by an external source to the system. In devices, larger driving voltages (1.5 - 2 V) are needed because of additional resistances (slow kinetics at the surface of the two electrodes, resistances of the electrolyte or due to the membrane, …). A voltage of 2 V can be brought by 3-4 commercial silicon solar cells in series.

At each electrode, the overpotential, i.e. the extra potential (E) over the standard potential of the redox couple that must be applied to drive a reaction at an electrode at a certain rate, can be minimized by using efficient electrocatalysts to enhance the electrode kinetics.

Compared to hydrogen produced by steam reforming which contains sulfur and carbon impurities, hydrogen produced by water electrolysis is clean.

1.2.Solar-powered water splitting for hydrogen production

1.2.1. From photosynthesis to photo-electrochemical cells

In nature, hydrogenases and nitrogenases are able to convert CO_2, N_2 and water into chemical energy (lipids, sugars) under ambient conditions and illumination. Inspired by this process, solar-powered water splitting cells were designed to perform water electrolysis (cf. **Inset 1**), without external voltage supply by reproducing the major functions of natural photosynthetic systems: photon adsorption and charge separation, long range electron transfer, and catalysis for water oxidation to oxygen and reduction to hydrogen.

Since the pioneering work of Fujishima and Honda in 1972,[8] photoelectrochemical (PEC) cells performing solar water splitting have been widely reported in the literature, both in academic journals[4,9] and in patents.[10] They can have many different configurations depending on the absorber, catalysts and co-catalysts, number of photoelectrodes, buried junctions, etc.[4,11]

The simplest photocatalytic system for water splitting is a semiconductor (cf. **Inset 2**) presented in Fig. 5:

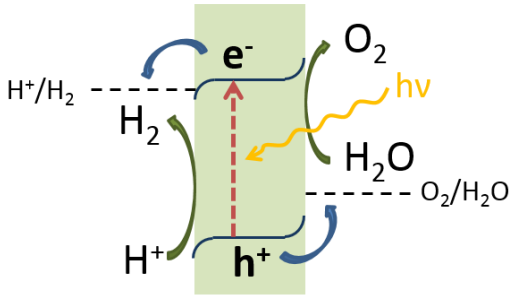

Fig. 5. Schematic representation of an ideal single semiconductor for water splitting. The valence band and the conduction band are straddling the H^+/H_2 and O_2/H_2O redox potentials, and the HER and OER kinetics are sufficient at the semiconductor surface.

Inset 2. Semiconductor

The materials responsible for the absorption of light in a photovoltaic device are semiconductors, which are characterized by a bandgap of a certain energy (E_g). This gap is the energetic separation between the valence electrons (in the valence band, VB) and the nearest free electronic states (in the conduction band, CB): $E_g = E_{CB} - E_{VB}$

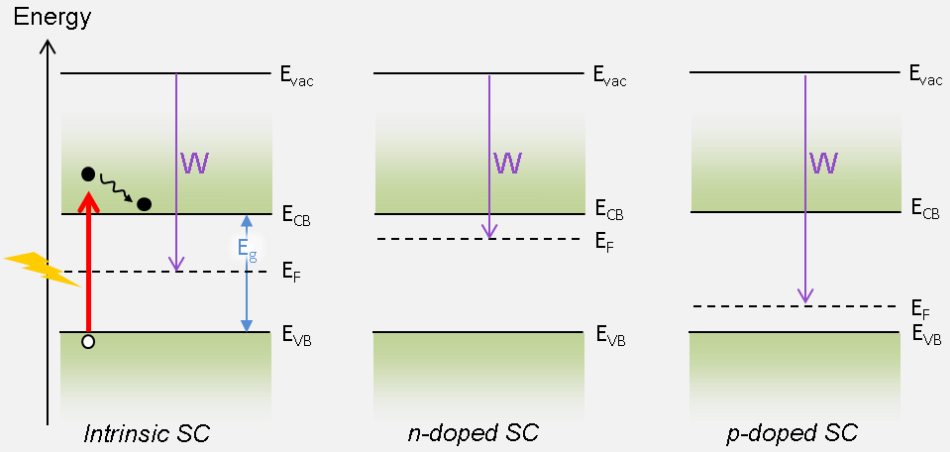

A material is generally considered a semiconductor (SC) when E_g is greater than the thermal energy available (e.g. around room temperature: 25 meV). Very few valence electrons can be excited to the conduction states by thermal activation, but the material non-conductive in the dark. The absorption of a photon of energy greater than E_g can excite an electron from the VB to the CB, generating two types of charge carriers. An unoccupied valence state is created, termed a 'hole' (white dot on the scheme), and the electron (black dot on the scheme) occupies a conduction state. The photon energy then resides in the potential energy difference between this excited electron-hole pair. The excited electron and hole will quickly undergo thermal relaxation, ending up at the conduction band edge (E_{CB}) and valence band edge (E_{VB}), respectively: all of the photon energy exceeding the gap energy will be dissipated as heat.

The Fermi level (E_F) is defined as the total electrochemical potential for electrons, and signifies the thermodynamic work that is required to add one electron to the material. It will be located at the middle of the bandgap if the SC is intrinsic, just above the valence band for a p-type doped SC, and just below the conduction band for a n-type doped SC. The work function (W) is the minimum thermodynamic work needed to remove an electron from the material to a point in the vacuum just outside the material. In practice, the work function value is considered to be the difference between the vacuum energy level and the Fermi level at the surface.

The ideal PEC device should meet several criteria (Fig. 5):[12,13]

- optical absorption in the IR-visible range (corresponding to the majority of the solar flux), i.e. with a bandgap smaller than 3 eV. Moreover, the bandgap must be larger than 2 eV with conduction and valence band edges properly aligned with the H^+/H_2 and O_2/H_2O redox couples ($E_{CB} < E°_{H+/H2}$ and $E_{VB} > E°_{O2/H2O}$) to be able to split water.
- high mobility of holes and electrons in the semiconductor
- sufficient kinetics for OER and HER at the electrode surface
- resistance to corrosion in aqueous electrolytes
- solar-to-hydrogen conversion yield (STH) higher than 10 %, competitive cost on an energy-equivalent basis, absence of toxic effects, simple fabrication processes, large availability of materials.

So far, no standalone semiconductor (as presented in Fig. 5) was found to be able to perform unassisted water splitting, because the criteria are sometimes going in different directions. For example, a semiconductor with a bandgap sufficiently high to split water (> 2 - 2.5 eV) will not absorb a great part of the solar spectrum, while a semiconductor with a lower bandgap (1.5-2 V) will absorb more light but its ability to split water will be compromised due to the small voltage. A smaller bandgap semiconductor will also lower the chances that the band edges will properly straddle the two electrochemical redox potentials. Besides, a single semiconductor with a suitable band structure for water splitting would not necessarily have sufficient kinetics for both hydrogen evolution and oxygen evolution, so that devices often incorporate catalysts to enhance the reaction rate. In fact, no material meeting all these criteria was discovered. Therefore, in practice, systems with different levels of complexity were developed.

For example, many devices are built with an additional bias, either brought by a PV cell connected in series with a photoelectrode, or by using two photoelectrodes, in so called tandem systems (Fig. 6). The absorbers can use complementary parts of the solar spectrum to maximize light absorption, and the photovoltages provided by the two systems are added so that it is possible to use smaller bandgaps than necessary for overall water splitting. In a tandem configuration, it is possible to develop separately each photoelectrode, with its own catalyst or protective layers. Each photoelectrode must only have one of the two bandgap edges properly positioned toward one of the two redox potentials (the conduction band above the H^+/H_2 level or the position of the valence band under the O_2/H_2O level). Thanks to this strategy, many materials, which could not be used for the full water splitting, can be used as a photoelectrode, combined or not with interfacial layers and/or catalysts.

Consequently, with the purpose of reaching high solar-to-hydrogen (STH) efficiencies and long-term stability, a variety of systems exists, combining different absorbing materials, configurations,

photovoltaic biases, catalysts, protective layers, etc in order to drive simultaneously and in an unassisted fashion the evolution of hydrogen and oxygen.

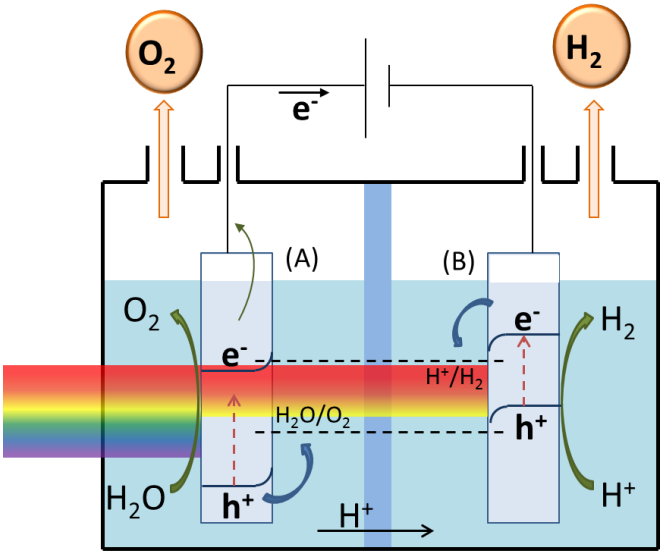

Fig. 6. Schematic representation of a tandem PEC cell for water splitting. In this example, the photoanode (A) absorbs blue/green light, the photogenerated electron is injected in the circuit and the hole oxidizes water into oxygen. The photocathode (B) absorbs the rest of the sunlight and the photogenerated electron is used to reduce protons into hydrogen. An electric generator (solar panel, potentiostat) can be used to provide an additional bias.

1.2.2. Taxonomy of PEC cells

As introduced previously, light-powered water splitting cells can be built from different materials and in different configurations. These systems producing hydrogen from solar energy and water are usually designated as photo-electrochemical cells despite the fact that they operate following different physical principles or technologies with various states of maturity.

An approach to analyze and compare solar-to-chemical energy converters, that is, only the devices which are storing solar energy into chemical bonds, is presented in a work from Jacobsson and coll.[11] It emphasizes the close relationship between a PV-electrolyzer and a monolithic PEC cell contrary to the traditional assumption in the literature that they are fundamentally different. The authors based their analysis by studying the main physical processes (photon absorption, charge carrier separation, charge carrier transport, and catalysis) in different intermediate devices between PEC cells to PV-electrolyzers, such as a buried junction with a window layer and a catalyst or tandem cells. Their point of view is not to say that these systems are equivalent in physical principles but that they are conceptually close so that a PV-biased electrosynthetic system should not be forgotten by the community of researchers working on photo-electrosynthetic systems. A striking example is the GaAs/$GaInP_2$ devices from Khaselev and Turner. The most cited (> 1000 citations) article reports 12.4

% solar-to-hydrogen (STH) efficiency for a monolithic device and is often cited as the record device for solar hydrogen production.[14] Then, they published another device described as integrated multijunction PV-electrolyzer based on the same materials in tandem, reaching 16 % STH efficiency and having a better stability (the absorber being outside of the electrolyte), which has been largely overlooked.[15]

Recently, the group of N. Lewis published a taxonomy for solar energy converters (into fuels or electricity) which allows the differentiation between devices from particulate photocatalysts in suspension to semiconductor/electrolyte junctions or solar-powered electrolyzers.[16] They take into account the number of junctions in the device. In this taxonomy, a junction is defined as an interface between two unlike materials where there are chemical and/or electrical potential gradients as well as kinetic asymmetries, which allows separation and transport of photogenerated charges. These photojunctions can be buried (i.e. not directly in contact with the electrolyte), solid-state (involving two semiconductors) or semiconductor/electrolyte. The taxonomy (Fig. 7) contains varied well-known systems such as:

- Solar electric cells (photovoltaic cell producing electricity), such as polycrystalline, CIGS (copper indium gallium selenide) thin film or organic solar cells
- PV-biased electrosynthetic cells (photovoltaic cell that produces fuel, consisting in buried photovoltaic junctions arranged electrically in series with electrocatalysts submerged in an electrolyte)
- Regenerative PEC cells, containing for example dye-sensitized solar cells (DSSCs), which are solar cells (producing electricity) based on a semiconductor/electrolyte junction. The species that is reduced or oxidized at the working/photoactive electrode is regenerated at the counter electrode, without change in the electrolyte composition.
- Photo-electrosynthetic cells, which are producing fuels at the semiconductor/electrolyte junction
- Photoelectrosynthetic particulate or molecular photocatalysts in suspension, with buried junctions and/or semiconductor/electrolyte junctions

These different systems can be combined, for example by using a solar electric cell or a regenerative PEC cell to bias a (photo)-electrosynthetic cell. The classification also takes into account if the cell has one or two photo-electrodes, connected to an additional electric solar cell or not. Indeed, for water splitting, several junctions are often needed to better utilize the solar spectrum and provide the 2 V necessary to drive the reaction at a significant operating current. Using the classification allows proper comparison between systems which are belonging to the same class and facilitates the identification of the research challenges and state-of-the-art for each type of system.

In this thesis, the photocathodes were classified based on the taxonomy described by Lewis and coll.[16]

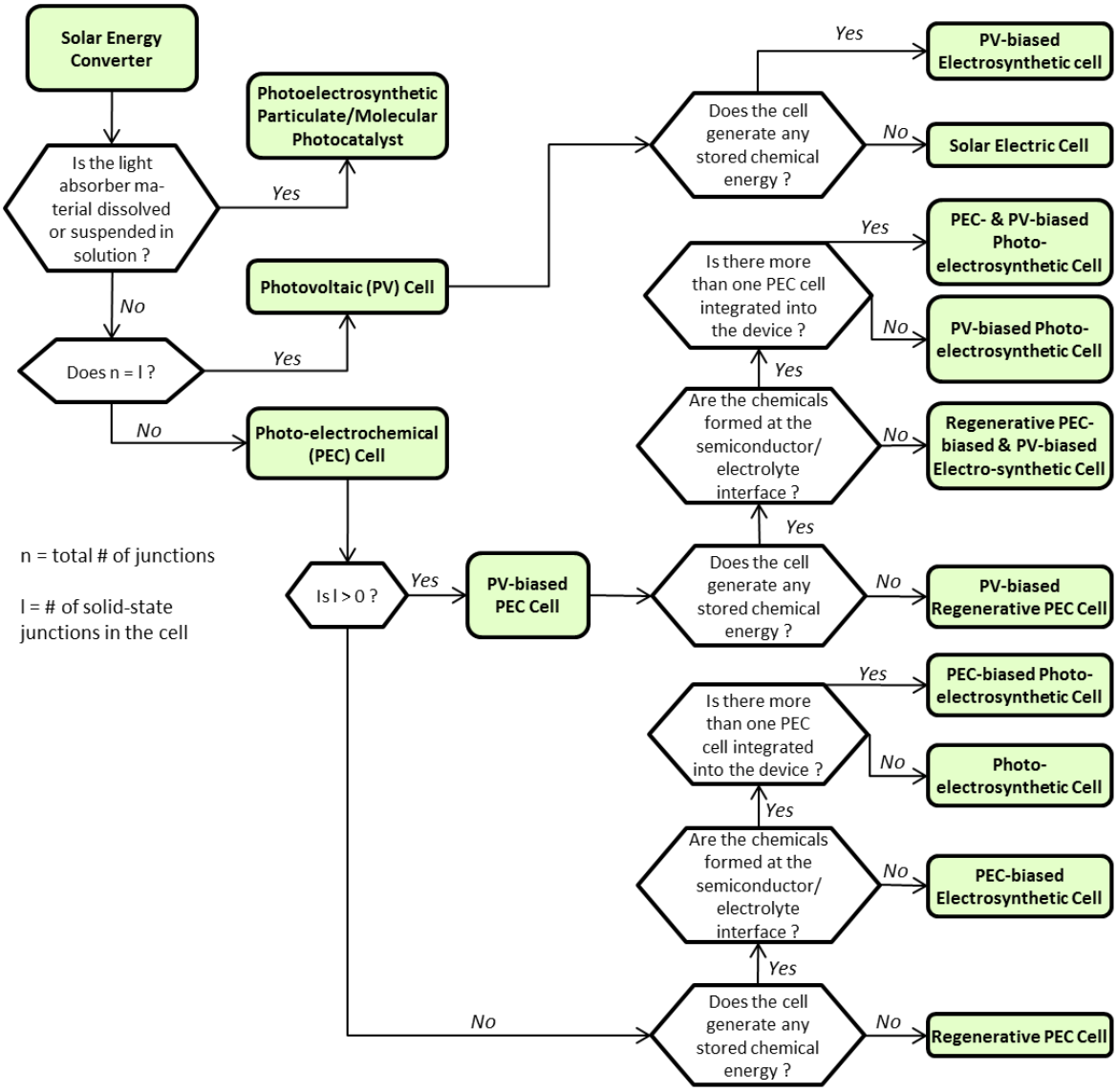

Fig. 7. A taxonomy for the classification of solar energy converters. For a device of interest, identify n (total number of junctions), m (number of semiconductor/electrolyte junctions), and l (number of buried junctions), then proceed through the flow chart to determine the appropriate name for the device. Note that the taxonomy does not address devices designed to use light to drive exergonic processes. Reproduced from Ref.[16] with permission from The Royal Society of Chemistry.

It is worth to note that a distinction can be made between wireless and wired configurations of PEC cells (Fig. 8). While the wireless device can be simply dropped in water and illuminated to split water, the wired configuration has the advantage that H_2 and O_2 are evolved in different compartments, removing the necessity to separate the gases.

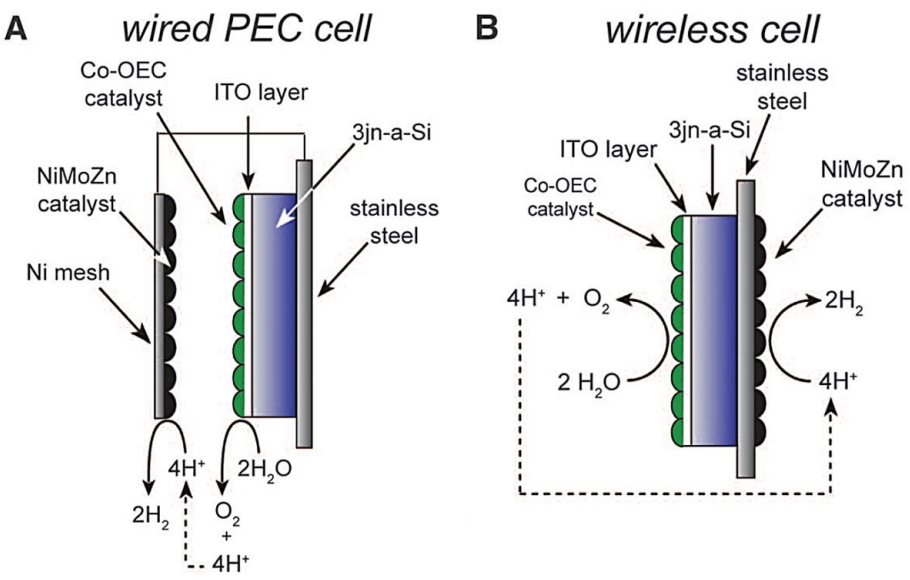

Fig. 8. Schematic representation of the wired (A) and wireless (B) configurations. A proton-exchange membrane can be inserted between the two electrodes of configuration (A). Reproduced from Ref[29] with permission from the American Association for the Advancement of Science.

1.2.3. Inorganic-based solar-to-hydrogen converters

1.2.3.1. Notable examples of inorganic-based solar-to-hydrogen converters (based on PV and PEC cells) in the literature

In this part, some examples of PEC devices are cited either for their historic importance or their considerable efficiencies. For more information, the reader can refer to detailed reviews.[4,9,10,17–23]

In 1972, Honda and Fujishima designed for the first time a PEC cell, based on a TiO_2 semiconductor electrode where O_2 was evolved, and H_2 was evolved at the Pt counter electrode (Fig. 9).[8] TiO_2 has a larger bandgap (3.2 V) than required for water splitting and band edges that straddle the H^+/H_2 and O_2/H_2O redox potentials. However, a bandgap of 3.2 V means that the semiconductor only absorbs light in the UV region, which represents about 3 % of sunlight at ground level. Moreover, TiO_2 was not able to directly reduce protons at its surface; a Pt cathode was used to perform the HER.

To improve the efficiency, performant devices were built by combining efficient semiconductors (usually with multijunctions to better utilize the solar spectrum) and catalysts, often based on expensive and rare materials such as platinum, ruthenium or indium. Visible light water splitting with a wireless multijunction cell was first demonstrated and patented by W. Ayers in 1983, with a variety of materials but without mention of the efficiency.[24] Among the record cells, one can cite the p-GaAs/n-GaAs/IL/p-$GaInP_2$//Pt (IL = interfacial layer) monolithic device in a wired configuration

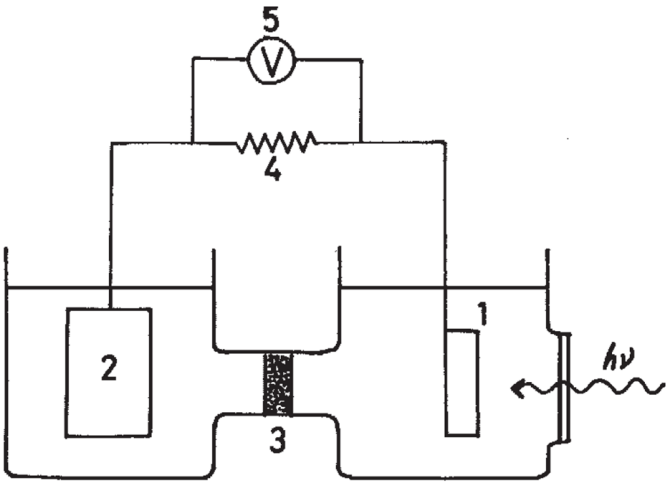

Fig. 9. Electrochemical cell with (**1**) the TiO_2 electrode and (**2**) the Pt electrode. Reproduced from Ref.[8] with permission from Nature Publishing Group.

developed by Turner and coll., consisting in two junctions: a buried p-n GaAs junction biasing a semiconductor ($GaInP_2$)/electrolyte junction. According to the taxonomy described in section 1.2.2, this cell is classified as a PV-biased photo-electrosynthetic cell. It reached 12.4 % STH efficiency.[14] By replacing the semiconductor/electrolyte junction by a n-p $GaInP_2$ junction and burying the two junctions by a platinum electrode, the PV-biased electrosynthetic cell reached an efficiency of 16.5 %[15] still in a wired configuration (and 7.8 % for the equivalent device based on a triple junction of a-Si/Pt). In a similar configuration, Tributsch and coll. reported a RuO_2/p-n AlGaAs/p-n Si/Pt cell, reaching over 18 % of solar to chemical energy conversion.[25] The two p-n junctions were buried so that they did not interact with the electrolyte, and the configuration could be considered as wired because the two electrodes were distinct. A wireless cell was designed by Kocha and coll. based on n-p GaAs/n-p $GaInP_2$/Pt, where H_2 and O_2 were both evolved on the Pt nanoparticles, with 4-10 % of STH conversion efficiency.[26]

To reduce the cost linked to the use noble metals, multi-junction silicon solar cells were designed with earth-abundant catalysts by Rocheleau and coll. (1998, 7.8 %, wired configuration),[27] Suzuki and coll. (2003, 2.5 %, wireless configuration)[28] and Nocera and coll. (2011, 4.7 % in wired configuration, 2.5 % in wireless configuration).[29] The wireless one chip photovoltaic device designed by Suzuki and coll. consisted in a silicon-based device with low-cost catalysts, sealed in epoxy resin except for the catalyst.[28] Nocera's group later named the wireless device "artificial leaf"[30] (Fig. 10), which consists of two earth-abundant catalysts for OER and HER on either sides of a triple-junction silicon solar cell.

An example of PEC device using other materials than silicon is the tandem cell consisting of a WO_3 n-type PEC cell (absorbing the blue/green part of the solar spectrum) biased with a dye-sensitized solar

cell (absorbing the remaining part of the solar spectrum) developed by Grätzel and coll. [31] 4.5% STH efficiency were obtained but hydrogen was evolved at a platinum cathode.

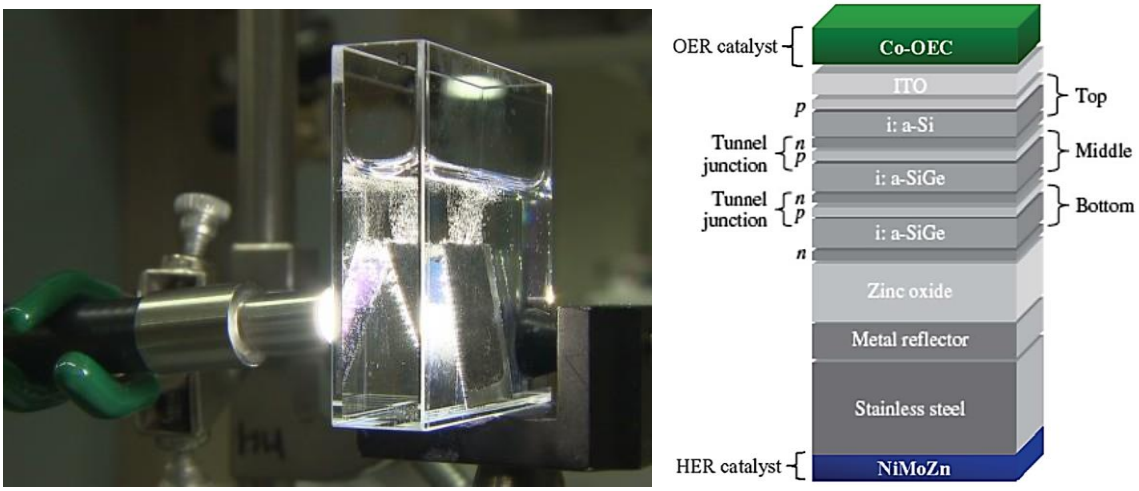

Fig. 10. Artificial leaf designed by Nocera's group. On the right, the schematic view of the device is presented. Reproduced from Ref.[30] with permission from the American Chemical Society.

1.2.3.2. Inorganic materials for low-cost photoelectrodes

Materials for noble metal-free photoanodes and photocathodes have been developed based on inorganic semiconducting compounds.

Many scientific efforts have focused on the development of n-type semiconductors for low-cost photoanodes,[4,32] such as $BiVO_4$,[33–35] WO_3,[36–38] Fe_2O_3,[39–41] TiO_2[42–44] and (oxy)nitrides (TaON,[45,46] Ta_3N_5[47,48]), as well as other semiconductors and compounds resulting from the combination of semiconductors. Fig. 11 presents a diagram of main semiconductors used for water splitting. The semiconductors on the right have sufficiently small bandgaps to absorb enough visible light, and due to the position of their valence band, they have enough potential to oxidize water. However, the conduction band is just above the redox level for water reduction, so that they have been used mostly as photoanodes.

In many of the above systems, the photoanode for OER is used with a Pt cathode for the HER, with or without bias. Contrary to photoanodes, for which promising low-cost and stable materials exist, efficient and low-cost materials for photocathodes have been less investigated (three times less articles based on Web Of Knowledge database in 2015). Silicon[49–52] and Cu_2O[53,54] have been used as light-harvesting modules, usually in combination with a HER catalyst, but they suffer from a relatively low stability and must be protected. Silicon processing usually requires a lot of energy, and Cu_2O, which can be electrodeposited, is an interesting material for low-cost fabrication of devices working in

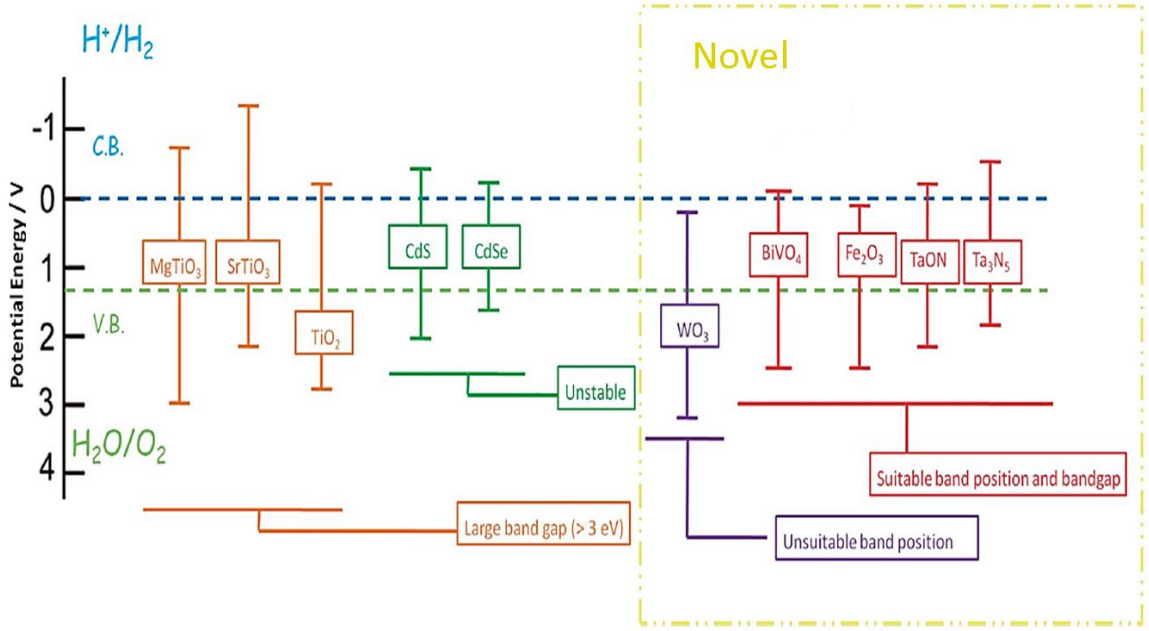

Fig. 11. Schematic illustration of bandgap positions of several semiconductors photocatalysts. Reproduced from Ref.[32] with permission from the Royal Society of Chemistry. The semiconductor materials on the left either have a too large bandgap (low visible light absorption) or are unstable. New materials includes $BiVO_4$, Fe_2O_3 or (oxy)nitrides.

alkaline media. It can be mentioned that alternative approaches derived from p-type dye-sensitized solar cells are also under investigation, by combining a dye-sensitized p-type semiconductor (NiO) and a catalyst for the HER (in solution or attached to the dye), with relatively low photocurrents (in the order of 10 µA).[21,55] In this thesis, a new type of photocathode based on low-cost organic semiconductors was investigated.

1.2.4. Organic semiconductors in PEC

1.2.4.1. Organic photovoltaics

Organic semiconductors (OSCs) are organic materials with an electron conduction band and a hole conduction band separated by a gap that confer it semiconducting properties. In 1977, Alan Heeger, Alan MacDiarmid and Hideki Shirakawa reported high conductivity in oxidized and iodine-doped polyacetylene.[56] They were awarded a Nobel Prize of chemistry in 2000 for the discovery and development of conductive polymers. Since then, many applications have been developed, such as organic light-emitting devices (OLED, widely commercialized in display applications, for example in new generations of smartphones), organic photovoltaic cells (OPV) and organic field-effect transistors (OFET). Organic solar cells are part of the third-generation solar cells,[57,d] comprising dye-sensitized

[d] The solar cells of the first generation are mainly based on silicon wafers (monocrystalline, polycrystalline silicon) and are the dominating technology of the market. Second generation solar cells are based on thin film

solar cells,[58,59] inorganic quantum dots or nanostructured semiconductors in arrays or combined with organic semiconductor polymer matrices[60] and all-organic solid-state cells (so-called organic solar cells).[61,62]

Organic conducting and semiconducting materials have a great potential for high-throughput manufacturing with processes in soft conditions, light weight and low amounts of raw materials compared to their inorganic counterpart. OPV cells now display over 10 % power conversion efficiency (PCE)[63] using abundant materials and low-cost processes. Among other advantages of organic semiconductors, the thin films can be deposited on flexible substrates such as PET, allowing roll-to-roll production of lightweight solar cells with a low energy payback time.[64] In addition, a wide variety of OSC materials can be obtained with different energy levels and bandgaps by chemical synthesis.[65] This tunability is advantageous to improve OPV cells but also in PEC systems, as it allows a fine adjustment of their energy levels to the redox potentials for water splitting and of the light absorption spectrum. Moreover, to cover a significant part of the required voltage for water splitting, open-circuit voltages near 1 V were reported for single junctions.[66–68]

Organic photovoltaic compounds consist of polymers (identical units (10-10^3) linked by a covalent bond) and molecules (Fig. 12), which present a backbone of sp^2-hybridized carbons (or nitrogen, oxygen, sulfur). The conjugation of their π-atomic orbitals along the backbone, i.e. the alternation of single σ carbon bonds and π+σ double bonds, results in the formation of delocalized π molecular orbitals.

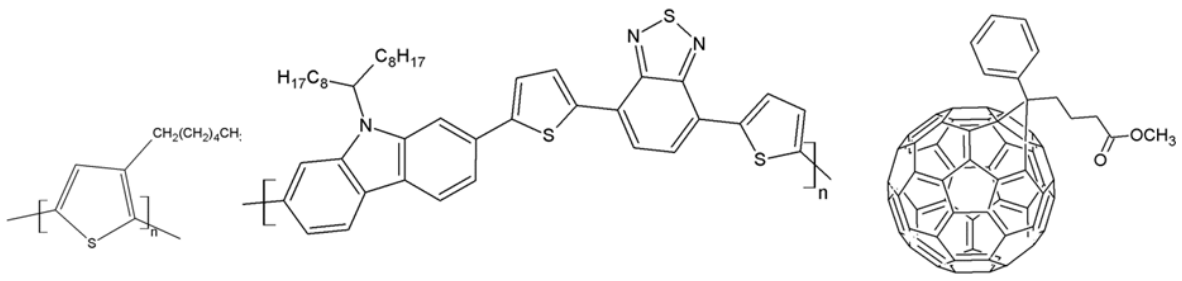

1 **2** **3**

Fig. 12. Structure of polymeric (1 and 2) donor materials., **1**: poly-(3-hexylthiophene) or P3HT, **2**: Poly[N-9'-heptadecanyl-2,7-carbazole-alt-5,5-(4',7'-di-2-thienyl-2',1',3'-benzothiadiazole)] or PCDTBT, and of a molecular acceptor material, **3**: [6,6]-phenyl C61-butyric acid methylester or PCBM or $PC_{61}BM$.

The frontier electronic levels (Highest Occupied Molecular Orbital, HOMO and Lowest Unoccupied Molecular Orbital, LUMO) determine the optical and electrical properties of the molecules. In a

technologies (single and multijunction cells based on CdTe, copper indium gallium selenium or CIGS, a-Si, micro-crystalline Si, …)

molecule, the electrons can be ejected from the HOMO (characterized by the ionization potential I_p) or captured by the LUMO (characterized by the electronic affinity E_A). When the molecule lengthens, the gap between the HOMO and LUMO levels decreases. If the length of the molecule increases indefinitely, the orbitals will be so close that they will form an energy band (Fig. 13). The ensemble of the π orbitals will form the valence band and the π* orbitals the conduction band. The HOMO and LUMO normally characterize an isolated molecule, but it is common to use them in the solid phase, the HOMO designating the top of the valence band and the LUMO the bottom of the conduction band. For organic semiconductors, the bandgap is defined as the difference between the HOMO and the LUMO.

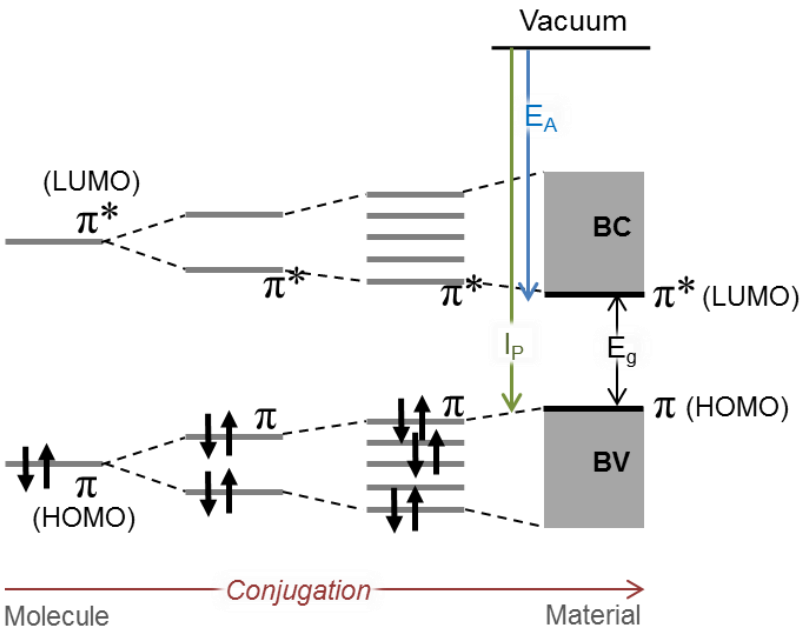

Fig. 13. Energy diagram of the π molecular orbitals when the conjugation length increases (either by the lengthening of the polymer chain or by interactions between molecules).

1.2.4.2. Working principle and structure of an organic photovoltaic solar cell

The working mechanism of photon flux conversion into electrical energy can be divided in four steps (Fig. 14):

1) photon absorption
2) exciton diffusion
3) exciton dissociation
4) carrier transportation and collection.

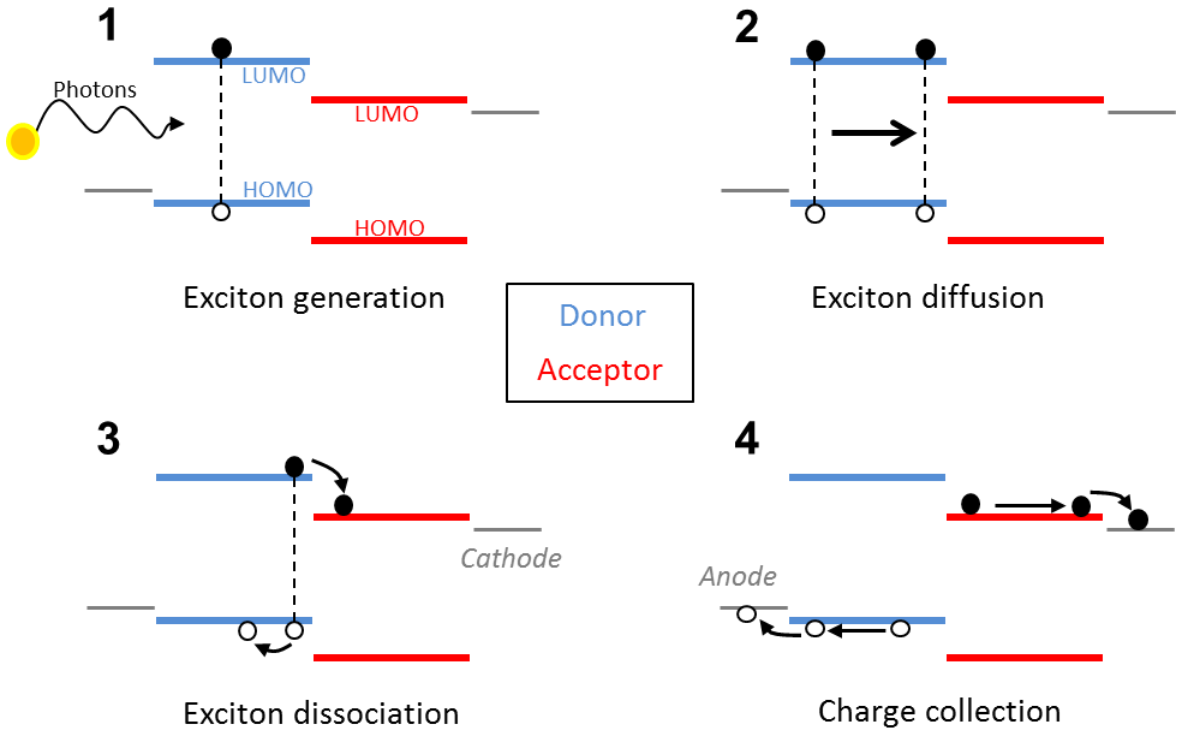

Fig. 14. Principle of the photovoltaic effect in an organic solar cell in the case of a bilayer device.

Firstly, an incident photon, arriving on the organic semiconductor and having an energy that exceeds the semiconductor bandgap, excites an electron to an unoccupied state above the bandgap, creating an electron-hole (e-h) pair, called an exciton. Contrary to inorganic semiconductors, in which the exciton is weakly bound (~10 meV) and is dissociated spontaneously, the binding energy (Coulomb force) of the exciton in the organic semiconductor is much higher (~0.1-1 eV) than the thermal activation energy at room temperature (~25 meV), so that a thermal dissociation is not allowed.

Secondly, the exciton diffuses inside the material until it reaches a dissociation site or recombines. Ideally, the size of the organic domain in which the exciton diffuses should be equal or lower than the diffusion length of the exciton, which is around 10-20 nm in organic materials. Excitons are mainly diffusing because it is a neutral quasi-particle and is thus not affected by external fields.

The third step is exciton dissociation. In polymer solar cells, the electron-hole pair which was created through absorption is held together by coulombic forces. However, for the solar cell to generate electricity, the electron and hole must be separated, and subsequently collected at electrodes of opposite polarity. In order to accomplish this, the exciton bond must be broken. This is done by introducing a secondary organic semiconductor in the active layer, which has an energetically lower lying LUMO-level, such that electron transfer between the two types of semiconductor is favorable. The material with the highest LUMO is called the electron donor while the other is called the electron acceptor. The exciton binding energy must be lower than the difference between the LUMO level of

the donor and the LUMO level of the acceptor. In state-of-the-art polymer solar cells, the heterojunction is between a polymer donor (for example poly-(3-hexylthiophene, P3HT) and an molecular acceptor (for example the fullerene derivative [6,6]-phenyl-C_{61}butyric acid methylester, PCBM). Most of the excitons are actually generated in the donor phase because of the higher absorption in the polymer than in the fullerene, and electrons are transferred to the fullerene acceptor.

During the fourth step, the charges then diffuse to the electrodes (the holes towards the anode in the donor and the electrons towards the cathode in the acceptor) and are injected in the electrodes, delivering a current and a voltage in the external circuit. Charge carrier mobility depends on how the frontier π orbitals overlap, and consequently on the morphology and crystallinity of the organic film. In the case of the bulk-heterojunction solar cells, the phase orientations are random. The current flow is controlled by the use of electrodes having sufficiently different work functions (the anode electrode is chosen with a high work function material and the cathode is selected with a low work function material, usually a metal).

Initially, the polymer (donor) and the fullerene (acceptor) were deposited in a bilayer configuration, similarly to inorganic semiconductors (p-n junction). But at the same time, the photons need to go through a certain thickness of active layer (100-200 nm) for the active layer to absorb most of them. Due to the small exciton diffusion length, the donor-acceptor layer was structured in a bulk heterojunction: a typical structure of organic solar cell (based on a polymer/fullerene bulk heterojunction) is shown in Fig. 15. The polymer donor (P3HT) and the fullerene acceptor (PCBM) form a 100-200 nm thick layer with separate domains of P3HT and PCBM. The layer is in-between two electrodes, typically a transparent one (indium tin oxide, ITO) and a metallic one (aluminum).

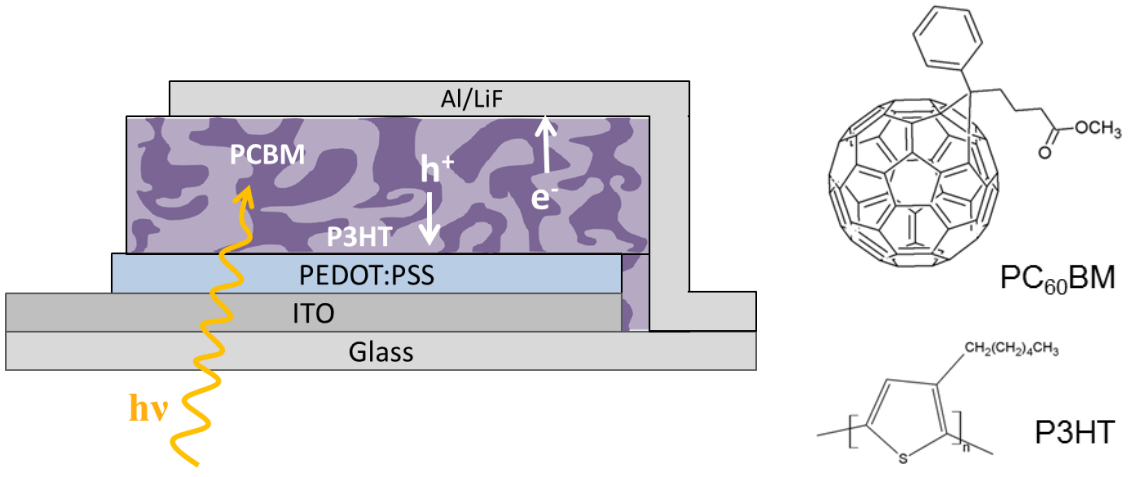

Fig. 15. Schematic view of a typical organic solar cell in normal structure, with the corresponding structures of the materials. The light is absorbed in the P3HT:PCBM layer.

Bulk heterojunctions were made by mixing both materials together and depositing them together (usually by spin-coating at laboratory scale) to form interconnected domains large of a few tens of nm

size, which form upon drying (and sometimes annealing).[69] The resulting three-dimensional nanoscale phase separation in the active layer increases the junction area and allows the formation of efficient solar cells.

In Fig. 15, a layer called a hole-extraction layer (HEL) and made of PEDOT:PSS (poly(3,4-ethylenedioxithiophene):poly(styrene sulfonate)) is used to improve the ITO-P3HT interface (smoothing of the ITO surface, improvement of charge collection in ITO).[70] A wide variety of materials (polymers and molecules) have been reported for the building of organic solar cells.[71–73]

1.2.4.3. PEC based on organic semiconductors

OSC have been used for solar water splitting devices in different configurations. In this part, a short review on significant devices is presented.

Photocathodes were built based on single OSCs such as polyacetylene, polyaniline, polypyrrole, poly-(3-methylthiophene) or poly-(3-hexylthiophene). These photoelectrodes were made in situ by electropolymerizing a monomer in solution onto a conductive electrode (for example ITO). Their photo-electrochemical behavior was studied and sometimes photo-electrosynthesizing properties were reported (hydrogen or other compounds). Only a few µA cm^{-2} photocurrent density were obtained in aqueous environment[74–78] and as demonstrated later, the photocurrents were not corresponding to production of hydrogen.[79]

Meanwhile, heterojunctions of two different organic semiconductors started to be developed in electric solar cell configurations to improve the exciton dissociation within the organic layer (cf. previous subsection). The works on P3HT/electrolyte junctions described before resulted in photocurrents of a few tens of µA, showing that the presence of an electrolyte was not enough to help charge separation, and that an acceptor was necessary to improve charge separation. Thus, in 2012, Abe and coll. built an ITO\P3HT:PCBM BHJ photoelectrode.[80] They did not use any interfacial layer between the ITO and the BHJ, but an electron acceptor or donor was added in the electrolyte to tailor the direction of the charge collection. They expected that the collection of either electrons or holes at the BHJ/electrolyte interface would decide whether the photoelectrode would be a photocathode or a photoanode respectively. Surprisingly, only a photoanodic current could be obtained, in the presence of the donor, but no photocathodic current was obtained with the acceptor, though holes from the P3HT are usually well transferred to the ITO. The same year, a P3HT:PCBM BHJ on ITO was used without catalyst as H_2-evolving photocathode in aqueous NaCl, Cl^- being used as sacrificial donor.[12] Tested in a two electrode configuration (with a Pt counter electrode), a peak current density of 100 nA cm^{-2} was reached. Stable photocurrents were obtained over 28 h, but the hydrogen bubbles were sticking to the surface.

To enhance proton reduction at the photocathode surface, a Pt catalyst was added at the top of an evaporated small-molecule (phthalocyanine/fullerene) p/n planar junction and generated 800 µA cm^{-2}

photocurrent density corresponding to H_2 evolution in aqueous phosphoric acid (pH = 2).[81] It was shown that the photophysical events within the bilayer (i.e., visible-light absorption, carrier generation at the p/n interface, conduction of electron and hole in each layer) were the same than in the corresponding solid-state photovoltaic cell. The difference lies in the fact that in a solid-state solar cell, the charge transfer at the organic semiconductor/metallic electrode interface is not limiting, while for the photoelectrode interfaced with an electrolyte, the rate-limiting charge transfer occurs at the solid/liquid interface (thus the presence of Pt). This work shows however that an organic bilayer that is usually a part of a solid-state photovoltaic cell can be turned into a photoelectrode in wet conditions.[82] Based on their previous work, Abe and coll. built a full PEC device with a H_2Pc/C_{60}/Pt photocathode and a perylene/H_2Pc photoanode in the water phase (Fig. 16).[83] Hydrogen was evolved from water but the photoanode needed a sacrificial donor (a compound that is oxidized at a lower potential than water).

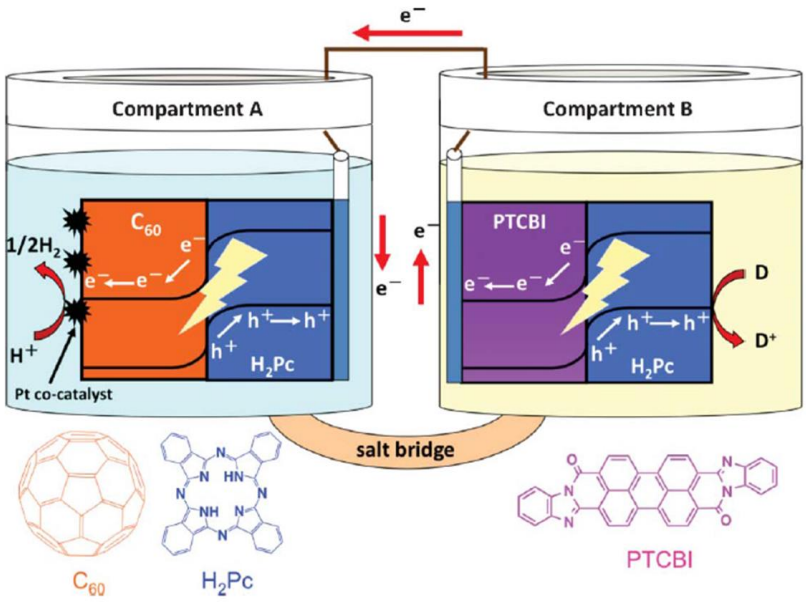

Fig. 16. Schematic illustration of the photocatalysis system of H_2Pc/C_{60}/Pt and PTCBI/H_2Pc. PTCBI = 3,4,9,10-perylenetetracarboxylic-bis-benzimidazole. D = donor compound (thiol). Reproduced from Ref.[83] with permission from the Royal Society of Chemistry.

It is worth to note that a PV-biased electrosynthetic cell was reported in 2013 by Janssen and coll.[84] It consisted in an all-solution-processed triple junction polymer solar cell with an open-circuit potential (V_{OC}) of 2.33 V, which was connected to an electrolyzer to perform water splitting (Fig. 17).

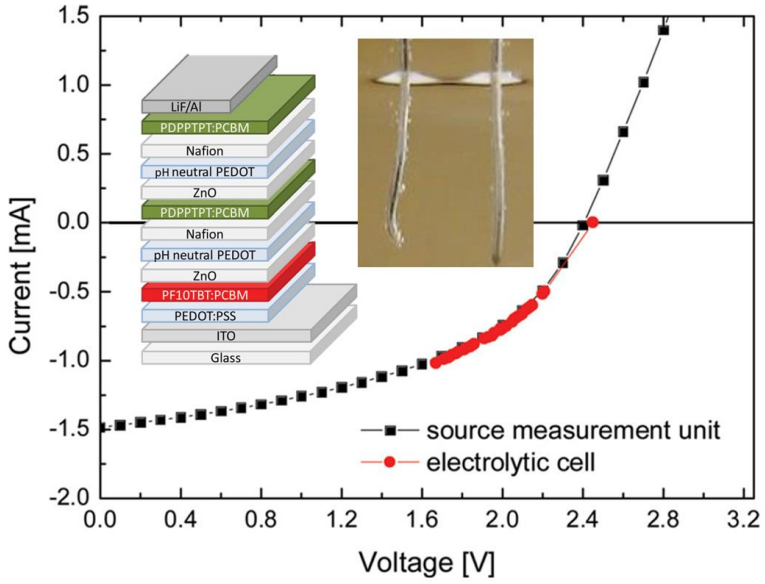

Fig. 17. Device structure of the triple junction (inset left); evolution of H_2 and O_2 (inset right); comparison of the I-V curve of the triple junction solar cell and of the electrolytic cell. Reproduced from Ref.[215] with permission from John Wiley & Sons.

At the beginning of this thesis work, no photocathode had been made with a P3HT:PCBM BHJ and a hole-extraction layer such as PEDOT:PSS. P3HT:PCBM had also not been interfaced with any catalyst to enhance charge transfer, even platinum. To avoid the use of this rare metal we decided to use an earth-abundant proton reduction catalyst, as described in Chapter 2.

Chapter 2. Proof-of-concept: synthesis and characterization of MoS_3 and its assembly onto P3HT:PCBM

The objectives of this chapter are to present the choice of catalyst used to increase the kinetics of the hydrogen evolution reaction (HER) at the photocathode surface, and to describe the building and testing of the first photocathodes. The MoS_3 catalyst is first synthesized and then characterized both in suspension and as a thin film. In particular, the electrochemical activity is tested to evaluate the conditions in which the photocathodes are going to be tested.

2.1. A brief literature overview of HER electrocatalysts

Efficient and cheap HER electrocatalysts are a key point for the development of future energy-converting devices. While platinum is the best catalyst for the HER, it is scarce and expensive[85,86] and incompatible with the wide-scale development of hydrogen-producing devices.[87] Thus, tremendous efforts are being invested in the search for non-precious and earth-abundant HER catalysts that can operate in aqueous conditions,[88,89] though it is still a challenge to equal the performance of platinum. In this part, a literature search on noble-metal free catalyst compatible with the deposition on organic semiconductors is presented.

2.1.1. Electrocatalyst overpotential

Fig. 18 presents a typical voltammogram (current density *vs* electrode potential) of an electrocatalyst (here, MoS_3) deposited on an electrode and tested in acidic media towards proton reduction into hydrogen. The electrolyte is deoxygenated with nitrogen to avoid the parasitic oxygen reduction current which could add up to the proton reduction current. A reduction current, characterized by a negative current density, appears at potentials more negative than –0.15 V, due to the exchange of electrons which are transferred from the electrode to protons. In this work, the studied current is always a reduction current, unless otherwise mentioned. Thus, for convenience, the current density will be expressed by its absolute value.

The reduction current of the HER appears at potentials more negative than the thermodynamic potential of H^+/H_2. The overpotential is defined as the potential added to the thermodynamic half-reaction potential of interest to experimentally observe the redox event at a given current density. For an electrolytic cell, it means that a higher voltage must be applied than what is thermodynamically expected to drive a reaction. An efficient electrocatalyst has therefore a low overpotential. In this thesis, the half-reaction potential of interest is $E^0_{H+/H2}$ and its value is 0 in our reference system. In Fig. 18, overpotentials to reach 1 and 5 mA cm^{-2} are presented: they are equal to 200 mV and 350 mV, respectively. An onset potential (i.e. the potential at which the reaction starts) is usually defined as the electrode potential to reach a current density threshold of 0.1 mA cm^{-2}.

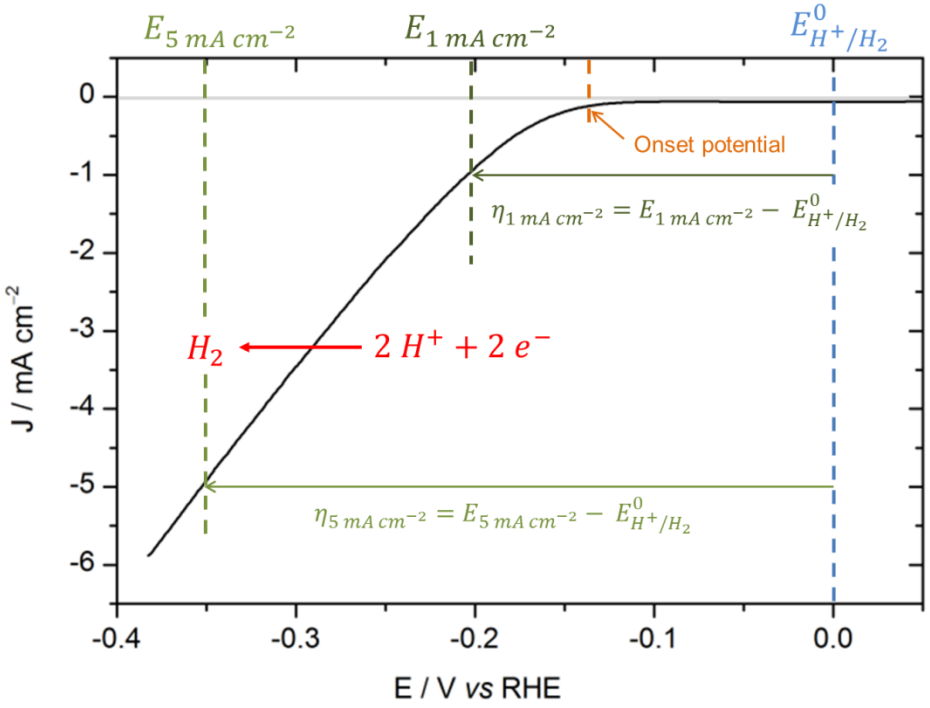

Fig. 18. Current density-potential curve (voltammogram) of a MoS_3 catalyst deposited on an electrode, in acidic aqueous media.

2.1.2. Specifications for the choice of the HER catalyst

The combination of the catalyst with organic photovoltaic devices adds some specifications related to the process or the OPV-catalyst interface. The specifications are listed as follows:

- The catalyst onset potential should be close to the thermodynamic potential of H^+/H_2.

It is important to use a catalyst with the lowest onset potential possible, so that the photovoltage is not wasted in overcoming the overpotential.

- It should be possible to form thin layers of catalyst with controllable and reproducible thickness on the organic layer.

The deposition of a catalytic layer on the active layer of an organic solar cell has an important role on the final performance of the device. The catalyst should moreover be processable from solution directly onto the organic solar cell (i.e. the catalyst should be already active before deposition, so that no further thermal or (electro)chemical treatment would be necessary after deposition to activate it). Moreover, it should not need an additive incompatible with the organic layer (e.g. Nafion, typically used to process Pt/C catalysts). A thickness range of 10 - 100 nm is targeted. The electrocatalyst may absorb light, and in the perspective of building tandem PEC cells (with two electrodes absorbing complementary parts of the solar spectrum), it would indeed be important not to use thicker films of a

catalyst to avoid the absorption of visible light. On the contrary, the control of thicknesses lower than 10 nm could be difficult on the soft organic substrate.

- The stability of the catalyst is an important aspect for the duration time of the photocathodes.

In particular, it was decided to test the photocathodes in acidic aqueous media, restraining to the catalysts active in acidic conditions.

- The energy level should be suitable for the coupling with an organic solar cell.

The energy level alignment between the catalyst and the lowest unoccupied molecular orbital (LUMO) level of the fullerene in the bulk heterojunction is important to allow photogenerated electrons to be transferred to the catalyst.

- It should be synthesized in soft conditions, and with a scalable process.

The synthesis should not involve many steps or high temperature treatments.

- The catalyst should be based on non-precious and earth-abundant elements.

The choice of a catalyst involves compromising between price and catalytic activity. Platinum is the best catalyst when one considers only the catalytic activity, thanks to its low overpotential (0.02 V at 1 mA cm^{-2} under acidic conditions[90]), but as noted above, it is not an earth-abundant material.

2.1.3. Earth-abundant HER catalysts

The objective of this section is to present the different types of earth-abundant HER catalysts. Extensive reviews are available in the literature.[89,91–96] The most commonly used elements for the construction of HER catalysts, except Pt, are either transition metals: iron (Fe), cobalt (Co), nickel (Ni), copper (Cu), molybdenum (Mo) and tungsten (W), or non-metals: boron (B), carbon (C), nitrogen (N), phosphorus (P), sulfur (S), and selenium (Se).[91]

The two main types of catalysts are homogeneous and heterogeneous catalysts. In homogeneous catalysis, the active species, whether molecular or nanoparticulate, are freely diffusing in solution. A heterogeneous catalyst is active in a different phase compared to the electrolyte. This type of catalyst does not need to be separated from the solution and is directly in contact with the electrode. For the purpose of building solid-state photocathodes, the direct contact of the catalyst with the photovoltaic cell is an advantage to collect the photogenerated charges without depending on the diffusion of the catalytic species. Thus, heterogeneous catalysts were chosen.

It can be however interesting to have a look in molecular catalysts, which usually provides deep insights in the mechanism of the catalyzed reaction and are a source of inspiration for the finding of heterogeneous catalysts. In living cells, hydrogenases[97,98] and nitrogenases[99] are the enzymes catalyzing effectively the HER in during photosynthesis, with Fe, Ni and Mo the only metals contained in their active sites. The challenges of using enzymes in solar water splitting applications are

caused by their long-term instability under ambient conditions and the low density of metal active sites compared to their large size.[88] Biomimetic and bioinspired compounds, artificially mimicking or derived from the active site of these enzymes, have been synthesized to overcome these aspects. They are usually in the form of metallic complexes, as for example the series of Ni-based molecular catalysts designed by DuBois and coll.[100] Several reviews are available to describe these homogeneous catalysts and the mechanism of HER, as well as their immobilization on electrode materials.[88,89,92] Bio-inspired catalysts developed at the laboratory[85,101,102] were considered but it would be challenging to immobilize them onto the organic layer.

A wide variety of inorganic compounds have been studied as heterogeneous catalysts, more or less by combining each of the above-mentioned elements. They include transition metals sulfides,[91,93,96] selenides,[91,96] carbides,[91,94,96] nitrides,[91,94,96] phosphides,[91,96] silicides,[96] borides,[96] but also alloys (e.g. Ni-Mo).[92] Solutions to enhance their performance and stability such as nanostructuration, chemical modification, structural modification or composite materials have been reported.[96] Transition metal chalcogenides (S, Se) are the largest class of earth-abundant HER-catalysts. Inspired by the catalytic center of nitrogenases and hydrogenases, molybdenum sulfides have been widely studied. Many different preparation methods exist, including at low temperature. Low onset overpotential of 150-180 mV can be achieved (and even lower with Co, Ni or Fe doping) in acidic media. Tungsten sulfides are similar to molybdenum sulfides though less developed and prepared only by high temperature processes or electrodeposition, incompatible with our organic substrate. Fe, Co and Ni sulfides have lower catalytic activity than Mo sulfides, though nanostructuration of Co sulfides appears to be promising. With selenide instead of sulfide, larger overpotential are needed for the HER, except for cobalt selenide, an efficient electrocatalyst but with preparation methods incompatible with the organic substrate. Metal carbides, nitrides and phosphides preparation methods are less convenient, involving thermal treatment of a precursor with a source of carbon, nitrogen or phosphorus, and often annealing prior to the tests. One of the most efficient compound of these classes are nickel molybdenum nitride and cobalt phosphide, both having an onset overpotential of a few tens of mV. Metal silicide and boride are recent families of HER electrocatalysts and exhibit modest performance.

Thus, among them, molybdenum sulfides were chosen for their convenient and varied preparation methods as well as their high electrocatalytic efficiency.

2.2. Molybdenum sulfides

Molybdenum sulfides had been known in the 90s as catalyst for hydrodesulfurization[103] and as a solid lubricant.[104] They can be found along different forms and crystallinity, depending on the oxidation state of Mo and S, as it was reviewed by Afanasiev.[105] Among transition metal sulfides catalysts, molybdenum sulfides have been suggested as active HER electrocatalysts by Hinnemann and coll. in 2005.[86] MoS_2 and amorphous MoS_x as well as the $[Mo_3S_4]^{4+}$ cluster have been studied as catalysts for

the HER, as described in the next section. Though the electrocatalytic performance is lower than platinum (overpotential of 150-180 mV)[106], it appears as a good alternative to platinum.

Moreover, molybdenum is not a scarce element. Though it ranks 54th in average crustal abundance, the production of molybdenum is classified in medium-low volume (33 kt to 1000 kt yr^{-1}), on a scale ranging from high volume (> 1 Mt yr^{-1}) to extremely low volume (< 1 kt yr^{-1}) chemical elements.[107] Molydenum is toxic only on its oxide form, especially during physical or metallurgical treatment when dust or fumes are produced, but molybdenum sulfides are not considered as hazardous.

2.2.1. MoS_2

MoS_2, known as molybdenite in the bulk form, is a crystal with a layered hexagonal structure made from S-Mo-S sheets held together in stacks by van der Waals interactions (Fig. 19). Bulk MoS_2 is a poor catalyst towards hydrogen evolution.[108] In 1991, silica-supported MoS_2 was reported as highly catalytic toward the HER but only in acidic aqueous solution containing vanadate (II).[109]

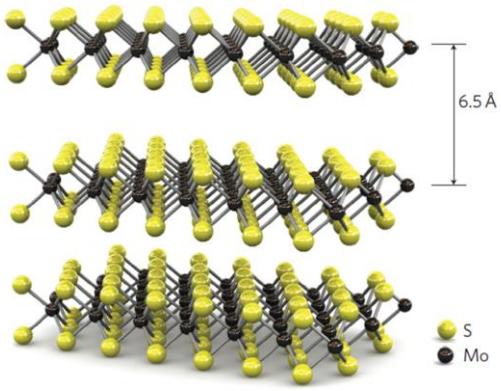

Fig. 19. Three-dimensional representation of the structure of MoS_2. Reproduced from Ref.[216] with permission from Nature Publishing Group.

In 2005, Hinnemann and coll. used density functional calculations to compare the free energy diagram for HER of hydrogen-producing enzymes and of an inorganic analogue, inspired by the catalytic center of nitrogenases. They found that the free energy of adsorbed H (ΔG_H) was close to zero.[86] Thus, they identified MoS_2 edges as potential catalysts for the HER, due to their adsorbed sulfur atoms, and the basal plane as catalytically inactive, so that it appeared important to nanostructure MoS_2 to increase the ratio of edges on basal sites. In the same work, the catalytic activity was verified for carbon-supported MoS_2 nanoparticles. The experimental proof that MoS_2 edges catalyze proton reduction was made in 2007 by Jaramillo and coll.[110]. Nanocrystals, which exhibit a high density of edges, were proved effective in catalyzing HER. In fact, they could add MoS_2 to the volcano plot of the exchange current density as a function of the Gibbs free energy of adsorbed atomic hydrogen (Fig. 20).

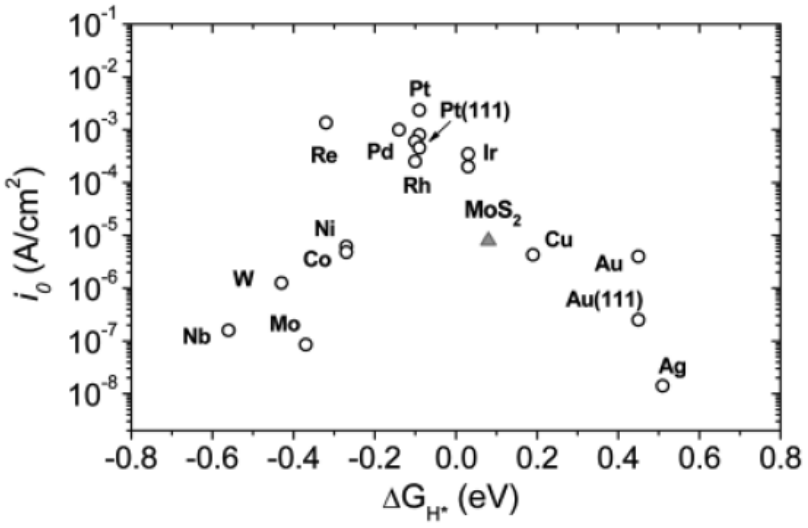

Fig. 20. Volcano plot, representing the exchange current density as a function of the Gibbs free energy of adsorbed atomic hydrogen (HER intermediate) for pure metals and for MoS_2 nanoparticles. Reproduced from Ref[110] with permission from the American Association for the Advancement of Science.

The optimal catalyst lies at the top of the volcano curve, i.e. Pt in the case of HER. At this point, the binding energy of hydrogen is neither too low (in which case the reactant would not be adsorbed enough) nor too high (in which case the products would not leave the surface, blocking the catalytic sites). As shown in Fig. 20, MoS_2 follows the trend observed for pure metals and compares well with existing catalysts.

However, MoS_2 preparation methods usually involve a thermal step which would prevent the formation of the catalyst directly on the organic photovoltaic layer. The catalyst would have to be prepared prior to deposition on the organic solar cell and the transfer of the annealed material would then be challenging. MoS_2 can also be electrodeposited from an aqueous solution directly on an electrode, without annealing step. But this method is not compatible with the fabrication of our devices, since the contact with water would cause an early degradation of the cells.

2.2.2. Molecular $[Mo_3S_4]^{4+}$ complex

Another type of molybdenum sulfide is the incomplete cubane-type $[Mo_3S_4]^{4+}$ cluster (found in salt form such as $[(H_2O)_6Mo_3S_4]Cl_4$), which consists of Mo and S in alternating corners of a cube with one Mo corner missing.[111] This amorphous material is active through under-coordinated sulfur atoms. It is synthesized in solution and can be deposited by dropcasting,[111] allowing the use of other solution-based deposition methods such as spin-coating or spray-coating. The HER onset potential was measured at –200 mV *vs* RHE. In the same work, a lower onset potential was obtained with $[Mo_3S_4]^{4+}$ multilayers on a graphite paper disk in a membrane electrode assembly. However, prior deposition, a treatment to make the substrate hydrophilic was found to be necessary, whereas the P3HT:PCBM layer that we used for the photocathodes is hydrophobic.

2.2.3. Amorphous MoS_3

This sulfur-rich compound was never obtained in a crystalline phase. The oxidation state of Mo has been controversial but was lately established to be +IV.[112]

It can be synthesized by aqueous hydrolysis of MoS_4^{2-} species (acidification of a thiomolybdate solution:[113] $MoS_4^{2-} + 2\,H^+ \rightarrow MoS_3 \downarrow + H_2S$) or by thermal decomposition of ammonium thiomolybdate salt[114] ($(NH_4)_2MoS_4 \rightarrow MoS_3 + 2\,NH_3$) at a temperature below 400 °C to avoid the formation of MoS_2 or MoO_3. It has also been electrodeposited by anodic oxidation of thiomolybdate[115,116] or by cyclic voltammetry stopping at anodic potential.[117] Electrodeposited amorphous films were thoroughly investigated by Pr. Xile Hu's group.[118] The synthesis of MoS_3 nanoparticles reported by Pr. Xile Hu by acidication of a molybdenum oxide and sodium sulfide solution leads to a suspension of nanoparticles.[119] The deposition of this suspension is compatible with organic solar cells, which would not stand chemical or high-temperature treatment, because the as-synthesized nanoparticles are already a functional catalyst, with an onset overpotential of approximately 180 mV and a faradaic yield close to unity. Moreover, the MoS_3 suspension can be deposited in thin films with different thicknesses to develop a greater surface area, thus increasing the number of active catalytic sites. Additionally, the synthesis is low-cost and scalable. These advantages led us to the choice of MoS_3 as catalyst for the photocathodes developed in this thesis. However, the energy band diagram has not been discussed.

2.2.4. Molybdenum sulfides in photocatalytic devices

Molybdenum sulfides are generally not photo-active catalysts, so that they must be used together with an absorber. Before presenting the performance of different photocatalytic devices based on molybdenum sulfides, the relevant characteristics are introduced in Fig. 21. They can be extracted from typical J-E curves obtained for a photocathode under illumination, compared to an electrode made of the catalyst only (or dark electrode). The photocurrent density is the difference between the current density under illumination and in the dark. A relevant value is the one taken at 0 V *vs* the reversible hydrogen electrode (RHE). The photovoltage is the difference between the voltage to reach a current density under illumination and the voltage to reach the same current density in the dark. The onset potential is the electrode potential at a current density of 0.1 mA cm^{-2}. Table 1 compares the photocurrent at 0 V *vs* RHE and onset potential of different PEC devices (or part of PEC devices) based on molybdenum sulfide co-catalysts

MoS_2 was used as a co-catalyst on different particulate photon absorbers such as CdS,[120,121] CdSe,[122] or TiO_2.[123] In a different approach, colloidal MoS_2 was used with a ruthenium complex by Li and coll.[124] An immobilized photoelectrode was prepared by electrodeposition of a nanocomposite polypyrrole-Ru/MoS_x film, delivering around 40 µA cm^{-2} at RHE potential.[125] However, photocurrents in the mA range were mostly obtained with silicon[50,126–128] and Cu_2O[53,129] semiconductors (Table 1). Mo_3S_4

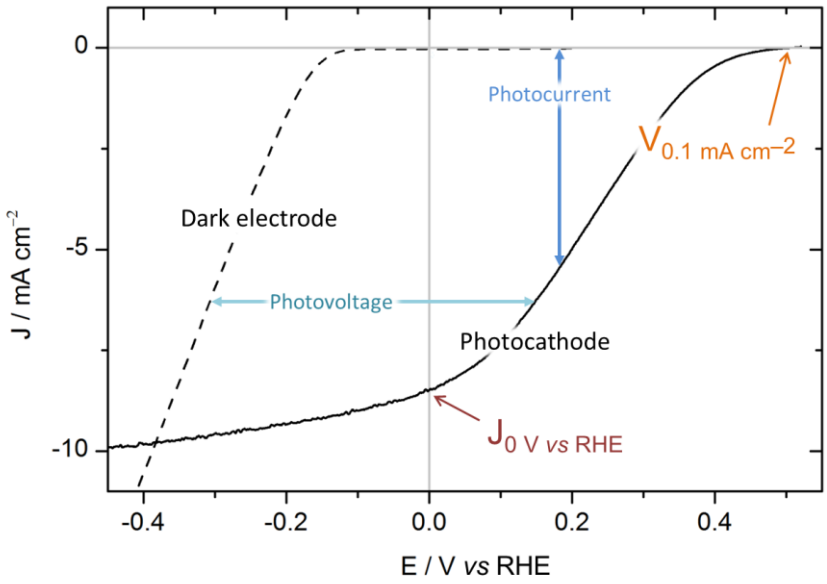

Fig. 21. Current density-potential curve of a photocathode with typical parameters extracted from the data.

cubane-like clusters were deposited by Chorkendorff and coll. on p-type Si and on pillar-structured Si, forming photocathodes for solar HER.[130] As for amorphous molybdenum sulfides, different photoabsorbers were tested, with significant photocurrents and photovoltages. For example, in situ-reduced MoS_3 was photosensitized by CdSe/CdS quantum rods by Alivisatos and coll.[131] Electrodeposited $Cu_2O\backslash MoS_x$ photocathodes were prepared by Hu and coll., and provided a 0.6 V photovoltage[53,129] Chorkendorff's group made a n^+p-Si\Ti\$MoS_x$ photocathode[51] and a n^+p-Si\Mo\$MoS_2$\$MoS_x$ device (MoS_2 was made by evaporation of Mo followed by sulfidization, and used as protective and active layer)[132] for hydrogen production and the effect of interlayers (Ti, Mo) on the performance and stability of the devices was studied.

Table 1. Photoelectrochemical devices using molybdenum sulfides as co-catalyst for the enhancement of hydrogen production from water. * After three MoS_x deposition steps.

	Devices and conditions	Cathodic photocurrent density at 0 V *vs* RHE	Onset potential (100 µA cm^{-2})
	Si-based devices		
Hou and coll.[130] 2011	$[Mo_3S_4]$ on p-Si (planar or pillars) *1 M $HClO_4$; AM 1.5 > 620 nm (28.3 mW cm^{-2})*	8 mA cm^{-2}	+ 0.15 V
Seger and coll.[51] 2012	Photo-electrodeposited MoS_x on Ti-n^+p-Si *1 M $HClO_4$; AM 1.5 > 635 nm (38.6 mW cm^{-2})*	17 mA cm^{-2}	+ 0.33 V (1 mA cm^{-2})
Tran and coll.[126] 2012	Photodeposited MoS_2 on p-type Si-NWs *Na_2SO_4 buffer solution pH 5; 100 mW cm^{-2}*	0.8 mA cm^{-2}	+ 0.25 V
Laursen and coll.[132] 2013	MoS_x/MoS_2/Mo on n^+p-Si *1 M $HClO_4$; 100 mW cm^{-2}*	12 mA cm^{-2} (16 mA cm^{-2} *)	+ 0.35 V (0.4 V*)
Huang and coll.[133] 2013	MoS_3 on Si NWs; *H_2SO_4 with 0.5 M K_2SO_4 (pH 1.7); W-halogen lamp 100 mW cm^{-2}*	24.9 mA cm^{-2}	+ 0.36 V
Zang and coll.[134] 2014	Electrodeposited MoS_3 on p-type Si-NWs *H_2SO_4-K_2SO_4 solution (pH 1); 120 W m^{-2}*	1.5 mA cm^{-2}	~ + 0.2 V
Seger and coll.[135] 2014	Mo_3S_4 on TiO_2/Ti/n^+p-Si *1 M $HClO_4$; AM 1.5 > 635 nm*	20 mA cm^{-2}	+ 0.32 V (1 mA cm^{-2})
Benck and coll.[50] 2014	MoS_2/Mo/n^+p-Si; Mo_3S_{13}/MoS_2/Mo/n^+p-Si *0.5 M H_2SO_4; simulated AM 1.5 solar illumination*	17 mA cm^{-2} 17 mA cm^{-2}	+ 0.32 V (0.5 mA cm^{-2}) + 0.40 V (0.5 mA cm^{-2})
Ding and coll.[127] 2014	Exfoliated 1T-MoS_2 on p-Si *0.5 M H_2SO_4; 1 sun (100 mW cm^{-2})*	17.6 mA cm^{-2}	+ 0.25 V
Zhang and coll.[128] 2015	MoS_2/TiO_2/n^+p-Si NWs *0.5 M H_2SO_4; simulated AM 1.5 G illumination (100 mW cm^{-2})*	15 mA cm^{-2}	+ 0.3 V
	Cu_2O-based devices		
Morales-Guio and coll.[53] 2014	Photo-electrodeposited MoS_x on Cu_2O\AZO\TiO_2 *pH 1; simulated AM 1.5 solar illumination*	5.7 mA cm^{-2}	+ 0.45 V

Morales-Guio and coll.[129] **2015**	Photo-electrodeposited MoS_{2+x} on Cu_2O\AZO\TiO_2 *1 M KOH; simulated AM 1.5 solar illumination*	6.3 mA cm^{-2}	+ 0.48 V
	Polymer-based devices		
Lattach and coll.[125] **2015**	Electrodeposited polypyrrole-Ru(2,2'-bipyridine)$_3^{2+}$/MoS_x *0.5 M H_2SO_4; 150 W Xe lamp with 400-700 nm filter*	~ 40 µA cm^{-2}	

2.3. From MoS_3 nanoparticles to electrocatalytic MoS_3 thin films

2.3.1. Synthesis

MoS_3 particles were synthesized according to a procedure reported by Prof. Xile Hu and coll.[119] A detailed procedure is given in the experimental section. In a typical preparation, molybdenum trioxide (MoO_3) is added to an aqueous solution of sodium sulfide (Na_2S), resulting in an alkaline light yellow solution (pH > 12). Under stirring, 6.0 M aqueous hydrochloric (HCl) acid is added dropwise until the pH is below 4 (Equ. 1).

$$Na_2S_{(aq.)} + MoO_{3\,(aq.)} \xrightarrow{HCl_{18\,\%}} MoS_{3\,(s.)} \qquad \text{Equ. 1}$$

The dark brown suspension is refluxed for 30 min. After cooling, the particles are separated by centrifugation and washed thoroughly with water, ethanol, ether, and finally dispersed in acetone by sonication. They are not dispersible in protonated solvents such as water, ethanol or isopropanol. The obtained sol (suspension of nanoparticles) is yellow-brown and very homogeneous, with concentrations of 5-15 g L^{-1}, and is stable when stored in a protected atmosphere (e.g. Ar-filled glovebox). As the particles are never really dried, the yield was evaluated by estimating the mass concentration of the suspension (by thermal gravimetric analysis and UV-visible spectroscopy); and it was 90-97 % depending on the separation of the nanoparticles during centrifugation.

The impact of the synthesis parameters had not been reported. Thus, the following parameters have been changed to study how they impact the material:

- the pH at the end of the synthesis
- the rate of the addition of acid
- the time of the boiling step
- the temperature of heating for the boiling step
- the decantation before filtration (the decantation was followed by UV-visible but no changes of absorption were visible along the time)

The parameters were studied following a methodology of experimentation, which is based on an experiment matrix (cf. Appendix 5) in order to limit the number of experiments. In our case, only four batches were prepared to evaluate the different parameters. The electrocatalytic activity was measured at a given potential to compare the results. The voltammetric analyses were not significantly different, and it was concluded that these parameters did not influence the electrocatalytic activity.

During synthesis, it was noticed that when the acidification was stopped too early (pH = 4), the particles were very small and difficult to separate, whereas a lower pH (pH = 2) caused the aggregation of the particles, easing the subsequent separation and washing process by centrifugation. But when the nanoparticles were redispersed in acetone, no visual difference could be observed. To ascertain that there was no effect on the particles, three batches were prepared, stopping at three different pHs: 2.0, 2.7 and 3.5. These batches were then analyzed by transmission electron microscopy (TEM) to evaluate the size of the nanoparticles, and by electrochemistry to verify the electrocatalytic activity.

2.3.2. Analysis of the MoS_3 suspension in acetone

2.3.2.1. Morphology

TEM analysis was performed on MoS_3 nanoparticles (pH at the end of the synthesis: 2.0). The MoS_3 suspension was deposited on a copper grid with a full amorphous carbon membrane.

As confirmed by the diffraction pattern (measured on agglomerated particles), the compound is completely amorphous. The particles do not have a regular form or size. Their size ranges from a few nanometers to bigger aggregates of several tens of nanometer (Fig. 22).

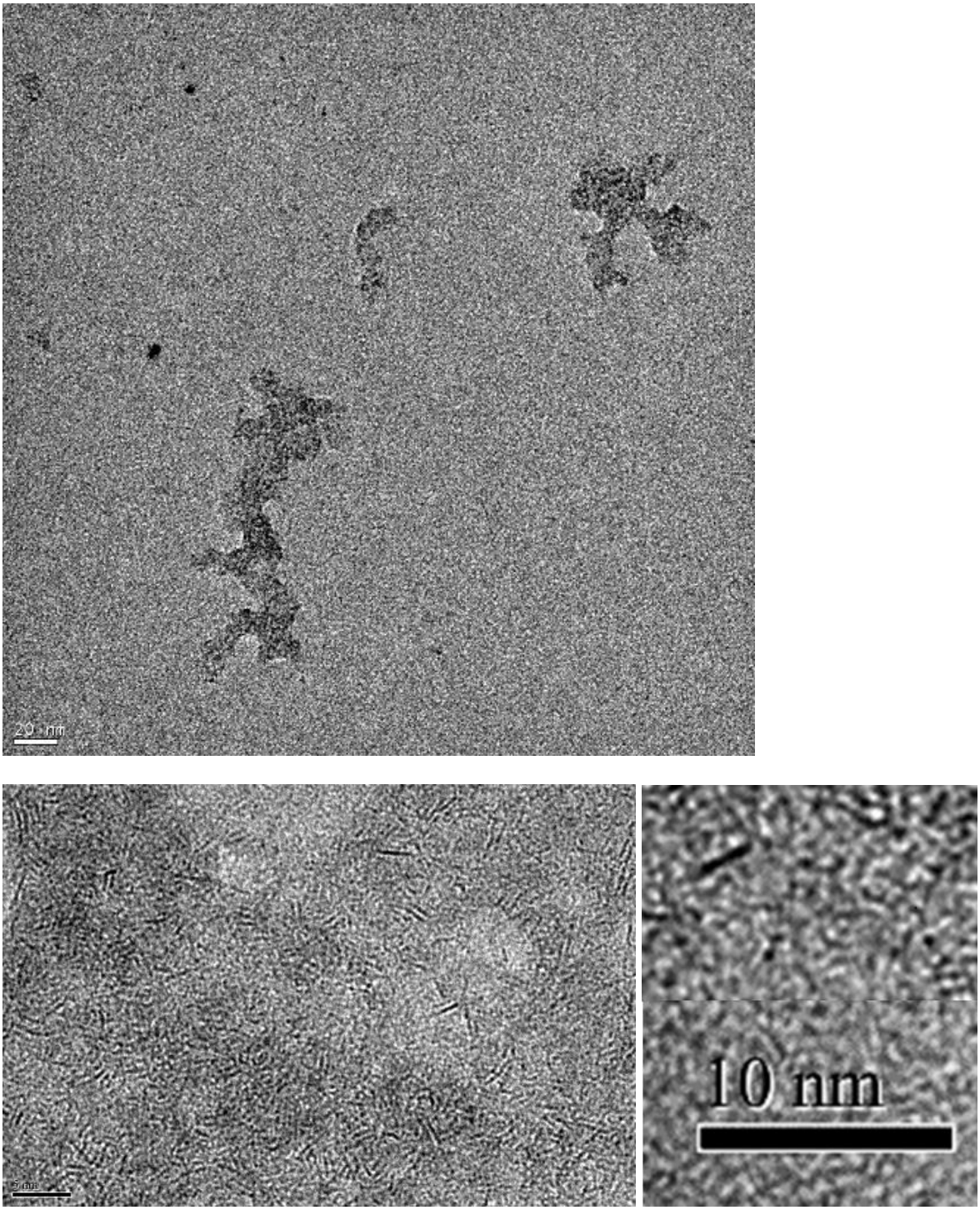

Fig. 22. *Up:* TEM analysis of precipitated MoS_3 nanoparticles (final pH was 2). Scale bar is 20 nm. *Down:* Scale bar: 5 nm (right). Enlarged area to show rods and small dark areas (Ø ~4Å), scale bar is 10 nm (left).

TEM analysis was performed for three batches of MoS_3 nanoparticles (pH at the end of the synthesis: 2.0, 2.7, 3.5, Fig. 23). Amorphous particles with similar sizes and shapes were obtained. It was concluded that the final pH had no significant influence on the individual particle size, especially since

the particle size distribution is broad. As it is easier to separate the particles when the synthesis is stopped at a low pH (under 3), all further syntheses were stopped at pH 2.5 approximately.

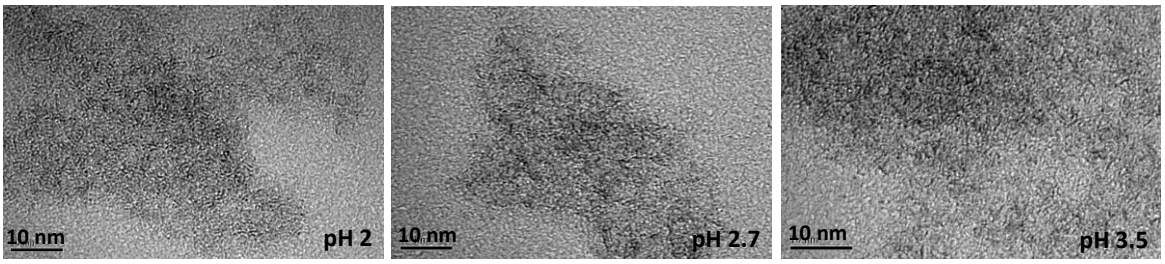

Fig. 23. TEM images of MoS_3 nanoparticles. The pH at the end of the precipitation was pH = 2.0, pH = 2.7 and pH = 3.5.

The structure of MoS_3 has been widely discussed since the first studies by Ratnasamy and coll.[136] Two main structures have been considered (Fig. 24): a-MoS_3 consisting of disordered chains[112] and MoS_3 built from Mo_3 triangles.[137]

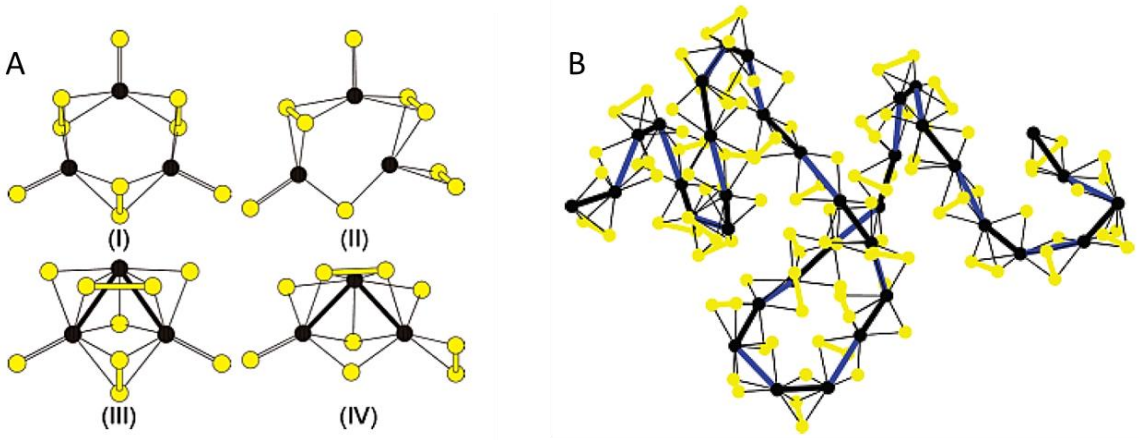

Fig. 24. (a) Energy-minimized isolated Mo_3S_9 clusters[138] (solid circles: Mo, yellow circles: S). (b) Portion of the $Mo^{IV}(S^{2-})_2(S_2^{2-})_{1/2}$ chain model (solid circles: Mo, yellow circles: S, Mo–Mo bonds: thick black line, long nonbonded Mo–Mo distance: blue line). Adapted with permission from Ref.[112]. Copyright (2004) American Chemical Society.

Hibble and coll. showed that the chain model and the formula $Mo^{IV}(S^{2-})(S_2^{2-})$ fits well with their experimental results.[112] At first, the small dark areas of ~4 Å diameter observed in MoS_3 nanoparticles (Fig. 22) were thought to correspond to triangular Mo_3 clusters surrounded by sulfur atoms[137] knowing that Mo-Mo distances lie in the observed range (≈ 2.7 Å and ≈ 3.7 Å)[138] while the 1-2 nm long rods better fitted with the chain model. However, more recent studies showed that the small rods might correspond to poorly crystalline MoS_2[139] located in the bulk of larger particles (10-100 nm). Further investigation would be necessary to have a more precise idea of the structure, which is still under discussion in the literature.

2.3.2.2.Composition: EDX, XPS

Energy-dispersive X-ray spectroscopy

When a sample is subjected to an X-ray beam, an electron of an inner shell can be excited, creating an electron-hole pair. An electron from a shell of higher energy can fill the hole and the energy is liberated as X-rays. The set of emitted X-rays is characteristic of the atomic structure, and can be used to identify an element. EDX analysis was carried out in Collège de France thanks to Pr. Laberty-Robert (UMR 7574 – Laboratoire de Chimie de la Matière Condensée) during TEM analysis.

EDX analysis (Fig. 25) shows molybdenum and sulfur, as well as residual traces of elements such as sodium and oxygen present in the starting materials, and carbon coming from atmospheric contamination. Mo and S peaks are overlapping, inducing quantification errors in the Mo:S atomic ratio. Thus, the ratio has been estimated by XPS.

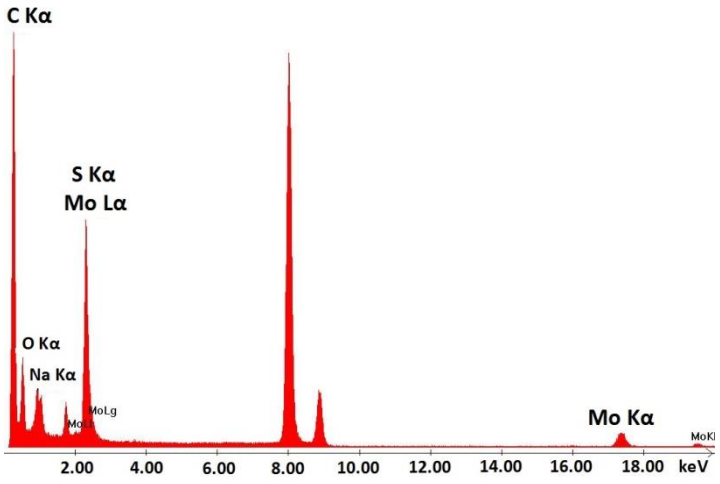

Fig. 25. EDX spectrum of MoS_3 particles (final pH = 2.7) deposited on a copper grid, measured on an aggregated area.

XPS

Contrary to EDX which probes in the bulk of the sample (1-2 µm in depth) by detecting emitted X-rays, XPS is a surface-sensitive technique, probing approximately the first 10-15 nm of the substrate by measuring the amount and kinetic energy of ejected electrons. The kinetic energy can be related to the binding energy of the electrons, which is also a characteristic of the electronic structure of each element present in the compound.

Chemical and electronic states of MoS_3 thin films deposited on indium tin oxide (ITO)-coated glass substrates, and commercial MoS_2 and MoO_3 were analyzed. MoS_2 and MoO_3 spectra are shown in Appendix 2.

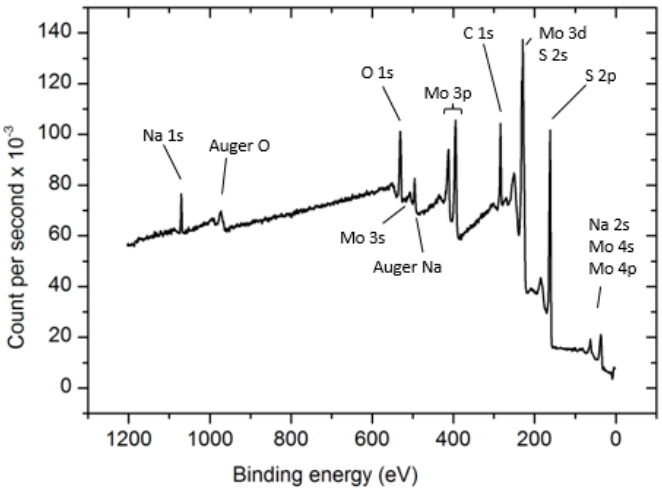

Fig. 26. X-ray photoelectron survey spectrum of spin-coated MoS_3 films (final pH = 3)

The main peaks in the XPS survey spectra (Fig. 26) come from molybdenum and sulfur, but some minor peaks corresponding to impurities are obtained, such as sodium and oxygen (present in the precursors used for the synthesis), and carbon (atmospheric contamination). It has been reported however that MoS_3 can be found in a hydrated form (e.g. $MoS_3.2H_2O$),[140] which can explain the presence of oxygen. The ratio of the S and Mo areas yielded to a S to Mo ratio of 2.9 in the as-synthesized compound, in agreement with the targeted material. Detailed spectra and analysis of Mo 3d and S 2p are presented in section 2.3.5.1.

MoS_3 was then processed into thin films in order to further characterize the material in the device conditions.

2.3.3. Deposition into thin films

Prior to the deposition of the catalyst on the organic solar cell, the electrocatalytic activity of the catalyst alone has been studied. Thin films of catalysts, deposited in a reproducible manner, are an important pre-requisite for the study of the electrochemical activity, which may be impacted by different factors such as thickness or roughness. From the MoS_3 suspension in acetone, different deposition techniques can be employed, depending on the scale of the device fabrication. In the article in which the synthesis of MoS_3 was published,[119] molybdenum sulfide was deposited by spray-coating or drop-casting, allowing deposition on a wide range of substrates.[119] For the purpose of depositing MoS_3 onto an OSC, it is important that the OSC does not remain in contact with the solvent for long periods of time. Drop-casting is not compatible, because the OSC would be in contact with the solvent for the time it takes to dry. Moreover, it would be difficult to homogeneously cover the entire OSC surface. Dip-coating, which is another thin film deposition technique, is also not compatible because the substrate is entirely in the solvent and is slowly taken out. Spray-coating and spin-coating are both interesting for our purpose, since it allows the deposition of thin films in a reproducible and scalable

manner, without prolonged contact with the solvent. Spin-coating and spray-coating are presented briefly in the following subsections.

2.3.3.1.Spin-coating

Spin-coating is a method to deposit a film from a suspension or a solution. The high-speed rotation of the substrate allows the material to spread on the surface and dry. The films are very well controlled by several parameters (rotation speed, concentration of the solution, …). Thus, spin-coating was initially chosen as it was suitable for the targeted thickness, i.e. in the range of 10 - 100 nm. However, the surface tension between the substrate and the solvent of the spin-coated solution is important. For example, a hydrophilic treatment (in a UV-ozone cleaner) was found necessary to form defect-free films.

The MoS_3 suspension is deposited on clean ITO-coated glass substrates (see the experimental section for the detailed procedure).

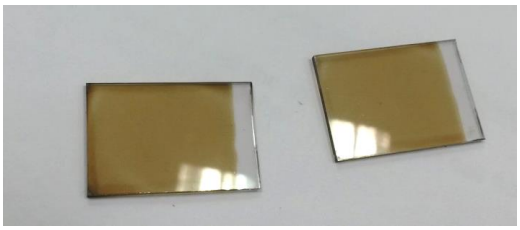

Fig. 27. Spin-coated films of MoS_3 on ITO-coated glass substrates.

The thickness was measured by profilometry on a scratch (approximately 100 µm wide). Changing the rotation speed or the acceleration rate did not change the thickness, which could be explained by the low viscosity of the suspension. Variation of the thickness of the layers was achieved by changing the concentration of the MoS_3 suspension (Fig. 28). Because the MoS_3 nanoparticles were obtained directly as a suspension of nanoparticles without any drying steps, the concentration could not be obtained by weighing a powder and dilute it in the right amount of solvent. Instead, the concentration was evaluated by thermogravimetric analysis (TGA).

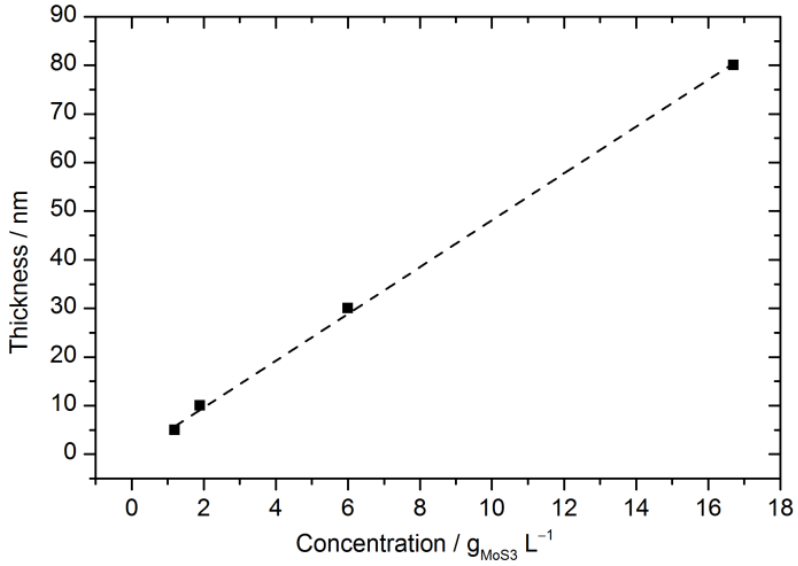

Fig. 28. Thickness of MoS_3 films deposited by spin-coating from MoS_3 suspensions in acetone with various concentrations. The thickness was measured on a thin scratch in the film by profilometry and the concentration was evaluated by TGA.

UV-visible spectroscopy was performed on the thin films to establish a calibration curve between thickness and absorbance at a given wavelength (for MoS_3 thin films on ITO: 350 nm), as a tool to measure the thickness without scratching the substrate (Fig. 29).

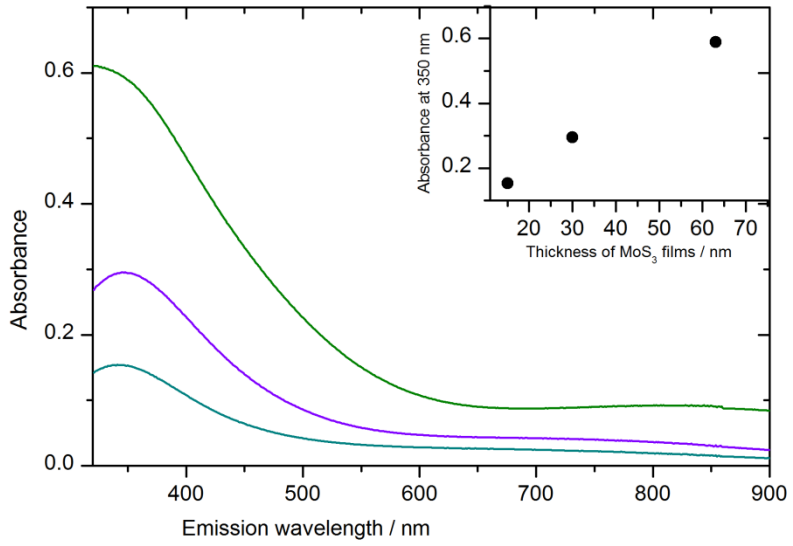

Fig. 29. UV-visible spectrum performed on MoS_3 films on ITO (blue / bottom line: 15 nm, purple / middle line: 30 nm; green / top line: 70 nm). Inset: absorbance at 350 nm *vs* thickness of the spin-coated MoS_3 film on ITO.

2.3.3.2.Spray-coating

Spray-coating is a method which has been developed in parallel to deposit MoS_3 layers. Since the substrate can be heated, spray-coating can be applied to a wide variety of substrates. High control and reproducibility can be achieved with the use of high-technology apparatus. In our conditions, MoS_3 films were sprayed with a simple airbrush, not allowing the same control and homogeneity. The airbrush was loaded with the suspension and sprayed onto a heated substrate, which is maintained vertically against a heated support (Fig. 30).

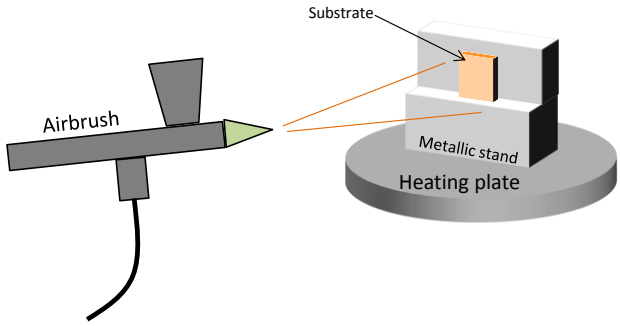

Fig. 30. Setup used for the spray in our lab. The airbrush was operated at 2.5 bar.

The sprayed film was not reflecting light (Fig. 31), indicating a higher roughness than the spin-coated films.

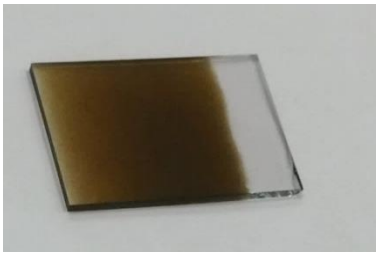

Fig. 31. Sprayed films of MoS_3 on ITO-coated glass substrates.

Pictures taken with an optical microscope (Fig. 32) allows the visualization of the grains in the case of sprayed films, while MoS_3 is much more homogeneously deposited by spin-coating.

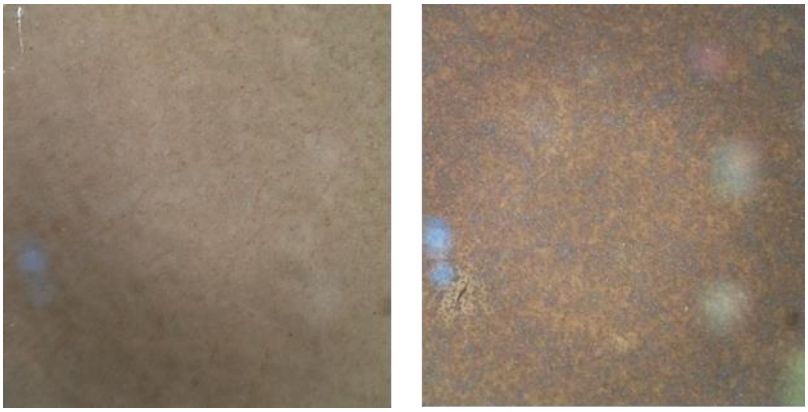

Fig. 32. Pictures taken with an optical microscope of a spin-coated film (left) and a sprayed film (right) of MoS_3

Profilometry carried out on these films confirms the difference of roughness (Fig. 33). Based on the arithmetic average of absolute values, the profile roughness is approximately 15 nm for the spin-coated film and 81 nm for the spray-coated film. Moreover, thicknesses achieved with sprayed films are larger (ranging from 100 nm to 1 µm, but with several hundreds of nanometers between the lowest and highest points of the film), partly because MoS_3 had to be sprayed for a long time to ensure complete coverage in our conditions. The incidence on the electrochemical performance is investigated in subsection 2.3.5.1.

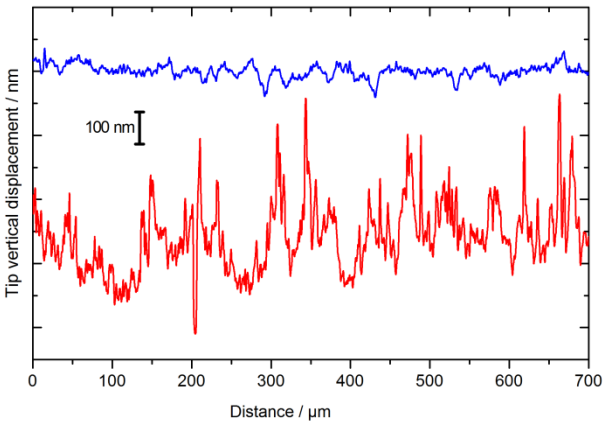

Fig. 33. Profiles measured by a profilometer, for a spin-coated (blue / top line) and a spray-coated (red / bottom line) film. An offset has been applied between the two profiles.

2.3.4. Analysis of the thin films

2.3.4.1. Energy band structure

In order to have enough energy to reduce protons, the photogenerated electrons must have a higher energy than the H^+/H_2 redox level. Thus, the Fermi level energy of the MoS_3 catalyst should be above the H^+/H_2 redox level. Moreover, in the organic photovoltaic layer, the photogenerated electrons have the energy of the LUMO of the acceptor molecule (PCBM) and are then transmitted to MoS_3. Thus, the Fermi level energy of MoS_3 should preferably be below the PCBM LUMO level. All in all, the Fermi level of MoS_3 should be between the LUMO level of PCBM and the H^+/H_2 redox level (Fig. 34).

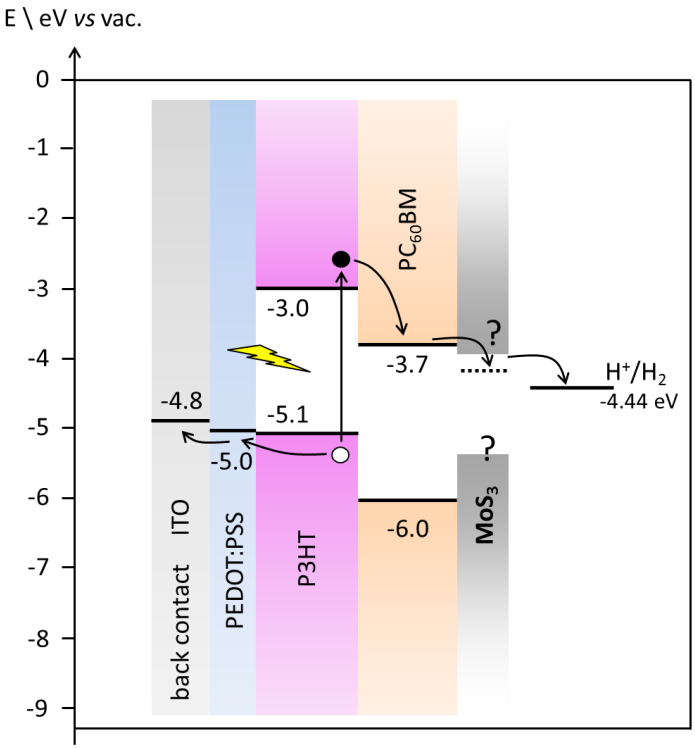

Fig. 34. Schematic illustration of the energy level alignment in the photocathode and the desired position of the MoS_3 work function between the LUMO level of PCBM and the Fermi level of the electrolyte.

The energy band diagram of MoS_3 has been evaluated in order to know where its conduction band and Fermi level were located comparatively to the LUMO level of PCBM and the redox level of the electrolyte. Different techniques were combined for this purpose.

Optical bandgap

MoS_3 is an amorphous semiconductor which absorbs part of the visible light, resulting in the promotion of an electron from the valence band to the conduction band, but it is not a photo-active catalyst. In the photocathode, the photovoltaic effect is entirely carried out within the organic

P3HT:PCBM layer and not by the catalyst. UV-visible spectroscopy was used here to determine the optical bandgap, that is, the threshold for photons to be absorbed, in order to have information on the energy band diagram of MoS_3.

When a semiconductor absorbs a photon, there are two types of optical transitions: direct and indirect. The direct transition involves photons only, while the indirect transition involves simultaneous interaction with lattice vibrations called phonons (Fig. 35).

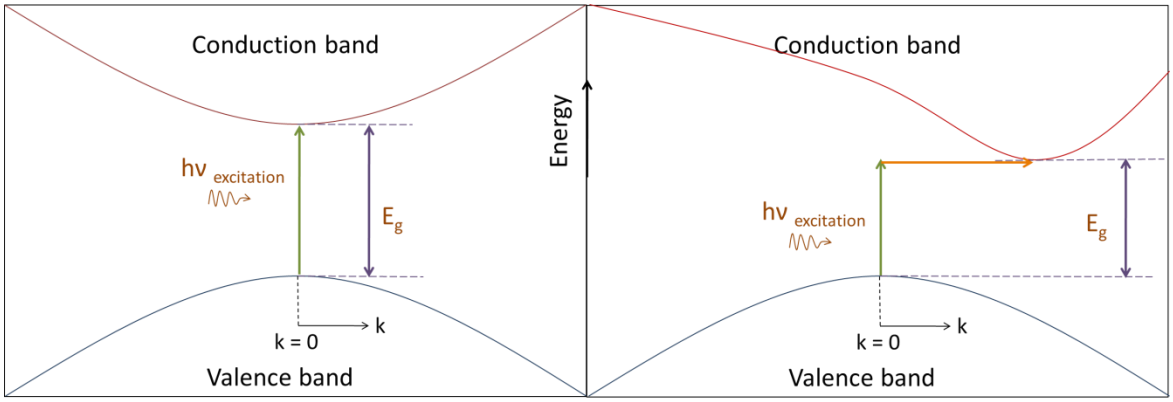

Fig. 35. Direct (left) and indirect (right) transitions from valence band to conduction band.

The determination of the optical bandgap of amorphous MoS_3 has been carried out on thin films deposited by spin-coating onto glass substrates (96 % optical transparency). Sprayed MoS_3 films were not analyzed because they have a higher roughness, which can modify the light path in the material and induce errors in the analysis. Film thicknesses in the range from 15 nm to 63 nm were deposited

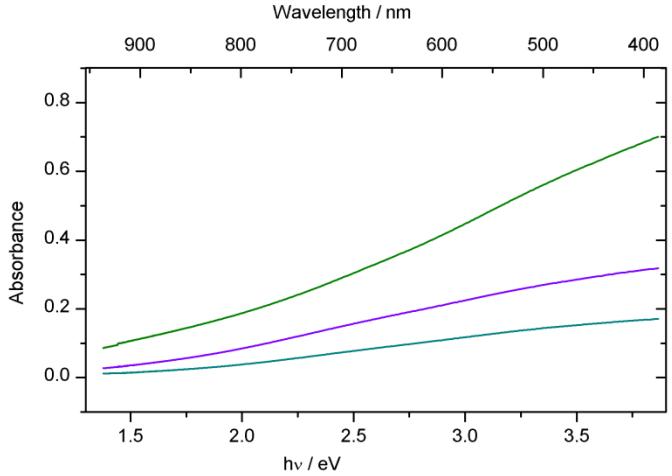

Fig. 36. Absorption spectra in the range of 1.4 to 3.8 eV for MoS_3 thin films on glass substrates (blue / bottom line: 15 nm; purple / middle line: 30 nm; green / top line: 63 nm).

on glass substrate. The optical transmission spectra were taken at room temperature and a glass substrate was always used as a reference in the double-beam spectrophotometer.

The spectral dependence of the absorption coefficient α was evaluated from the transmission spectra by using the following relation:

$$\alpha = -\frac{\ln T}{t} \qquad \text{Equ. 2}$$

where T is the transmission and t is the thickness of the films.

In the high absorption region ($\alpha > 10^4$ cm^{-1}), the spectral dependence of the absorption coefficient can be described by the Tauc relation for amorphous semiconductors:[141,142]

$$\alpha = \frac{C}{h\nu}(h\nu - E_g)^n \qquad \text{Equ. 3}$$

C is a constant, h is Planck's constant, E_g is the average bandgap of the material and n depends on the type of transition. For n = ½, E_g is a direct allowed bandgap, and for n = 2, E_g is an indirect allowed transition.

For a direct transition, the average energy gap can be estimated with the following relation:

$$(\alpha h\nu)^2 = C\,(h\nu - E_g) \qquad \text{Equ. 4}$$

For an indirect transition, the relation is:

$$(\alpha h\nu)^{1/2} = C\,(h\nu - E_g) \qquad \text{Equ. 5}$$

The procedure consists in plotting $(\alpha h\nu)^2$ versus $h\nu$ and $(\alpha h\nu)^{1/2}$ versus $h\nu$. From the plot leading to the straight plot, it can be inferred whether the fundamental bandgap is direct or indirect. Then the bandgap value is estimated by extrapolating the linear region of the curve to the energy axis, as shown in Fig. 37.

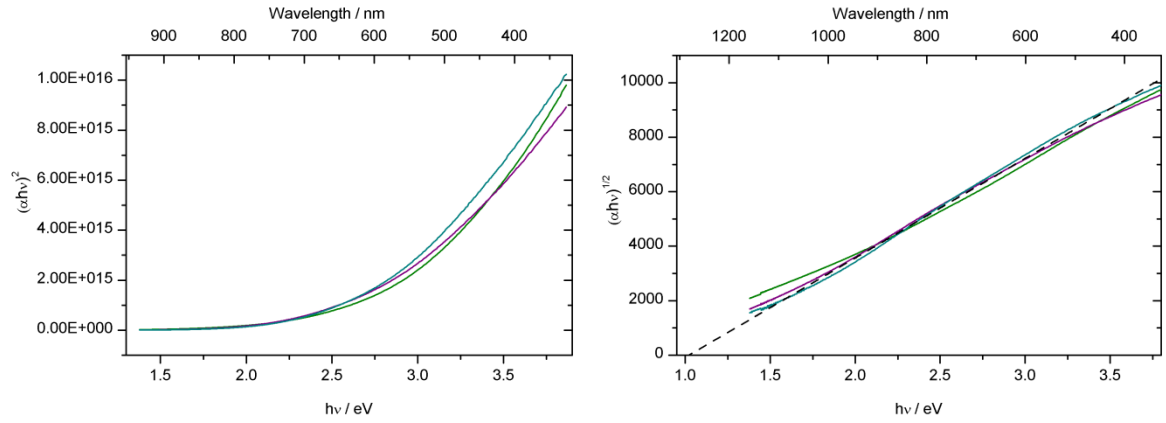

Fig. 37. Plots $(\alpha h\nu)^2$ versus $h\nu$ and $(\alpha h\nu)^{1/2}$ versus $h\nu$ for MoS_3 films on glass (blue: 15 nm, purple: 30 nm, green: 63 nm). On the right, the linear part has been extrapolated to the abscissa from the curve of the 15 nm film (dashed line).

The transition type appears to be indirect, with an optical band gap value close to 1 eV. Table 2. presents the optical band gap values obtained with the different thicknesses.

Film thickness	**15 nm**	**30 nm**	**63 nm**
Optical band gap (eV)	1.02	0.92	0.79

Table 2. Optical band gap calculated from $(\alpha h\nu)^{1/2}$ versus $h\nu$ plots (i.e. in the case of an indirect band gap) for MoS_3 thin films deposited by spin coating

Considering the imperfect linearity of the lines, the value of the optical bandgap has been taken at 0.9 ± 0.1 eV.

Electrochemical bandgap, valence and conduction bands

Cyclic voltammetry (CV) has been employed in the quantitative estimation of the HOMO and LUMO levels of electro-active molecular species for organic electronics.[143] The electrochemical determination of the band structure of semiconducting nanoparticles in suspension has also been reported.[144–146] Like organic compounds, semiconductors undergo electron transfer, through the valence band edge and conduction band edge. The current onset potential of oxidation (resp. reduction) peak can be linked to the edge of the valence band (E_{VB}) (resp. conduction band E_{CB}) because electronic transfers are allowed when the energy levels of the band and of the electrode potential are aligned. From these values, an electrochemical band gap energy $E_{g,el}$ can be calculated. It differs from the optical band gap energy $E_{g,opt}$: these two energy gaps refer to different processes. $E_{g,el}$ is the energy required to remove

an electron from the highest occupied level of a particle in the material and place this electron in the lowest unoccupied level of an independent identical particle of the material. $E_{g,opt}$ is the minimum photon energy needed to create an interacting electron–hole pair within the material. The optical bandgap is thus usually lower than the electrochemical bandgap because the electron-hole pair, which has a binding energy, does not need to be separated on two different particles.

Voltammetric measurements were performed in a conventional three-electrode setup in N_2-saturated 0.5 M H_2SO_4. The electrochemical analysis is detailed in section 2.3.5. MoS_3 was sprayed on FTO to be used as working electrode. Fig. 38 left shows the electrochemical response of MoS_3 when the potential is swept towards anodic potentials and Fig. 38 right when the initial scan direction is towards cathodic potentials.

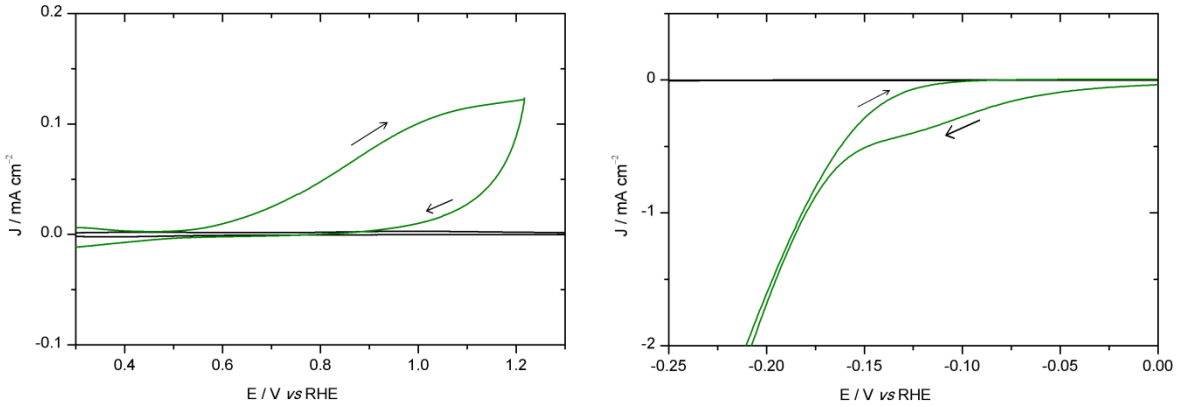

Fig. 38. *Left*: cyclic voltammograms (50 mV s^{-1}) in N_2-saturated 0.5 M H_2SO_4 with starting scan direction towards anodic potentials. *Right*: cyclic voltammograms (50 mV s^{-1}) in N_2-saturated 0.5 M H_2SO_4 with starting scan direction towards cathodic potentials Black line: background scan of FTO. Green line: MoS_3 on FTO.

The peak starting with an onset at 0.6 V is assigned to the oxidation of the filled valence band of MoS_3. The valence band maximum (or edge) should be the first state oxidized in the voltammetry measurement, in the absence of surface states. This hypothesis can be discussed since MoS_3 probably has surface states in the bandgap, or at least tailing band edges, due to its amorphous nature, which can be oxidized before the valence band. By taking the absolute potential of the RHE (which is equivalent to the NHE in these conditions), the onset oxidation potential (E_{ox}) can be converted to the VB energy versus vacuum (E_{VB}) by way of the equation: $E_{VB} = -[4.44 + E_{ox\ vs\ RHE}]$ eV. The energy of the VB edge is thus calculated at approximately –5.05 eV *vs* vacuum.

During the initial cathodic scan, a reduction peak started at −0.05 V. This peak is analyzed in section 2.3.5.1. Similarly to the oxidation peak, the reduction can be assigned to the edge of the conduction band, and is calculated at −4.4 eV.

The electrochemical band gap is thus approximately 0.65 V, in the same range than the optical bandgap.

This method has the advantage of being simple and easy to carry out. However, the use of cyclic voltammetry to investigate the band structure and electronic properties of semiconductors remains a complicated method. The thickness of the material layer, the surface state, etc…, can significantly influence the electrochemical responses.

X-ray photoelectron spectroscopy (XPS)

A valence band spectrum can be obtained with XPS. The energy of the electrons corresponds to the energy of the valence band and of inner levels. It was measured on a spin-coated film of MoS_3 on glass. The difference between the Fermi level (cf. Inset 2) and the valence band was measured at approximately 0.8 eV (Fig. 39).

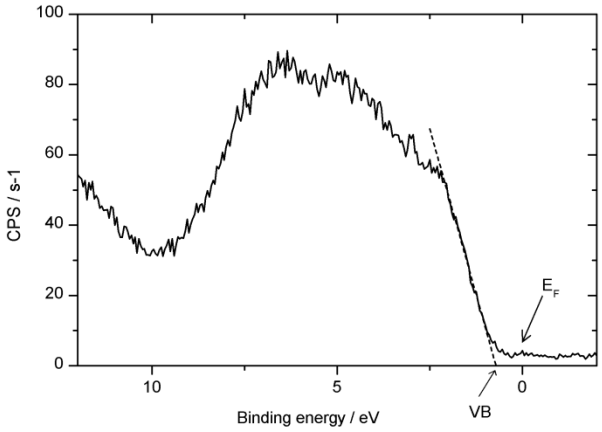

Fig. 39. Valence band spectrum measured by XPS. Calibration was carried out with gold as reference. The Fermi level is by definition at 0 eV, and the valence band is extrapolated to y = 0 at 0.8 eV.

For this type of experiment, ultraviolet photoelectron spectroscopy (UPS) would allow a more accurate determination of the valence band spectrum and the Fermi level.

Kelvin probe force microscopy

Kelvin Probe Force Microscopy (KPFM) is a contactless technique which evaluates the work function of a material. The working principle is based on the difference of surface potentials between a metallic probe and the studied material. When two metals are in contact, their Fermi levels line up. If they are kept at a small distance, a difference of electric potentials exists, and the system can be considered as a capacitance. If the two metals are connected in an electrical circuit with a voltage source, the voltage difference can be cancelled by the application of the voltage by the source. However, the access to this tension is not straightforward, as the current change (when the voltage is changed) is transient, so that

the measured current is zero. The solution is to vibrate the probe with a piezoelectric. The change in the distance between the materials causes the capacitance to charge and discharge itself. The current is thus oscillating (around 0).

During a KPFM measurement, the voltage is changed regularly and the current is measured. The voltage which cancels the current is the voltage corresponding to the Fermi level difference between the two materials. As the Fermi level of the probe is known, the Fermi level of the studied material is inferred from the measurement. Fig. 40 shows the data obtained for MoS_3 deposited on glass by spin-coating. A value of 0.3 eV is obtained, which is the Fermi level difference between the gold probe and the sample. With the gold work function taken at 5.1 eV, it corresponds to a work function of 5.4 eV for MoS_3. Because the measurements are very sensitive to the surface state (absorbed molecules, roughness, …) as well as the quality of the vacuum in the KPFM setup, other materials were tested and their work function were compared to literature values. They were always found larger (approximately 0.8-0.9 eV larger) than the reported values. As an example, the work function of mesoporous TiO_2 was measured at 5.8 eV, larger than the ~4.9 eV values reported in the literature.[147] MoS_3 work function was corrected by 0.9 eV, bringing its value down to 4.3 eV. This value places the Fermi level right under the conduction band edge.

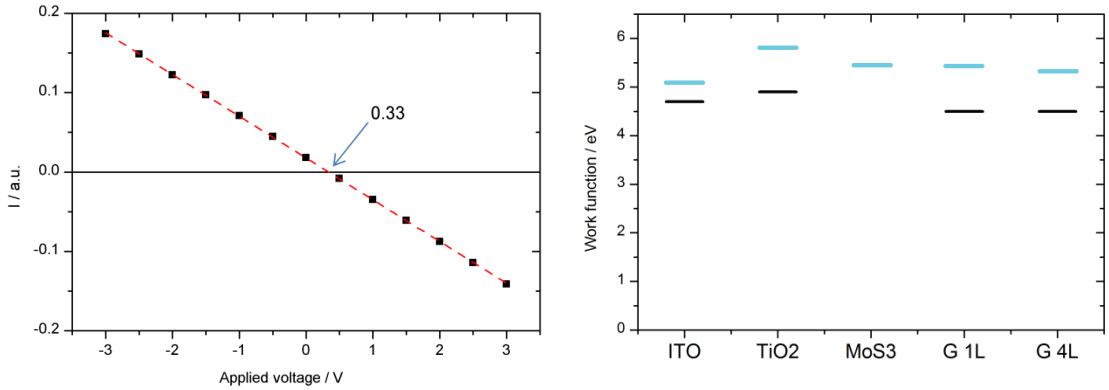

Fig. 40. *Left*: data points obtained by KPFM for MoS_3 spin-coated on glass. Red dashed line: linear fit of the experimental points. *Right*: Measured work function (blue dashes) and values from the literature (black dashes) for ITO, TiO_2, MoS_3 and graphene (G 1L = graphene monolayer, G 4L = graphene multilayer with approximately 4 layers), deposited on glass substrates.

Energy diagram of MoS_3 and its impact on the energy diagram of the device

From the results of all the different techniques, an energy band diagram of MoS_3 can be drawn (Fig. 41 left) based on the optical bandgap value of 0.9 eV (UV-visible spectroscopy), the valence band level at –5.1 eV (electrochemistry) and the difference between the valence band and the Fermi level of 0.8 eV (placing the conduction band at –4.3 eV). The values should be taken at ± 0.2 eV because of

the use of several experimental techniques. The Fermi level of MoS_3 is located approximately between the LUMO level of PCBM and the Fermi level of the electrolyte, as desired (Fig. 41 right).

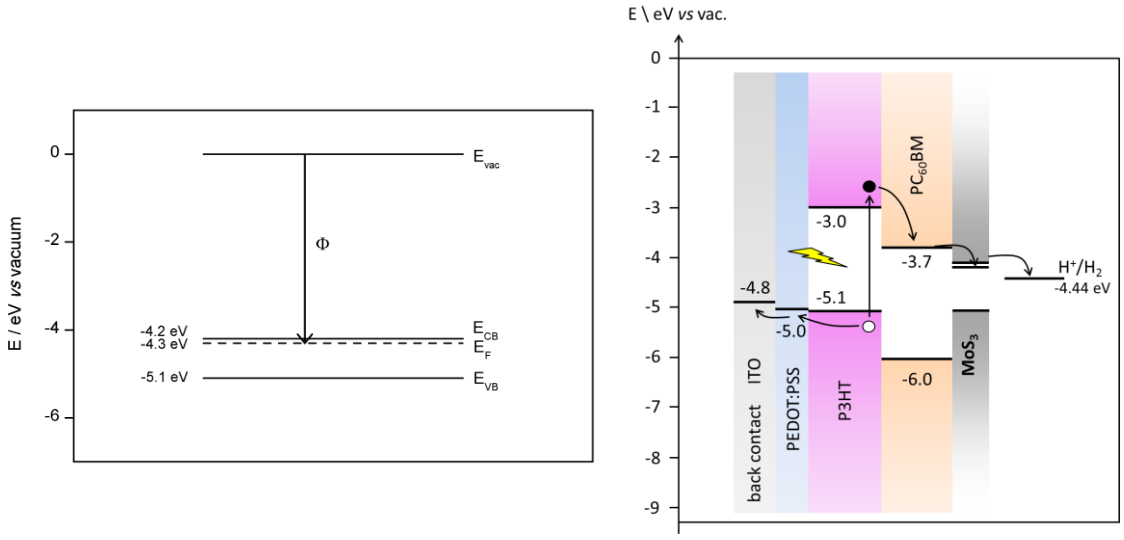

Fig. 41. Energy band diagram of MoS_3 (left) and schematic illustration of the energy level alignment in the photocathode with the obtained Fermi level of MoS_3 (right).

2.3.5. Electrocatalytic activity of MoS_3

In this part, the electrocatalytic activity of MoS_3 has been studied in order to further characterize the material and to determine the optimal working conditions of the catalyst in which the photocathodes would be tested. First, the catalyst was deposited on a transparent conducting electrode, ITO, with the methods developed in section 2.3.3. ITO-coated glass substrates were chosen because MoS_3 thin films can be deposited by spin-coating over a large area and these substrates are the same one that are later used for the photocathodes. Once the deposition of the catalyst has been performed, the MoS_3 films onto ITO have been used as a working electrode. The electrocatalytic activity has been tested toward several parameters, such as proton concentration or film thickness.

2.3.5.1. Cyclic voltammetry

Voltammetry is an electrochemical experiment consisting in sweeping the working electrode potential in a time-linear fashion and measuring the current going through the working electrode. In a cyclic voltammetry experiment, the electrode potential is swept between two potentials during one or several cycles.

A CV of a typical spin-coated MoS_3 film in N_2-saturated aqueous 0.5 M H_2SO_4 is presented in Fig. 42 (red line). The onset reduction potential is *ca.* –0.15 V *vs* RHE.

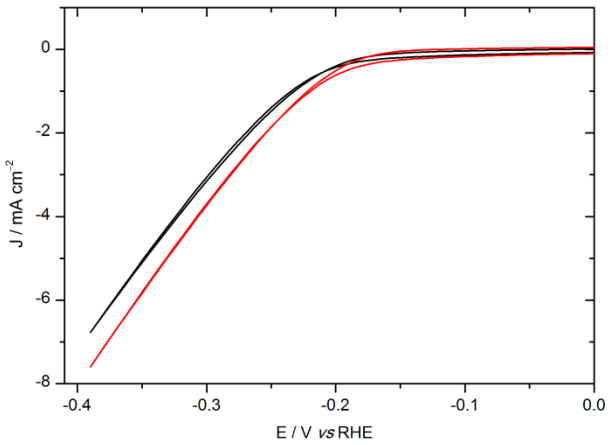

Fig. 42. Cyclic voltammetry (50 mV s^{-1}), second cycle, of MoS_3 films deposited by spray (black line, 30nm) and spin-coating (red line, 30nm), in 0.5 M H_2SO_4. Electrode area: 0.5 cm². The configuration was a three-electrode (working electrode / WE: MoS_3 ; reference electrode / RE: Ag/AgCl KCl 3.5 M ; counter electrode / CE : carbon plate or glassy carbon).

The same behavior is observed for spray-coated MoS_3 films (Fig. 42, black line). Despite their different morphology, they show similar electrocatalytic properties as spin-coated films.

Electrochemical impedance spectroscopy (EIS) was carried out on spin-coated MoS_3 (15 nm) on ITO samples in 0.5 M H_2SO_4 at –0.22 V *vs* RHE (close after the onset potential of the HER), from 100 000 Hz to 0.03 Hz. From the impedance spectrum, the charge transfer resistance was evaluated at 120 Ω cm^2. At –0.22 V *vs* RHE, on the CV curve, the calculated resistance (based on the slope at this potential value) was 115 Ω cm^2, fitting well with the impedance.

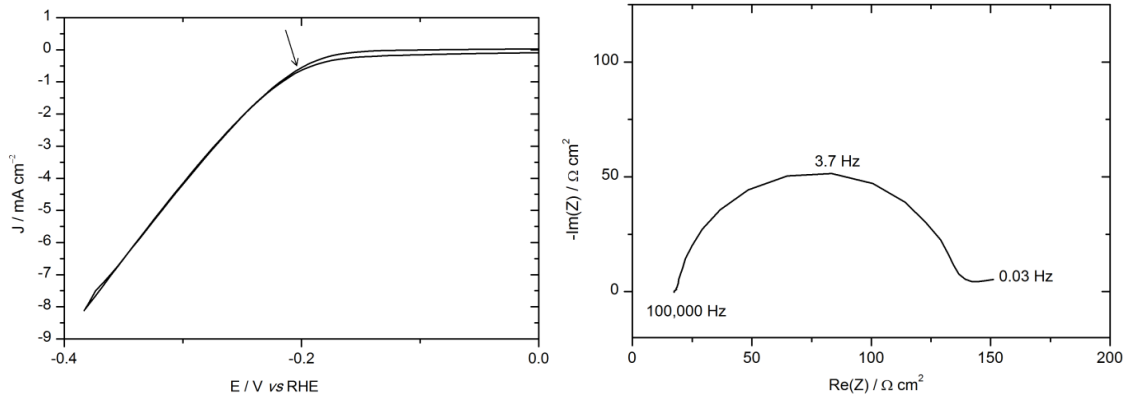

Fig. 43. *Left*: cyclic voltammetry (50 mV s^{-1}) of MoS_3 film deposited by spin-coating (30nm), in 0.5 M H_2SO_4 with an arrow indicating the potential at which the impedance spectrum was carried out. *Right*: Impedance spectrum of the same MoS_3 film, at a bias voltage of –0.22 V *vs* RHE. Electrode area: 0.5 cm².

Influence of pH at the end of the synthesis on the electrochemical activity

In a previous section (2.3.2.1), three different batches of MoS_3 nanoparticles had been synthesized by acidification ending at pH 2, 2.7 and 3.5. TEM analysis was performed and no difference in the size of the particles could be observed. To verify the electrochemical properties of these three different batches, MoS_3 films on ITO were deposited on ITO. The particles synthesized at different pH displayed similar catalytic current density and onset potential, as shown in Fig. 44.

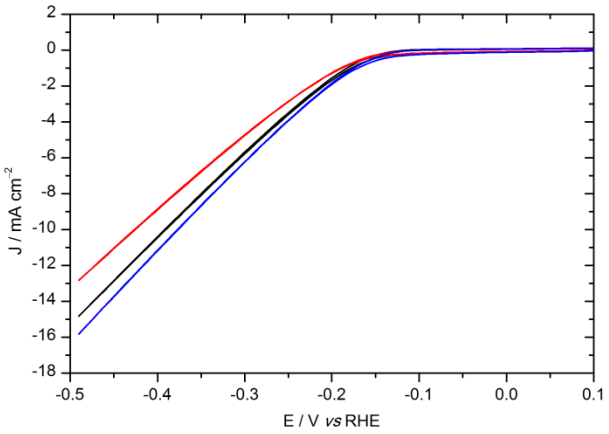

Fig. 44. Cyclic voltammetry at 50 mV s^{-1} in 0.5 M H_2SO_4 of MoS_3 films (30 nm, deposition by spin coating on an ITO-coated glass substrate) for a synthesis ending at pH 2 (black), 2.7 (red) and 3.5 (blue). Electrode area: 0.5 cm^2.

According to electrochemical analyses, MoS_3 could be synthesized by acidification until pH was 2. This is an advantage for the preparation of the particles, because at pH 2 they were aggregated and their separation and washing was much easier, without impact on the electrocatalytic properties.

Thermal treatment

MoS_3 films have been heated at temperatures up to 150°C to study their resistance to thermal treatment and the impact of thermal treatment on electrocatalytic activity. Indeed, in Chapters 3 and 4, the photocathodes were sometimes heated after the deposition of the catalyst, depending on the underlying layers. Again, no impact was observed, as shown in Fig. 45.

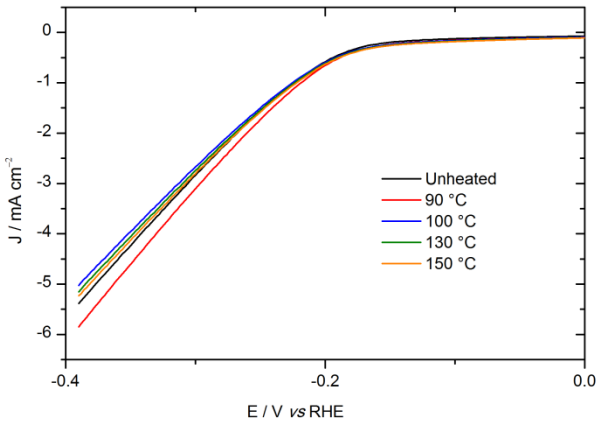

Fig. 45. Cyclic voltammetry (second cycle) at 50 mV s^{-1} in 0.5 M H_2SO_4 of MoS_3 films (30 nm, deposition by spin coating on an ITO-coated glass substrate) heated at different substrate temperature in air. Electrode area: 0.5 cm^2.

Electrochemical modification of MoS_3

An additional reduction process occurs from –0.05 V only during the forward sweep of the first voltammogram (Fig. 46), as previously reported in the literature.[119]

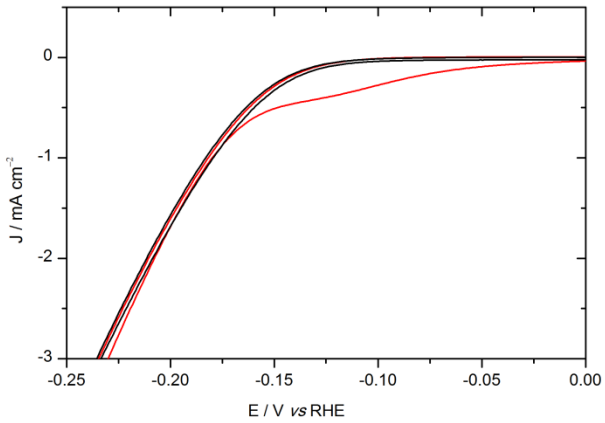

Fig. 46. First cycle (red) and second cycle (black) of MoS_3 deposited on ITO. 0.28 cm^2, 2 mV s^{-1}.

To understand the origin of this reduction process, XPS analysis was carried out on spin-coated MoS_3 films, before and after a cyclic voltammetry (CV) experiment. Quantification based on S 2p and Mo 3d areas was carried out using Wagner coefficients.

The XPS survey spectra do not show any significant difference, except for peak intensities (Fig. 47). The sodium peak almost disappeared, probably because this residual sodium from the synthesis dissolved in the electrolyte.

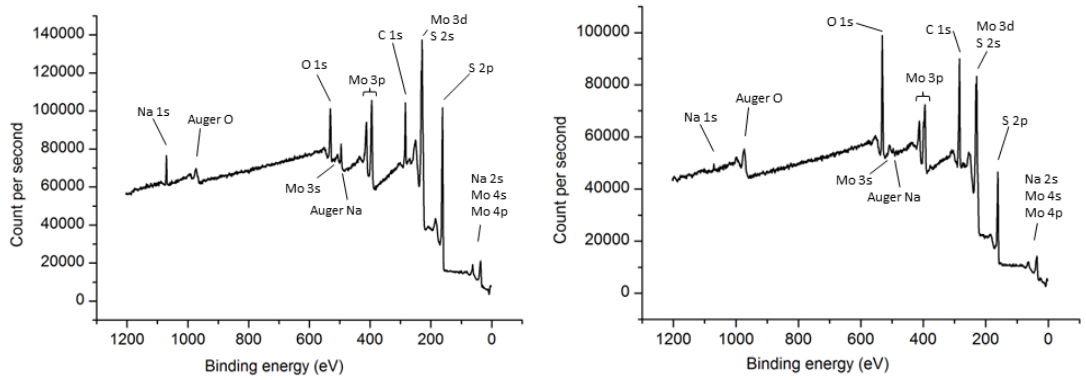

Fig. 47. X-ray photoelectron survey spectrum of spin-coated MoS_3 films (final pH = 3) before (left) and after (right) cyclic voltammetry (2 cycles at 50 mV s^{-1}, from 0 to –0.4 V *vs* RHE).

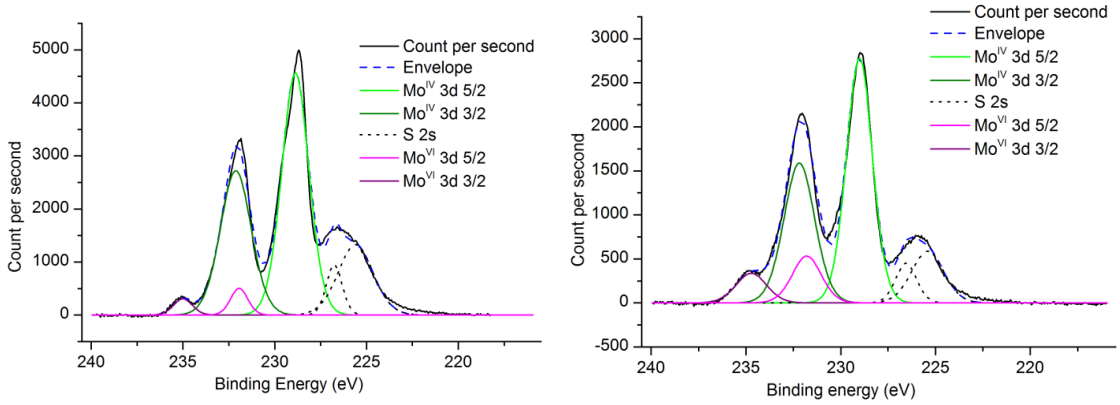

Fig. 48. XPS spectra of Mo 3d (same sample as survey) before (left) and after (right) cyclic voltammetry as in Fig. 42 (red line). Mo^{IV} $3d_{5/2}$ (light green line), Mo^{IV} $3d_{3/2}$ (dark green line), Mo^{VI} $3d_{5/2}$ (light purple line), Mo^{VI} $3d_{3/2}$ (dark purple line), S 2s (black dots), and envelope (blue dashes). Mo 3d spectra before (after) CV show binding energies of Mo $3d_{5/2}$ and Mo $3d_{3/2}$ at 228.9 eV (229.0 eV) and 232.1 eV (232.2 eV) respectively corresponding to Mo^{IV}. Mo^{VI} from the residual MoO_3 starting material is also observed at 231.9 and 235.0 eV (before CV) and 231.8 and 234.7 eV (after CV).

On both Mo 3d spectra (before and after CV, Fig. 48), the main Mo 3d signals correspond to Mo in the +IV oxidation state, as previously reported.[119,148] Mo^{VI} from the residual MoO_3 starting material is also observed.

Analysis of the S 2p region before and after CV reveals two types of sulfur atoms, sulfides (S^{2-}) and disulfides (S_2^{2-}).

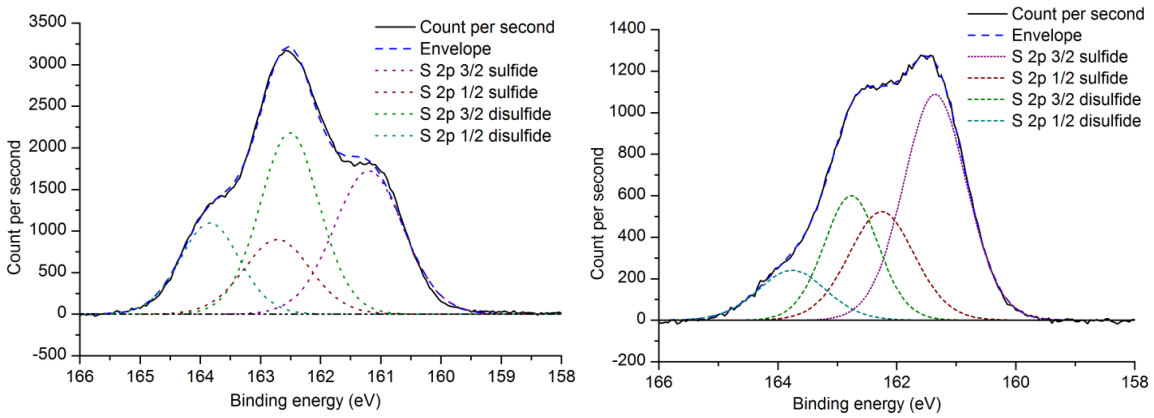

Fig. 49. XPS spectra of S 2p (same sample as survey), before (left) and after (right) cyclic voltammetry as in Fig. 42 (red line). S $2p_{3/2}$ of sulfide S^{2-} (pink dots), S $2p_{1/2}$ of sulfide S^{2-} (red dots), S $2p_{3/2}$ of disulfide S_2^{2-} (green dots), S $2p_{1/2}$ of disulfide S_2^{2-} (light blue dots), and envelope (blue dashes). Before (after) CV, peaks at 161.2 (161.3) and 162.7 (162.3) eV are assigned to S $2p_{3/2}$ and S $2p_{1/2}$ signals of sulfide (S^{2-}) anions while peaks at 162.5 (162.8) and 163.8 (163.8) eV correspond to S $2p_{3/2}$ and S $2p_{1/2}$ signals of disulfide (S_2^{2-})

.

Contrary to the molybdenum spectrum, which showed that Mo remained mostly in the +IV oxidation state, the sulfur signal changes after CV. The initial sulfide to disulfide ratio was 1.1, fitting well with the formula $Mo^{IV}(S^{2-})(S_2^{2-})$ for MoS_3.[112] This ratio then increased from 1.1 to 2.1, due to the disappearance of disulfide anions in the compound. At the same time, the S:Mo ratio went from 2.9 to 2.1.

All these observations indicate that the composition in the film evolves during CV as previously reported with transformation of a MoS_3 phase (corresponding to $Mo^{IV}(S^{2-})(S_2^{2-})$) into a MoS_x ($x > 2$) phase containing less disulfide anions.[119] This modification is occurring only during the first cycle, or the first seconds of a chronoamperometric experiment. When the catalyst is deposited on the photocathode, this modification occurring at the beginning is not impacting the experiment, due to its short duration compared to that of the experiment.

Substrate: FTO/ITO/Gold

Different substrates were tested as support electrode for the MoS_3 catalyst. It was found that the electrocatalytic activity was not depending on the conductive electrode (Fig. 50).

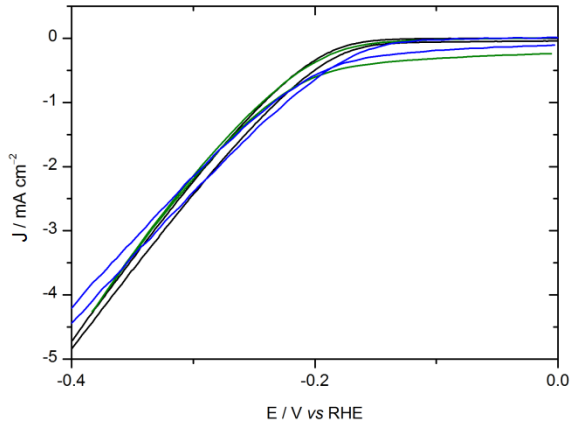

Fig. 50. CV in N_2-saturated 0.5 M H_2SO_4 at 50 mV s^{-1} for spin-coated MoS_3 films deposited on ITO (black), FTO (blue) and gold (green).

2.3.5.2. Fabrication of mixed MoS_3:TiO_2 electrodes

In bulk-heterojunction polymer solar cells, densely packed n-type oxide TiO_2 is often placed between the light-harvesting active layer and the charge-collecting electrode.[149,150] This interfacial material improves the performance of the solar cell[151] thanks to its good electron transport properties and the long-term stability is also enhanced since TiO_2 prevents direct contact between oxygen or water and the active layer.[149,152,153] In addition, this large band-gap (3.2 eV) semiconductor is transparent to visible light and thus does not compete with the organic light-harvesting layer.

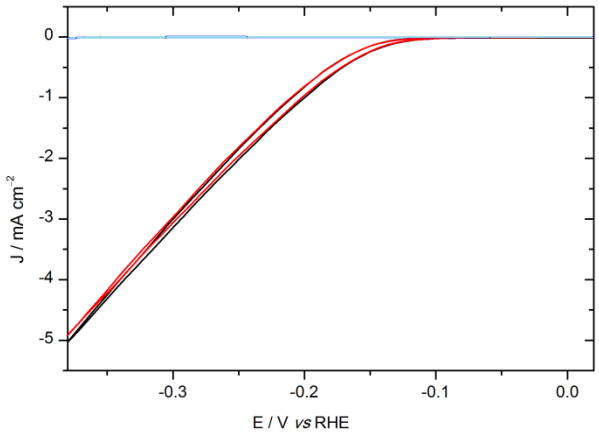

Fig. 51. Cyclic voltammetry (1 mV s^{-1}) of TiO_2 (blue, 160 ± 10 nm), MoS_3 (red, 70 ± 5 nm) and TiO_2:MoS_3 (black, 330 ± 80 nm) films deposited by spin-coating on ITO-coated glass substrates, in N_2-saturated 0.5 M H_2SO_4. All layers were annealed at 120 °C for 30 min. The substrate was illuminated with chopped visible light (same as used for the test of photocathodes).

Thus, the MoS_3 material was mixed with commercially available TiO_2 particles. This mixed

TiO_2:MoS_3 suspensions (v/v = 1/1, approximate mass ratio 2:1) have been deposited by spin-coating on ITO and annealed at 120 °C for 10 minutes, in order.to analyze its electrocatalytic activity.

Cyclic voltammograms were measured at 1 mV s^{-1} in 0.5 M H_2SO_4 for mixed TiO_2:MoS_3 (approximate mass ratio: 2:1) -coated electrodes (Fig. 51), under illumination with chopped visible light. Mixed TiO_2:MoS_3 electrodes (330 ± 80 nm thickness) display similar onset potential and catalytic HER current to MoS_3 (70 nm thickness) alone. Moreover, TiO_2 did not add any electrocatalytic or photocatalytic activity to MoS_3.

Zinc oxide is also a n-type oxide commonly used in organic photovoltaics as electron-collecting layer.[154,155] ZnO nanoparticles were also tested as mixed MoS_3:ZnO catalyst but low current densities were obtained for ITO\MoS_3:ZnO electrodes so that it was not assembled onto the photocathodes.

2.3.5.3. Performance and stability of MoS_3 and TiO_2:MoS_3 films with different thicknesses

The electrocatalytic activity of MoS_3 and TiO_2:MoS_3 electrodes with various thicknesses was studied by cyclic voltammetry and the stability by chronoamperometry, in order to verify that the catalytic layer was active in the targeted thickness range.

The CV of MoS_3 films of different thicknesses was performed and the results are shown in Fig. 52. The electrocatalytic activity was not found to be significantly different in terms of current density and onset potentials. Even the 200 nm-thick MoS_3 film has an electrocatalytic activity similar to that of the 100 nm-thick film.

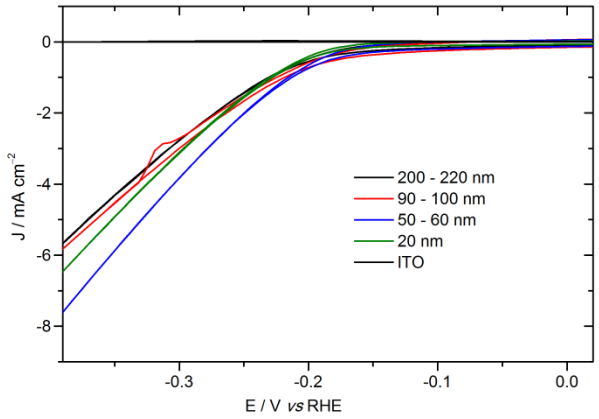

Fig. 52. Cyclic voltammetry (second cycle) at 50 mV s^{-1} in 0.5 M H_2SO_4 of MoS_3 films (different thicknesses) deposited by spin-coating on an ITO-coated glass substrates. Electrode area: 0.5 cm^2.

The stability of the electrocatalytic activity of the MoS_3 catalyst in 0.5 M H_2SO_4 was evaluated by chronoamperometric measurements performed at –0.3 V *vs* RHE. Three different films with thicknesses of 70, 35 and 20 nm were tested for 1 h (Fig. 53).

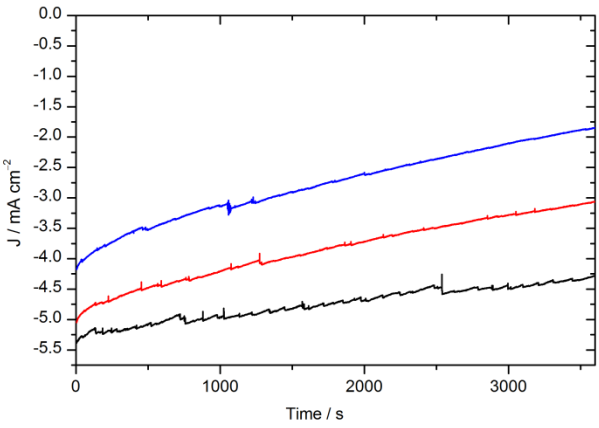

Fig. 53. Chronoamperometry at –0.3 V *vs* RHE in 0.5 M H_2SO_4. Black / bottom line: 70 nm, red / middle line: 35 nm, blue / top line: 20 nm.

Generally, the current density during constant-potential electrolysis of thicker films was more stable,

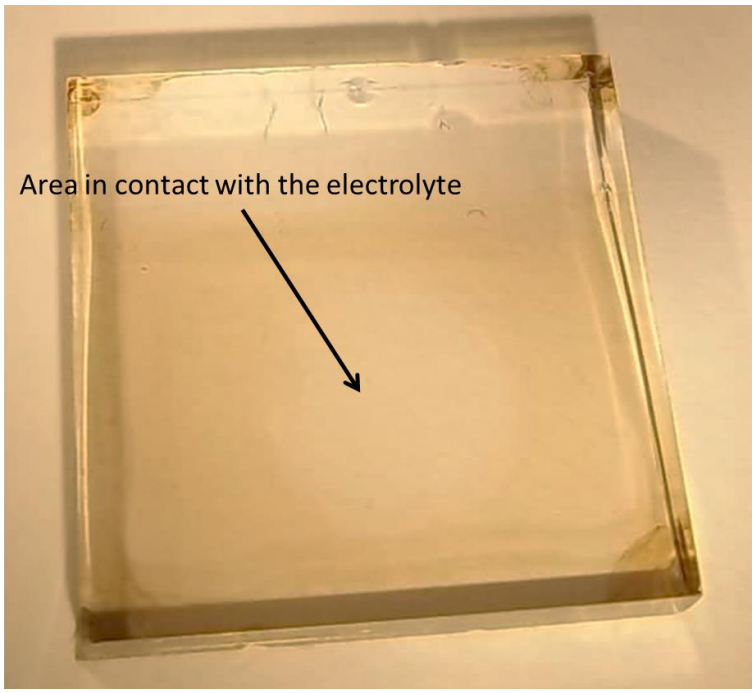

Fig. 54. Photography of MoS_3 (15 nm, deposition by spin-coating) after three cycles of CV carried out in degased 0.5 M H_2SO_4.

probably an effect of the initial higher amount of catalyst. The decrease of current density can be explained by a gradual dissolution of the catalyst during electrolysis in the acidic media (Fig. 54).

The stability of sprayed MoS_3 films is similar to that of the spin-coated films, as shown in Fig. 55.

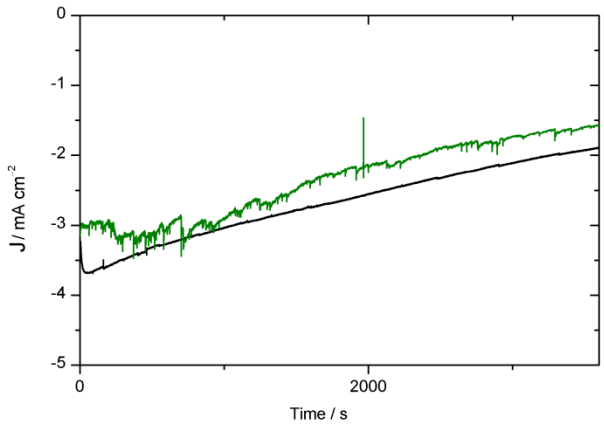

Fig. 55. Chronoamperometry at –0.3 V *vs* RHE in 0.5 M H_2SO_4 of spin-coated MoS_3 (black) and sprayed MoS_3 (green).

The smoother aspect of the curve obtained with the spin-coated film can be explained by the fact that sprayed films are rougher. The H_2 bubbles seem to be sticking to the surface more in the case of sprayed films, and their release causes the sudden increases of the current due to the release of active surface. Moreover, SEM images taken before and after the chronoamperometric measurements in Fig. 56 (spin-coating films) and Fig. 57 (sprayed films) show that pieces of sprayed MoS_3 have been detaching from the surface, probably because of the H_2 bubbles pulling the catalyst.

Spin coating, before electrolysis:

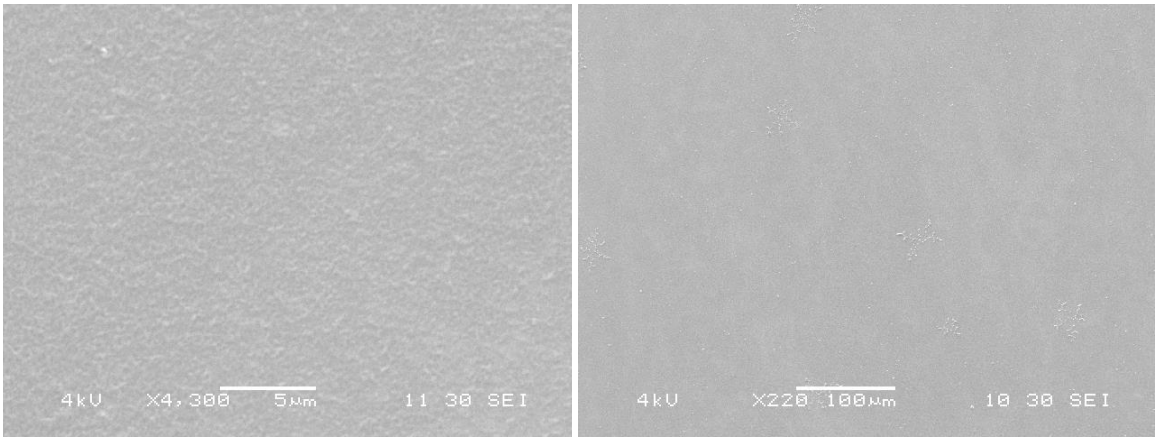

Spin coating, after electrolysis:

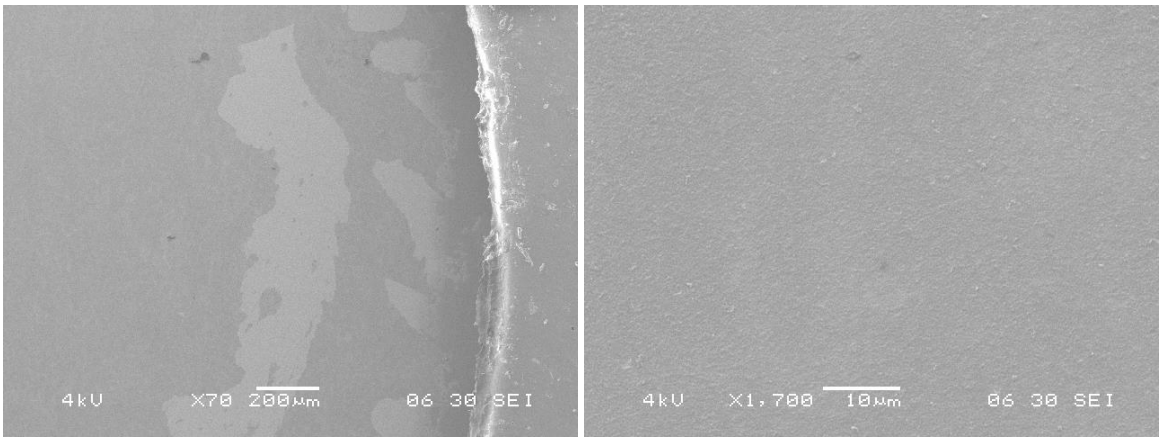

Fig. 56. SEM pictures of spin-coated MoS_3 film on ITO, taken before (up) and after (down) electrolysis. Most of the material is still on the substrate and the catalyst detached itself only on areas near the electroplating tape delimitating the electrochemical area.

Spray, before electrolysis:

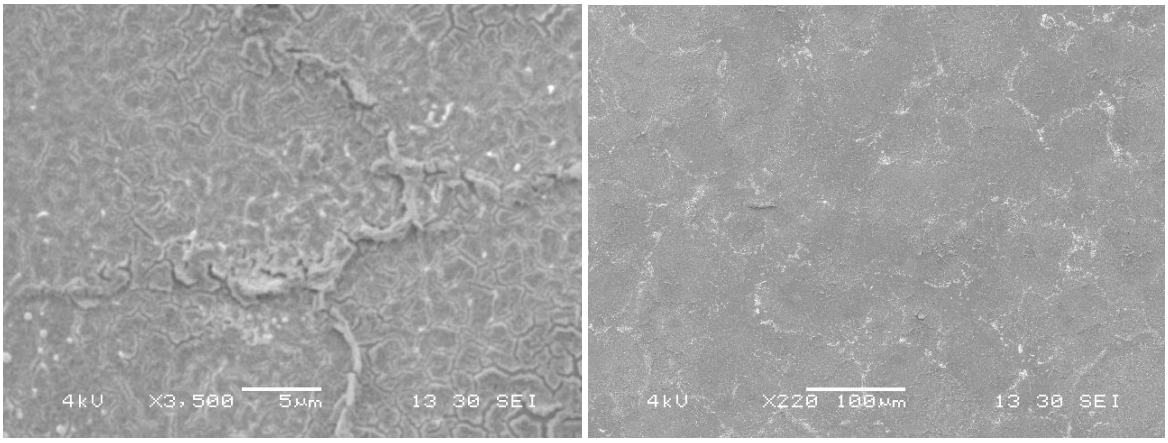

Spray, after electrolysis:

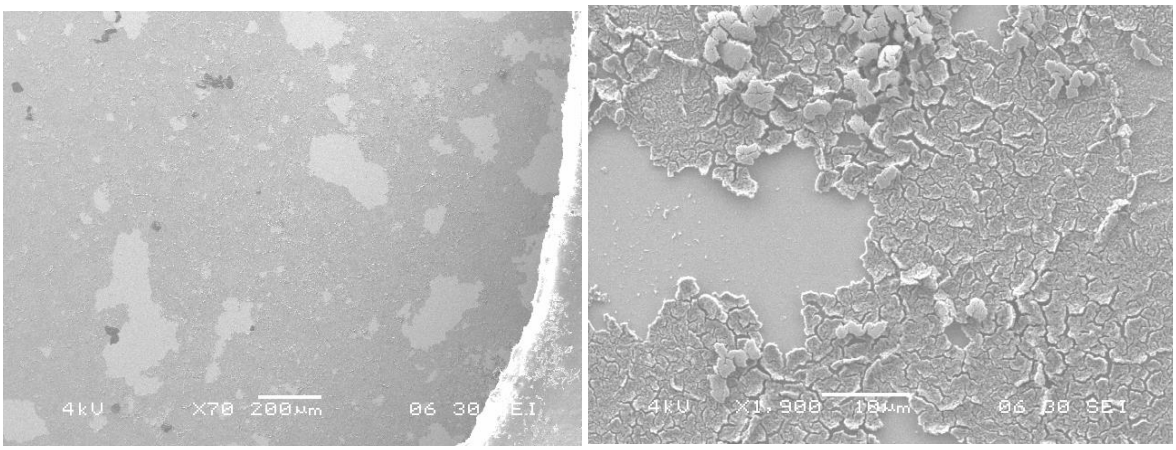

Fig. 57. SEM pictures of sprayed MoS_3 film on ITO, taken before (up) and after (down) electrolysis. The sprayed film is rougher than the spin-coated film. The catalyst detached itself in areas all over the electrochemical area.

To conclude, MoS_3 films from 20 to 200 nm were electrocatalytically active and the stability of sprayed and spin-coated films was similar.

The stability of MoS_3:TiO_2 mixed electrodes (deposited by spray) was tested. The film thickness was measured by profilometry at approximately 600 nm and 1000 nm. The roughness was however very high so that the difference between the lowest and the highest point could sometimes reach more than 1 µm. The relatively high thickness of the films is counterbalanced by the transparency of TiO_2 to visible light.

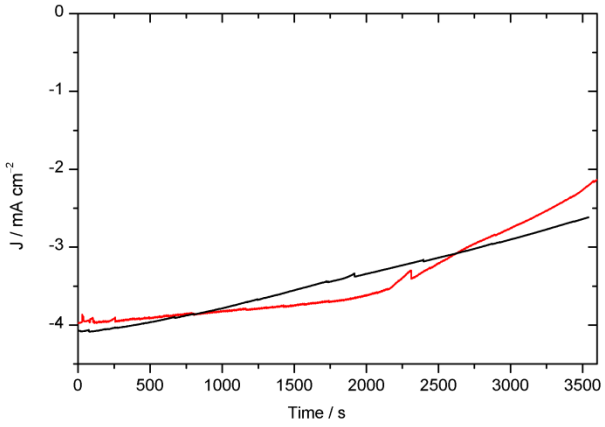

Fig. 58. Chronoamperometry at –0.3 V *vs* RHE in 0.5 M H_2SO_4. Black: ~ 1000 nm, red: ~ 600 nm.

Chronoamperometry performed at –0.3 V *vs* RHE (Fig. 58) showed similar current density than MoS_3 films (Fig. 55) as well as a 50 % decrease of the current density at –0.4 V over 1 h.

2.3.5.4. Comparison with Pt

The MoS_3 suspension and a Pt/C ink (cf. experimental section) were drop-casted onto a glassy carbon (GC) electrode mounted on a rotating shaft, and both catalysts were tested in N_2-saturated 0.5 M H_2SO_4 at a rotation speed of 800 rpm. The onset potential was approximately 0 V *vs* RHE for Pt/C and –0.15 V for MoS_3 (Fig. 59), and similar slopes were obtained. It is worth to note that current densities

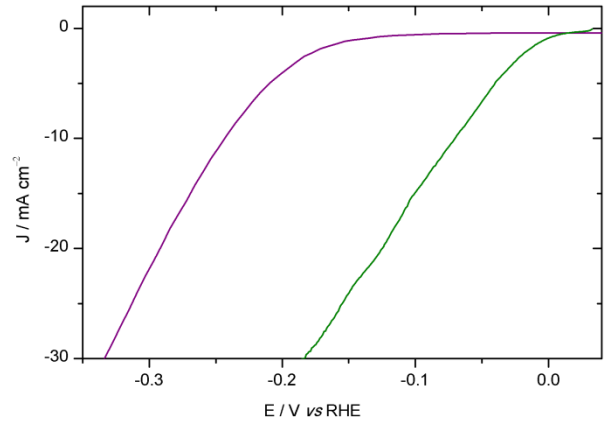

Fig. 59. CV in N_2-saturated 0.5 M H_2SO_4 for drop-casted MoS_3 (purple line, on the left) and Pt/C (green line, on the right) on a glassy carbon rotating disk electrode (RDE) (rotation speed was 800 rpm).

obtained with GC\$MoS_3$ were significantly increased compared to ITO\$MoS_3$ (one order of magnitude). Possible causes for the higher current density of GC\$MoS_3$ are the rotation of the electrode, the higher roughness of the GC electrode compared to the ITO one, its conductivity, as well

as the deposition of MoS_3 by dropcasting on GC which may further increase the roughness of the catalytic film.

2.3.5.5. Faradic efficiency

When the electrocatalytic activity of a catalyst is studied, one important characterization is the Faradic efficiency. The Faradic efficiency is used to evaluate the proportion of charges which actually reduce protons into hydrogen, among other reduction reactions which might occur. This is important because the hydrogen production by the photocathodes, in this thesis, is indirectly measured through the reduction current. Experimentally, the Faradic efficiency is determined by carrying out electrolysis at a constant potential and comparing the calculated hydrogen production (with the amount of charges passed in the circuit) to the actual amount measured by gas chromatography.

The production of hydrogen could not be quantified accurately. In this work, based on all the data found in the literature (MoS_3 in different forms: electrodeposited, nanoparticles, …),[118] a Faradic efficiency of 100 % is assumed for the testing of the photocathodes and the calculation of the photocathode efficiencies.

2.3.5.6. Electrochemical performance of MoS_3 in electrolytes at different pH values

In the first studies of the catalyst, the high proton concentration (0.5 M H_2SO_4) was kept to verify the activity of our synthesized catalyst compared to the literature. As the photocathodes would have to be tested in this acidic media, which might impact the performances of the photocathode, the electrocatalytic activity of MoS_3 has been tested in diluted H_2SO_4 (in 0.1 M Na_2SO_4).

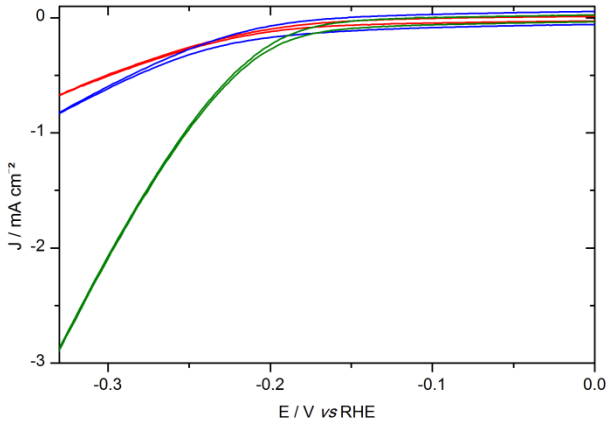

Fig. 60. Cyclic voltammetry (50 mV s^{-1}) of MoS_3 films (deposited by spin-coating, 30 nm), on ITO-coated glass substrates), in electrolyte with decreasing H_2SO_4 concentration by dilution in 0.1 M Na_2SO_4 (green: 0.5 M H_2SO_4, blue: 0.1 M H_2SO_4, red: 0.05 M H_2SO_4). Electrode area: 0.5 cm^2.

The onset potentials of the HER are similar in electrolytes with different proton concentrations but the current densities are lower in 0.1 M and 0.05 M H_2SO_4 than in 0.5 M H_2SO_4. For the photocathodes,

an additional overvoltage to reach several mA cm^{-2} was not desirable. To avoid losing all the photovoltage provided by the solar cell in overcoming the overpotential requirement of the catalyst, a concentration of 0.5 M (corresponding to 1 N in protons) was kept.

2.4. Characterization of P3HT:PCBM solar cells

In the previous section, the MoS_3 catalyst was synthesized and characterized in suspension as well as in the form of thin films deposited either by spin-coating or by spray-coating. Importantly, the conditions for its electrocatalytic activity were determined to be in acidic aqueous media for film thickness ranging from 15 to 200 nm. In this section P3HT:PCBM-based solar cells are fabricated and characterized without catalyst, in a solid-state solar cell configuration (Fig. 61, top). This was done before undertaking the fabrication of photocathodes to verify their performance of the photovoltaic materials. Briefly, an ITO-coated glass substrate with two gold contacts and an ITO-free area was coated with a PEDOT:PSS layer by spin-coating. PEDOT:PSS (poly(3,4-ethylenedioxythiophene):poly(styrene sulfonate) is a hole-extraction layer (~ 40 nm) which improve the selectivity of the ITO anode. Then, the polymer-fullerene blend (P3HT:PCBM) was deposited by

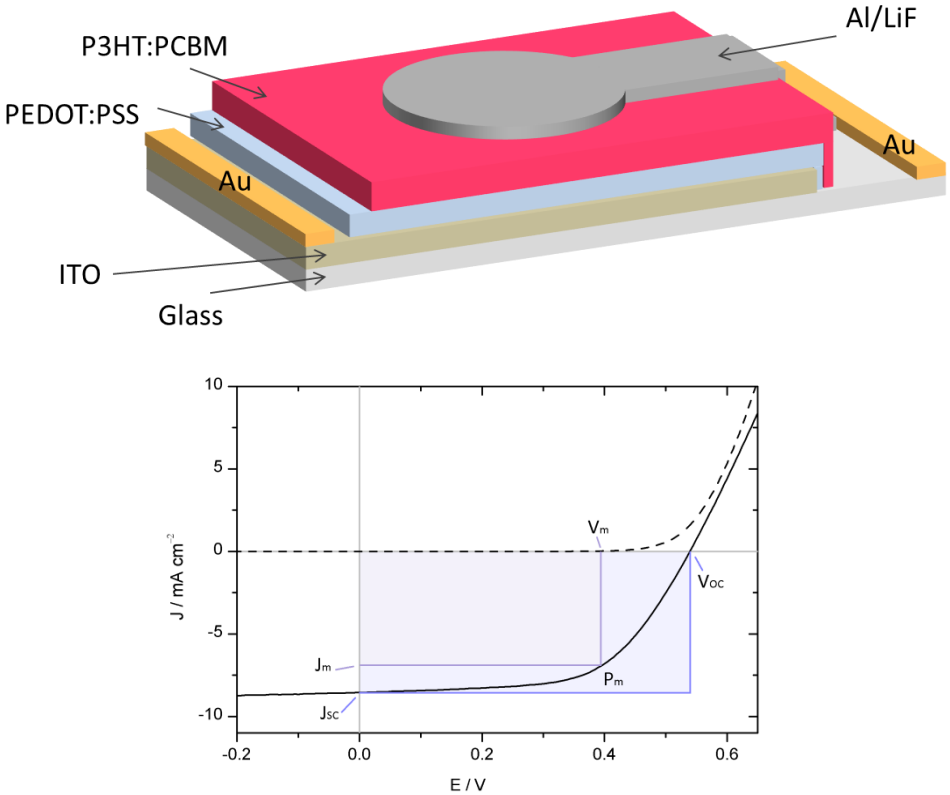

Fig. 61. Structure (top) and current density-voltage curves (down) of an ITO\PEDOT:PSS\P3HT:PCBM\LiF\Al solar cells prepared in our conditions (full line: under illumination; dashed line: in the dark). Exposed area: 0.28 cm².

spin-coating (~ 180 nm). Finally, a LiF\Al cathode (1.2 nm and 100 nm respectively) was evaporated in a Joule evaporator under vacuum. LiF interface layers are commonly used between aluminum and the organic semiconductors. Different causes have been suggested for the improvement of the interface: formation of quasi-Ohmic contacts for electrons,[156] doping of the acceptor material by Li or modification of the work function of the electrode through dipole formation.[157]

The solar cell is characterized by linearly sweeping the voltage between the ITO anode and the aluminum cathode. Fig. 61 (down) presents the current density-voltage curves of the as-prepared solar cell. In the dark, the curve has the characteristic of a diode, with a positive dark current starting at 0.5 V. Under illumination, a photocurrent appears in the opposite direction of the dark current, resulting from the photovoltaic effect of the cell. The characteristic figures-of-merit of a solar cell are the open-circuit voltage (V_{OC}, in V), the short-circuit current density (J_{SC}, in mA cm^{-2}), the fill factor (FF) and the power conversion efficiency (PCE). In the case of an ideal diode, the current density would be equal to the J_{SC} (or zero in the dark) until the V_{OC} was reached, at which point the current density would suddenly increase vertically. In an organic solar cell, the V_{oc} depends on the difference between the energy levels of the highest occupied molecular orbital (HOMO) of the electron-donating polymer (here, P3HT) and the lowest unoccupied molecular orbital (LUMO) of the electron-accepting material (here, PCBM). The fill factor is the ratio of the maximum power that can be obtained with such a solar cell under operation (P_m) and the power that would be obtained in the case of an ideal diode (V_{OC} x J_{SC}), as in Equ. 6. In Fig. 61, it is visualized by the ratio of the J_m x V_m area on the J_{SC} x V_{OC} area. The PCE is the ratio of the power output on the power input P_{in} (i.e. light, in mW cm^{-2}) taken at the maximum power point (Equ. 7).

$$FF = \frac{P_m}{V_{OC} \times J_{SC}} = \frac{V_m \times J_m}{V_{OC} \times J_{SC}} \qquad \text{Equ. 6}$$

$$PCE = \frac{P_m}{P_{in}} = \frac{FF \times V_{OC} \times J_{SC}}{P_{in}} \qquad \text{Equ. 7}$$

The characteristics of the ITO\PEDOT:PSS\P3HT:PCBM\LiF\Al solar cell are presented in

Table 3.

V_{OC}	J_{SC}	FF	PCE
0.54 V	8.6 mA cm^{-2}	60 %	2.75 %

Table 3. V_{OC}, J_{SC}, FF and PCE obtained with the ITO\PEDOT:PSS\P3HT:PCBM\LiF\Al solar cell measured in Fig. 61

These values are not the highest that can be obtained with this structure and these materials. Indeed, 4-5 % can be achieved in carefully controlled conditions.[158,159] For the fabrication of the photocathodes, the solar cells that we used as base were processed as the one measured here.

2.5. Assembly and characterization of the ITO\PEDOT:PSS\P3HT:PCBM\MoS_3 photocathode

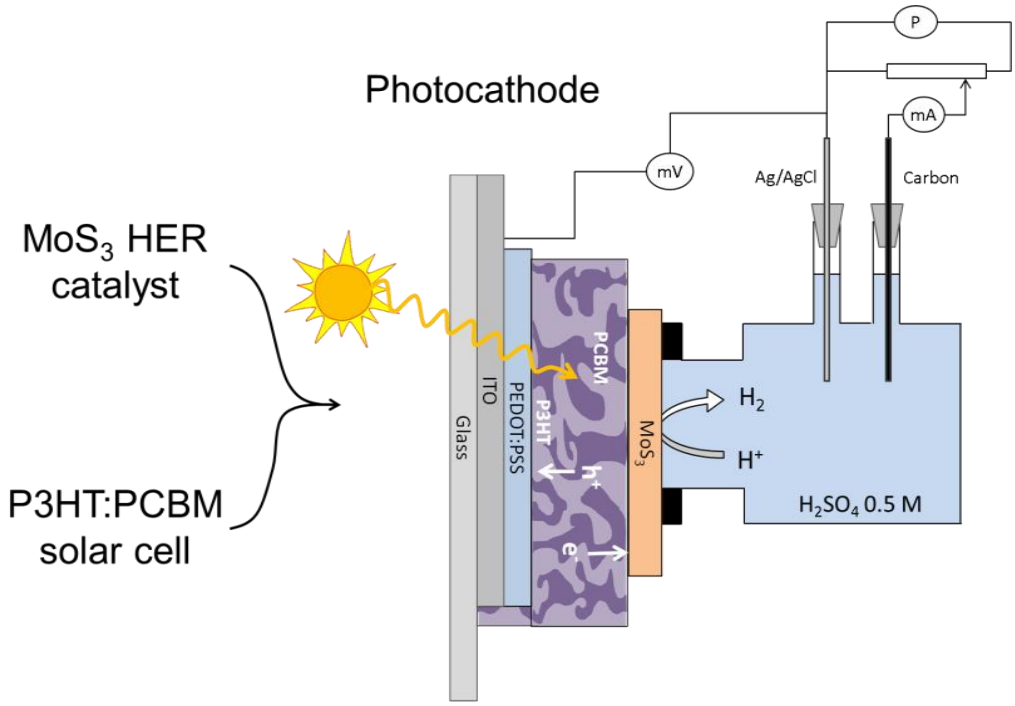

Fig. 62. Architecture of the MoS_3/P3HT:PCBM H_2-evolving photocathode inserted in the cell used in this study for photo-electrochemical measurements

The photocathodes were fabricated by assembling the MoS_3-based catalytic layer and the polymer-fullerene bulk heterojunction, following the structure shown in Fig. 62. The hole-extraction layer (PEDOT:PSS) and the photovoltaic active layer (P3HT:PCBM) were successively deposited by spin-coating on ITO-coated glass substrates. Then, instead of evaporating the aluminum cathode, the catalytic layer (MoS_3 or mixed TiO_2:MoS_3) was deposited. Our primary goal was to use spin-coating. However, even by adding Nafion or surfactants such as Brij® in the MoS_3 suspension, it could not be spin-coated onto the P3HT:PCBM layer, since neither the suspension of MoS_3 nor that of mixed TiO_2:MoS_3 correctly wet the P3HT:PCBM layer. We therefore used spray-coating, which could be sprayed onto the heated substrate. With spray, the assessment of the thickness of the catalytic layer was difficult to measure on the soft P3HT:PCBM substrate but it was evaluated by spraying on a glass substrate next to the solar cells.

Two photocathodes were prepared: one containing a catalytic layer based on MoS_3 (approximately 200 nm) and a second one with a mixed TiO_2:MoS_3 catalytic layer (approximately 600 nm). In order to discriminate between the effects of MoS_3 and TiO_2 on the performances, two reference photoelectrodes were also prepared, one without catalytic layer and another one only with a TiO_2 layer. We then investigated the photo-electrocatalytic performances of the two photocathodes containing either MoS_3 or mixed TiO_2:MoS_3 as a catalytic layer. The photocathodes were interfaced with a 0.5 M H_2SO_4 aqueous solution as shown in Fig. 62 and irradiated with visible light from a mercury-xenon lamp filtered from UV radiation. Fig. 63 shows the photocurrent densities obtained for both photocathodes at an electrode potential of –0.05 V *vs* Ag/AgCl (0.16 V *vs* RHE). The photocurrent density obtained for the ITO\PEDOT:PSS\P3HT:PCBM\MoS_3 photocathode (30 µA cm^{-2}, red trace) is only slightly higher than the one measured for the same stack but lacking the catalyst layer used as a reference (25 µA cm^{-2}, black trace). By contrast, the photocathode with the mixed TiO_2:MoS_3 catalytic layer yields a higher photocurrent density (> 100 µA cm^{-2}, green trace), probably because of a more efficient charge extraction from the P3HT:PCBM layer. It is worth to note that photocathodes with platinum on carbon instead of MoS_3 almost not photocurrent was obtained. The causes are investigated in Chapter 3, section 3.3.3.

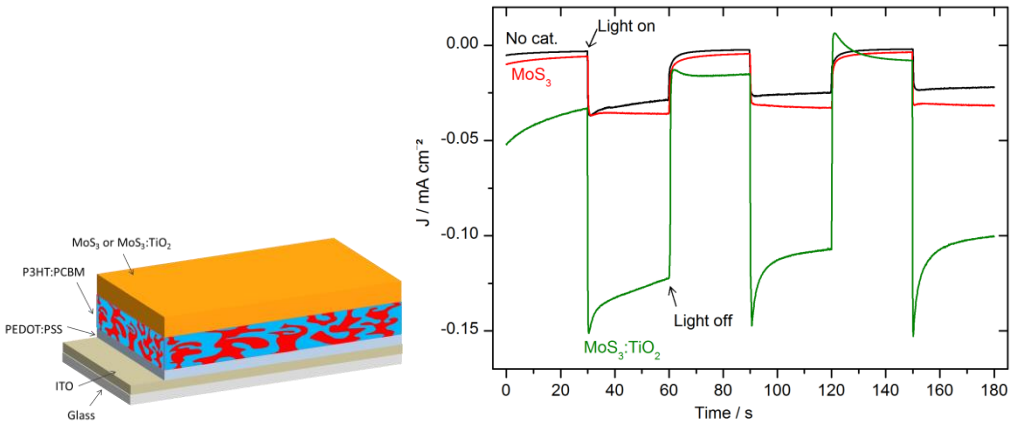

Fig. 63. Electrolysis at a bias potential of +0.16 V *vs* RHE, with chopped visible light, in 0.5 M H_2SO_4. Black: ITO\PEDOT:PSS\P3HT:PCBM, red: ITO\PEDOT:PSS\P3HT:PCBM\$MoS_3$, green: ITO\ PEDOT:PSS\P3HT:PCBM\$TiO_2$:$MoS_3$ (with the highest photocurrent density). Electrode area: 0.5 cm^2.

Voltammetry measurements were carried out at 5 mV s^{-1} from 0.55 to –0.4 V *vs* RHE, under chopped visible light (Fig. 64). Fig. 64 *right* shows the two voltammograms (in the dark and under illumination) that can be extracted from the chopped-light voltammogram obtained in Fig. 64 *left* and represents the photocurrent density between the dark and light current densities.

The photocurrent of the different photocathodes are first compared. The photocurrent of the reference photocathode without the catalytic layer (ITO\PEDOT:PSS\P3HT:PCBM) was approximately 30 µA

cm^{-2} and barely increased when the electrode potential was swept to negative potentials. The photocurrent displayed by the ITO\PEDOT:PSS\P3HT:PCBM\MoS_3 photocathode significantly

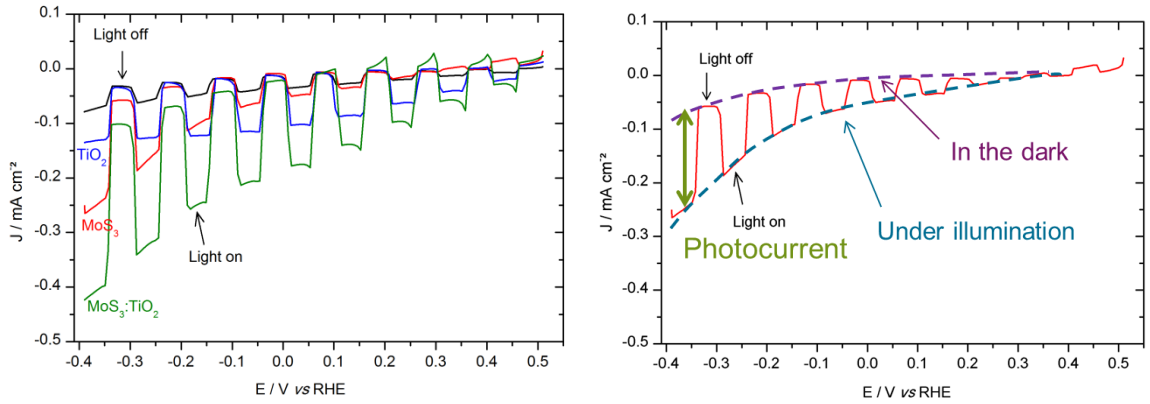

Fig. 64. *Left*: Voltammograms recorded at 5 mV s^{-1} in 0.5 M H_2SO_4 with chopped visible light for several photocathodes. Black: ITO\PEDOT:PSS\P3HT:PCBM (reference), red: ITO\PEDOT:PSS\P3HT:PCBM\$MoS_3$ photocathode, blue: ITO\PEDOT:PSS\P3HT:PCBM\$TiO_2$ photocathode, green: ITO\PEDOT:PSS\P3HT:PCBM\$TiO_2$:$MoS_3$ photocathode. Electrode area: 0.5 cm^2. *Right*: same ITO\PEDOT:PSS\P3HT:PCBM\$MoS_3$ photocathode as in the left figure, with extracted CVs in the dark (purple dashed line) and under illumination (blue dashed line) with the photocurrent density in-between (green arrow).

differed from the reference photocathode (without catalyst) only for potentials more negative than 0 V *vs* RHE, which corresponds to the thermodynamic potential for H_2 evolution at pH 0: the photocurrent density at 0 V *vs* RHE was only 50 µA cm^{-2}. The ITO\PEDOT:PSS\P3HT:PCBM\$TiO_2$ photocathode displayed a photocurrent density of 100 µA cm^{-2} which did not increase when the potential was more negative. By contrast, the ITO\PEDOT:PSS\P3HT:PCBM\$TiO_2$:$MoS_3$ photocathode presented increased photocurrent density values (180 µA cm^{-2} at 0 V *vs* RHE and up to 400 µA cm^{-2} at –0.4 V *vs* RHE), due to the catalytic role of MoS_3 for the reduction of protons. The addition of TiO_2 seems to improve the electron extraction from the OPV layer and then to transfer them to the catalyst.

This is corroborated by the increased onset potential (defined by the potential to obtain an arbitrary value of 0.1 mA cm^{-2}, cf. Chapter 2, section 2.1.1) of the ITO\PEDOT:PSS\P3HT:PCBM\$TiO_2$:$MoS_3$ photocathode (0.23 V *vs* RHE) compared to the photocathode with only MoS_3 (–0.14 V). Indeed, the photovoltage (potential difference between the potential to reach a given current density under illumination and the potential to reach the same current density in the dark) of the ITO\PEDOT:PSS\P3HT:PCBM\$TiO_2$:$MoS_3$ photocathode is 0.23 V – (–0.15 V) = 0.38 V at 0.1 mA cm^{-2}. The photovoltage of the ITO\PEDOT:PSS\P3HT:PCBM\$MoS_3$ photocathode is however here 10-20 mV.

It can be noted that the dark current density of the four photocathodes was low even at potentials more negative than –0.2 V *vs* RHE, when MoS_3 should start to evolve hydrogen when used as a dark

electrode (ITO\MoS_3). That effect is due to the diode behavior of the PEDOT:PSS\P3HT:PCBM photovoltaic part, which blocks the current at negative potentials in the dark.

Electrolyses at +0.16 V *vs* RHE were carried out for 45 min to study the stability of the devices (Fig. 65). The photocurrent of the ITO\PEDOT:PSS\P3HT:PCBM\$TiO_2$:$MoS_3$ photocathode decreased by 30 % along that time. By contrast, the photocurrent of the ITO\PEDOT:PSS\P3HT:PCBM\$MoS_3$ photocathode decreased by 75 %. TiO_2 also improved the stability of the device.

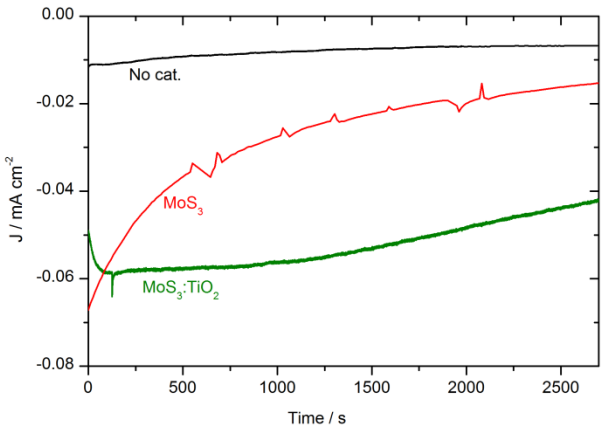

Fig. 65. Electrolysis at +0.16 V *vs* RHE of photocathodes in 0.5 M H_2SO_4, under illumination. Black: ITO\PEDOT:PSS\P3HT:PCBM (reference), red: ITO\PEDOT:PSS\P3HT:PCBM\$MoS_3$ photocathode, green: ITO\PEDOT:PSS\P3HT:PCBM\$TiO_2$:$MoS_3$ photocathode. Electrode area: 0.5 cm².

A sample of gas was taken from the gas above the electrolyte in the test cell. Hydrogen was detected by gas chromatography during this experiment but the faradic yield was difficult to estimate because of the large volume of electrolyte (Fig. 66).

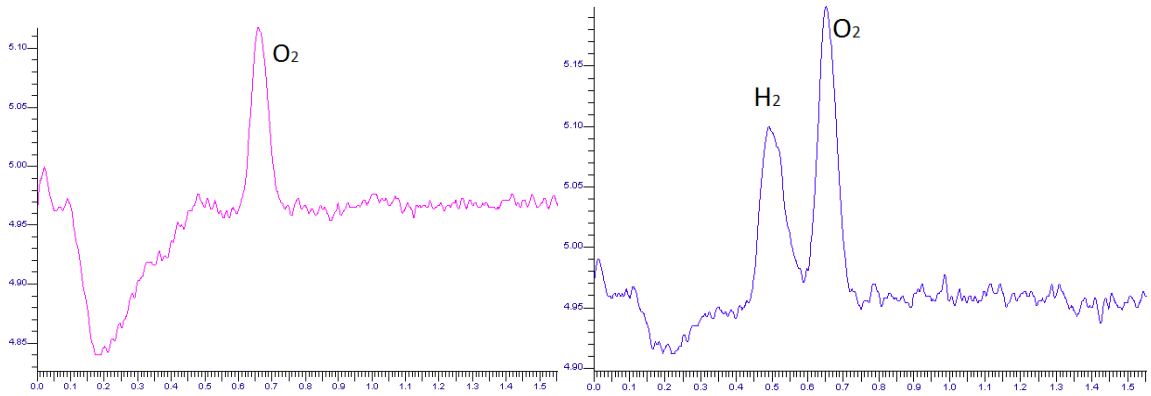

Fig. 66. H_2 detection (gas chromatography) before and after electrolysis during 30 min at +0.16 V *vs* RHE for the ITO\PEDOT:PSS\P3HT:PCBM\TiO_2:MoS_3 photocathode.

2.6. Conclusions on Chapter 2

The above results demonstrate the possibility to exploit OPV technology for the construction of a novel type of PEC devices harvesting visible light. The catalytic layer has been synthesized and characterized prior to its deposition on a polymer-fullerene bulk heterojunction. The multilayer device was then interfaced with aqueous acidic media and a photocurrent density of 50 μA cm^{-2} at 0 V *vs* RHE was obtained. To improve the BHJ-catalyst performance, TiO_2 was mixed in MoS_3 and the optimal stack displayed an onset potential for light-driven H_2 production 380 mV more positive than the onset HER potential measured at a TiO_2:MoS_3 electrode in the dark. The photovoltage compares with the 540 mV open circuit potential (V_{OC}) measured for the solid-state solar cells based on the same P3HT:PCBM light-harvesting layer and produced in the laboratory under similar conditions, confirming the ability of the photocathode to use the photogenerated charges to produce hydrogen. Thus, the next chapter reports on the optimization of the photocathode with interfacial layers between the P3HT:PCBM and the MoS_3 catalyst.

Chapter 3. Study of electron-extracting interfacial layers to enhance the performance of the photocathodes

In the previous chapter, a photocathode based on the photosensitization of a non-precious catalyst, MoS_3, by a P3HT:PCBM bulk heterojunction (BHJ) was studied in aqueous media. MoS_3 was chosen as it is a noble metal-free hydrogen evolution catalyst (with an overpotential of 150 mV[118]) and it could be solution-processed directly onto thin OSC films without thermal or chemical treatment. Hydrogen was photo-produced with a current density of 180 µA cm^{-2} at the reversible hydrogen electrode (RHE) potential. The current density, however, remains lower than expected since P3HT:PCBM solar cells can deliver a short circuit current density of 10 mA cm^{-2} under 100 mW cm^{-2} of illumination. Thus, current densities of the milliampere magnitude should be attainable based on the current density-potential curves of MoS_3 and of the organic solar cell. In 2014, after the publication of our first photocathodes, a device based on a P3HT:PCBM photocathode was reported to produce hydrogen from HCl-acidified acetonitrile solution with a cobaloxime catalyst in solution. A photocurrent density of 1 mA cm^{-2} corresponding to hydrogen production was obtained, which is considerably higher than previously reported devices based on the same materials. Their device could also work as a regenerative PEC cell, when the photocathode was interface with a redox shuttle, with a J_{SC} of 4 mA cm^{-2} and the inverted structure (i.e. with the collection of holes at the interface with the electrolyte) could be used as photoanode in a regenerative PEC cell. These results show that a higher range of photocurrent density could be obtained with the same photoactive material (P3HT:PCBM).[160]

The possibility to enhance the performance in aqueous media of our system was investigated through the introduction of a dense and conductive layer between the P3HT:PCBM layer and the MoS_3 catalyst. This interfacial layer (EEL) could indeed suppress two possible causes of the low photocurrent obtained with the ITO\PEDOT:PSS\P3HT:PCBM\MoS_3 photocathodes: inefficient charge transfer between P3HT:PCBM and MoS_3, and a problem of stability of the P3HT:PCBM layer in aqueous media.

In the OPV field, different types of interfacial materials such as metals, semiconducting materials (inorganic metal oxides, organic compounds such as polymers or graphene), and dipole layers (self-assembled monolayers or SAMs, salts) have been developed to increase the PCE of organic solar cells.[157] Interfacial layers should meet several requirements: promotion of the formation of an Ohmic contact between electrodes and active layer, sufficient conductivity to reduce resistive losses, chemical and physical stability to prevent reactions between active layer and electrode, processing from solution and at low temperature, mechanical robustness to support multilayer processing, good film forming properties, and production at low cost.[151] Inorganic semiconducting interfacial layers should also have a large bandgap to confine excitons in the active layer, appropriate energy levels to improve charge selectivity for corresponding electrodes, and low absorption in the Vis-NIR wavelengths to minimize optical losses.

For protection against chemical corrosion, layers must be thin enough to allow interfacial charge transfer and thick enough to provide sufficient chemical resistance against the electrolyte. In Chapter

3, we investigate how to enhance the performance in aqueous media of our system[161] through the introduction of an electron-extracting layer between the P3HT:PCBM layer and the MoS_3 catalyst. The different materials are: (1) a metallic material used to improve electronic collection and electronic transfer to the catalyst, (2) a solution-processed oxide, and (3) a nanocarbon layer used as fully organic interfacial layer. The effect of interlayers between the MoS_3 catalyst and the P3HT:PCBM BHJ on the photocatalytic performance is investigated by studying the photocurrent and photovoltage of the different photocathodes, compared with the electrocatalytic activity of the bare catalyst, MoS_3

3.1. Metallic layers

In order to improve the current density previously obtained with ITO\PEDOT:PSS\P3HT:PCBM\$MoS_3$ in aqueous electrolyte, we decided to use a LiF\Al layer intercalated between P3HT:PCBM and MoS_3. LiF\Al is widely used as a cathode material for organic solar cells, as it has a suitable work function which efficiently collects the electrons from the fullerene derivative acceptor. It consists of a thin LiF layer (1.2 nm) and a metallic aluminum layer (typically 100 nm) evaporated under vacuum onto the P3HT:PCBM bulk heterojunction. In this configuration, MoS_3 is not acting both as electron-collecting layer and catalyst, but only as catalyst. The constructions with ITO\PEDOT:PSS\P3HT:PCBM\LiF\Al\$MoS_3$ architectures did however not exhibit promising properties since the aluminum layer got rapidly oxidized in the acidic electrolyte despite the presence of the spin-coated catalyst overlayer (Fig. 67). Such an oxidative process was evidenced by the observation of anodic dark currents (light off), which could not be completely reversed even under illumination (light on).

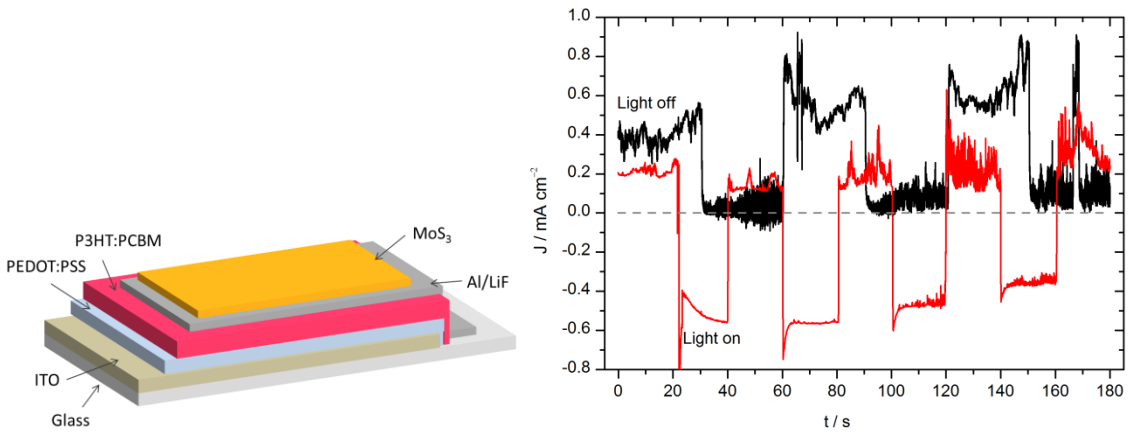

Fig. 67. Electrolysis at a bias potential of +0.15 V *vs* RHE in 0.5 M H_2SO_4 with chopped visible light for ITO\PEDOT:PSS\P3HT:PCBM\LiF\Al\$MoS_3$ (black) and ITO\PEDOT:PSS\P3HT:PCBM\LiF\Al\$MoS_3$:$TiO_2$ (red) photocathodes. Electrode area: 0.5 cm^2.

The measured current density is the macroscopic result from a balance between reduction and oxidation processes. When the current is positive, the dominant process is oxidation, while the negative current results from a dominant reduction process. In other words, the cathodic photocurrent corresponding to H_2 evolution was always found lower than the oxidation dark current. Using a mixed MoS_3:TiO_2 catalyst, as described in Chapter 2 (section 2.3.5.3), thicker catalyst films were deposited. In that case, the photocurrent density (about 0.8 mA cm^{-2}) was significantly higher than the dark oxidation current density (about 0.2 mA cm^{-2}), as shown in Fig. 67. Nevertheless, such performances were not stable with time and continuous operation resulted in a concomitant decrease of the photocurrent density and increase of the dark current density as the aluminum layer progressively dissolved in the acidic media.

To protect the Al layer, a metallic titanium layer was evaporated on top of Al. Ti had already been used as a protective layer in a Si-based photocathode.[51,52,162,163] Organic photocathodes with a titanium overlayer were fabricated starting from ITO\PEDOT:PSS\P3HT:PCBM\LiF\Al by depositing a 30 nm thick Ti layer in a Joule evaporator. The voltammogram recorded in 0.5 M H_2SO_4 electrolyte under chopped illumination is presented in Fig. 68, with the J-V curve of the equivalent solar cell for comparison.

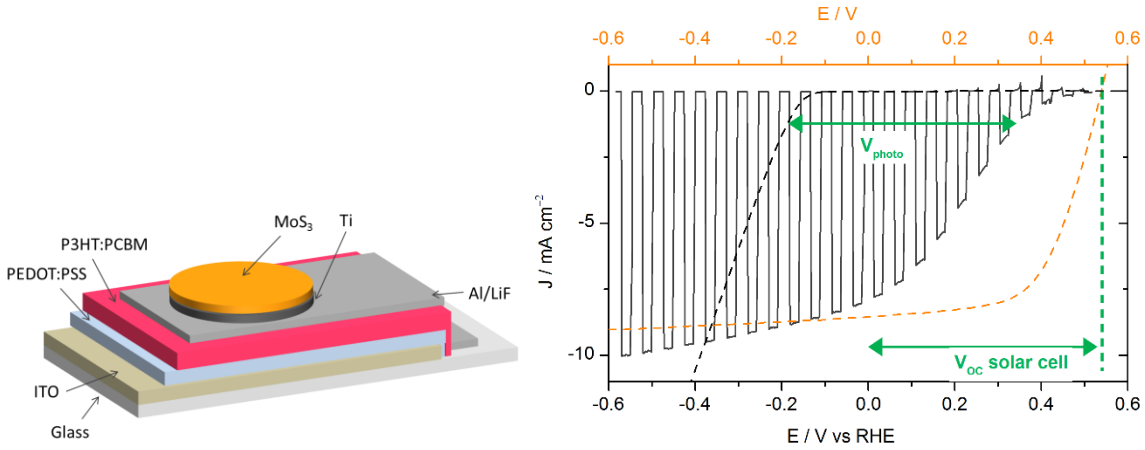

Fig. 68. Voltammogram recorded at 50 mV s^{-1} in 0.5 M H_2SO_4 with chopped visible light for an ITO\PEDOT:PSS\P3HT:PCBM\LiF\Al\Ti\$MoS_3$ photocathode (black line, electrode area 0.32 cm^2), and recorded at 5 mV s^{-1} in 0.5 M H_2SO_4 for an ITO\$MoS_3$ cathode (black dashed line, electrode area 0.28 cm^2). Potentials are referred to the RHE (bottom axis). The current density-voltage curve of an ITO\PEDOT:PSS\P3HT:PCBM\LiF\Al solar cell (orange dashed line, top axis) is shown for comparison.

The performances of the photoelectrodes were significantly improved compared to our previous devices, with a photocurrent density value of 8 mA cm^{-2} at 0 V *vs* RHE and reaching 10 mA cm^{-2} at more cathodic potentials. The onset of light-driven HER (values were taken at 0.1 mA cm^{-2}) was observed at + 0.48 V *vs* RHE. Dark HER onset was found at –0.15 V *vs* RHE (black dashed line in

Fig. 68), as expected for MoS_3 under these conditions.[119] The light-driven anodic shift of the HER, called photovoltage V_{photo} in the following, was thus found equal to 0.6 V at 1 mA cm^{-2}, close to the open-circuit voltage (V_{OC}) of the organic solar cell (approximately 0.6 V). For illuminated photoelectrodes, current limitation occurs at quite negative potentials, which contrasts with the behavior of electrodes based on MoS_3 electrocatalyst alone, which J-E curve continues to increase when decreasing the potential. This plateau (typically 10 mA cm^{-2}) thus does not correspond to a H^+-diffusion-limited current. It likely originates from saturation of the solar cell as observed in typical current density-voltage solar cell characteristics shown in Fig. 68. To test this hypothesis, the power of the light source was changed. As shown in Fig. 69a, the saturation current density changed accordingly. This confirms that the photocurrent value at low potential is limited by the photocurrent produced by the organic solar cell. Moreover, in the range of 0 to 0.5 V, the J-E curve of the photocathode was shifted by approximately 150 mV compared to the solar cell. This value seems to correspond to the overpotential requirement of the MoS_3 catalyst. Indeed, Fig. 69b shows the electro- and photoelectro-chemical HER activity of the unsensitized and OSC-sensitized MoS_3 and Pt/C (platinum on carbon) catalysts. Similarly to MoS_3, the voltammogram of the illuminated ITO\PEDOT:PSS\P3HT:PCBM\LiF\Al\Ti\Pt/C photocathode was anodically shifted by a photovoltage close to the V_{OC} of the solar cell (i.e. approximately 0.6 V) as compared to the voltammogram of the ITO\Pt/C cathode. The difference of onset potential of both MoS_3 and Pt catalysts was reflected in the difference of onset potentials of the two photocathodes. Fig. 69 thus shows that both photocurrent and photovoltage are optimal with the LiF\Al\Ti interlayer.

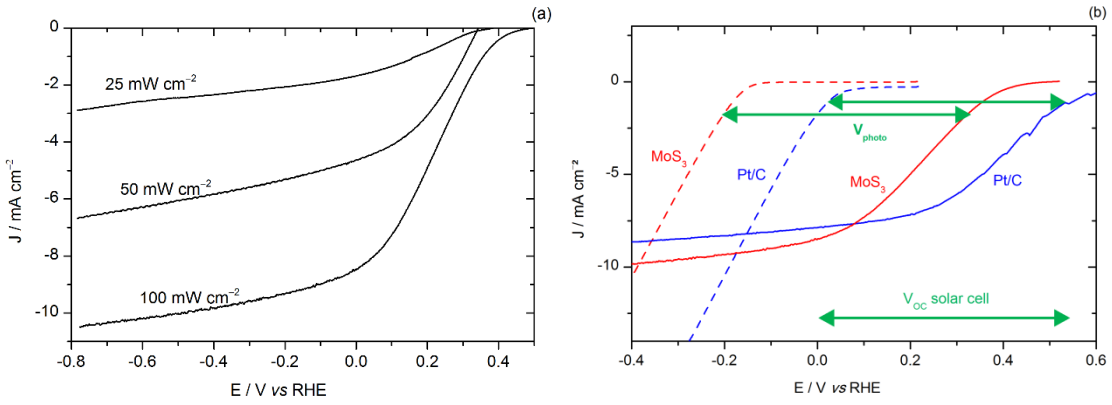

Fig. 69. (a) Voltammograms recorded at 50 mV s^{-1} in 0.5 M H_2SO_4 with visible light illumination for an ITO\PEDOT:PSS\P3HT:PCBM\LiF\Al\Ti\$MoS_3$ photocathode. The power of the light source was changed from ~ 100 mW cm^{-2} to ~ 25 mW cm^{-2}. New photocathodes were taken for each test with a different power source. Electrode area: 0.32 cm^2. (b) Voltammogram recorded at 5 mV s^{-1} in 0.5 M H_2SO_4 for an ITO\$MoS_3$ cathode (red dotted line) and an ITO\Pt/C cathode (blue dotted line) and at 50 mV s^{-1} with visible light illumination (100 mW cm^{-2}) for an ITO\PEDOT:PSS\P3HT:PCBM\LiF\Al\Ti\$MoS_3$ photocathode (red line), and an ITO\PEDOT:PSS\P3HT:PCBM\LiF\Al\Ti\Pt/C photocathode (blue line).

Despite their satisfying performance, the photocurrent density decreased under operation (Fig. 70). This was attributed to the fact that the electrolyte could reach the aluminum layer through the Ti layer, resulting in the lift-off of the LiF\Al\Ti\MoS_3 metallic layer, as observed during the experiment.

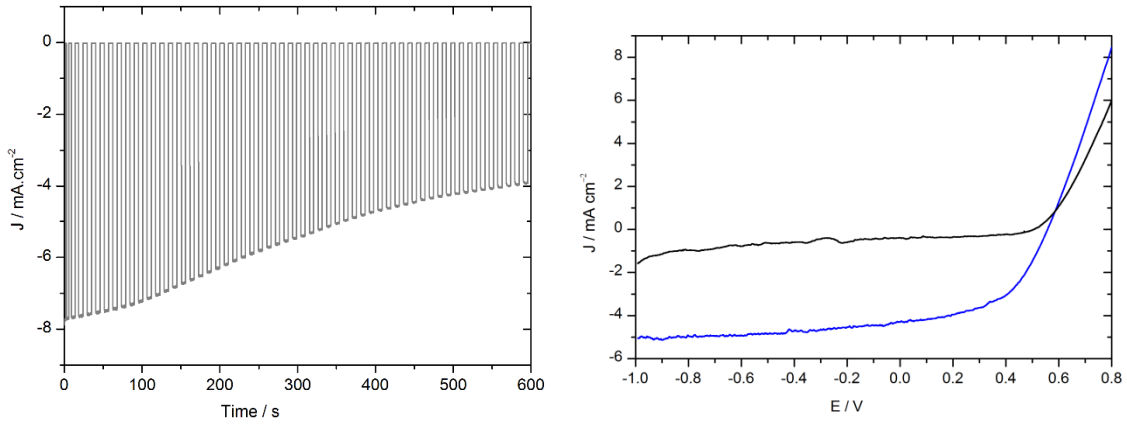

Fig. 70. *Left:* Chronoamperometry at 0 V *vs* RHE in 0.5 M H_2SO_4 with chopped visible light for an ITO\PEDOT:PSS\P3HT:PCBM\LiF\Al\Ti\$MoS_3$ photocathode. Electrode area: 0.28 cm^2. *Right:* Current density-voltage curve measured for an ITO\PEDOT:PSS\P3HT:PCBM\LiF\Al\Ti\$MoS_3$ photocathode before (blue) and after (black) a photoelectrolysis experiment. The cell was measured in a two-electrode configuration using the potentiostat by short-circuiting the reference electrode on the counter electrode and contacting the ITO and the aluminum.

To overcome the stability issue due to the aluminum layer, photocathodes were made the LiF/Al. As shown in Fig. 71 *left*, the photocurrent displayed by the photocathode without LiF\Al (blue curve) was similar in intensity to that measured on the photocathode with LiF\Al\Ti. However the HER onset of the new photocathode was 150 mV more negative than the former one containing the LiF/Al layer. Actually the photovoltage provided by the solar cell is limited to 0.45 V (from –0.15 to +0.32 V *vs* RHE), compared to 0.6 V with LiF\Al\Ti. The lower photovoltage obtained without the LiF/Al layer can be attributed to the difference in the metals work functions (Fig. 71 *right*), which changes the work function of the cathode.

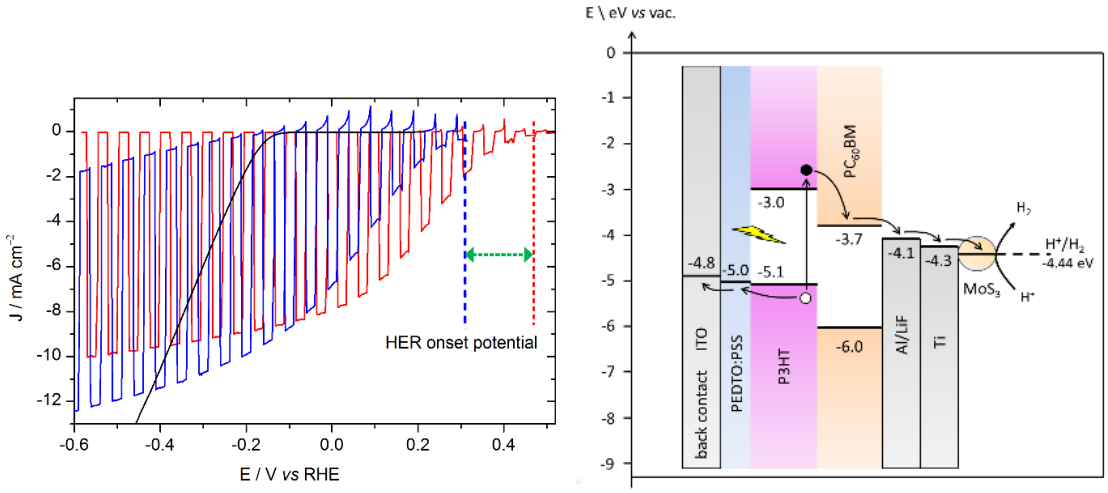

Fig. 71. *Left*: Voltammograms recorded at 50 mV s^{-1} in 0.5 M H_2SO_4 with chopped visible light. Red: ITO\PEDOT:PSS\P3HT:PCBM\LiF\Al\Ti\$MoS_3$ photocathode (electrode area: 0.32 cm^2); blue: ITO\PEDOT:PSS\P3HT:PCBM\Ti\$MoS_3$ (0.28 cm^2). The green arrow represents the shift of the HER onset potential of 150 mV. The photocurrent density (12 mA cm^{-2}) is higher than what can be expected for a P3HT:PCBM-based solar cell, but this can be explained by the significant dark current and by the light source, which is a Hg-Xe lamp delivering 100 mW cm^{-2} but with a different spectrum than the solar spectrum. *Right*: Diagram representing the energy level diagram of the device in contact with the electrolyte. Electrons and holes are represented by black and white dots respectively.

Stability measurements were then performed with chopped light at 0 V *vs* RHE. The results are presented in Fig. 72.

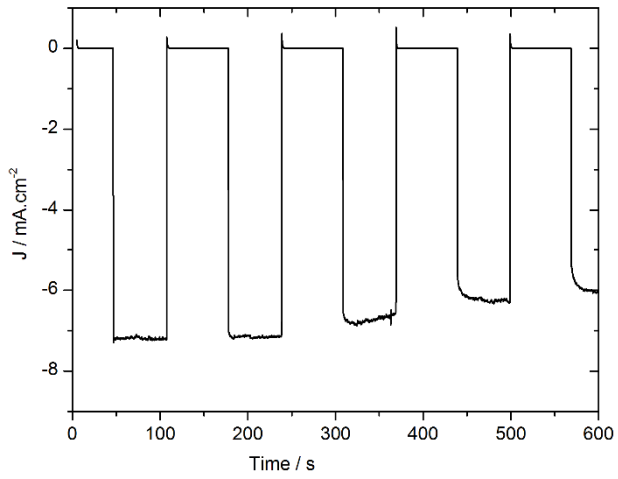

Fig. 72. Chronoamperometry at 0 V *vs* RHE in 0.5 M H_2SO_4 with chopped visible light for a ITO\PEDOT:PSS\P3HT:PCBM\Ti\MoS_3 photocathode (black). Electrode area: 0.28 cm^2.

The use of titanium as the sole interfacial layer increased the stability under operation, with a loss of only 12% of the photocurrent over 10 min while the same photocathode with a LiF/Al/Ti interfacial

layer was found to lose 45% of its performance under similar conditions (Fig. 70). Moreover, after one hour, the titanium layer was not peeled off as the LiF/Al/Ti layer was, but the current density was reduced to from 7 mA cm^{-2} to 2 mA cm^{-2}. The decrease of the photocurrent density for the ITO\PEDOT:PSS\P3HT:PCBM\Ti\MoS_3 photocathode could be caused by the increase of the thickness of the native oxide layer, which is semiconducting,[162] but also from the gradual loss of electrocatalytic activity of the MoS_3 catalyst. Nevertheless, devices made without an aluminum layer were found significantly more stable.

Photocathodes were prepared with a LiF\Ti interlayer to verify that the difference between the ITO\PEDOT:PSS\P3HT:PCBM\LiF\Al\Ti\$MoS_3$ and ITO\PEDOT:PSS\P3HT:PCBM\Ti\$MoS_3$ did not come from the absence of LiF in the second one. LiF and Ti were however evaporated in two different places, so that the LiF layer was exposed briefly to air prior to the Ti evaporation.

The results are presented in Fig. 73.

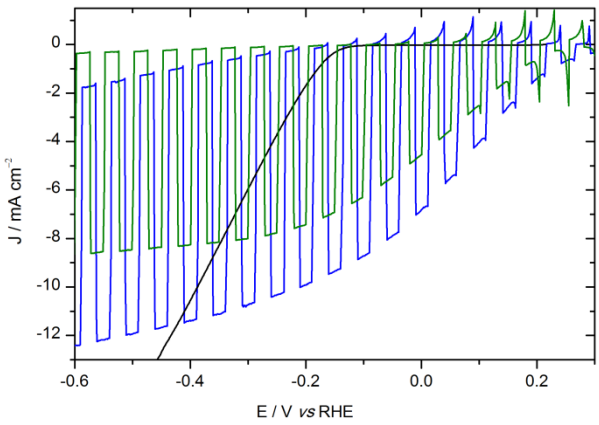

Fig. 73. Voltammograms recorded at 50 mV s^{-1} in 0.5 M H_2SO_4 with chopped visible light. Green: ITO\PEDOT:PSS\P3HT:PCBM\LiF\Ti\$MoS_3$ photocathode (electrode area: 0.28 cm^2); blue: ITO\PEDOT:PSS\P3HT:PCBM\Ti\$MoS_3$ (0.28 cm^2). Voltammogram recorded at 5 mV s^{-1} in 0.5 M H_2SO_4 for an ITO\$MoS_3$ cathode (black line, electrode area 0.28 cm^2).

The onset potential of the ITO\PEDOT:PSS\P3HT:PCBM\LiF\Ti\$MoS_3$ is only 10 mV smaller than without LiF, but the photocurrent density is reduced and the HER slope is lower, which could be explained by LiF inducing contact resistances in the device. The ITO\PEDOT:PSS\P3HT:PCBM\LiF\Ti\$MoS_3$ photocathode tested in Fig. 73 did not present any short circuit but other devices sometimes had short-circuits which resulted in a dark current starting at the onset potential of the MoS_3 catalyst.

Stability measurements performed at 0 V *vs* RHE are presented in Fig. 74. Over half an hour, the stability is similar for both photocathodes. However, the photocurrent density is lower in the case of LiF\Ti, in accordance with the previous experiment.

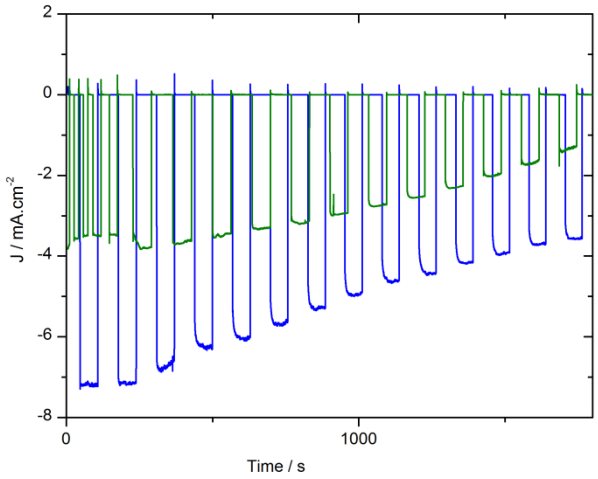

Fig. 74. Chronoamperometry at 0 V *vs* RHE in 0.5 M H_2SO_4 with chopped visible light for a ITO\PEDOT:PSS\P3HT:PCBM\Ti\$MoS_3$ photocathode (blue) and an ITO\PEDOT:PSS\P3HT:PCBM\LiF\Ti\$MoS_3$ photocathode (green). Electrode area: 0.28 cm^2.

To summarize, the use of metallic layers dramatically increased the efficiencies of the photocathode compared to the first photocathodes that we reported which displayed photocurrent densities limited to 180 µA cm^{-2}. These interfacial layers bury the P3HT:PCBM layer and electronically separate the catalyst/electrolyte interface and the photovoltaic cell. The bulk heterojunction providing the photovoltage and driving force for HER is therefore not impacted by the redox potential of interest (H^+/H_2). It also explains why the J-E curves obtained with these photocathodes are shaped like the J-V curves of the solar cells: all photogenerated electrons are collected by the metallic layer and then transferred to MoS_3 for catalysis. As no direct liquid-semiconductor junction is formed, these devices can be identified as part of a PV-biased electrosynthetic cell following the taxonomy described in Chapter 1,[16] which is bringing the device a step away from the direct sensitization of a catalyst, that is, a step closer to a PV-electrolyzer.[11]

Finding chemically resistant, conductive and water-tight materials is still a challenging task, but metallic titanium is close to meeting all the criteria. Indeed, contrary to aluminum, it does not dissolve in acidic water, and is conductive. However, in terms of photovoltage, the use of a Ti interfacial layer alone shifts the J-E curve 150 mV more negative than with a combined Ti/Al layer. In the next part, a solution-processed material as interfacial layer was studied.

3.2. Solution-processed electron-extracting layer: sol-gel TiO_x

Metal oxides have been used on inorganic absorbers to passivate the surface and increase the efficiency of organic solar cells.[164] Among them, TiO_2 and ZnO have been demonstrated as protective layers improving the performance of photocatalytic devices. The photocurrent density of n^+p-Si/Pt photocathodes from Chorkendorff's group increased from 18 to 22 mA cm^{-2} when a TiO_2 interfacial

layer was added[162]. Lin and coll. made TiO_2-protected amorphous Si photocathodes with a Ni-Mo catalyst and observed an increased stability compared to the photocathodes without TiO_2.[165] In our previous work, mixed TiO_2: MoS_3 was used instead of MoS_3 to improve charge collection from PCBM to MoS_3 and add electronic conductivity. However, this layer was mesoporous due to the nanoparticles of TiO_2. The deposition of dense TiO_2 layers can be performed by directly spin-coating a sol gel precursor, and this n-type oxide has been previously used in organic solar cells to increase the efficiency thanks to its role as electron collecting layer in tandem solar cell[150] and as an optical spacer.[152] As it is cast directly on P3HT:PCBM, a compact layer is obtained, so that a property of diffusion barrier to H_2O and O_2 also contributes to the improvement of the cells.[152] It also shows good electron selectivity. However, as it is prepared at low temperature, the oxide is amorphous and must be used in thin layers (< 10 nm) so as not to induce significant resistive losses. Fig. 75 shows that a 7 nm-thick TiO_x layer impacts slightly the performance of MoS_3 by adding approximately 20 mV of overpotential to the existing one for the HER.

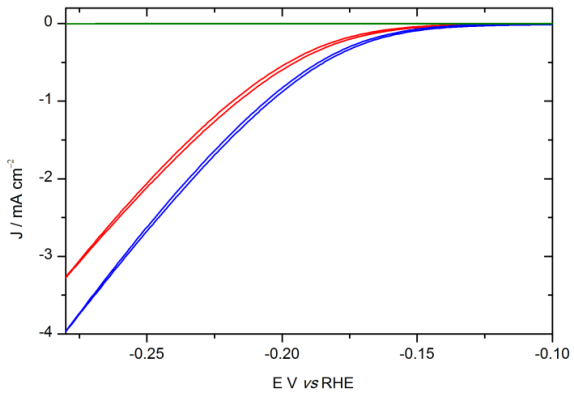

Fig. 75. Second cycle of a CV in N_2-saturated 0.5 M H_2SO_4 at 5 mV s^{-1} for an ITO\$MoS_3$ electrode (blue) and an ITO\$TiO_x$\$MoS_3$ electrode (red). MoS_3 was deposited by spray in both cases. The green line is a CV of an ITO\$TiO_x$ electrode showing no electrocatalytic activity in this potential range.

Fig. 76 shows the results obtained with the TiO_x layer between MoS_3 and P3HT:PCBM.

Photocurrent densities of about 70 µA cm^{-2} were obtained at RHE potential during chopped-light voltammetry, which is slightly better than the photocathodes without TiO_x, especially at higher cathodic potentials. Though the PCE of the corresponding solid-state ITO\PEDOT:PSS\P3HT:PCBM\TiO_x\LiF\Al solar cell is 1.4 % (*vs* 2.8 % for the ITO\PEDOT:PSS\P3HT:PCBM\LiF\Al solar cell) with a J_{SC} of 6.8 mA cm^{-2} (Fig. 77), this photocurrent density obtained with the photocathode was low. The TiO_x electron collecting layer was

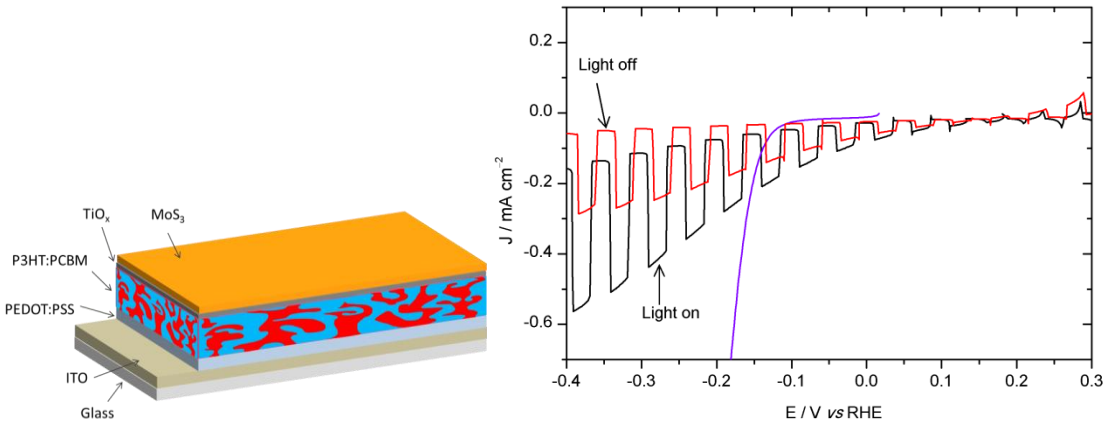

Fig. 76. Voltammograms recorded in 0.5 M H_2SO_4 at 50 mV s s^{-1} with chopped visible light for an ITO\PEDOT:PSS\P3HT:PCBM\$MoS_3$ photocathode (red, 0.32 cm^2), an ITO\PEDOT:PSS\P3HT:PCBM\$TiO_x$\$MoS_3$ photocathode (black, 0.32 cm^2), and an ITO\$MoS_3$ cathode (purple, 5 mV s^{-1}, 0.28 cm^2).

improving charge collection at high overpotentials, but the V_{OC} was not improved compared to Ti, resulting in a low photocurrent density at 0 V *vs* RHE.

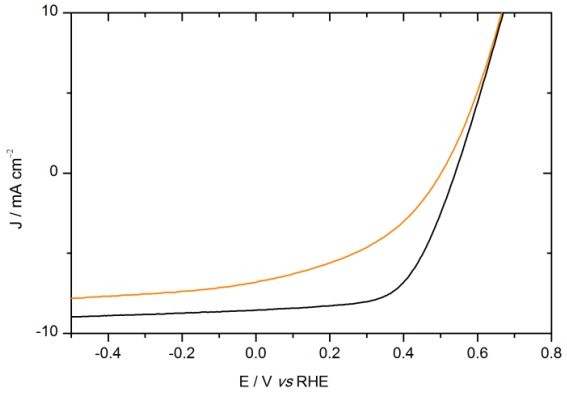

Fig. 77. Current density-voltage curve of an ITO\PEDOT:PSS\P3HT:PCBM\TiO_x\LiF\Al solar cell (orange line) and of an ITO\PEDOT:PSS\P3HT:PCBM\LiF\Al solar cell (black line).

Moreover, very thin TiO_x interfacial layers were used to limit resistive losses, so that its stability in acidic media was low, as shown in Fig. 78. The photocurrent density was dropping quickly, while the V_{OC} on the voltammogram was shifting towards cathodic potentials. On the anodic side of the V_{OC}, the photocurrent was inverted and increased at the second cycle. The oxidation photocurrent density increasing with the following cycles are probably due to the start of the voltammogram at + 0.4 V without pre-polarization.

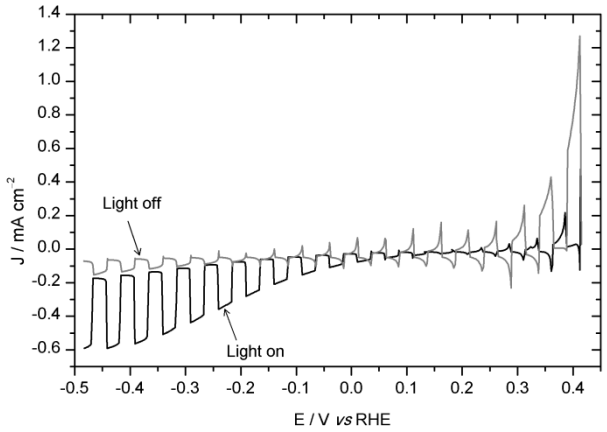

Fig. 78. Voltammograms recorded at 50 mV s^{-1} in 0.5 M H_2SO_4 with visible light illumination for an ITO\PEDOT:PSS\P3HT:PCBM\$TiO_x$\$MoS_3$ photocathode. First (black) and second (grey) sweeps. Electrode area: 0.06 cm².

A very similar work was published by Haro and coll. in 2015, in which they deposited sol-gel TiO_x in layers up to 50 nm on P3HT:PCBM.[166] A thin layer of Pt (~ 0.5 nm) was then sputtered on top of the TiO_x as a catalyst for proton reduction and the photocathode was tested in acidic aqueous media (0.1 M Na_2SO_4 acidified to pH 2 with H_2SO_4). 600 µA cm^{-2} were obtained at the RHE potential, but no information is provided on the onset potential of the HER. However, the use of a thicker TiO_x layer (successive deposition of 50 nm TiO_x and 0.5 nm Pt carried out three times) reduced the photocurrent density to 300 µA cm^{-2}. These current densities are significantly higher than in our case, and they are stable over 3 hours. Their explanation was that they used cross-linked PEDOT:PSS to prevent the delamination of the whole cell when it was plunged into water. Our devices were however not plunged entirely into water but only a circle of the top layer (catalyst layer) was in contact with the electrolyte, so that delamination was observed only when the P3HT:PCBM was accidentally scratched, causing a direct contact between the PEDOT:PSS and the electrolyte. In addition, if the only reason of the low current densities obtained in our case was caused by a low PEDOT:PSS stability, we would have expected that at least the first cycle would produce significant photocurrents. The improvement of performance in their case probably originates from the preparation method of the TiO_x layer (which is not too resistive), and its thickness, which bury the P3HT:PCBM junction, as described with the metallic layers at the beginning of this Chapter.

The deposition of dense and conducting TiO_2 layers can be performed by atomic layer deposition (ALD)[52,163] or by reactive sputtering.[162] However, ALD necessitates long deposition times, which might not be compatible with the organic solar cells, even if the substrate temperature was low (e.g. 80 °C), and for reactive sputtering a final annealing at 400 °C was shown to be necessary for the stability of the TiO_2 layer used on the photocathode.[162] Such layers would still be very interesting to test in a

further work, even with a low-temperature annealing, because thicker layers can be deposited, which could provide protection from the electrolyte.

To improve the photocurrent while keeping soft processing conditions of interfacial layers, we decided to study the possibility to deposit nanocarbons.

3.3. Nanocarbons

3.3.1. Graphene

The ultimate conducting organic material, graphene, being hydrophobic and conductive at the same time, appeared as the ideal target material. Indeed, with this continuous and atomically thin material, both protection from water and transfer of electrons by tunneling could be expected. Placed between the P3HT:PCBM layer and MoS_3, it was expected to meet both criteria of stability and electronic transfer. Graphene has been used as electron-collecting layer, for photovoltaic cells or phocatalysis applications:[167] it has been transferred once on a Si-based photocathode, the monolayer of graphene acting both as a catalyst and a passivation layer;[168] Li-doped graphene oxide was spin-coated as an electron-entracting layer with TiO_x.[169] Also with TiO_x, a graphene derivative, graphene oxide, was stamped with thermal release tape on the active layer.[170] Roll-to-roll production of graphene and its transfer on various substrates are promising for applications in transparent electrodes.[171]

However, depositing one continuous and single layer of graphene onto P3HT:PCBM turned out to be very challenging. High quality monolayered graphene is synthesized by CVD on a copper substrate, and two types of methods exist to transfer graphene onto the target substrate: wet transfers[172] (involving a mechanical support such as PMMA), and dry transfers[173,174] (involving thermal release tapes or PDMS-based stamps). Typically, in a wet transfer process, PMMA is spin-coated on top of the graphene, and the copper foil is etched. After some rinsing steps the floating PMMA\graphene is deposited onto the target substrate by plunging the substrate into water and slowly taking it out. Once dried, the PMMA is removed with acetone. The detailed procedure is provided in the experimental section. Dry transfer techniques usually involve thermal release tape or PDMS-based stamps.[173,174] Small areas can be transferred but in our case, the areas are between 0.1 - 1 cm². Moreover, the transfer is strongly depending on the target substrate: while it is quite easy on SiO_2/Si substrates, it is more difficult on P3HT:PCBM (all the more so that it is much more difficult to characterize whether graphene has been transferred or not). Different methods were tested, for both dry and wet transfers. Dry-transferred layers were inevitably incomplete and damaged (Fig. 79 *right*), whereas during wet transfer layers, which are usually continuous and intact (Fig. 79 *left*), one major drawback appeared. Indeed, the step of plunging the substrate in water to deposit the PMMA\graphene caused the delamination of PEDOT:PSS.

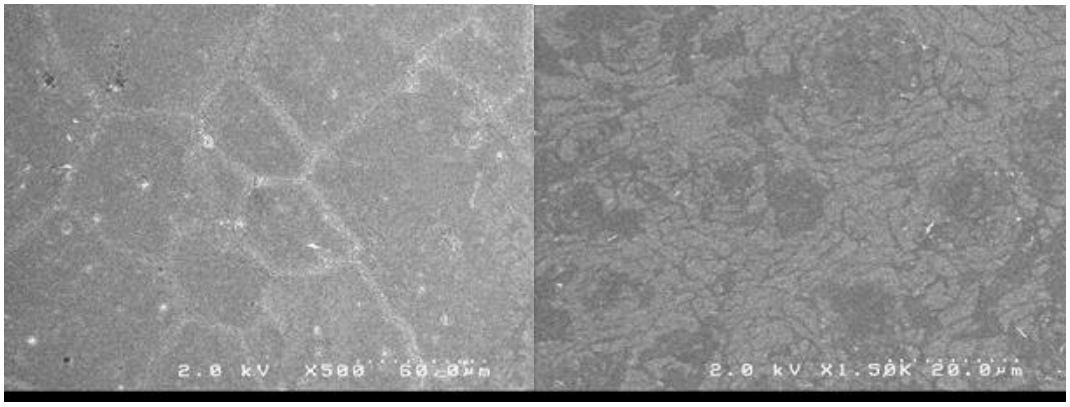

Fig. 79. Graphene monolayers transferred onto SiO_2/Si substrates by the wet transfer method (*left*) and by a dry transfer method (thermal release tape, *right*).

Some devices were tested by using dry transfer techniques, but graphene was never properly deposited onto the organic layer. Contrary to the silicon substrates, on which dry transfer was possible, the transfer of graphene on P3HT:PCBM did not work: the graphene layer seemed to stick on the thermal release tape, and the tape damaged the P3HT:PCBM layer. Besides, SEM analysis could not show any trace of graphene on P3HT:PCBM, though it would probably be difficult to see. Other techniques were tested, for example by using a tape with a hole as mechanical support for the PMMA/graphene to be able to dry it before deposition, but without success.

3.3.2. Fullerene C_{60}

We then decided to use the 0D equivalent of the graphene, i.e. C_{60}. C_{60} is an organic molecule with a work function located between PCBM and MoS_3, which makes it suitable as interfacial material for transferring the photogenerated electrons to MoS_3. Deposition of thin layers is well-controlled with the use of vacuum evaporation. 50 nm of C_{60} were evaporated on P3HT:PCBM and the MoS_3 suspension was then sprayed onto the C_{60}. The voltammogram recorded under chopped light is presented in Fig. 80.

Compared to our first photocathodes (without any interfacial layers, reaching 180 µA cm^{-2}), the saturation photocurrent density and photovoltage are greatly enhanced. The photocurrent density for ITO\PEDOT:PSS\P3HT:PCBM\$C_{60}$\$MoS_3$ photocathode is about 1 mA cm^{-2} at 0 V *vs* RHE (black line in Fig. 80) without any metallic interlayer. Again, the onset potential of the HER is shifted in the anodic direction from –0.15 V *vs* RHE (MoS_3 in the dark) to +0.18 V *vs* RHE (light-driven HER), i.e. the photosensitizer provides a photovoltage of 0.33 V under operating conditions.

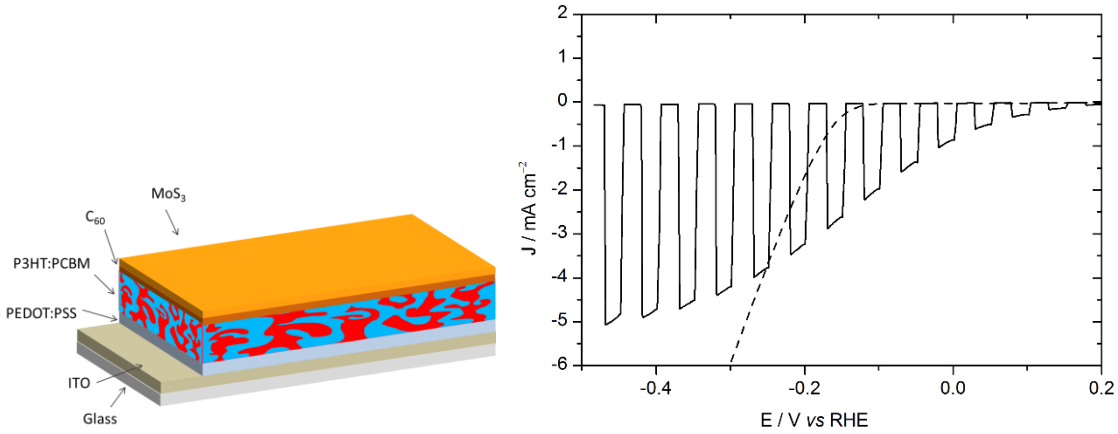

Fig. 80. Voltammogram recorded at 50 mV s^{-1} in 0.5 M H_2SO_4 with chopped visible light for an ITO\PEDOT:PSS\P3HT:PCBM\$C_{60}$\$MoS_3$ photocathode (electrode area: 0.06 cm^2). The polarization curve of ITO\$MoS_3$ recorded at 5 mV s^{-1} is shown for comparison (dashed line, electrode area: 0.28 cm^2).

The J-V curves of the ITO\PEDOT:PSS\P3HT:PCBM\$C_{60}$\LiF\Al solid-state solar cell (Fig. 81) and of the corresponding ITO\PEDOT:PSS\P3HT:PCBM\$C_{60}$\$MoS_3$ photocathode are differing from each other more than the ITO\PEDOT:PSS:\P3HT:PCBM\LiF\Al solid-state solar cell and the corresponding ITO\PEDOT:PSS\P3HT:PCBM\LiF\Al\Ti\$MoS_3$ photocathode (Fig. 68).

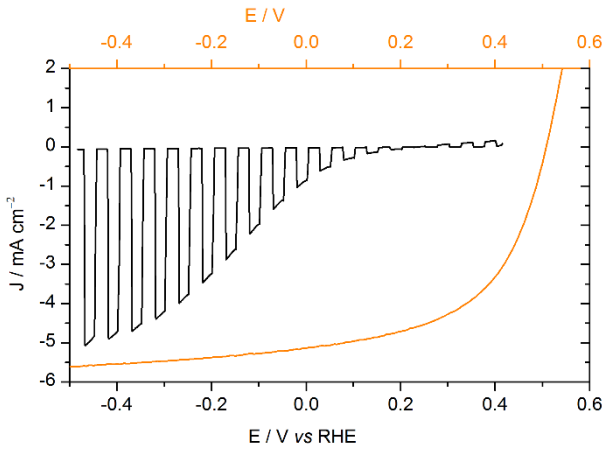

Fig. 81. Current density-voltage curve of an ITO\PEDOT:PSS\P3HT:PCBM\$C_{60}$\LiF\Al solar cell (orange line, top axis). Voltammogram recorded at 50 mV s^{-1} in 0.5 M H_2SO_4 with chopped visible light for an ITO\PEDOT:PSS\P3HT:PCBM\$C_{60}$\$MoS_3$ photocathode (black line, bottom axis, same as in Fig. 80, electrode area: 0.06 cm^2).

Indeed, the current density of the photocathode with C_{60} does not reach the saturation obtained in the corresponding solar cell, while this saturation is reached for the photocathode with the LiF\Al\Ti interfacial layer. This could arise from a higher resistance in electronic transfer from C_{60} to MoS_3 than

from Al\Ti to MoS_3, but also from the fact that the ITO\PEDOT:PSS\P3HT:PCBM\$C_{60}$\$MoS_3$ photocathode does not benefit from the reflectivity of the metallic layer of the ITO\PEDOT:PSS\P3HT:PCBM\LiF\Al\Ti\$MoS_3$ photocathode, which enhances the photocurrent density. Moreover, both V_{OC} and J_{SC} of the solid-state ITO\PEDOT:PSS\P3HT:PCBM\$C_{60}$\LiF\Al solar cell are lower compared to the ITO\PEDOT:PSS\P3HT:PCBM\LiF\Al solar cell (Fig. 82), possibly because of resistive losses due to the limited C_{60} conductivity of about 10^{-7} S cm^{-1}.[175] When LiF was evaporated between P3HT:PCBM and C_{60}, slightly better performances were obtained in terms of photocurrent and photovoltage but no trend was observed concerning the stability. Both C_{60} and LiF\$C_{60}$ resulted in a stabilization of the onset potential around 0 V *vs* RHE.

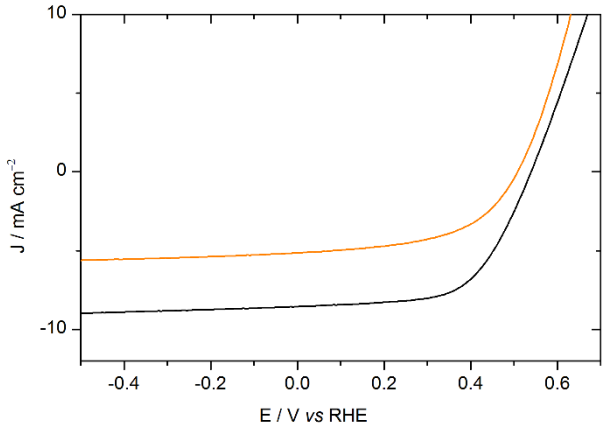

Fig. 82. Current density-voltage curve of an ITO\PEDOT:PSS\P3HT:PCBM\C_{60}\LiF\Al solar cell (orange line) and of an ITO\PEDOT:PSS\P3HT:PCBM\LiF\Al solar cell (black line).

The hydrophobic nature of C_{60}[176] was expected to ensure better stability of the underlying P3HT:PCBM layer by preventing water from reaching it. However Fig. 83 shows that the photocathodes based on C_{60} interlayers degrade rapidly. The second scan already shows both a decrease of the photocurrent density and a shift of the onset HER potential under irradiation towards more negative potentials, finally stabilizing near the equilibrium potential.

These results are consistent with the previous results regarding the effect of a layer burying the P3HT:PCBM BHJ in the whole architecture and suppressing the semi-conductor/electrolyte interface, which is the case with the metallic layers (cf. section 3.1). During the first cycle, the C_{60} layer does not contain water and partly separates the P3HT:PCBM material from the electrolyte. In the following cycles, the water progressively diffuses into the C_{60} layer and progressively reaches the P3HT:PCBM, as if there was no more interfacial layer protecting the device, explaining the shift in the onset HER potential as well as the decrease of photocurrent. This is also consistent with the relatively low

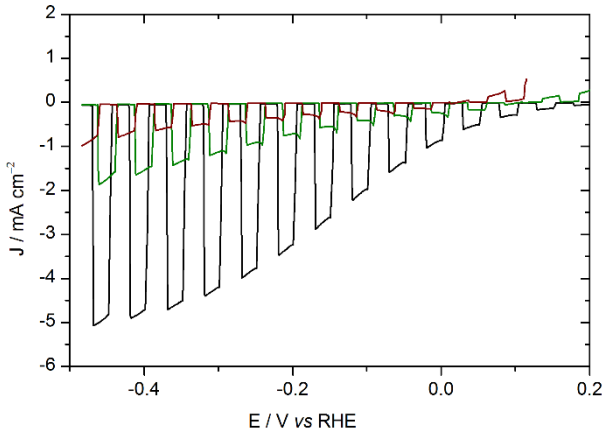

Fig. 83. Voltammograms recorded at 50 mV s^{-1} in 0.5 M H_2SO_4 with chopped visible light for the same ITO\PEDOT:PSS\P3HT:PCBM\$C_{60}$\$MoS_3$ photocathode. Black: 1st cycle (same as Fig. 80); green: 2nd cycle; brown: 3rd cycle. Electrode area: 0.06 cm^2. The oxidation current appearing at anodic potentials was also appearing in configurations without C_{60}: thus, the oxidation current was not attributed to a possible reaction or degradation of C_{60} but more probably to the absence equilibration time between the measurements.

performance obtained with the TiO_x layer. As the TiO_x layer is very thin and probably not very stable in acidic media, it results in the P3HT:PCBM bulk heterojunction being unburied, interacting again with the H^+/H_2 redox level, as for the ITO\PEDOT:PSS\P3HT:PCBM\$MoS_3$ system or the ITO\PEDOT:PSS\P3HT:PCBM\$C_{60}$\$MoS_3$ during the following cycles.

Other possible causes could explain the rather good photocurrent obtained with C_{60} as interfacial layer, for example a suitable band alignment between PCBM and the electrolyte, a better charge extraction from the P3HT:PCBM BHJ, or a better quality of film deposition. However, these reasons do not explain the loss of photocurrent density. Moreover, the explanation given before is consistent with the results obtained in Chapter 4.

Nevertheless, the C_{60} layer increases the photocurrent density at RHE potential to 1 mA cm^{-2} without any metallic layer. As a further investigation in this subsection, we considered the possibility of depositing C_{60} derivatives using wet deposition processes.

3.3.3. Amorphous carbon

As the fullerene improved the photocathode performance, we then investigated amorphous carbon as interfacial layer, as its deposition can be very simple and the raw material does not need complicated synthesis processes. Amorphous carbon has been used as interfacial layer for a Cu_2O photocathode,[177] but it was prepared by calcination (550 °C) of spin-coated glucose. We used a simple carbon sputter to deposit approximately 50 nm of carbon, and the MoS_3 suspension was spin-coated on top of this layer. With TiO_x between P3HT:PCBM and sputtered carbon, the photocurrent density was 1 µA cm^{-2} (Fig.

84). Without TiO_x, the photocurrent (in the range of 1 µA) was inverted, i.e. the current under illumination, though still negative, was lower than the dark current.

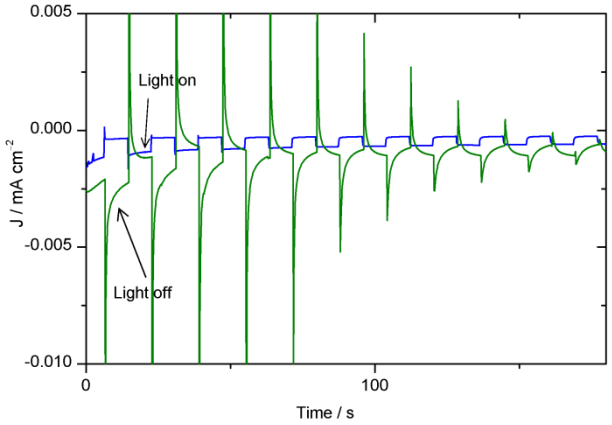

Fig. 84. Chronoamperometry at 0 V *vs* RHE in 0.5 M H_2SO_4 with chopped visible light for an ITO\PEDOT:PSS\P3HT:PCBM\C\$MoS_3$ photocathode (green) and an ITO\PEDOT:PSS\P3HT:PCBM\$TiO_x$\C\$MoS_3$ photocathode (blue). Electrode area: 0.28 cm^2. The photocurrent of the ITO\PEDOT:PSS\P3HT:PCBM\C\$MoS_3$ photocathode (green line) is inversed, and the photocurrent of the ITO\PEDOT:PSS\P3HT:PCBM\$TiO_x$\C\$MoS_3$ photocathode (blue line) is not inversed but sometimes inversed after a few minutes.

The inversion of the photocurrent was also observed when the Pt/C catalyst was deposited directly onto the P3HT:PCBM, similarly to the ITO\PEDOT:PSS\P3HT:PCBM\MoS_3 photocathodes made in Chapter 2. Instead of displaying higher photovoltage and photocurrent density than with MoS_3, the photocurrent density obtained with the ITO\PEDOT:PSS\P3HT:PCBM\Pt/C photocathode was low (1-2 µA cm^{-2}) and inverted, even with a TiO_x layer between P3HT:PCBM and Pt/C (Fig. 85).

Pure platinum could not be tested as catalyst but it has been reported as efficient catalyst deposited on semiconductors for photocathodes.[162] As the Pt/C catalyst contains 60 wt. % of carbon black, it seems that the low performance of Pt/C comes from the carbon content, which is consistent with the photocathodes made with the amorphous carbon layer. Its work function has been reported to be 5.24 eV,[178] so that the Fermi level (–5.24 eV) is located at a lower energy than the redox potential of H^+/H_2 (–4.44 eV). A possible explanation would then be that the carbon work function is too high for the electrons to reduce protons. By contrast, the LUMO level of C_{60} is reported to be ca. –4.5 eV, a value that is much closer to the redox potential of H^+/H_2 (–4.44 eV). These results show that materials have to be carefully chosen to function as efficient interfacial layers.

These interfacial layers showed improved charge transfer compared to the initial cells without interfacial layers. In order to further investigate the impact of the interlayer on the photocathode performance the results were carefully analyzed by means of two figures-of-merit measuring the

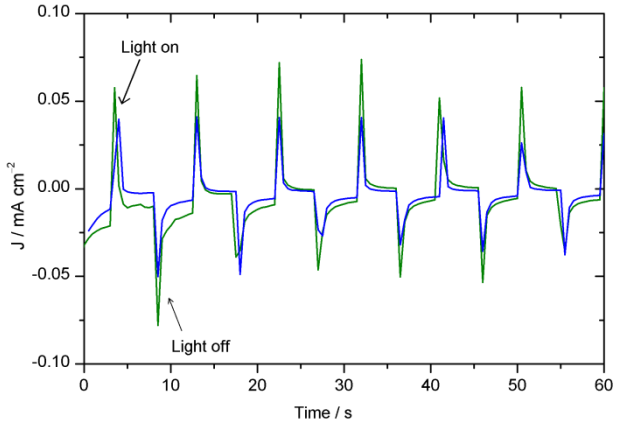

Fig. 85. Chronoamperometry at 0 V *vs* RHE in 0.1 M $HClO_4$ with chopped visible light for an ITO\PEDOT:PSS\P3HT:PCBM\Pt/C photocathode (green) and an ITO\PEDOT:PSS\P3HT:PCBM\TiO_x\Pt/C photocathode (blue) . Electrode area: 0.28 cm^2. As we noticed that the Pt/C catalyst (deposited on ITO) performed better in $HClO_4$ than in H_2SO_4, the photocathodes were tested in both conditions but the photocurrent was inverted in both cases.

amount of power saved by the electrode under operation, $\Phi_{saved,ideal}$ and $\Phi_{saved,NPAC}$, as recently proposed par Lewis and coworkers.[179]

3.4. Comparison of the photocathodes performance

The solar-to-hydrogen conversion efficiency is usually calculated in a two-electrode configuration in which the whole water splitting reaction is performed, without the support of external bias, according to Equ. 8.[4,179]

$$\mathrm{STH} = \left[\eta_F \times \frac{|J_{SC}\ (\mathrm{mA\ cm^{-2}})| \times 1.23\ (\mathrm{V})}{P_{in}\ (\mathrm{mW\ cm^{-2}})}\right]_{\mathrm{AM\ 1.5\ G}} \qquad \text{Equ. 8}$$

where J_{SC} is the short-circuit photocurrent density, η_F the Faradaic efficiency for hydrogen evolution, and P_{in} the incident illumination power density. However, to evaluate the properties of a single photoelectrode performing one of the two half-reactions, without the losses arising from the other components of the cell (overpotential requirement, mass transport limitations at the counter electrode, solution Ohmic losses between the working and counter electrode, etc.), the photoelectrode is tested in a three-electrode configuration, without taking into account the polarization to drive the counter reaction at the counter electrode. In this case, power-saved metrics are adapted figures-of-merit. They are defined as the ratio between P_{saved} and the input solar power P_{in}. At any current I, P_{saved} is the product of the current I and the difference between the potential required to drive a half-reaction at a

selected working electrode at this current in the dark, $E_{dark}(I)$, and the potential required to drive the same half reaction at the photoactive electrode in the light, $E_{light}(I)$.[179]

The power-saved ratio $\Phi_{saved,ideal}$ (Equ. 9) relative to RHE, i.e. an ideally non-polarizable dark electrode, provides information on the ability of a photocathode to achieve hydrogen evolution at potentials more positive than the thermodynamic potential of H^+/H_2. Indeed, solar-to-chemical energy storage implies that the chemical reaction is performed with a lower energy input as compared to the reaction in the dark. The power-saved ratio $\Phi_{saved,ideal}$ measures the performance of a single photoelectrode tested under illumination and is extracted from the maximum power point of its current density-potential curve:[4,179]

$$\Phi_{saved,ideal} = \eta_F \times \frac{|J_m| \times [E_{light}(J_m) - E_{RHE}]}{P_{in}} = \frac{|J_m| \times E_{light}^{vs\ RHE}(J_m)}{P_{in}} \qquad \text{Equ. 9}$$

The potential is referenced to the thermodynamic potential of the half reaction (H^+/H_2) at the pH of the electrolyte, i.e. referenced to the RHE, and the current density is in mA cm^{-2}. $\Phi_{saved,ideal}$ is obtained at the maximum power P_m where the voltage is $E_{light}(J_m)$ and the current density is J_m (Fig. 86). P_{in} is the power of the incident illumination in mW cm^{-2}. The Faradaic efficiency η_F for hydrogen evolution is assumed to be 100 %, as reported in the literature.[119]

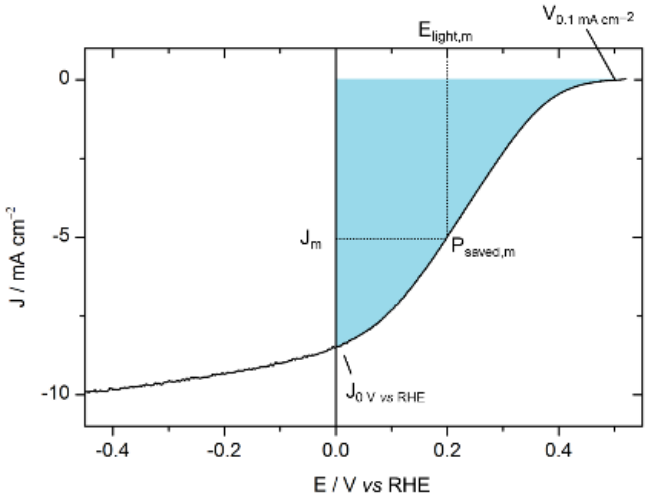

Fig. 86. Current density-potential characteristic of an ITO\PEDOT:PSS\P3HT:PCBM\LiF\Al\Ti\MoS_3 photocathode.

Table 4 presents $\Phi_{saved,ideal}$ for the different photocathodes. The current density at 0 V *vs* RHE and onset potential (arbitrary taken at 0.1 mA cm^{-2}) are also presented for comparison between the cells.

	$V_{0.1\ mA\ cm^{-2}}$ / V	$J_{0\ V\ vs\ RHE}$ / mA cm^{-2}	$\Phi_{saved,ideal}$
ITO\PEDOT:PSS\P3HT:PCBM**MoS_3**	–0.15	0.05	0.003 %
ITO\PEDOT:PSS\P3HT:PCBM**TiO_2:MoS_3**	0.23	0.18	0.02 %
ITO\PEDOT:PSS\P3HT:PCBM**LiF\Al\Ti\MoS_3**			
100 mW cm^{-2}	0.48	8.47	0.64 %
50 mW cm^{-2}	0.34	4.61	0.78 %
25 mW cm^{-2}	0.34	1.73	0.44 %
ITO\PEDOT:PSS\P3HT:PCBM**LiF\Al\Ti\Pt/C**	0.67	7.87	1.18 %
ITO\PEDOT:PSS\P3HT:PCBM**Ti\MoS_3**	0.32	6.81	0.24 %
ITO\PEDOT:PSS\P3HT:PCBM**TiO_x\MoS_3**	–0.03	0.078	0.004 %
ITO\PEDOT:PSS\P3HT:PCBM**C_{60}\MoS_3**	0.24	0.86	0.03 %

Table 4, $V_{0.1\ mA\ cm^{-2}}$, $J_{0\ V\ vs\ RHE}$ and $\Phi_{saved,ideal}$ of the different photocathodes measured under illumination (100 mW cm^{-2}). $V_{0.1\ mA\ cm^{-2}}$ is the voltage necessary to obtain a current density that was arbitrary chosen at 0.1 mA cm^{-2}, and $J_{0\ V\ vs\ RHE}$ is the current density obtained at the thermodynamic potential.[e]

First, for identical absorber and interlayer (ITO\PEDOT:PSS\P3HT:PCBM\LiF\Al\Ti) but with two different catalysts (MoS_3 and Pt/C), the $\Phi_{saved,ideal}$ are significantly different, equal to 0.64 % and 1.18 % respectively. This difference mainly comes from the onset potential that is higher with Pt/C (0.67 V) than with MoS_3 (0.48 V, about 200 mV smaller). This is due to the additional overpotential of MoS_3 to catalyze the HER, as shown in Fig. 69b. The short-circuit current density is similar with both MoS_3 and Pt/C because the saturation current is reached for both photocathodes at a positive potential, but the current density at the maximum power point is slightly higher in the case of the Pt/C catalyst

[e] For the photocathodes with a metallic interfacial layer, two different areas were taken into account for $\Phi_{saved,ideal}$ calculation: the current density J_{mp} was multiplied by the electrode area in contact with the electrolyte, while P_{in} was referred to the lightened area (0.5 cm²), as this area would collect the electrons and transport them to the electrochemical area. If no distinction is made between these two areas, it results in an overestimation of the $\Phi_{saved,ideal}$ value (1.00 %, 1.84 %, and 0.43 % for LiF\Al\Ti\$MoS_3$, LiF\Al\Ti\Pt/C and Ti\$MoS_3$, respectively).

because the saturation current is reached before than in the case of the MoS_3 catalyst. For the ITO\PEDOT:PSS\P3HT:PCBM\Ti\MoS_3 photocathode, $\Phi_{saved,ideal}$ is 0.24 %, i.e. 2.7 times less than with the same catalyst (MoS_3) but different interlayer (LiF\Al\Ti), because the photocatalytic onset potential is closer to 0 V *vs* RHE (0.32 V) and the saturation current is not reached at a positive potential (so that the current density at 0 V *vs* RHE is lower than the saturation current density). The photocathode with the C_{60} interlayer coupled with MoS_3 has the onset potential of 0.24 V, close to that with Ti, but the $J_{0\ V\ vs\ RHE}$ is much lower, resulting in a slowly increasing HER slope and a small value of $\Phi_{saved,ideal}$ (0.03 %). The photocathodes with the TiO_x EEL or without any EEL have low onset potentials, barely above 0 V *vs* RHE, resulting in low $\Phi_{saved,ideal}$ values (0.004 % and 0.003 %).

$\Phi_{saved,ideal}$ depends on the efficiency of both the photoproduction of charges in P3HT:PCBM and their utilization by the catalyst, which are not differentiated in this figure-of-merit. It may thus be interesting to consider another quantity, which is less catalyst-dependent: the power-saved metric relative to a non-photoactive dark electrode with an identical catalyst and measured in an identical three-electrode electrochemical cell. The photovoltage at a given current density is thus evaluated from the potential under illumination compared to that of the same catalyst directly deposited on ITO, as presented in Fig. 87.

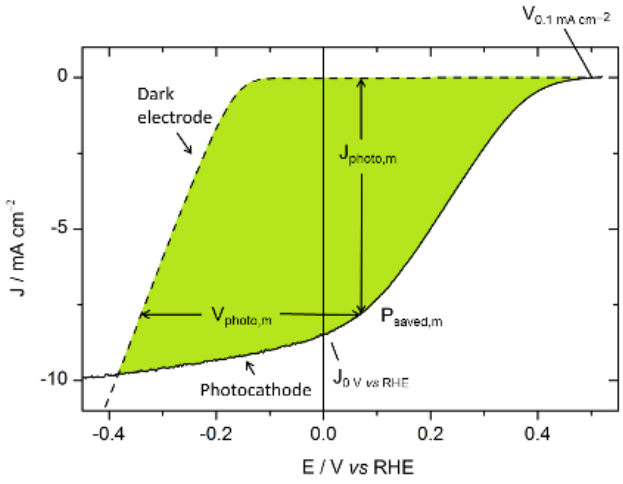

Fig. 87. Current density-voltage characteristic of an ITO\PEDOT:PSS\P3HT:PCBM\LiF\Al\Ti\$MoS_3$ photocathode (black line) and of an ITO\$MoS_3$ dark cathode (black dashed line).

$\Phi_{saved,NPAC}$ (NPAC = non-photoactive, identical catalyst) is calculated following Equ. 10:

$$\Phi_{saved,NPAC} = \eta_F \times \frac{|J_{photo,m}| \times [E_{light}(J_{photo,m}) - E_{dark}(J_{photo,m})]}{P_{in}}$$
$$= \eta_F \times \frac{|J_{photo,m}| \times V_{photo,m}}{P_{in}} \quad \text{Equ. 10.}$$

In Equ. 10, η_F is the Faradaic efficiency assumed to be 100 % again, P_{in} is the power of the incident illumination, and $J_{photo,m}$ and $V_{photo,m}$ are the photocurrent density and photovoltage at the maximum power point.

Fig. 88 shows the curves used in the case of the MoS_3 catalyst and the LiF\Al\Ti interfacial layer.

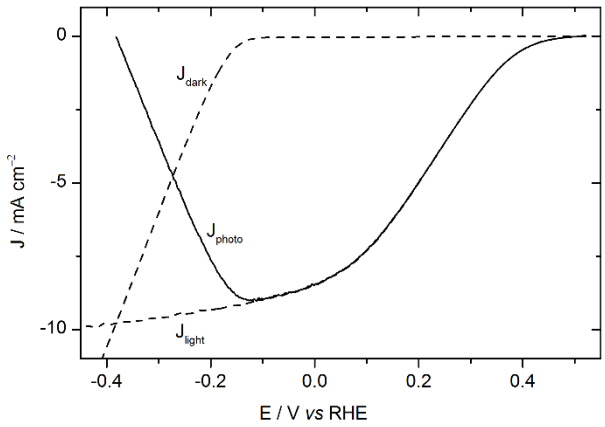

Fig. 88. Current density-voltage curve of an ITO\PEDOT:PSS\P3HT:PCBM\LiF\Al\Ti\$MoS_3$ photocathode (dashed line, J_{light}) and an ITO\$MoS_3$ cathode (dashed line, J_{dark}). The difference between J_{light} and J_{dark}, i.e. the photocurrent density J_{photo}, is plotted *vs* E_{light}.

The photocurrent density J_{photo} is the difference between the current density under illumination (J_{light}), i.e. measured for the ITO\PEDOT:PSS\P3HT:PCBM\LiF\Al\Ti\$MoS_3$ photocathode) and of the catalyst (J_{dark}, measured for ITO\$MoS_3$). As expected, J_{photo} increases at the same rate as J_{light} when the voltage is swept in the cathodic direction (Fig. 88). Once the onset of the HER of the catalyst is reached, J_{photo} decreases with the increase of J_{dark}.

From these data, the photovoltage V_{photo} is obtained by subtracting U_{dark} from U_{light} at matching current densities. J_{photo} as a function of V_{photo} is shown in Fig. 89 (left Y-axis).

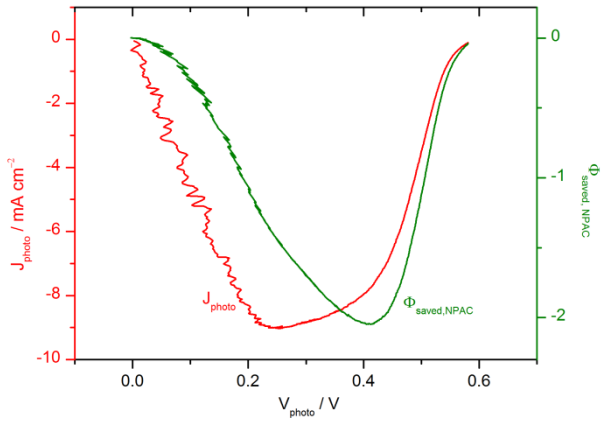

Fig. 89. J_{photo} *vs* V_{photo} (red line, left axis) and $\Phi_{saved,NPAC}$ *vs* V_{photo} (green line, right axis) plots of an ITO\PEDOT:PSS\P3HT:PCBM\LiF\Al\Ti\MoS_3 photocathode.

The photocurrent density of the ITO\PEDOT:PSS\P3HT:PCBM\LiF\Al\Ti\MoS_3 reaches its maximum value of 9.0 mA cm^{-2} for a photovoltage of 0.25 V (Fig. 89, left Y-axis). The photovoltage to reach 0.1 mA cm^{-2} is 0.58 V, as determined previously (Table 4).

The maximum value is taken at this new maximum power point which is referred to the activity of the catalyst in the dark, and not to the thermodynamic potential of the reaction, so that the photovoltage of the photocathode is highlighted compared to the effect of the catalyst and its overpotential requirement. For the comparison of a photoelectrode, $\Phi_{saved,ideal}$ and $\Phi_{saved,NPAC}$ are both important values because $\Phi_{saved,ideal}$ reflects the optimum power point for the use of the photoelectrode in practical applications (i.e. depending on the performance of both the photovoltaic material and the catalyst) while $\Phi_{saved,NPAC}$ reflects the photovoltage and photocurrent of a photocathode independently from the overpotential requirement of the catalyst. Thus, this second figure-of-merit can be applied even when the photocurrent of the photocathode appears at negative potentials (*vs* the thermodynamic potential of the reaction of interest, i.e. the RHE potential in our case).

Table 5 presents the parameters obtained by the first and second calculation method.

	$\Phi_{saved,ideal}$	$\Phi_{saved,NPAC}$
ITO\PEDOT:PSS\P3HT:PCBM**LiF****Al****Ti****MoS_3**		
100 mW cm^{-2}	0.64 % (J_m = 5.1 mA cm^{-2}, V_m = 0.20 V)	2.05 % ($J_{photo,m}$ = 7.8 mA cm^{-2}, $V_{photo,m}$ = 0.41 V)
50 mW cm^{-2}	0.78 % (J_m = 3.0 mA cm^{-2}, V_m = 0.21 V)	1.90 % ($J_{photo,m}$ = 4.1 mA cm^{-2}, $V_{photo,m}$ = 0.36 V)
25 mW cm^{-2}	0.44 % (J_m = 0.9 mA cm^{-2}, V_m = 0.19 V)	0.95 % ($J_{photo,m}$ = 1.3 mA cm^{-2}, $V_{photo,m}$ = 0.29 V)
ITO\PEDOT:PSS\P3HT:PCBM**LiF****Al****Ti****Pt/C**	1.42 % (J_m = 6.0 mA cm^{-2}, V_m = 0.31 V)	1.64 % ($J_{photo,m}$ = 6.7 mA cm^{-2}, $V_{photo,m}$ = 0.39 V)
ITO\PEDOT:PSS\P3HT:PCBM**Ti****MoS_3**	0.24 % (J_m = 3.9 mA cm^{-2}, V_m = 0.11 V)	1.30 % ($J_{photo,m}$ = 7.7 mA cm^{-2}, $V_{photo,m}$ = 0.30 V)
ITO\PEDOT:PSS\P3HT:PCBM**TiO_x****MoS_3**	0.002 % (J_m = 0.03 mA cm^{-2}, V_m = 0.15 V)	0.004 % ($J_{photo,m}$ = 0.08 mA cm^{-2}, $V_{photo,m}$ = 0.09 V)
ITO\PEDOT:PSS\P3HT:PCBM**C_{60}****MoS_3**	0.006 % (J_m = 0.4 mA cm^{-2}, V_m = 0.008 V)	0.14 % ($J_{photo,m}$ = 2.1 mA cm^{-2}, $V_{photo,m}$ = 0.30 V)

Table 5. For different photocathodes measured at 100 mW cm^{-2}: $\Phi_{saved,ideal}$ and $\Phi_{saved,NPAC}$ at maximum power point with their corresponding current density and potential (J_{mp} and V_{mp}, $J_{photo,mp}$ and $V_{photo,mp}$). Similarly to Table 4, two different areas were taken into account when metallic layers were used: the current density $J_{photo,mp}$ was multiplied by the electrode area in contact with the electrolyte, while P_{in} was referred to the lightened area (0.5 cm^2).

First, we can compare $\Phi_{saved,NPAC}$ and $\Phi_{saved,ideal}$ for the same system (with LiF\Al\Ti as interlayer and MoS_3 as catalyst): they are significantly different. $\Phi_{saved,NPAC}$ (2.05 %) is 3.2 times larger than $\Phi_{saved,ideal}$ (0.64 %). This higher $\Phi_{saved,NPAC}$ is due to both a higher photovoltage and a higher photocurrent at which the maximum power point is obtained: $V_{photo,m}$ is 0.41 V while V_m is only 0.20 V. This 0.21 V loss is a consequence of the overpotential requirement of the catalyst, and in the photocathode, a significant part of the photovoltage is thus used to overcome the overpotential requirement of MoS_3 to mediate HER. Moreover, the photocurrent density $J_{photo,m}$ (7.8 mA cm^{-2}) is 50 % larger than J_m (5.1 mA cm^{-2}) because the saturation photocurrent is barely reached at positive potentials (towards the RHE). On the contrary, with the Pt/C catalyst (ITO\PEDOT:PSS\P3HT:PCBM\LiF\Al\Ti\Pt/C photocathode), which mediates HER at much lower overpotential values than MoS_3, the difference between the two figures-of-merit is much less: $\Phi_{saved,NPAC}$ (1.64 %) is only 1.2 times $\Phi_{saved,ideal}$ (1.42 %), because the photovoltage does not need

to be used for overcoming the overpotential of the catalyst (V_m and $V_{photo,m}$ are 0.31 V and 0.39 V respectively).

In a next step, $\Phi_{saved,NPAC}$ and $\Phi_{saved,ideal}$ can be compared for two photocathodes with different catalysts (Pt/C and MoS_3) but with identical interfacial layers (LiF\Al\Ti). In this case, $\Phi_{saved,NPAC}$ with MoS_3 and with Pt (2.05 % and 1.64 %) are closer than the $\Phi_{saved,ideal}$ (0.64 % and 1.42 %) because the maximum photovoltages in both photocathodes are similar (0.41 V and 0.39 V), as well as the maximum photocurrent densities (7.8 and 6.7 mA cm^{-2}). Thus, $\Phi_{saved,NPAC}$ is independent from the catalyst performance, and is a suitable figure-of-merit for the comparison of different light-harvesting modules. It is illustrated by the ITO\PEDOT:PSS\P3HT:PCBM\Ti\MoS_3 photocathode, whose $\Phi_{saved,NPAC}$ is 1.3 %, i.e. 1.6 times less than with the LiF\Al\Ti interfacial layer (2.05 %) with identical catalysts (MoS_3). It shows that the lower efficiency obtained with Ti is due to the light-harvesting part and not to the catalyst overpotential requirement. This effect is even more pronounced with the TiO_x and the C_{60} interlayers.

To conclude, the use of the power-saved ratios allowed a quantified comparison of the different electron-extracting layers and catalysts used to construct the photocathodes.

3.5. Conclusions on Chapter 3

Photocathodes based on P3HT:PCBM solar cells and a noble metal-free catalyst, MoS_3, evolve hydrogen at RHE potential through the introduction of electron-extracting interfacial layers, which improved the charge transfer from the photocathode to the catalyst mediating proton reduction. Moreover, these interfacial layers buried the P3HT:PCBM p/n junction. Especially with metallic layers, the full driving force of the solar cell was exploited to drive the HER.

The organic cell provides a photovoltage of 0.6 V which is close to the open circuit potential measured in solid state devices when the metallic LiF\Al\Ti layer is used, while the photocurrent density at RHE potential reaches 8 mA cm^{-2}, corresponding to a value of NPAC power-saved ratio of 2.05 %. Increased stability is obtained by using only Ti as interfacial layer, though it results in a NPAC power-saved ratio of 1.30 %. The photovoltage and photocurrent density are lower in the case of C_{60}, probably because of resistive losses appearing at the interfaces. However, the use of amorphous carbon showed that every material is not necessarily suitable as EEL. In the next chapter, the hole-extraction layer is changed to other materials typically used in the OPV field to investigate the origin of the low performance obtained without EEL.

Chapter 4. Study of the hole-extraction layer to improve the performance and stability of the photocathodes

In Chapter 2, the first photocathode based on the photosensitization of MoS_3 by the P3HT:PCBM has been investigated. Directly deposited on the organic layer, MoS_3 (mixed with TiO_2) produced hydrogen at reversible hydrogen electrode (RHE) potential with a current density of 180 µA cm^{-2}. The ITO\PEDOT:PSS\P3HT:PCBM\$MoS_3$ photocathodes that we prepared were not as efficient as expected for the photoproduction of hydrogen in aqueous 0.5 M H_2SO_4 (50 µA cm^{-2}). The equivalent solid-state solar cell (without MoS_3, and with an evaporated LiF\Al cathode, i.e. ITO\PEDOT:PSS\P3HT:PCBM\LiF\Al) had a power conversion efficiency (PCE) of 2.8 % in our conditions, so that we did not think that PEDOT:PSS was at the origin of the limitation. On the contrary, we tried to use of interfacial layers (LiF\AL\Ti, Ti, or C_{60}) between the BHJ and the catalyst, i.e. electron-extracting layers (EEL). This was the subject of Chapter 3, in which we investigated EEL between the P3HT:PCBM and MoS_3, which increased the photocurrent density up to several mA cm^{-2}. A current density of 8 mA cm^{-2} at RHE potential was obtained with metallic interlayers between P3HT:PCBM and MoS_3. Using a C_{60} or a LiF\$C_{60}$ layer, hydrogen was evolved at RHE potential with almost 2 mA cm^{-2} but the resistive losses associated to the C_{60} layer and to the electronic transfer from C_{60} to MoS_3 decreased the efficiency due to low fill factor and current density. These photocathodes suffered from a low stability with a drop of the photocurrent density over time (Al dissolved in water and C_{60} was porous), and the processes to deposit the EELs were rather time-consuming (series of vacuum evaporations). Moreover, the experiments suggested that the photocathode in direct contact with the electrolyte could not transfer the electrons photogenerated in P3HT:PCBM to MoS_3 to reduce the protons. Consequently, the role of the interfacial layers was attributed to the lowering or suppression of this detrimental effect by spatially separating the P3HT:PCBM from the electrolyte. But since these interfacial layers were not stable over long time, the electrolyte always ended up reaching the P3HT:PCBM layer. Moreover, the LiF\Al\Ti layer was peeled off.

We decided to study the effect of the hole-extraction layers. In P3HT:PCBM-based solid-state organic solar cells, the theoretical maximum open-circuit voltage (V_{OC}) is generally defined as the energetic difference between the HOMO of the donor material and the LUMO of the acceptor material, minored with the excitons binding energy. In actual devices, the output is typically 300-500 mV lower than the maximum due to current leakage at interfaces. Interfacial layers between the bulk heterojunction and the electrodes limit the losses by preventing current leakage leading to counterdiode formation. The interfacial layer located between the ITO (anode) and the BHJ in the normal configuration is called hole-extraction layer (HEL), or electron-blocking layer, though it has not always both properties. The HEL avoids electron leakage from the direct contact between the acceptor (PCBM) and the anode, and planarizes the ITO surface. Moreover, the HEL aids photogenerated hole extraction because the typical transparent electrode ITO is generally not matching the HOMO energy of the donor polymers. Thus, the use of interfacial layers between the bulk heterojunction and the electrodes helps the realization of the maximum theoretical open-circuit voltage.[180] Used in the first two chapters, the

widely used PEDOT:PSS HEL, or more precisely in the case of PEDOT:PSS, HIL (hole injection layer), is a thin layer deposited from solution by spin-coating, which is efficient in solid-state solar cells.[70] Actually, PEDOT:PSS is strongly doped with free charge carriers and is assimilated to a metallic electrode. Semiconducting metal oxide HEL materials were developed to avoid the loss of performance of solid-state OPV cells in long-term use associated with the acidity of PEDOT:PSS which causes the ITO to degrade. Moreover, PEDOT:PSS is hygroscopic, so that its use for photocathodes might prematurely affect the photocathode stability. We therefore investigated the effect of the HEL on the performance and the stability of the devices by using other typical materials for HEL such as NiO_x, MoO_x, and graphene oxide.

4.1.Role of the hole-extraction layer

In this part, all devices were made with an electrochemical area of 0.06 cm² (it was 0.28 cm² in the previous parts). Similarly to solid state OPV cells, lowering the electrode area is increasing the edge effects. Control devices made with a 0.28 cm² electrochemical area showed that the current density was artificially doubled with the 0.06 cm² area.

4.1.1. No interfacial layer

A photocathode without HEL nor EEL was built with the ITO\P3HT:PCBM\MoS_3 architecture, in order to start from the simplest structure. This photocathode was then studied in 0.5 M H_2SO_4 under chopped illumination. The results are shown in Fig. 90. Surprisingly, the photocurrent density at RHE potential was much higher without PEDOT:PSS (3 mA cm^{-2} *vs* 70 µA cm^{-2} during the first cycle, and around 1.5 mA cm^{-2} in the following cycles). The onset potential was also positive from the RHE

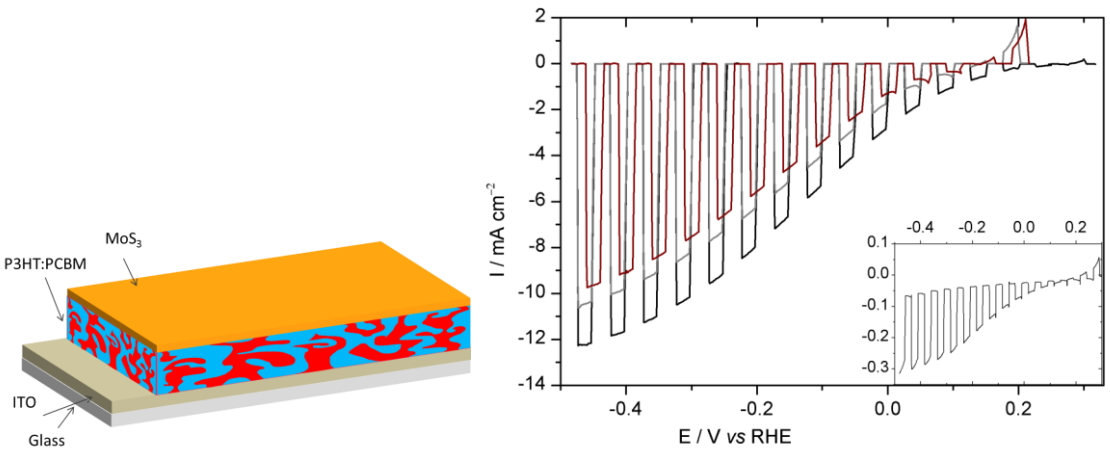

Fig. 90. Voltammogram recorded at 50 mV s^{-1} in 0.5 M H_2SO_4 with chopped visible light for an ITO\PEDOT:PSS\P3HT:PCBM\$MoS_3$ *(inset)* and ITO\P3HT:PCBM\$MoS_3$ photocathode (black: 1st cycle, gray: 3rd cycle, brown: 5th cycle). Electrode area: 0.06 cm^2.

potential (0.2 V) and stabilized at +0.13 V, while the one of the photocathode with PEDOT:PSS was shifting towards cathodic potentials and stabilizing at about 0 V *vs* RHE.

A chronoamperometry was performed at RHE potential with the same substrate that was used to perform the cyclic voltammetry (Fig. 91). The photocurrent density decreased at first and hydrogen bubbles were visibly sticking to the surface. By bubbling N_2 at the surface, the bubbles were removed and the photocurrent increased. The initial losses of photocurrent are therefore attributed to the decrease of the active area due to hydrogen bubbles. Over an hour, the photocurrent density remained stable around 400 µA cm^{-2}.

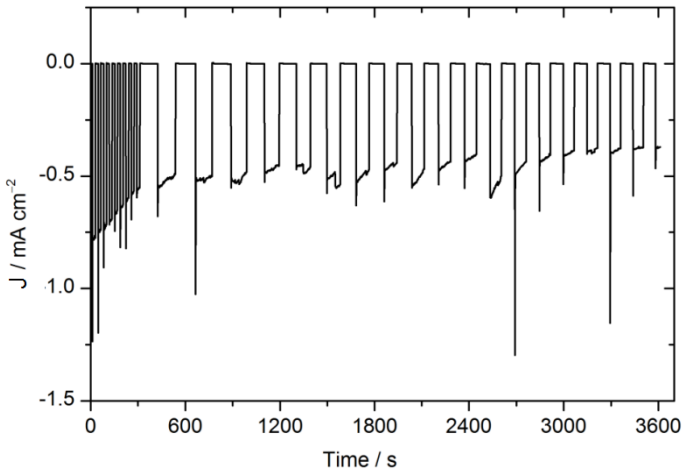

Fig. 91. Chronoamperometry at 0 V *vs* RHE in 0.5 M H_2SO_4 with chopped visible light for a ITO\P3HT:PCBM\MoS_3 photocathode, performed after 5 voltammetric experiments. Electrode area: 0.06 cm^2. Same device as in Fig. 90.

However, the results were not always reproducible, probably because of the ITO\P3HT:PCBM interface is not well controlled. Indeed, the work function of ITO is very sensitive to the different treatments, such as the UV-ozone treatment which is performed before the active layer deposition. One of the reasons why HEL are used is that it sets the work function of the anode.

The results of the voltammetry and chronoamperometry show that:

- contrary to our assumption that P3HT:PCBM needed protection from the electrolyte (with electron-extracting layers), the P3HT:PCBM is able to withstand contact with the aqueous acidic electrolyte, at least during one hour, without significant loss of performance.

- PEDOT:PSS was probably a cause of the low performance of the previous devices (ITO\PEDOT:PSS\P3HT:PCBM-based photocathodes), but not because of its stability towards the electrolyte, contrary to what has been suggested in Ref.[166] In this article, delamination of the photocathode was observed when it was in contact with the electrolyte,

and it was explained by the hydrophilicity of PEDOT:PSS. In our case, delamination caused by water was observed only if the entire ITO\PEDOT:PSS\P3HT:PCBM-based photocathode was plunged into the electrolyte, because water reached the PEDOT:PSS through the sides. Here, only a disc was in contact with the electrolyte thanks to a rubber seal and a specially designed electrochemical cell. Delamination was not observed on the area in contact with the electrolyte for the ITO\PEDOT:PSS\P3HT:PCBM\MoS_3 photocathode tested in Fig. 90 (inset), indicating that the low performance observed was not related to PEDOT:PSS stability. Moreover, the hydration of the PEDOT:PSS might have induced changes in the work function, but if it was the cause of the low performance, the first voltammogram would probably be more performant than what has been obtained, and in the following cycles the photovoltage and photocurrent would gradually decrease.

- the photocurrent density is much higher without the PEDOT:PSS HEL, even if it the reproducibility is not perfect, and even after 3 cycles, the onset potential is around 0.1 V *vs* RHE while the one of the ITO\PEDOT:PSS\P3HT:PCBM\MoS_3 is negative (–0.15 V at 0.1 mA cm^{-2}). This effect could be explained by a lower hole extraction barrier at the P3HT:PCBM/ITO interface when the device is used in a photoelectrochemical configuration.

This last point is further discussed in the following sections, in which more data is available for the interpretation. To study the ITO\P3HT:PCBM interface, we used a different HEL, replacing PEDOT:PSS with NiO_x to have a controlled interface.

4.1.2. Nickel oxide (NiO_x)

Pure and stoichiometric NiO is an insulator, while non-stoichiometric NiO_x is a p-type semiconducting oxide[181] used as HEL in organic solar cells because its work function lies close to the HOMO of P3HT. The p-type conductivity of NiO originates from two positively charged holes which accompany each Ni^{2+} vacancy in the lattice.[181] To avoid resistive losses due to the low crystallinity of the solution-processed NiO_x, the layer must be kept thin enough, i.e. around 5-10 nm (in this work, around 7-8 nm). After annealing at 320 °C, the substrates were subjected to 15 min UV-ozone treatment to increase the work function, resulting on a change of color from colorless to lightly gray, probably due to the formation of the oxidized $Ni^{III}OOH$. Indeed, NiO is electrochromic and its oxidized form, NiOOH, is responsible for the black color.[182] However, this color disappeared within minutes even after immediate transfer in the glovebox. In our conditions, the power conversion efficiency of the ITO\NiO_x\P3HT:PCBM\LiF\Al solar cell was 1.75 %, i.e. less than the ITO\PEDOT:PSS\P3HT:PCBM\LiF\Al solar cell (2.75 %).

ITO\$NiO_x$\P3HT:PCBM\$MoS_3$ photocathodes were tested in 0.5 M H_2SO_4. Fig. 92 shows the voltammograms of the photocathodes with and without NiO_x. The onset potential (measured on the

first cycle) of the ITO\$NiO_x$\P3HT:PCBM\$MoS_3$ photocathode increased from 0.2 V to 0.4 V compared to the ITO\P3HT:PCBM\$MoS_3$ photocathode. The photocurrent density reached 4.3 mA cm^{-2} at 0 V *vs* RHE. The photocurrent did not reach a clear saturation, though it did not increase linearly with cathodic potentials. Moreover, the onset potential was still 0.4 V after 3 cycles. These results were obtained for a NiO_x layer of approximately 7-8 nm. Thicker NiO_x layers (15 nm and 30 nm) resulted in similar onset potentials but poorer photocurrent densities (respectively 60 % and 40 %), because of the additional resistivity.

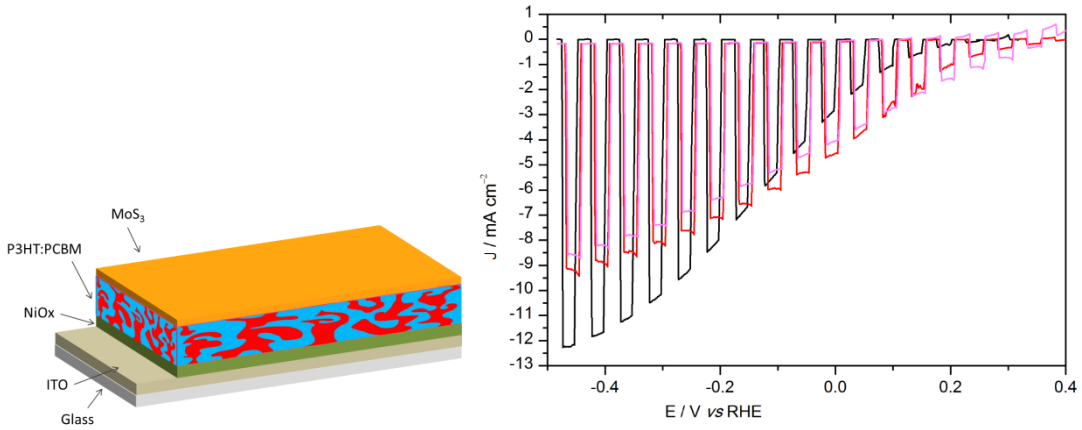

Fig. 92. Voltammogram recorded at 50 mV s^{-1} in 0.5 M H_2SO_4 with chopped visible light for an ITO\P3HT:PCBM\$MoS_3$ *(black)* and an ITO\$NiO_x$\P3HT:PCBM\$MoS_3$ *(red: 1st cycle; pink: 2nd cycle)* photocathodes. Electrode area: 0.06 cm^2.

The stability of the devices has been tested by electrolysis under chopped light at RHE potential.

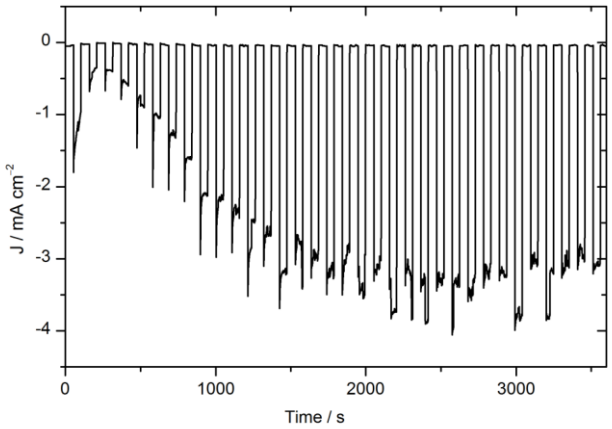

Fig. 93. Chronoamperometry at 0 V *vs* RHE in 0.5 M H_2SO_4 with chopped visible light for an ITO\$NiO_x$\P3HT:PCBM\$MoS_3$ photocathode, performed after 3 voltammetric experiments. Electrode area: 0.06 cm². Same device as in Fig. 92.

All chronoamperometry experiments carried out with NiO_x devices presented the same pattern (Fig. 93): first, a decrease of the current density to a few hundreds of µA cm^{-2} in a few minutes, and an increase of the photocurrent for approximately half an hour. Then the current density is stable (here around 3 mA cm^{-2}). After 1.5 hours, it starts to decrease slightly but the current density was still 90 % of its highest value after 3 hours.

NiO_x has a work function which has been reported to be 5.1-5.5 eV,[183,184] larger than that of PEDOT:PSS (4.9-5.2 eV).[185–188] In the next part, graphene oxide is used as an HEL, because its work function lies around 4.9-5.4 eV[189,190] (depending on the oxygen content), approximately between the work functions of PEDOT:PSS and NiO_x.

4.1.3. Graphene oxide

Owing to their solution processability, unique two-dimensional structure, and tunable electronic structures, graphene oxide (GO) and its derivatives have been used as a new class of efficient hole- and electron-extraction materials in polymer solar cells as reviewed by Liu and coll.[191] In particular, GO has been often used as HEL.[192–195] Unlike graphene, whose synthesis and processing require specific setups and treatments, GO can be produced very easily in large amounts and at a low cost. In this work, GO was prepared using the standard Hummers[196,197] method followed by spontaneous exfoliation in water. The suspension was then centrifuged to removed unexfoliated graphite particles. GO flakes formed a gel in the supernatant. This gel was lyophilized and the dry GO was used to prepare a suspension in DI water (8 mg mL^{-1}). The GO suspension was then deposited by spin-coating and subsequently annealed at 150 °C for 15 min in air to recover some of the conducting properties of graphene. The film color changed from brown to gray due to this partial reduction. Fig. 94 shows the voltammogram of the photocathodes with GO and NiO_x as HEL.

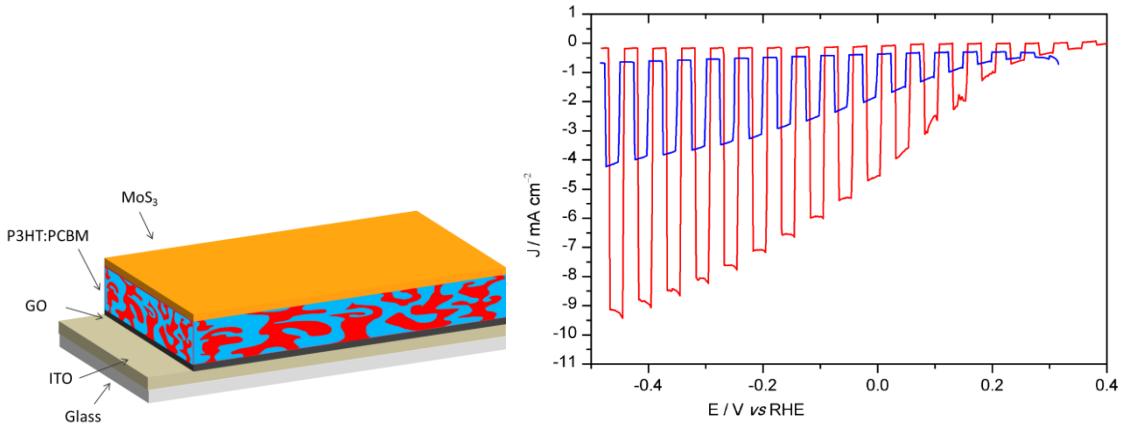

Fig. 94. Voltammogram recorded at 50 mV s^{-1} in 0.5 M H_2SO_4 with chopped visible light for an ITO\$NiO_x$\P3HT:PCBM\$MoS_3$ *(red)* and an ITO\GO\P3HT:PCBM\$MoS_3$ *(blue)* photocathodes. Electrode area: 0.06 cm^2.

The onset potential (measured on the first cycle) of the ITO\GO\P3HT:PCBM\MoS_3 photocathode was slightly lower (~0.25 V) than with NiO_x (0.4 V) but higher than without HEL (0.2 V). The photocurrent density at RHE potential was about 1.8 mA cm^{-2}, i.e. less than NiO_x or no HEL. The current density did not reach a plateau. However, at further cathodic potentials, the photocurrent increased at a slower pace than with NiO_x; this was attributed to the resistive effect of the GO layer. The graphene oxide thickness was varied by decreasing the concentration of the suspension. It turned out that with a smaller thickness, the performance was worse. This effect could arise from a more complete coverage of the ITO compared to the concentrated suspension, in which aggregates had formed.

The dark current density of about 500 µA cm^{-2} was present during the first voltammogram and decreased in the following voltammograms (Fig. 95 left), and did not change much with the potential. This dark current could be attributed to electron collection by the GO layer instead of only holes, resulting in the absence of saturation current and in a significant dark current corresponding to further reduction of GO.

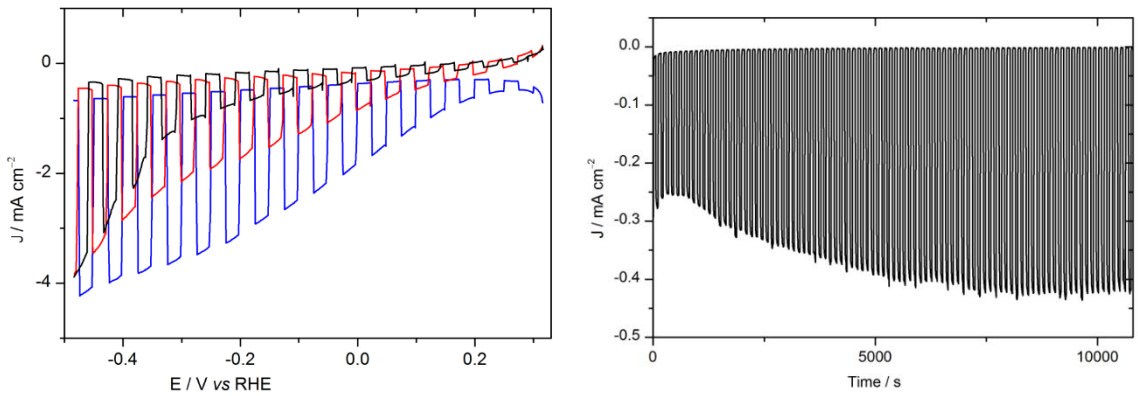

Fig. 95. *Left*: voltammogram recorded at 50 mV s^{-1} in 0.5 M H_2SO_4 with chopped visible light for an ITO\GO\P3HT:PCBM\$MoS_3$ photocathode (blue: 1st cycle, red: 2nd cycle, and green: 3rd cycle). *Right*: chronoamperometry at 0 V *vs* RHE in 0.5 M H_2SO_4 with chopped visible light for an ITO\GO\P3HT:PCBM\$MoS_3$ photocathode, performed after 4 voltammetric experiments. Electrode area: 0.06 cm^2.

The photocurrent density decreased with increasing number of voltammograms (Fig. 95 left) while the photocurrent density at RHE potential for 3 hours increased during the first hour (similarly to NiO_x but to a smaller extent) and was stable for 3 hours (Fig. 95 right). The photocurrent density was around 400 µA cm^{-2}, less than with NiO_x, in accordance with the voltammetric experiments (Fig. 94).

GO did not prove more efficient than NiO_x. We then decided to use another HEL material which has a greater work function than NiO_x or GO.

4.1.4. Molybdenum oxide (MoO_x)

In the field of organic photovoltaics, the search for alternative materials as HEL selected also n-type oxides such as MoO_3, WO_3 or V_2O_5. Contrary to NiO, which is a p-type oxide, these n-type materials have a conduction band close to the HOMO level of typical polymers for OPV. They were deposited by evaporation and have a definite work function around 6.9 eV[198]. Few examples of simple solution-processed layers exist, and the work function (6.0-6.8 eV[198–202]). Recently, a low-temperature process was developed to make MoO_x thin films with a sol-gel precursor without forming nanoparticles before deposition.[203] This allows the deposition of flat films with low roughness. For the fabrication of the photocathodes, the MoO_x precursor was spin-coated in the glovebox and annealed at 150 °C in air. P3HT:PCBM was then deposited as before, in the glovebox, and MoS_3 was sprayed in air onto the heated substrate (80 °C), completing the fabrication of ITO\$MoO_x$\P3HT:PCBM\$MoS_3$ devices at temperatures never going over 150 °C.

Fig. 96 presents the voltammogram obtained with such photocathodes.

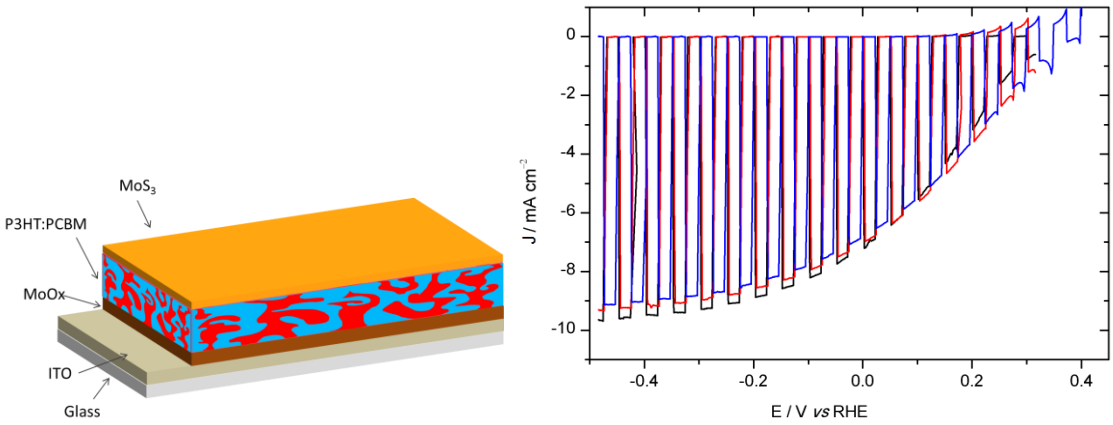

Fig. 96. Voltammograms in N_2-saturated 0.5 M H_2SO_4 of an ITO\$MoO_x$\P3HT:PCBM\$MoS_3$ photocathode (electrode area: 0.06 cm²) with chopped visible light illumination. Black: 1st cycle, red: 2nd cycle, blue: 3rd cycle

The onset potential for a photocurrent density of 0.1 mA cm^{-2} is above 0.4 V *vs* RHE, compared to –0.15 V for the MoS_3 catalytic dark electrode. This represents a > 0.53 V positive shift of the onset potential. Compared to GO, it did not shift towards cathodic potentials. The current density at 0 V *vs* RHE is 6.9 mA cm^{-2}.The voltammogram presents a saturation current from approximately –0.2 V *vs* RHE, which was not observed with NiO_x or GO. It seems that MoO_x is a good hole collecting material which is less resistive than NiO_x and GO.

Photocathodes with MoO_x HEL were expected to be quite stable, since no evolution of the voltammogram was observed after 3 cycles (Fig. 96). The photocurrent density at RHE potential is shown in Fig. 97 and started at more than 6 mA cm^{-2} and decreased regularly. After 1 h the current density was 60 % lower but was still 2 mA cm^{-2}. This loss probably comes from the high current density, causing a faster degradation of the MoS_3 catalyst.

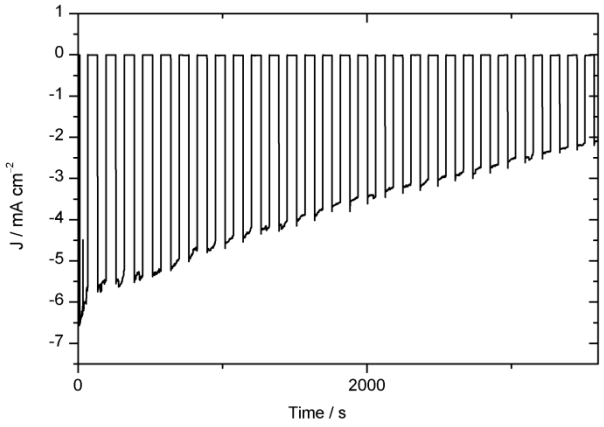

Fig. 97. Chronoamperometry at 0 V *vs* RHE in N_2-saturated 0.5 M H_2SO_4 with chopped visible light for an ITO\$MoO_x$\P3HT:PCBM\$MoS_3$ photocathode, performed after 3 voltammetric experiments. Electrode area: 0.06 cm². Same device as in Fig. 96.

HEL greatly improved the performance of the photocathodes, especially MoO_x which proved to be a very promising HEL in terms of photocurrent and photovoltage of the resulting photocathode.

4.1.5. Discussion

4.1.5.1. Energy band diagram

Previous results obtained with ITO\PEDOT:PSS\P3HT:PCBM\EEL\$MoS_3$ photocathodes (Chapter 3) were made with electron-extracting layer (EEL), which buried the P3HT:PCBM BHJ. The great enhancement of the performance was attributed to the fact that the EEL prevented the direct interaction of P3HT:PCBM and PEDOT:PSS, and also to the enhanced the electronic transfer between P3HT:PCBM and MoS_3. The photocurrents obtained without any HEL showed however that the limitation of the photocurrent in the ITO\PEDOT:PSS\P3HT:PCBM\$MoS_3$ photocathodes did not arise from a poor electronic transfer from the P3HT:PCBM layer to the MoS_3 catalyst. On the contrary, by changing the HEL, photocurrent densities up to 8-10 mA cm^{-2} were obtained without any EEL.

To formulate a hypothesis on the origin of the increasing photocurrents obtained with the different HEL, it is necessary to establish energy band diagrams of the photocathodes in contact with the electrolyte as well as the solid-state solar cells. Before constructing the diagram of the organic photocathodes, it can be useful to summarize the construction of these diagrams in the case of inorganic semiconductors.

In an inorganic p-n junction, for example, in a crystalline silicon p-n bilayer junction (Si doped with boron and phosphorus, respectively), the energy band diagram in the dark can be drawn as presented in Fig. 98:

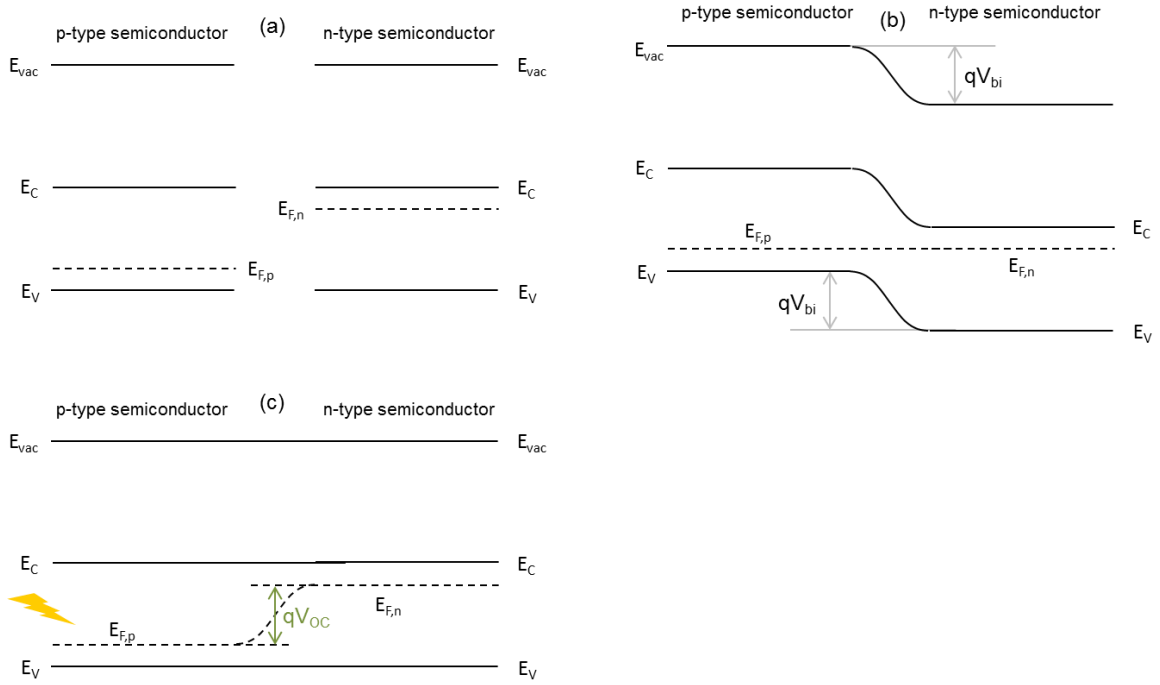

Fig. 98. Si p-n junction (a) before contact, (b) after contact and at equilibrium, (c) under illumination. E_{vac}, E_C, E_V, $E_{F,n}$ and $E_{F,p}$ stand for the vacuum level (the energy to which an electron must be raised to be free from all forces from the solid), the conduction band edge, the valence band edge, and the electron and hole quasi-Fermi levels, respectively. $E_{F,n}$ and $E_{F,p}$ are very close to the conduction and valence band edge, respectively, so that the V_{OC} (open-circuit voltage) is approximately equal to the bandgap.

Before contact, both p-type Si and n-type Si have the same valence band energy (E_V) and conduction band energy (E_C), and their Fermi levels are different due to different dopant types. When they are brought in contact, as there is a carrier gradient concentration, the electrons of n-type Si will diffuse to p-type Si and the holes of p-type Si will diffuse to n-type Si until the Fermi levels equilibrate. Redistribution of electrons and holes produces a built-in potential V_{bi}, under which the carriers drift and form a drift current, whose direction is opposite to the diffusion current. When equilibrium is reached, the two currents are equivalent and there is no net current flow inside the junction, and the Fermi levels are the same. The layer in which the bands are bent is a depletion region (in which there is a lack of minority charge carriers). When Si is irradiated with light, photogenerated excitons are immediately dissociated into free electrons and holes because their binding energy is low. They drift into opposite directions under the force of the built-in potential (electrons towards the n-Si and holes towards the p-Si). Thus, the potential in the p-Si increases and the potential in the n-Si decreases, generating the photo-voltage, which tends to cancel the built-in potential (they are equal under open-circuit conditions). The built-in potential is necessary for the photovoltaic conversion.

In Fig. 98, the behavior of the p-n junction in the dark and under illumination was described. In the case of organic materials, it is different. Firstly, the diagram of bulk heterojunctions is usually

simplified as if it was a bilayer. Secondly, instead of n-type and p-type, organic semiconductors are classified as donor or acceptor materials, depending on the relative position of their HOMO and LUMO levels. OSCs are not or almost not doped and can be considered as intrinsic semiconductors. By analogy with silicon semiconductors, the band bending which would occur when the two semiconductors are brought in contact would be completed in a layer with an infinite thickness. Consequently, the bands of organic semiconductors are represented by flat levels in the dark. In the diagram, it is customary to represent the HOMO and LUMO levels at their level in the dark, even under illumination, as it fits well with the experimental results. More advanced models have studied positive and negative charge transfer (or polaron) states under illumination, which are corresponding to molecular orbitals occupied by a single charge, and are located in the HOMO-LUMO gap.[204]

To construct the band diagram in the dark, each material as a layer (including P3HT and PCBM) is drawn with its energy levels. The diagram consists in the P3HT:PCBM junction, which is between an anode (ITO with a HEL) and a cathode or the electrolyte. In the case of an organic solid-state solar cell (ITO\PEDOT:PSS\P3HT:PCBM\LiF\Al), the cathode is LiF\Al. In the case of the photocathode, there

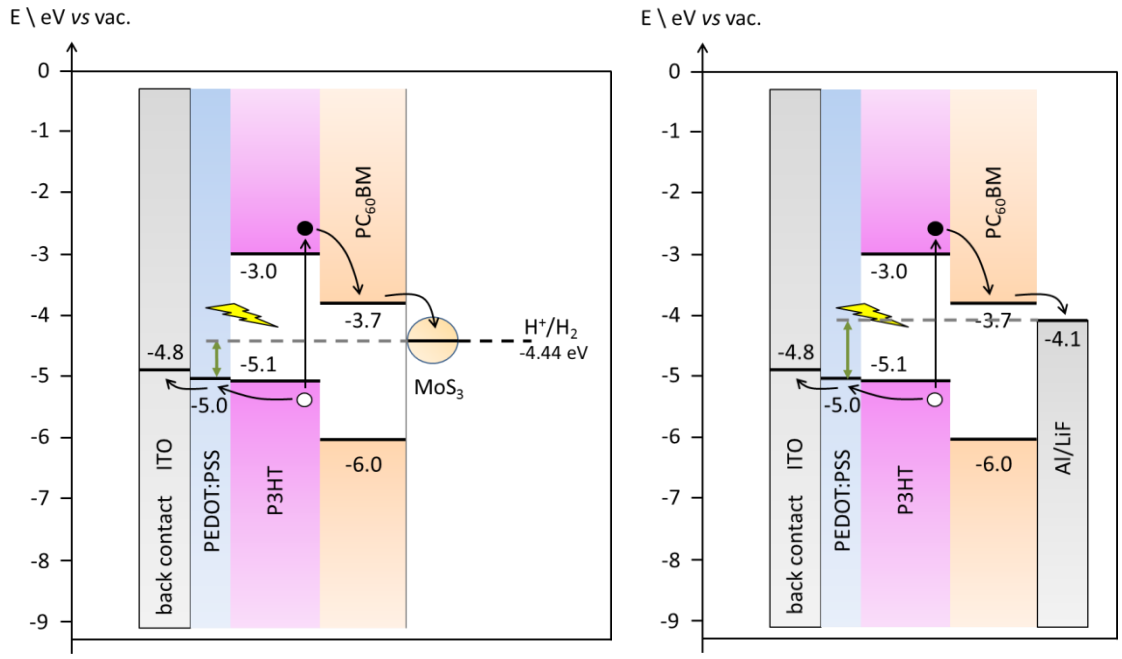

Fig. 99. Energy band diagram of an ITO\PEDOT:PSS\P3HT:PCBM\$MoS_3$\\$H^+/H_2$ photocathode (left) as used in Chapter 2, and of the corresponding ITO\PEDOT:PSS\P3HT:PCBM\LiF\Al solar cell (right).

is no metallic cathode but the electrolyte. Similarly to a metal, it is a reservoir of charge carriers with a definite Fermi level. Moreover, because the MoS_3 layer consists in a porous layer of nanoparticle aggregates, we assumed that the MoS_3 nanoparticles tune themselves to the Fermi level of the electrolyte and that the electrolyte will be directly in contact with the P3HT:PCBM. Thus, the

electrolyte is not a cathode but its role is similar. Fig. 99 presents the energy band diagrams of an ITO\PEDOT:PSS\P3HT:PCBM\MoS_3 photocathode in contact with an acidic electrolyte and of an ITO\PEDOT:PSS\P3HT:PCBM\LiF\Al solid-state solar cell.

For an inorganic solar cell, the built-in potential provided by the p-n junction is enough for the photovoltaic effect to occur, even if the electrodes have the same work function (Fermi level). Analogously, in organic photovoltaic bilayer heterojunctions, the donor and acceptor phases are separated and form selective contacts to the anode and the cathode. However, in bulk heterojunctions, the two phases are intimately mixed: there is no preferred direction for the internal field, the electrons and holes created within the volume have no net resulting direction in which to move. Therefore, a symmetry breaking condition is essential in bulk heterojunctions, and this can be achieved by using two electrodes of different work function. No photovoltaic effect will be observed if the electrodes have the same work functions (cf. Chapter 1, section 1.2.4.2). Interfacial layers on each electrodes are reported to determine the polarity of the device by creating an electrical field between the two electrodes.[157] In fact, when the electrode work functions are located between the HOMO and LUMO of the organic semiconductors, the V_{OC} of the device will depend on the work function difference of the two electrodes.

The work functions between the anode (ITO side) and the cathode, or the electrolyte, are compared in order to understand why the replacement of PEDOT:PSS by other HEL increased the performance of the photocathodes.

The values of work function used here are taken from the literature. The work function of Al is 4.1 eV[205] but its modification by LiF decreases the value to <4.1 eV.[206] The Fermi level of the redox electrolyte is –4.5 eV. First, we consider PEDOT:PSS as HEL (Fig. 99). The difference between the anode and cathode work function is 4.9 – 4.1 = 0.8 eV (and probably more, since the work function of LiF\Al is smaller than 4.1 eV) for the solar cell (sufficient for allowing the photovoltaic effect) and the work function difference between the anode and the electrolyte is only 4.9 – 4.5 = 0.4 eV for the photocathode. On the contrary, the work function of NiO_x is higher (5.1-5.5 eV)[183,184] so that in the case of the photocathode, the work function difference is ~0.8 eV, larger than with PEDOT:PSS. Assuming a work function of 5.2 eV for GO (4.9-5.4 eV[189190]) and 6.2 eV for MoO_x (6.0-6.8 eV[198–202]), the work function difference between the anode and the electrolyte is then around 0.7 eV with GO and 1.7 eV for MoO_x in photocathode configuration (Fig. 100).

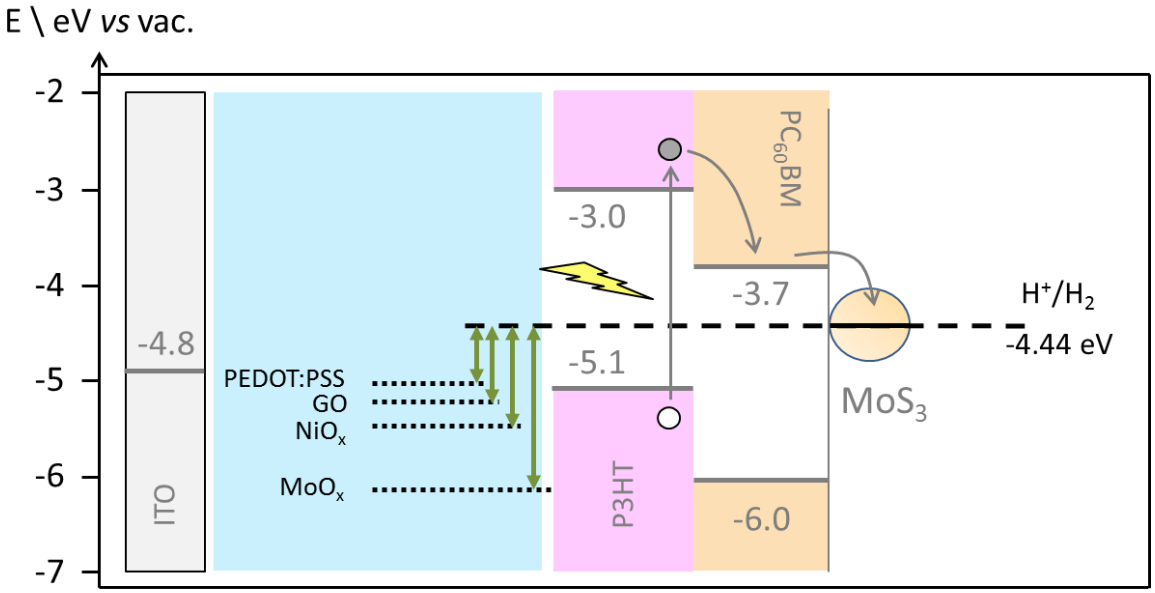

Fig. 100. Energy band diagram of an ITO\HEL\P3HT:PCBM\$MoS_3$\\$H^+/H_2$ photocathode with different HELs (PEDOT:PSS, GO, NiO_x, MoO_x).

The work function difference between the anode and the electrolyte, providing an electric field in the cell, increases with the increase of the work function of the anode side. This could explain the better results obtained for the photocathodes with a HEL having a larger work function.

The ratiometric power-saved figures-of-merit used in Chapter 3 are interesting tools for the comparison of the photocathodes. Table 6 presents the parameters obtained for $\Phi_{saved,ideal}$ and $\Phi_{saved,NPAC}$ (data are taken from the first voltammogram carried out on each sample).

	$V_{0.1\ mA\ cm^{-2}}$	$J_{0\ V\ vs\ RHE}$	$\Phi_{saved,ideal}$	$\Phi_{saved,NPAC}$
ITO**PEDOT:PSS**\P3HT:PCBM\ **MoS_3**	–0.15	50 µA cm^{-2}	0.004 % J_m = 29 µA cm^{-2}, V_m = 0.15 V	0.007 % $J_{photo,m}$ = 80 µA cm^{-2}, $V_{photo,m}$ = 0.09 V
ITO**GO**\P3HT:PCBM**MoS_3**	0.22 V	1.8 mA cm^{-2}	0.13 % J_m = 0.8 mA cm^{-2}, V_m = 0.17 V	0.26 % $J_{photo,m}$ = 1.5 mA cm^{-2}, $V_{photo,m}$ = 0.17 V
ITO**NiO_x**\P3HT:PCBM**MoS_3**	0.37 V	4.5 mA cm^{-2}	0.28 % J_m = 2.2 mA cm^{-2}, V_m = 0.13 V	1.23 % $J_{photo,m}$ = 5.1 mA cm^{-2}, $V_{photo,m}$ = 0.24 V
ITO**MoO_x**\P3HT:PCBM**MoS_3**	0.40 V	6.7 mA cm^{-2}	0.73 % J_m = 3.6 mA cm^{-2}, V_m = 0.20 V	2.10 % $J_{photo,m}$ = 6.2 mA cm^{-2}, $V_{photo,m}$ = 0.34 V

Table 6. For different photocathodes measured at 100 mW cm^{-2} (first voltammogram): $V_{0.1\ mA\ cm^2}$, $J_{0\ V\ vs\ RHE}$, $\Phi_{saved,ideal}$ and $\Phi_{saved,NPAC}$ at maximum power point with their corresponding current density and potential (J_{mp} and V_{mp}, $J_{photo,mp}$ and $V_{photo,mp}$).

The data presented in Table 6 shows that the onset potential goes from –0.15 V (with the PEDOT:PSS HEL) to 0.40 V (with the MoO_x HEL). Similarly, the current density at the RHE potential is increasing from 50 µA cm^{-2} to 6.7 mA cm^{-2}. In response, both $\Phi_{saved,ideal}$ and $\Phi_{saved,NPAC}$ increase. The catalyst is in all cases MoS_3: the overpotential is thus always the same and it means that 0.15-0.2 V of the photovoltage is necessary lost for overcoming it. It explains part of the difference between $\Phi_{saved,NPAC}$ and $\Phi_{saved,ideal}$: due to the overpotential, all J-E curves are cathodically shifted by 0.15 V compared to an ideal catalyst, so that part of the J-E curve is negative to the RHE, resulting in lower values of $\Phi_{saved,ideal}$ than of $\Phi_{saved,NPAC}$.

Fig. 101 *left* presents the $\Phi_{saved,NPAC}$ plotted against the work functions of the materials used as HEL and Fig. 101 *right* the photovoltage and photocurrent density against the work functions.

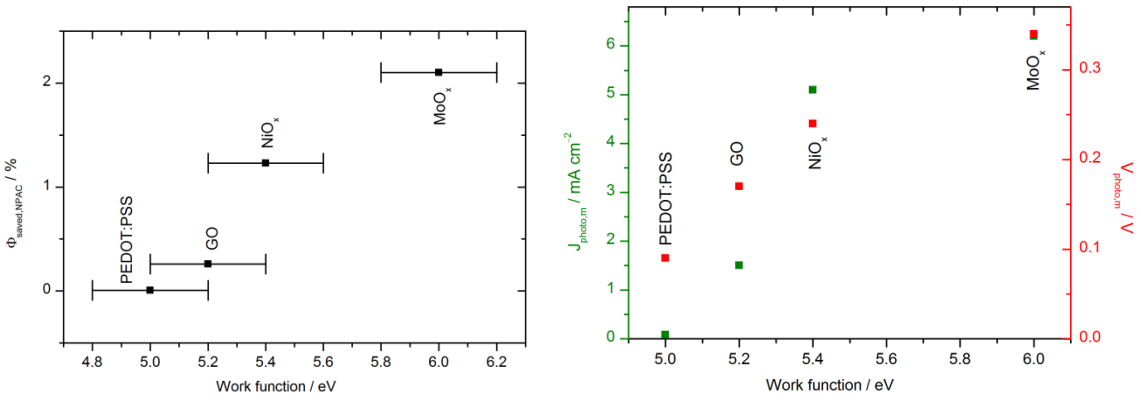

Fig. 101. *Left:* $\Phi_{saved,NPAC}$ *vs* work function and *right:* $V_{photo,m}$ (V) and $J_{photo,m}$ (mA cm^{-2}) obtained with the photocathodes with different HEL materials.

The increase of $\Phi_{saved,NPAC}$ is caused by a combined increase of the photovoltage and of the photocurrent density (Fig. 101 *right*), but the latter seems to have a greater part in the evolution of $\Phi_{saved,NPAC}$. Though the values are from the literature and are given at an error margin of ± 0.2 eV, it seems that the efficiency of the light-harvesting module is related to the work function of the HEL, in accordance with the conclusions of the previous section regarding the effect of EELs.

4.1.5.2. Classification

The classification of these photocathodes is not straightforward. The photocathodes with the metallic EEL were easily classified in PV-biased electrosynthetic cells because there was only one photojunction (as defined by Lewis and coll.,[16] an interface between two unlike materials where there are chemical and/or electrical potential gradients as well as kinetic asymmetries, which allows separation and transport of photogenerated charges). The photojunction was solid-state, and the metallic layer ensured that there was no semiconductor-electrolyte junction.

In some cases, a solid-state semiconductor junction can form an additional photojunction with the electrolyte. In this case, there is a constraint on the conduction band edge position of the acceptor material compared to the redox level of the electrolyte.[207] This constraint can be lifted by burying the junction so that no direct liquid-semiconductor junction is formed.

In the case of the photocathodes without EEL, the P3HT:PCBM solid-state photovoltaic junction is still present. However, the question which arises is whether the P3HT:PCBM-electrolyte junction is an addition photojunction or not. In the first case, the PCBM LUMO level (–3.7 eV) would need to be above the electrolyte Fermi level (–4.5 eV), a condition which is verified.

This has an impact on the classification of the photocathodes of Chapter 4. If the OSC-electrolyte interface is considered as a photojunction, then the photocathode can be classified as a PV-biased

photoelectrosynthetic cell. But if the electrolyte only plays a role as electrode, as part of the hypothesis that has been discussed in the previous section, then the photocathode is classified as PV-biased electrosynthetic cell. However, the photocurrent densities and photovoltages of the photocathodes without metallic layers match well with the values of the single solid-state P3HT:PCBM photo-junction. Thus, the OSC-electrolyte interface is probably not a photojunction, though this needs to be verified.

In one case (Chapter 3) the solid-state junction is buried and in the second case (Chapter 4) it is not. Consequently, though it might appear contradictory at first, they are classified in the same group of PV-biased electrosynthetic cells.

4.2. Combining efficient HEL and EEL

Before this work on HEL, electron-extracting layers (EEL) were developed to improve ITO\PEDOT:PSS\P3HT:PCBM-based photocathodes. In particular, C_{60} was studied as a non-metallic EEL. Combining the effect of the EEL with the HEL used in Chapter 4, C_{60} was deposited on ITO\MoO_x\P3HT:PCBM-based photocathodes. LiF was used between P3HT:PCBM and C_{60} because at that time, we believed that the photocathodes performed better with LiF than without. In Chapter 3, we showed that it is actually roughly the same.

The combination of the MoO_x HEL with LiF\C_{60} and C_{60} is presented in Fig. 102.

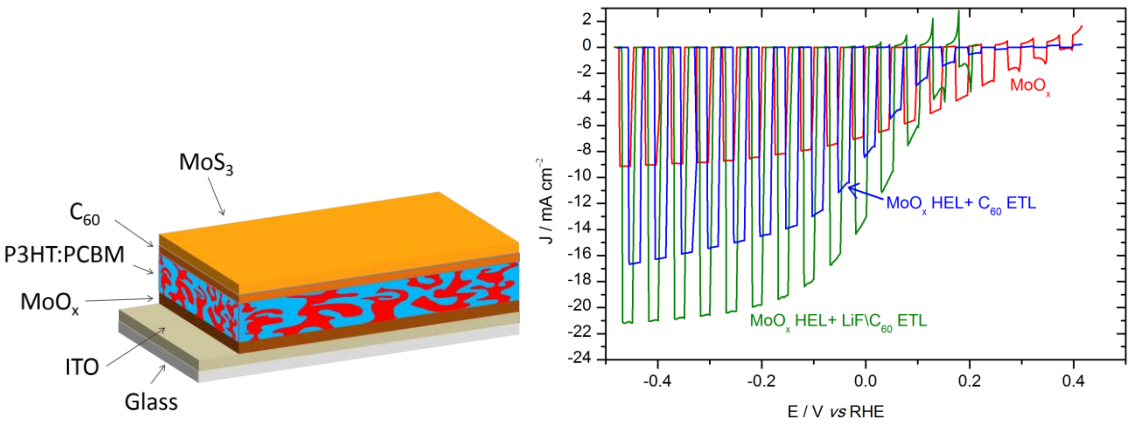

Fig. 102. Voltammograms in N_2-saturated 0.5 M H_2SO_4 with chopped visible light for an ITO\$MoO_x$\P3HT:PCBM\$MoS_3$ (red), an ITO\$MoO_x$\P3HT:PCBM\$C_{60}$\$MoS_3$ (blue), and an ITO\$MoO_x$\P3HT:PCBM\LiF\$C_{60}$\$MoS_3$ (green) photocathodes. Electrode area: 0.06 cm²

With C_{60} layers, the overall shape of the J-E curve is closer to an ideal diode. However, the onset potential ($V_{0.1\,mA\,cm^2}$) is shifted by 150 mV in the cathodic direction (0.25 V with C_{60}, 0.40 V without): it can be explained by the fact that C_{60} has a higher work function, which brings it closer to the work function of the anode, thus decreasing the work function difference between the two sides.

But at 0 V *vs* RHE, the photocurrent density is higher (9 and 14 mA cm^{-2} for C_{60} and LiF\C_{60} respectively, *vs* 7 mA cm^{-2} without EEL).

In the end, the operating point in a full PEC configuration will determine which of the photocathodes is the most suitable: if the PEC cell is operated at a low current density (< 5 mA cm^{-2}), the photovoltage is more important with the ITO\$MoO_x$\P3HT:PCBM\$MoS_3$ photocathode. At a higher current density, the ITO\$MoO_x$\P3HT:PCBM\LiF\$C_{60}$\$MoS_3$ photocathode will be more interesting.

The stability of the devices was evaluated at 0 V *vs* RHE. The photocurrent density obtained with the C_{60} layer was higher than without C_{60} but both photocathodes suffered from a decrease of the photocurrent density after 2 h (by 90 % without C_{60} and by 60 % with C_{60}). As mentioned earlier, the decrease of the photocurrent density could be associated with the high current density, which causes the catalyst to degrade.

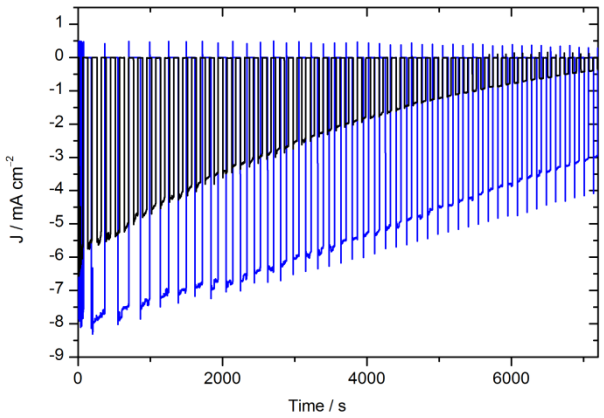

Fig. 103. Chronoamperometry at 0 V *vs* RHE in N_2-saturated 0.5 M H_2SO_4 with chopped light illumination for an ITO\$MoO_x$\P3HT:PCBM\$C_{60}$\$MoS_3$ photocathode (blue) and an ITO\$MoO_x$\P3HT:PCBM\$MoS_3$ photocathode (black). Electrode area: 0.06 cm^2

4.3. Conclusions on Chapter 4

Replacing the PEDOT:PSS layer by other HELs in the photocathode led to promising results. Without any EEL, these photocathodes reached photocurrent densities of several mA cm^{-2} and photovoltages up to 0.6 V. Contrary to the photocathodes with the metallic EEL, the P3HT:PCBM junction was not buried and the electron collection by MoS_3 to mediate HER was effective. Interestingly, the performance seems to be related to the work function of the HEL: increased photocurrent and photovoltage are obtained with a HEL of higher work function. The comparison of the different parameters and figures-of-merit does not disprove the hypothesis of the effect of the HEL work function on the performance of the devices. But it would be worth investigating this behavior, which could lead to increased performances. However, a more stable catalyst is necessary to investigate the effective stability of P3HT:PCBM in contact with the acidic electrolyte.

Conclusions and outlook

The combination of MoS_3 nanoparticles as a H_2-evolving catalyst with the core of an organic photovoltaic cell yields a novel type of photoelectrode achieving the reductive half reaction involved in water splitting. This system is based on earth-abundant elements and can be easily processed using spin-coating and spray-casting methods. The optimization of the thickness of the catalytic MoS_3 layer and its combination with TiO_2 led to an increased electron transport at the interface between the light-harvesting and charge generating core and the catalytic layer (Chapter 2).

Thanks to the introduction of interfacial layers (Al, Ti, TiO_x, C_{60}) between P3HT:PCBM and MoS_3 (Chapter 3), the charge transfer from the photocathode to the catalyst mediating proton reduction was improved and resulted in high current densities (x20 compared to the devices without HEL, i.e. several mA cm^{-2}) and a 0.6 V photovoltage. Moreover, these interfacial layers buried the P3HT:PCBM p/n junction, removing the influence of the redox Fermi level on the device. The performance of the photocathodes was discussed with the help of two metrics evaluating the amount of saved power compared to a dark electrode.

To further improved the performance and stability of the devices, the PEDOT:PSS HEL was replaced with other HELs (graphene oxide, NiO_x, MoO_x) having increasing work functions values (Chapter 4). Photocurrent densities and photovoltages compared well with solid-state solar cells. A hypothesis consistent with the results obtained within this thesis was suggested to describe the device operation. In particular, the work function difference between the HEL and the electrolyte seems to be important, in order to provide a sufficient asymmetry in the device to allow charge separation. The results described in Chapter 4 are preliminary and are at the basis of further experiments to develop and confirm the hypothesis.

To conclude, organic-based photocathodes were developed until a device made of three layers (MoO_x as HEL, P3HT:PCBM as photovoltaic layer, and MoS_3 as HER catalyst) deposited by spin-coating with annealing at T < 150 °C was able to efficiently produce hydrogen in aqueous acidic medium (pH=0). Density of current of 6.9 mA cm^{-2} were obtained at 0 V *vs* RHE. These photocathodes were able to sustain three hours of electrolysis under illumination with a loss of 60 % of the photocurrent. This work highlights the potential of these hybrid photocathodes.

Building a photocathode is one step toward the building of the tandem PEC cell for overall water splitting. A diagram presented in Fig. 104 shows how tandem cells combining a photoanode and photocathode can afford overall water splitting. When the two current-potential curves cross, the addition of the photovoltage of each photoelectrode exceeds the voltage requirement and the system is able to split water at the current density of the crossing.

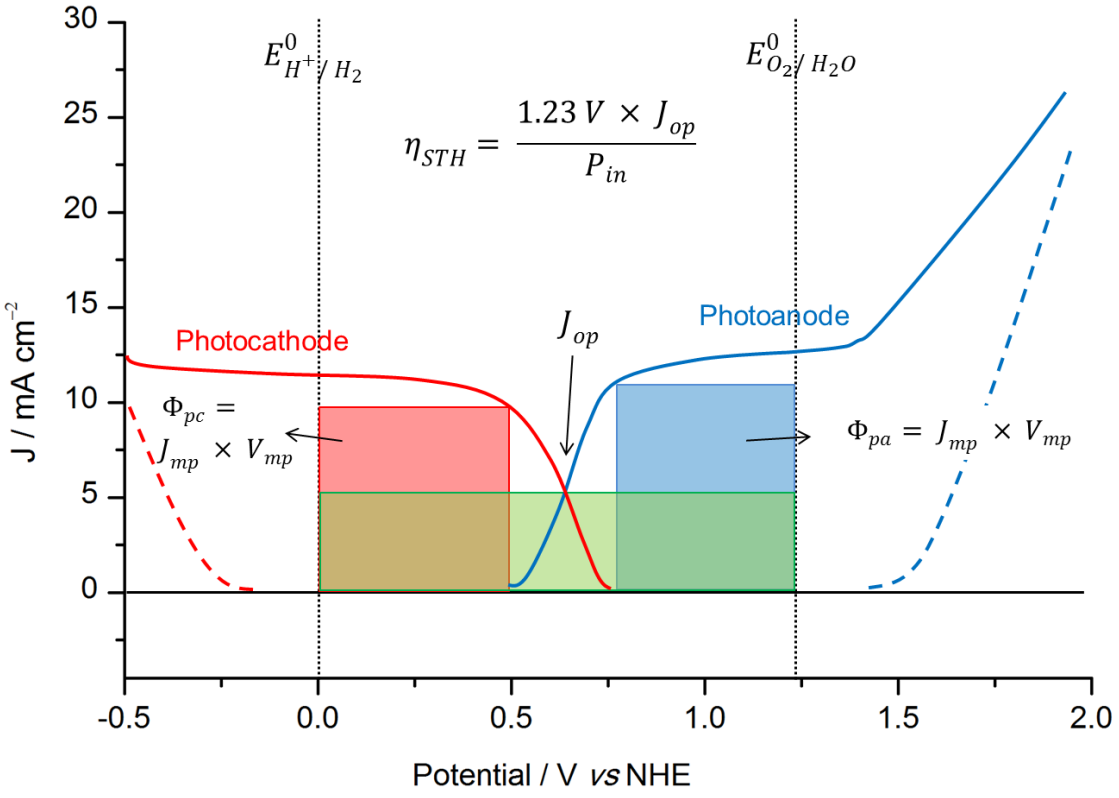

Fig. 104. Overlaid current density-potential curves for a photocathode (red) and a photoanode (blue) with the projected overall efficiency for water splitting. Adapted with permission from Ref.[4] Copyright 2010 American Chemical Society.

The requirements for the photoelectrodes, in addition to being based on earth-abundant materials, are the following:

- They should be active and stable in the same electrolyte
- If possible, they should each absorb a complementary part of the solar spectrum to optimize sunlight absorption
- The addition of the photovoltages of the photoanode and the photocathode should be higher than the 1.5-2 V (thermodynamic potential of water splitting: 1.23 V, and additional overpotentials) needed to achieve water splitting

With the objective of integrating the hybrid photocathodes developed here in a full water splitting PEC cells, a rational improvement of their performance must be done through the combination of interfacial layers, new catalysts and others organic semiconductor materials. Indeed, in this thesis, only P3HT:PCBM was used, limiting the photovoltage to 0.6 V. It means that the photoanode photovoltage would have to be larger than 1 V. Thus other organic and polymeric photovoltaic materials with better performance, e.g. PCDTBT (poly[N- 9'-heptadecanyl-2,7-carbazole-alt-5,5-(4,7-di-2-thienyl-2',1',3'-

benzothiadiazole])[153] and $PC_{71}BM$, can be used to increase the photovoltage and the photocurrent values at potentials positive from the RHE, so as to lower the photovoltage that the photoanode has to provide. At the same time, earth-abundant catalysts such as cobalt phosphide[91,208] or nickel phosphide[91,209] with a smaller overpotential than MoS_3 could be used to gain more voltage, as well as stability. The stability of the devices must indeed be further improved for their integration into practical application. Though the P3HT:PCBM layer was stable for a few hours in acidic media, a more durable protection of the photo-active components against corrosion is needed. For this, EELs need to be further developed with conducting but watertight materials.

On the photoanode side, the building an OPV-based photoanode, analogous to the photocathode but with an inverted structure and an OER catalyst, does not seem to be realistic. Organic materials are indeed sensitive to oxidizing conditions, and the photoanode surface would be in the presence of both O_2 and protons. Considering the specifications cited above, it seems that metal oxide materials are adapted for the photoanodes. However, most of the metal oxide photoanodes have bandgaps in the 2 – 2.5 eV range, meaning that they absorb light with wavelengths smaller than 620 nm (blue-green region). However, our P3HT:PCBM-photocathodes absorb wavelengths up to 650 nm.[210] One of the advantages of organic photovoltaics is that thanks to chemical synthesis, low-bandgap (< 2 eV) polymers[211] have been developed in order to absorb more in the red region. These polymers, such as PCDTBT as cited above, could be used to build a photocathode with a suitable light absorption and photovoltage.

Among metal oxide materials, tungsten oxide (WO_3, E_g = 2.6 eV) forms stable and inexpensive photoanodes, absorbing blue wavelengths (up to 500 nm, approximately 12 % of sunlight) and highly stable against photocorrosion in acidic media (pH < 4).[36] WO_3 could be considered as complementary photoanode with our photocathodes in acidic media. Hematite (Fe_2O_3, E_g = 2 eV) has emerged as a promising photoanode material due to its significant light absorption (up to 600 nm), abundance and stability in neutral and alkaline media.[212] Similarly, $BiVO_4$ has a visible response up to 500 nm, a high stability in neutral pH and a relatively large underpotential for water oxidation, suitable for a tandem device in neutral media.[213] However, Fe_2O_3 and $BiVO_4$ could be used if the photocathodes could be made functional in neutral or alkaline media. To do this, the organic layer could be combined with a catalyst active at these pH values, such as cobalt phosphide.[214]

Notations

Ag/AgCl	Reference electrode Ag/AgCl (KCl 3.5 M)
Al	Aluminum
AM 1.5 G	Air mass 1.5 global
BHJ	Bulk heterojunction
C_{60}	Buckminster fullerene
CB	Conduction band
CO_2	Carbon dioxide
Cu_2O	Copper oxide
DI water	Deionized water
DSSC	Dye-sensitized solar cell
E_{CB}	Conduction band energy
EDX	Energy-dispersive X-ray spectroscopy
E_F	Fermi level energy
E_g	Bandgap energy
EIS	Electrochemical impedance spectroscopy
EEL	electron-extracting layer
E_{VB}	Valence band energy
FF	Fill factor
FTO	Fluorine tin oxide
GC	Glassy carbon
GO	Graphene oxide
H^+	Proton
H_2O	Water
H_2SO_4	Sulfuric acid
HEL	Hole-extraction layer
HER	Hydrogen evolution reaction
HOMO	Highest occupied molecular orbital
Hydrogen, H_2	Dihydrogen gas
ITO	Indium Tin Oxide
J_{cat}	Current of the catalytic electrode
J_{dark}	Current in the dark
J_{light}	Current under illumination
J_{photo}	Photocurrent
J_{SC}	Short-circuit current density
LiF	Lithium fluoride
LUMO	Lowest unoccupied molecular orbital
M	mol L-1
MoO_3, MoO_x	Molybdenum trioxide, non-stechiometric molybdenum oxide
MoS_2	Molybdenum disulfide
MoS_3	Molybdenum trisulfide

MoS_x	Amorphous molybdenum sulfide
Na_2S	Sodium sulfide
Na_2SO_4	Sodium sulfate
NHE	Normal hydrogen electrode
NiO, NiO_x	Nickel oxide, non-stechiometric nickel oxide
Nitrogen, N_2	Dinitrogen gas
NP	Nanoparticles
OER	Oxygen evolution reaction
OPV	Organic photovoltaic
OSC	Organic semiconductor
Oxygen, O_2	Dioxygen gas
P3HT	Poly-(3-hexylthiophene)
P3MT	Poly-(3-methylthiophene)
$PC_{61}BM$, $PC_{71}BM$	Phenyl-C_{61}-butyric acid methyl ester ; Phenyl-C_{71}-butyric acid methyl ester
PCDTBT	Poly[N- 9'-heptadecanyl-2,7-carbazole-alt-5,5-4,7-di-2-thienyl-2',1',3'-benzothiadiazole]
PCE	Power conversion efficiency
PEC	Photo-electrochemical
PEDOT:PSS	Polystyrenesulfonate-doped polyethylenedioxythiophene
PEMFC	Proton-exchange membrane fuel cell
P_m	Maximum power
Pt	Platinum
Pt/C	Platinum nanoparticles on carbon
PV	Photovoltaic
PVDF	Polyvinylidene difluoride
RDE	Rotating disk electrode
RDS	Rate-determining step
RHE	Reversible hydrogen electrode
rpm	round per minute
SC	Semiconductor
SEM	Scanning Electron Microscopy
STH	Solar-to-hydrogen
TEM	Transmission electron microscopy
TGA	Thermogravimetric analysis
Ti	Titanium
TiO_2, TiO_x	Titanium dioxide, amorphous titanium oxide
TW	Terawatt
UV	Ultra-violet
VB	Valence band
V_{OC}	Open-circuit voltage
V_{photo}	Photovoltage or photopotential
vs	versus
W	Work function
XPS	X-ray photoelectron spectroscopy
ΔG	Gibbs free energy
$\Phi_{saved,ideal}$	Power-saved ratio relative to an ideal non-polarizable dark electrode
$\Phi_{saved,NPAC}$	Power-saved ratio relative to a non-photoactive dark electrode with an identical catalyst

References

1 R. E. Smalley, *MRS Bull.*, 2005, **30**, 412–417.

2 N. S. Lewis and D. G. Nocera, *Proc. Natl. Acad. Sci. U. S. A.*, 2006, **103**, 15729–15735.

3 D. G. Nocera, *Energy Environ. Sci.*, 2010, **3**, 993–995.

4 M. G. Walter, E. L. Warren, J. R. McKone, S. W. Boettcher, Q. Mi, E. A. Santori and N. S. Lewis, *Chem. Rev.*, 2010, **110**, 6446–6473.

5 B. D. James, G. N. Baum, J. Perez and K. N. Baum, *Technoeconomic Analysis of Photoelectrochemical (PEC) Hydrogen Production*, 2009.

6 B. A. Pinaud, J. D. Benck, L. C. Seitz, A. J. Forman, Z. Chen, T. G. Deutsch, B. D. James, K. N. Baum, G. N. Baum, S. Ardo, H. Wang, E. Miller and T. F. Jaramillo, *Energy Environ. Sci.*, 2013, **6**, 1983–2002.

7 M. Carmo, D. L. Fritz, J. Mergel and D. Stolten, *Int. J. Hydrogen Energy*, 2013, **38**, 4901–4934.

8 A. Fujishima and K. Honda, *Nature*, 1972, **238**, 37–38.

9 Z. Li, W. Luo, M. Zhang, J. Feng and Z. Zou, *Energy Environ. Sci.*, 2013, **6**, 347–370.

10 S. Protti, A. Albini and N. Serpone, *Phys. Chem. Chem. Phys.*, 2014, **16**, 19790–19827.

11 T. J. Jacobsson, V. Fjällström, M. Edoff and T. Edvinsson, *Energy Environ. Sci.*, 2014, **7**, 2056–2070.

12 E. Lanzarini, M. R. Antognazza, M. Biso, A. Ansaldo, L. Laudato, P. Bruno, P. Metrangolo, G. Resnati, D. Ricci and G. Lanzani, *J. Phys. Chem. C*, 2012, **116**, 10944–10949.

13 F. C. Krebs, M. Hösel, M. Corazza, B. Roth, M. V. Madsen, S. A. Gevorgyan, R. R. Søndergaard, D. Karg and M. Jørgensen, *Energy Technol.*, 2013, **1**, 378–381.

14 O. Khaselev and J. A. Turner, *Science*, 1998, **280**, 425–427.

15 O. Khaselev, A. Bansal and J. A. Turner, *Int. J. Hydrogen Energy*, 2001, **26**, 127–132.

16 A. C. Nielander, M. R. Shaner, K. M. Papadantonakis, S. A. Francis and N. S. Lewis, *Energy Environ. Sci.*, 2015, **8**, 16–25.

17 F. E. Osterloh, *Chem. Mater.*, 2008, **20**, 35–54.

18 K. Sun, S. Shen, Y. Liang, P. E. Burrows, S. S. Mao and D. Wang, *Chem. Rev.*, 2014, **114**, 8662–8719.

19 A. Kudo and Y. Miseki, *Chem. Soc. Rev.*, 2009, **38**, 253–278.

20 X. Chen, S. Shen, L. Guo and S. S. Mao, *Chem. Rev.*, 2010, **110**, 6503–6570.

21 Z. Yu, F. Li and L. Sun, *Energy Environ. Sci.*, 2015, **8**, 760–775.

22 T. M. Gür, S. F. Bent and F. B. Prinz, *J. Phys. Chem. C*, 2014, **118**, 21301–21315.

23 K. S. Joya, Y. F. Joya, K. Ocakoglu and R. van de Krol, *Angew. Chem. Int. Ed.*, 2013, **52**, 10426–10437.

24 W. Ayers, 1984, Patent US4466869.

25 S. Licht, B. Wang, S. Mukerji, T. Soga, M. Umeno and H. Tributsch, *Int. J. Hydrogen Energy*, 2001, **26**, 653–659.

26 S. S. Kocha, D. Montgomery, M. W. Peterson and J. A. Turner, *Sol. Energy Mater. Sol. Cells*, 1998, **52**, 389–397.

27 R. E. Rocheleau, E. L. Miller and A. Misra, *Energy Fuels*, 1998, **12**, 3–10.

28 Y. Yamada, N. Matsuki, T. Ohmori, H. Mametsuka, M. Kondo, A. Matsuda and E. Suzuki, *Int. J. Hydrogen Energy*, 2003, **28**, 1167–1169.

29 S. Y. Reece, J. A. Hamel, K. Sung, T. D. Jarvi, A. J. Esswein, J. J. H. Pijpers and D. G. Nocera, *Science*, 2011, **334**, 645–648.

30 D. G. Nocera, *Acc. Chem. Res.*, 2012, **45**, 767–776.

31 M. Grätzel, *CatTech*, 1999, **3**, 4–18.

32 J. Gan, X. Lu and Y. Tong, *Nanoscale*, 2014, **6**, 7142–7164.

33 Y. Park, K. J. McDonald and K.-S. Choi, *Chem. Soc. Rev.*, 2013, **42**, 2321–2337.

34 F. F. Abdi, L. Han, A. H. M. Smets, M. Zeman, B. Dam and R. van de Krol, *Nat. Commun.*, 2013, **4**, 2195.

35 P. M. Rao, L. Cai, C. Liu, I. S. Cho, C. H. Lee, J. M. Weisse, P. Yang and X. Zheng, *Nano Lett.*, 2014, **14**, 1099–1105.

36 X. Liu, F. Wang and Q. Wang, *Phys. Chem. Chem. Phys.*, 2012, **14**, 7894–7911.

37 Q. Mi, Y. Ping, Y. Li, B. Cao, B. S. Brunschwig, P. G. Khalifah, G. A. Galli, H. B. Gray and N. S. Lewis, *J. Am. Chem. Soc.*, 2012, **134**, 18318–18324.

38 K. Sivula, F. Le Formal and M. Grätzel, *Chem. Mater.*, 2009, **21**, 2862–2867.

39 M. Rioult, H. Magnan, D. Stanescu and A. Barbier, *J. Phys. Chem. C*, 2014, **118**, 3007–3014.

40 D. K. Zhong, J. Sun, H. Inumaru and D. R. Gamelin, *J. Am. Chem. Soc.*, 2009, **131**, 6086–6087.

41 I. Cesar, A. Kay, J. A. G. Martinez and M. Grätzel, *J. Am. Chem. Soc.*, 2006, **128**, 4582–4583.

42 B. Liu, H. M. Chen, C. Liu, S. C. Andrews, C. Hahn and P. Yang, *J. Am. Chem. Soc.*, 2013, **135**, 9995–9998.

43 J. H. Park, S. Kim and A. J. Bard, *Nano Lett.*, 2005, **6**, 24–28.

44 I. S. Cho, Z. Chen, A. J. Forman, D. R. Kim, P. M. Rao, T. F. Jaramillo and X. Zheng, *Nano Lett.*, 2011, **11**, 4978–4984.

45 M. Higashi, K. Domen and R. Abe, *J. Am. Chem. Soc.*, 2012, **134**, 6968–6971.

46 M. Higashi, K. Domen and R. Abe, *Energy Environ. Sci.*, 2011, **4**, 4138–4147.

47 B. A. Pinaud, P. C. K. Vesborg and T. F. Jaramillo, *J. Phys. Chem. C*, 2012, **116**, 15918–15924.

48 H. X. Dang, N. T. Hahn, H. S. Park, A. J. Bard and C. B. Mullins, *J. Phys. Chem. C*, 2012, **116**, 19225–19232.

49 S. W. Boettcher, E. L. Warren, M. C. Putnam, E. A. Santori, D. Turner-Evans, M. D. Kelzenberg, M. G. Walter, J. R. Mckone, B. S. Brunschwig, H. A. Atwater and N. S. Lewis, *J. Am. Chem. Soc.*, 2011, **133**, 1216–1219.

50 J. D. Benck, S. C. Lee, K. D. Fong, J. Kibsgaard, R. Sinclair and T. F. Jaramillo, *Adv. Energy Mater.*, 2014, **4**, 1400739.

51 B. Seger, A. B. Laursen, P. C. K. Vesborg, T. Pedersen, O. Hansen, S. Dahl and I. Chorkendorff, *Angew. Chem. Int. Ed.*, 2012, **51**, 9128–9131.

52 B. Seger, S. D. Tilley, T. Pedersen, P. C. K. Vesborg, O. Hansen, M. Grätzel and I. Chorkendorff, *J. Mater. Chem. A*, 2013, **1**, 15089–15094.

53 C. G. Morales-Guio, S. D. Tilley, H. Vrubel, M. Grätzel and X. Hu, *Nat. Commun.*, 2014, **5**, 3059.

54 C.-Y. Lin, Y.-H. Lai, D. Mersch and E. Reisner, *Chem. Sci.*, 2012, **3**, 3482–3487.

55 Z. Ji, M. He, Z. Huang, U. Ozkan and Y. Wu, *J. Am. Chem. Soc.*, 2013, **135**, 11696–11699.

56 H. Shirakawa, E. J. Louis, A. G. MacDiarmid, C. K. Chiang and A. J. Heeger, *J. Chem. Soc. Chem. Commun.*, 1977, 578–580.

57 J. Yan and B. R. Saunders, *RSC Adv.*, 2014, **4**, 43286–43314.

58 M. Grätzel, *J. Photochem. Photobiol. C Photochem. Rev.*, 2003, **4**, 145–153.

59 A. Hagfeldt, G. Boschloo, L. Sun, L. Kloo and H. Pettersson, *Chem. Rev.*, 2010, **110**, 6595–6663.

60 A. J. Nozik, M. C. Beard, J. M. Luther, M. Law, R. J. Ellingson and J. C. Johnson, *Chem. Rev.*, 2010, **110**, 6873–6890.

61 B. Kippelen and J.-L. Brédas, *Energy Environ. Sci.*, 2009, **2**, 251–261.

62 S. Günes, H. Neugebauer and N. S. Sariciftci, *Chem. Rev.*, 2007, **107**, 1324–1338.

63 M. A. Green, K. Emery, Y. Hishikawa, W. Warta and E. D. Dunlop, *Prog. Photovolt: Res. Appl.*, 2015, **23**, 1–9.

64 N. Espinosa, M. Hösel, M. Jørgensen and F. C. Krebs, *Energy Environ. Sci.*, 2014, **7**, 855–866.

65 J. Roncali, *Chem. Rev.*, 1997, **97**, 173–205.

66 J. C. Bijleveld, R. A. M. Verstrijden, M. M. Wienk and R. A. J. Janssen, *Appl. Phys. Lett.*, 2010, **97**, 073304.

67 A. Najari, P. Berrouard, C. Ottone, M. Boivin, Y. Zou, D. Gendron, W.-O. Caron, P. Legros, C. N. Allen, S. Sadki and M. Leclerc, *Macromolecules*, 2012, **45**, 1833–1838.

68 J. Warnan, A. El Labban, C. Cabanetos, E. T. Hoke, P. K. Shukla, C. Risko, J. L. Brédas, M. D. McGehee and P. M. Beaujuge, *Chem. Mater.*, 2014, **26**, 2299–2306.

69 Y. Huang, E. J. Kramer, A. J. Heeger and G. C. Bazan, *Chem. Rev.*, 2014, **114**, 7006–7043.

70 Y. Kim, A. M. Ballantyne, J. Nelson and D. D. C. Bradley, *Org. Electron.*, 2009, **10**, 205–209.

71 L. Dou, J. You, Z. Hong, Z. Xu, G. Li, R. A. Street and Y. Yang, *Adv. Mater.*, 2013, **25**, 6642–6671.

72 N. Kaur, M. Singh, D. Pathak, T. Wagner and J. M. Nunzi, *Synth. Met.*, 2014, **190**, 20–26.

73 Y.-J. Cheng, S.-H. Yang and C.-S. Hsu, *Chem. Rev.*, 2009, **109**, 5868–5923.

74 S. N. Chen, A. J. Heeger, Z. Kiss, A. G. MacDiarmid, S. C. Gau and D. L. Peebles, *Appl. Phys. Lett.*, 1980, **36**, 96–98.

75 S. Yanagida, A. Kabumoto, K. Mizumoto, C. Pac and K. Yoshino, *J. Chem. Soc. Chem. Commun.*, 1985, 474–475.

76 O. A. El-Rashiedy and S. Holdcroft, *J. Phys. Chem.*, 1996, **100**, 5481–5484.

77 T. Abe and K. Nagai, *Org. Electron.*, 2007, **8**, 262–271.

78 G. Suppes, E. Ballard and S. Holdcroft, *Polym. Chem.*, 2013, **4**, 5345–5250.

79 G. M. Suppes, P. J. Fortin and S. Holdcroft, *J. Electrochem. Soc.*, 2015, **162**, H551–H556.

80 T. Abe, M. Ichikawa, T. Hikage, S. Kakuta and K. Nagai, *Chem. Phys. Lett.*, 2012, **549**, 77–81.

81 T. Abe, S. Tobinai, N. Taira, J. Chiba, T. Itoh and K. Nagai, *J. Phys. Chem. C*, 2011, **115**, 7701–7705.

82 T. Abe, Y. Tanno, T. Ebina, S. Miyakushi and K. Nagai, *ACS Appl. Mater. Interfaces*, 2013, **5**, 1248–1253.

83 T. Abe, J. Chiba, M. Ishidoya and K. Nagai, *RSC Adv.*, 2012, **2**, 7992–7996.

84 W. Li, A. Furlan, K. H. Hendriks, M. M. Wienk and R. A. J. Janssen, *J. Am. Chem. Soc.*, 2013, **135**, 5529–5532.

85 A. Le Goff, V. Artero, B. Jousselme, P. D. Tran, N. Guillet, R. Métayé, A. Fihri, S. Palacin and M. Fontecave, *Science*, 2009, **326**, 1384–1387.

86 B. Hinnemann, P. G. Moses, J. Bonde, K. P. Jørgensen, J. H. Nielsen, S. Horch, I. Chorkendorff and J. K. Nørskov, *J. Am. Chem. Soc.*, 2005, **127**, 5308–5309.

87 R. B. Gordon, M. Bertram and T. E. Graedel, *Proc. Natl. Acad. Sci. U. S. A.*, 2006, **103**, 1209–1214.

88 V. S. Thoi, Y. Sun, J. R. Long and C. J. Chang, *Chem. Soc. Rev.*, 2013, **42**, 2388–2400.

89 P. Du and R. Eisenberg, *Energy Environ. Sci.*, 2012, **5**, 6012–6021.

90 W. Sheng, H. A. Gasteiger and Y. Shao-Horn, *J. Electrochem. Soc.*, 2010, **157**, B1529–B1356.

91 X. Zou and Y. Zhang, *Chem. Soc. Rev.*, 2015, 10.1039/C4CS00448E.

92 J. R. McKone, S. C. Marinescu, B. S. Brunschwig, J. R. Winkler and H. B. Gray, *Chem. Sci.*, 2014, **5**, 865–878.

93 D. Merki and X. Hu, *Energy Environ. Sci.*, 2011, **4**, 3878–3888.

94 W.-F. Chen, J. T. Muckerman and E. Fujita, *Chem. Commun.*, 2013, **49**, 8896–8909.

95 B. Winther-Jensen and D. R. MacFarlane, *Energy Environ. Sci.*, 2011, **4**, 2790–2798.

96 M. S. Faber and S. Jin, *Energy Environ. Sci.*, 2014, **7**, 3519–3542.

97 A. Volbeda and J. C. Fontecilla-Camps, *Dalt. Trans.*, 2003, 4030–4038.

98 D. J. Evans and C. J. Pickett, *Chem. Soc. Rev.*, 2003, **32**, 268–275.

99 S. C. Lee and R. H. Holm, *Proc. Natl. Acad. Sci. U. S. A.*, 2003, **100**, 3595–3600.

100 M. L. Helm, M. P. Stewart, R. M. Bullock, M. R. DuBois and D. L. DuBois, *Science*, 2011, **333**, 863–866.

101 P. D. Tran, A. Le Goff, J. Heidkamp, B. Jousselme, N. Guillet, S. Palacin, H. Dau, M. Fontecave and V. Artero, *Angew. Chem. Int. Ed.*, 2011, **50**, 1371–1374.

102 E. S. Andreiadis, P.-A. Jacques, P. D. Tran, A. Leyris, M. Chavarot-Kerlidou, B. Jousselme, M. Matheron, J. Pécaut, S. Palacin, M. Fontecave and V. Artero, *Nat. Chem.*, 2013, **5**, 48–53.

103 R. Prins, V. H. J. De Beer and G. A. Somorjai, *Catal. Rev. Sci. Eng.*, 1989, **31**, 1–41.

104 T. Spalvins, *J. Vac. Sci. Technol. A*, 1987, **5**, 212–219.

105 P. Afanasiev, *Comptes Rendus Chim.*, 2008, **11**, 159–182.

106 A. B. Laursen, S. Kegnæs, S. Dahl and I. Chorkendorff, *Energy Environ. Sci.*, 2012, **5**, 5577–5591.

107 P. C. K. Vesborg and T. F. Jaramillo, *RSC Adv.*, 2012, **2**, 7933–7947.

108 W. Jaegermann and H. Tributsch, *Prog. Surf. Sci.*, 1988, **29**, 1–167.

109 A. Sobczynski, *J. Catal.*, 1991, **131**, 156–166.

110 T. F. Jaramillo, K. P. Jørgensen, J. Bonde, J. H. Nielsen, S. Horch and I. Chorkendorff, *Science*, 2007, **317**, 100–102.

111 T. F. Jaramillo, J. Bonde, J. Zhang, B.-L. Ooi, K. Andersson, J. Ulstrup and I. Chorkendorff, *J. Phys. Chem. C*, 2008, **112**, 17492–17498.

112 S. J. Hibble and G. B. Wood, *J. Am. Chem. Soc.*, 2004, **126**, 959–965.

113 H. W. Wang, P. Skeldon, G. E. Thomson and G. C. Wood, *J. Mater. Sci.*, 1997, **2**, 497–502.

114 R. I. Walton, A. J. Dent and S. J. Hibble, *Chem. Mater.*, 1998, **10**, 3737–3745.

115 G. Laperriere, B. Marsan and D. Belanger, *Synth. Met.*, 1989, **29**, F201–F206.

116 D. Bélanger, G. Laperrière, F. Girard, D. Guay and G. Tourillon, *Chem. Mater.*, 1993, **5**, 861–868.

117 D. Merki, S. Fierro, H. Vrubel and X. Hu, *Chem. Sci.*, 2011, **2**, 1262–1267.

118 C. G. Morales-Guio and X. Hu, *Acc. Chem. Res.*, 2014, **47**, 2671–2681.

119 H. Vrubel, D. Merki and X. Hu, *Energy Environ. Sci.*, 2012, **5**, 6136–6144.

120 X. Zong, H. Yan, G. Wu, G. Ma, F. Wen, L. Wang and C. Li, *J. Am. Chem. Soc.*, 2008, **130**, 7176–7177.

121 X. Zong, G. Wu, H. Yan, G. Ma, J. Shi, F. Wen, L. Wang and C. Li, *J. Phys. Chem. C*, 2010, **114**, 1963–1968.

122 F. A. Frame and F. E. Osterloh, *J. Phys. Chem. C*, 2010, **114**, 10628–10633.

123 S. Kanda, T. Akita, M. Fujishima and H. Tada, *J. Colloid Interface Sci.*, 2011, **354**, 607–610.

124 X. Zong, Y. Na, F. Wen, G. Ma, J. Yang, D. Wang, Y. Ma, M. Wang, L. Sun and C. Li, *Chem. Commun.*, 2009, 4536–4538.

125 Y. Lattach, J. Fortage, A. Deronzier and J.-C. Moutet, *ACS Appl. Mater. Interfaces*, 2015, **7**, 4476–4480.

126 P. D. Tran, S. S. Pramana, V. S. Kale, M. Nguyen, S. Y. Chiam, S. K. Batabyal, L. H. Wong, J. Barber and J. Loo, *Chem. - Eur. J.*, 2012, **18**, 13994–13999.

127 Q. Ding, F. Meng, C. R. English, M. Cabán-Acevedo, M. J. Shearer, D. Liang, A. S. Daniel, R. J. Hamers and S. Jin, *J. Am. Chem. Soc.*, 2014, **136**, 8504–8507.

128 L. Zhang, C. Liu, A. B. Wong, J. Resasco and P. Yang, *Nano Res.*, 2015, **8**, 281–287.

129 C. G. Morales-Guio, L. Liardet, M. T. Mayer, S. D. Tilley, M. Grätzel and X. Hu, *Angew. Chem. Int. Ed.*, 2015, **54**, 664–667.

130 Y. Hou, B. L. Abrams, P. C. K. Vesborg, M. E. Björketun, K. Herbst, L. Bech, A. M. Setti, C. D. Damsgaard, T. Pedersen, O. Hansen, J. Rossmeisl, S. Dahl, J. K. Nørskov and I. Chorkendorff, *Nat. Mater.*, 2011, **10**, 434–438.

131 M. L. Tang, D. C. Grauer, B. Lassalle-Kaiser, V. K. Yachandra, L. Amirav, J. R. Long, J. Yano and A. P. Alivisatos, *Angew. Chem. Int. Ed.*, 2011, **50**, 10203–10207.

132 A. B. Laursen, T. Pedersen, P. Malacrida, B. Seger, O. Hansen, P. C. K. Vesborg and I. Chorkendorff, *Phys. Chem. Chem. Phys.*, 2013, **15**, 20000–20004.

133 Z. Huang, C. Wang, L. Pan, F. Tian, X. Zhang and C. Zhang, *Nano Energy*, 2013, **2**, 1337–1346.

134 G.-L. Zang, G.-P. Sheng, C. Shi, Y.-K. Wang, W.-W. Li and H.-Q. Yu, *Energy Environ. Sci.*, 2014, **7**, 3033–3039.

135 B. Seger, K. Herbst, T. Pedersen, B. Abrams, P. C. K. Vesborg, O. Hansen and I. Chorkendorff, *J. Electrochem. Soc.*, 2014, **161**, H722–H724.

136 P. Ratnasamy, L. Rodrique and A. J. Leonard, *J. Phys. Chem.*, 1973, **77**, 2242–2245.

137 A. Müller, E. Diemann, E. Krickemeyer, H. J. Walberg, H. Bögge and A. Armatage, *Eur. J. Solid State Inorg. Chem.*, 1993, **30**, 565–572.

138 H. Jiao, Y.-W. Li, B. Delmon and J.-F. Halet, *J. Am. Chem. Soc.*, 2001, **123**, 7334–7339.

139 I. Bezverkhy, P. Afanasiev and M. Lacroix, *Inorg. Chem.*, 2000, **39**, 5416–5417.

140 S. J. Hibble, D. A. Rice, D. M. Pickup and M. P. Beer, *Inorg. Chem.*, 1995, **34**, 5109–5113.

141 J. Tauc, *Mater. Res. Bull.*, 1968, **3**, 37–46.

142 J. Tauc, R. Grigorovici and A. Vancu, *Phys. Status Solidi*, 1966, **15**, 627–637.

143 C. M. Cardona, W. Li, A. E. Kaifer, D. Stockdale and G. C. Bazan, *Adv. Mater.*, 2011, **23**, 2367–2371.

144 J. Liu, W. Yang, Y. Li, L. Fan and Y. Li, *Phys. Chem. Chem. Phys.*, 2014, **16**, 4778–4788.

145 S. K. Haram, B. M. Quinn and A. J. Bard, *J. Am. Chem. Soc.*, 2001, **123**, 8860–8861.

146 M. Amelia, C. Lincheneau, S. Silvi and A. Credi, *Chem. Soc. Rev.*, 2012, **41**, 5728–5743.

147 G. Xiong, R. Shao, T. C. Droubay, A. G. Joly, K. M. Beck, S. A. Chambers and W. P. Hess, *Adv. Funct. Mater.*, 2007, **17**, 2133–2138.

148 T. Nann, S. K. Ibrahim, P. M. Woi, S. Xu, J. Ziegler and C. J. Pickett, *Angew. Chem. Int. Ed.*, 2010, **49**, 1574–1577.

149 J. Y. Kim, S. H. Kim, H.-H. Lee, K. Lee, W. Ma, X. Gong and A. J. Heeger, *Adv. Mater.*, 2006, **18**, 572–576.

150 J. Y. Kim, K. Lee, N. E. Coates, D. Moses, T.-Q. Nguyen, M. Dante and A. J. Heeger, *Science*, 2007, **317**, 222–225.

151 H.-L. Yip and A. K.-Y. Jen, *Energy Environ. Sci.*, 2012, **5**, 5994–6011.

152 K. Lee, J. Y. Kim, S. H. Park, S. H. Kim, S. Cho and A. J. Heeger, *Adv. Mater.*, 2007, **19**, 2445–2449.

153 S. H. Park, A. Roy, S. Beaupré, S. Cho, N. Coates, J. S. Moon, D. Moses, M. Leclerc, K. Lee and A. J. Heeger, *Nat. Photonics*, 2009, **3**, 297–302.

154 S. Ben Dkhil, D. Duché, M. Gaceur, A. K. Thakur, F. B. Aboura, L. Escoubas, J.-J. Simon, A. Guerrero, J. Bisquert, G. Garcia-Belmonte, Q. Bao, M. Fahlman, C. Videlot-Ackermann, O. Margeat and J. Ackermann, *Adv. Energy Mater.*, 2014, **4**, 1400805.

155 M. J. Tan, S. Zhong, J. Li, Z. Chen and W. Chen, *ACS Appl. Mater. Interfaces*, 2013, **5**, 4696–4701.

156 B. F. Bory, P. R. F. Rocha, R. A. J. Janssen, H. L. Gomes, D. M. De Leeuw and S. C. J. Meskers, *Appl. Phys. Lett.*, 2014, **105**, 123302.

157 R. Steim, F. R. Kogler and C. J. Brabec, *J. Mater. Chem.*, 2010, **20**, 2499–2512.

158 G. Li, V. Shrotriya, J. Huang, Y. Yao, T. Moriarty, K. Emery and Y. Yang, *Nat. Mater.*, 2005, **4**, 864–868.

159 M. Reyes-Reyes, K. Kim, J. Dewald, R. López-Sandoval, A. Avadhanula, S. Curran and D. L. Carroll, *Org. Lett.*, 2005, **7**, 5749–5752.

160 A. Guerrero, M. Haro, S. Bellani, M. R. Antognazza, L. Meda, S. Gimenez and J. Bisquert, *Energy Environ. Sci.*, 2014, **7**, 3666–3673.

161 T. Bourgeteau, D. Tondelier, B. Geffroy, R. Brisse, C. Laberty-Robert, S. Campidelli, R. de Bettignies, V. Artero, S. Palacin and B. Jousselme, *Energy Environ. Sci.*, 2013, **6**, 2706–2713.

162 B. Seger, T. Pedersen, A. B. Laursen, P. C. K. Vesborg, O. Hansen and I. Chorkendorff, *J. Am. Chem. Soc.*, 2013, **135**, 1057–1064.

163 B. Seger, D. S. Tilley, T. Pedersen, P. C. K. Vesborg, O. Hansen, M. Grätzel and I. Chorkendorff, *RSC Adv.*, 2013, **3**, 25902–25907.

164 R. Liu, Z. Zheng, J. Spurgeon and X. Yang, *Energy Environ. Sci.*, 2014, **7**, 2504–2517.

165 Y. Lin, C. Battaglia, M. Boccard, M. Hettick, Z. Yu, C. Ballif, J. W. Ager and A. Javey, *Nano Lett.*, 2013, **13**, 5615–5618.

166 M. Haro, C. Solis, G. Molina, L. Otero, J. Bisquert, S. Gimenez and A. Guerrero, *J. Phys. Chem. C*, 2015, **119**, 6488–6494.

167 D. Chen, H. Zhang, Y. Liu and J. Li, *Energy Environ. Sci.*, 2013, **6**, 1362–1387.

168 U. Sim, T.-Y. Yang, J. Moon, J. An, J. Hwang, J.-H. Seo, J. Lee, K. Y. Kim, J. Lee, S. Han, B. H. Hong and K. T. Nam, *Energy Environ. Sci.*, 2013, **6**, 3658–3664.

169 G. Kakavelakis, D. Konios, E. Stratakis and E. Kymakis, *Chem. Mater.*, 2014, **26**, 5988–5993.

170 D. H. Wang, J. K. Kim, J. H. Seo, I. Park, B. H. Hong, J. H. Park and A. J. Heeger, *Angew. Chem. Int. Ed.*, 2013, **52**, 2874–2880.

171 S. Bae, H. Kim, Y. Lee, X. Xu, J.-S. Park, Y. Zheng, J. Balakrishnan, T. Lei, H. R. Kim, Y. Il Song, Y.-J. Kim, K. S. Kim, B. Ozyilmaz, J.-H. Ahn, B. H. Hong and S. Iijima, *Nat. Nanotechnol.*, 2010, **5**, 574–578.

172 X. Li, Y. Zhu, W. Cai, M. Borysiak, B. Han, D. Chen, R. D. Piner, L. Colombo and R. S. Ruoff, *Nano Lett.*, 2009, **9**, 4359–4363.

173 K. S. Kim, Y. Zhao, H. Jang, S. Y. Lee, J. M. Kim, J.-H. Ahn, P. Kim, J.-Y. Choi and B. H. Hong, *Nature*, 2009, **457**, 706–710.

174 M. Cox, A. Gorodetsky, B. Kim, K. S. Kim, Z. Jia, P. Kim, C. Nuckolls and I. Kymissis, *Appl. Phys. Lett.*, 2011, **98**, 123303.

175 K. Rikitake, T. Akiyama, W. Takashima and K. Kaneto, *Synth. Met.*, 1997, **86**, 2357–2358.

176 J. Labille, J. Brant, F. Villiéras, M. Pelletier, A. Thill, A. Masion, M. Wiesner, J. Rose and J.-Y. Bottero, *Fullerenes, Nanotubes, Carbon Nanostruct.*, 2006, **14**, 307–314.

177 Z. Zhang, R. Dua, L. Zhang, H. Zhu, H. Zhang and P. Wang, *ACS Nano*, 2013, **7**, 1709–1717.

178 M. Kaukonen, R. M. Nieminen, S. Pöykkö and A. P. Seitsonen, *Phys. Rev. Lett.*, 1999, **83**, 5346–5349.

179 R. H. Coridan, A. C. Nielander, S. A. Francis, M. T. McDowell, V. Dix, S. M. Chatman and N. S. Lewis, *Energy Environ. Sci.*, 2015, DOI:10.1039/C5EE00777A.

180 M. D. Irwin, D. B. Buchholz, A. W. Hains, R. P. H. Chang and T. J. Marks, *Proc. Natl. Acad. Sci. U. S. A.*, 2008, **105**, 2783–2787.

181 J. R. Manders, S.-W. Tsang, M. J. Hartel, T.-H. Lai, S. Chen, C. M. Amb, J. R. Reynolds and F. So, *Adv. Funct. Mater.*, 2013, **23**, 2993–3001.

182 G. Boschloo and A. Hagfeldt, *J. Phys. Chem. B*, 2001, **105**, 3039–3044.

183 J.-Y. Jeng, K.-C. Chen, T.-Y. Chiang, P.-Y. Lin, T.-D. Tsai, Y.-C. Chang, T.-F. Guo, P. Chen, T.-C. Wen and Y.-J. Hsu, *Adv. Mater.*, 2014, **26**, 4107–4113.

184 E. L. Ratcliff, J. Meyer, K. X. Steirer, A. Garcia, J. J. Berry, D. S. Ginley, D. C. Olson, A. Kahn and N. R. Armstrong, *Chem. Mater.*, 2011, **23**, 4988–5000.

185 N. Koch, A. Kahn, J. Ghijsen, J.-J. Pireaux, J. Schwartz, R. L. Johnson and A. Elschner, *Appl. Phys. Lett.*, 2003, **82**, 70–72.

186 J. Huang, P. F. Miller, J. S. Wilson, A. J. De Mello, J. C. De Mello and D. D. C. Bradley, *Adv. Funct. Mater.*, 2005, **15**, 290–296.

187 V. Shrotriya, G. Li, Y. Yao, C.-W. Chu and Y. Yang, *Appl. Phys. Lett.*, 2006, **88**, 073508.

188 Y.-J. Xing, M.-F. Qian, D.-Z. Guo and G.-M. Zhang, *Chinese Phys. B*, 2014, **23**, 038504.

189 P. V. Kumar, M. Bernardi and J. C. Grossman, *ACS Nano*, 2013, **7**, 1638–1645.

190 J.-M. Yun, J.-S. Yeo, J. Kim, H.-G. Jeong, D.-Y. Kim, Y.-J. Noh, S.-S. Kim, B.-C. Ku and S.-I. Na, *Adv. Mater.*, 2011, **23**, 4923–4928.

191 J. Liu, M. F. Durstock and L. Dai, *Energy Environ. Sci.*, 2014, **7**, 1297–1306.

192 Y.-J. Jeon, J.-M. Yun, D.-Y. Kim, S.-I. Na and S.-S. Kim, *Sol. Energy Mater. Sol. Cells*, 2012, **105**, 96–102.

193 S.-S. Li, K.-H. Tu, C.-C. Lin, C.-W. Chen and M. Chhowalla, *ACS Nano*, 2010, **4**, 3169–3174.

194 X. Liu, H. Kim and L. J. Guo, *Org. Electron.*, 2013, **14**, 591–598.

195 H. Yamaguchi, J. Granstrom, W. Nie, H. Sojoudi, T. Fujita, D. Voiry, M. Chen, G. Gupta, A. D. Mohite, S. Graham and M. Chhowalla, *Adv. Energy Mater.*, 2014, **4**, 1300986.

196 W. S. J. Hummers and R. E. Offeman, *J. Am. Chem. Soc.*, 1958, **80**, 1339.

197 J. Zhao, S. Pei, W. Ren, L. Gao and H. M. Cheng, *ACS Nano*, 2010, **4**, 5245–5252.

198 J. Meyer, S. Hamwi, M. Kröger, W. Kowalsky, T. Riedl and A. Kahn, *Adv. Mater.*, 2012, **24**, 5408–5427.

199 S. Chuang, C. Battaglia, A. Azcatl, S. McDonnell, J. S. Kang, X. Yin, M. Tosun, R. Kapadia, H. Fang, R. M. Wallace and A. Javey, *Nano Lett.*, 2014, **14**, 1337–1342.

200 C. Battaglia, X. Yin, M. Zheng, I. D. Sharp, T. Chen, S. McDonnell, A. Azcatl, C. Carraro, B. Ma, R. Maboudian, R. M. Wallace and A. Javey, *Nano Lett.*, 2014, **14**, 967–971.

201 I. Irfan, A. J. Turinske, Z. Bao and Y. Gao, *Appl. Phys. Lett.*, 2012, **101**, 093305.

202 I. Hancox, P. J. Sullivan, K. V. Chauhan, N. Beaumont, L. A. Rochford, R. A. Hatton and T. S. Jones, *Org. Electron.*, 2010, **11**, 2019–2025.

203 S. R. Hammond, J. Meyer, N. E. Widjonarko, P. F. Ndione, A. K. Sigdel, A. Garcia, A. Miedaner, M. T. Lloyd, A. Kahn, D. S. Ginley, J. J. Berry and D. C. Olson, *J. Mater. Chem.*, 2012, **22**, 3249–3254.

204 S. Braun, W. R. Salaneck and M. Fahlman, *Adv. Mater.*, 2009, **21**, 1450–1472.

205 W. M. Haynes, in *CRC Handbook of Chemistry and Physics, 95th edition*, 2011, pp. 12–124.

206 C. J. Brabec, S. E. Shaheen, C. Winder, N. S. Sariciftci and P. Denk, *Appl. Phys. Lett.*, 2002, **80**, 1288–1290.

207 T. J. Jacobsson, V. Fjällström, M. Sahlberg, M. Edoff and T. Edvinsson, *Energy Environ. Sci.*, 2013, **6**, 3676–3683.

208 E. J. Popczun, C. G. Read, C. W. Roske, N. S. Lewis and R. E. Schaak, *Angew. Chem. Int. Ed.*, 2014, **53**, 5427–5430.

209 Z. Huang, Z. Chen, Z. Chen, C. Lv, H. Meng and C. Zhang, *ACS Nano*, 2014, **8**, 8121–8129.

210 L. Li, G. Lu and X. Yang, *J. Mater. Chem.*, 2008, **18**, 1984–1990.

211 E. Bundgaard and F. C. Krebs, *Sol. Energy Mater. Sol. Cells*, 2007, **91**, 954–985.

212 K. Sivula, F. Le Formal and M. Grätzel, *ChemSusChem*, 2011, **4**, 432–449.

213 M. Zhong, T. Hisatomi, Y. Kuang, J. Zhao, M. Liu, A. Iwase, Q. Jia, H. Nishiyama, T. Minegishi, M. Nakabayashi, N. Shibata, R. Niishiro, C. Katayama, H. Shibano, M. Katayama, A. Kudo, T. Yamada and K. Domen, *J. Am. Chem. Soc.*, 2015, **137**, 5053–5060.

214 J. Tian, Q. Liu, A. M. Asiri and X. Sun, *J. Am. Chem. Soc.*, 2014, **136**, 7587−7590.

215 S. Esiner, H. van Eersel, M. M. Wienk and R. A. J. Janssen, *Adv. Mater.*, 2013, **25**, 2932–2936.

216 B. Radisavljevic, A. Radenovic, J. Brivio, V. Giacometti and A. Kis, *Nat. Nanotechnol.*, 2011, **6**, 147–150.

Experimental section

1. General

Solvents and reagents are from commercial sources and are used without purification unless otherwise mentioned.

MoO_3, anhydrous Na_2S, sulfuric acid: 98 %, 1,2-dichlobenzene **(**anhydrous, 99%), Potassium ferricyanide(III), Nickel acetate: **Aldrich**

HCl: Chlorhydric acid 37% AnalaR NORMAPUR® ACS, ISO, Reag.Ph.Eur. for analysis

TiO_2: Solaronix, TiO_2 HT-L/SC 3%wt in alcoholic and acidic media

ZnO: Sigma Aldrich, Zinc oxide, dispersion of nanoparticles, 40 wt. % in ethanol, <130 nm particle size (DLS); Batch: MKBH7691

PEDOT:PSS: Heraeus Clevios™ P VP AI 4083 for spin-coated devices, supplied by Ossila Limited

P3HT: M104 (M101 during the first year), RR = 96.6%, Ossila

$PC_{61}BM$ (purity > 99 %), $PC_{71}BM$: Solenne BV

CVD Graphene monolayer (G1L) was obtained from collaborators and multilayer (G4L) was purchased from Graphene Supermarket.

2. Analysis techniques

2.1. Electrochemical equipment

Potentiostat. BioLogic Model VSP 0254

Electrochemistry. Electrochemical measurements were performed in a three-electrode configuration. For polarization and electrolysis measurements, a glassy carbon plate was used as the auxiliary electrode and a home-made Ag/AgCl (KCl 3.5 M) electrode was used as the reference electrode. Potentials are quoted against the Reversible Hydrogen Electrode (i.e. the apparent standard potential of the H^+/H_2 couple at the given pH). The potential of the Reversible Hydrogen Electrode (RHE) is defined as $E_{RHE} = -0.059$ pH. Thus potentials measured versus the Ag/AgCl electrode can be converted versus the RHE by using the following formula: $E_{vs\ RHE} = E_{vs\ Ag/AgCl} + E°_{Ag/AgCl} + 0.059$ pH. With a pH of 0, the formula becomes: $E_{vs\ RHE} = E_{vs\ Ag/AgCl} + 0.217$ (V). The $[Fe(CN)_6]^{3-}/[Fe(CN)_6]^{4-}$ couple ($E^0 = 0.56$ V *vs* SHE in HCl 0.1 M) has then been used for the standardization of the measurements.

Prior to any measure in 0.5 M H_2SO_4, the electrolyte was degased with N_2 for at least 30 min. During measure, a N_2 flow was maintained above the electrolyte.

Impedance spectra were carried out in 0.5 M H_2SO_4 at –0.22 V *vs* RHE (close to the onset potential of MoS_3-catalysed HER), from 100 000 Hz to 0.1 Hz (or 0.01 Hz).

Photo-electrochemistry. The experimental setup used for the photo-electrochemistry is the same as the typical electrochemical setup used previously. The working electrode is the photocathode, connected to the Potentiostat at the ITO side. The MoS_3 side is in contact with the electrolyte, the sample is illuminated on the glass\ITO side by a light source.

Light source. The samples were illuminated with a 200 W mercury-xenon lamp (Oriel, ozone free) operated at 106 W coupled with a Spectra-Physics 59472 UV cut-off filter (λ >400 nm), while the light was carried to the sample with an optical fiber allowing 380 to 800 nm wavelengths. Irradiance at the substrate surface was measured to 100 mW cm^{-2} thanks to a Coherent PowerMax-USB PM150-50C Power Sensor. However, because the mercury-xenon lamps has two intense peaks between 550 and 600 nm, so that though the power is 100 mW cm^{-2}, it corresponds to more than 1 sun (approximately 1.7 sun, considering the measures carried out on a solar cell in our lab and in Orgatech, where a solar simulator is used). An electronic shutter controller (Newport) with a function generator GX 240 (Metrix) delivering a square signal was used to switch off and on the light at a given frequency.

2.2. Solar cell characterization

The current-voltage characteristics of organic photovoltaic cells were independently measured with a Keithley 2635 system Source Meter under nitrogen atmosphere. They were deposited onto an ITO-coated substrate with an etched side for the cathodic contact. A LiF\Al cathode (0.28 cm^2) was deposited under vacuum in a Joule evaporator (< 10^{-6} mbar, 0.4 Å s^{-1} for 1.2 nm LiF and 0.15 nm s^{-1} for 100 nm Al). The samples were illuminated through the glass substrate.

2.3. XPS-analysis

XPS. XPS data were collected by an Axis Ultra DLD (Kratos Analytical) under ultra-high vacuum conditions (< 10^{-8} Torr), using a monochromatic Al Kα X-ray source (1486.6 eV). The spectra were analyzed with CasaXPS Software. For insulating substrates, an unfocused electron cloud was used to compensate the charges. Before and after each measurement, the Au $4f_{7/2}$ peak was measured on a pure gold sample determining the binding energy shift and allowing the recalibration of energies.

For quantification, relative sensitivity factors from the supplier were used.

2.4. Microscopy techniques

TEM/EDX. TEM pictures were taken on a TECNAI 120 Spirit G2 from FEI and a CCD camera on column bottom Orius from Gatan in 4K steps. Energy-dispersive analysis (EDX) was similarly carried out. The suspension was drop-cast on a copper Delta Microscopy TEM grid coated with carbon.

SEM. The morphology of thin films was investigated with a SEM Hitachi S-4500.

3. Equipments

Tapes. Electroplating tape (Vinyl Film 470 for electroplating applications, from 3M™) was used for the masks of the photocathodes. For spin-coating, a very thin tape (3M™ Polyester Film Tape 850 Silver) was used to protect one side of the sample. In any other case, repositionable Magic Scotch tape was used.

Airbrush. Deposition of layers by spray-coating was carried out by an Aztek A470 airbrush with a 9344C nozzle and nitrogen at an operating pressure of 2.5 bar.

An airbrush is loaded with the suspension and sprayed onto a substrate, which was vertically fixed on a heated sample holder (for MoS_3, the temperature of the substrate holder was set at 85 °C, and at 100 °C for MoS_3:TiO_2). Electroplating tape was used to spray on a definite surface of the substrate (the surface in contact with the electrolyte for electrochemical experiments).

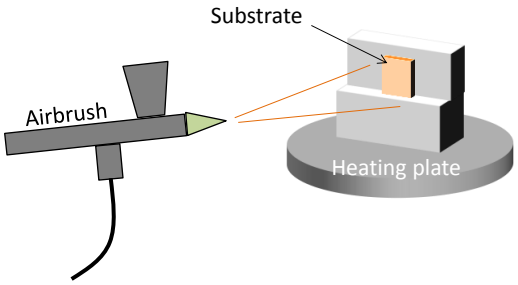

With this method, the amount of sprayed material is not easily controlled, and the thickness is thus evaluated by profilometry as previously described. When the substrate is for example a photocathode, it is not possible to scratch it, since it has to be further tested. In that case, a bare glass substrate is sprayed at the same time and rate as the photocathode to get a rough idea of the thickness of the film.

Spin-coater. Deposition of layers by spin-coating in air was carried out by a Laurell Technologies Corporation device, model WS-400B-6NPP/LITE/OND, under N_2 purge. The spin-coater used in glovebox was a Spincoat G3P-8 from Specialty Coating Systems.

Spin-coating is used to deposit uniform thin films on flat surfaces. A solution of coating material is deposited on the substrate, and spread by centrifugal forces during high speed rotation. The excess solution is spun off the edges while the resulting film dries.

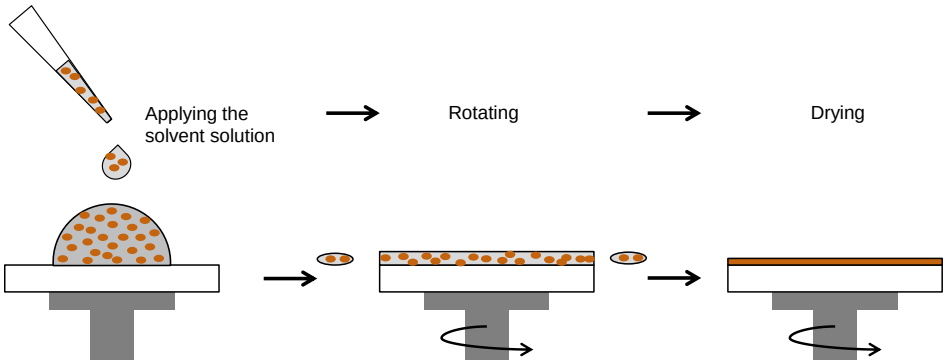

The solution or suspension must be homogeneous. Control of the thickness of the layers is achieved by changing the concentration of the solution or the rotating speed, depending on the type of solution (solution of polymers or of molecules, etc).

Profilometer. Thickness of the deposited layers was measured with an Ambios Technology Inc. profilometer, model XP-200 Sylus, on a scratched region. For solid films which cannot be scratched properly such as TiO_x, the film is deposited onto a softer film (e.g. TiO_x can be spin-coated onto a PEDOT:PSS or P3HT:PCBM layer whose thickness is known, and the thickness is measured before/after TiO_x deposition). Another method is to hide a small area with a polyester film tape, and to measure the step after removing the tape.

UV-visible spectroscopy. UV-Visible spectra were performed with a Perlin Elmer - Lambda 650 spectrometer with a tungsten-halogen and a deuterium lamp and a R955 photomultiplier detector (resolution 190 to 900nm).

TGA. Determination of concentrations of suspensions and analysis of compounds were carried out with a Q50 V20.10 Build 36 device, with a platinum pan and nitrogen as balance and sample gas.

Gas chromatography. Hydrogen production was monitored with a Perkin-Elmer Clarus 500 gas chromatograph equipped with a porapack Q 80/100 column (6' 1/8") thermostated at 40 °C and a TCD detector thermostated at 100°C.

Syringes. BD Syringes with luer lock were used with syringe filters (typically PVDF, 45 µm, 13 mm diameter).

Glovebox. Ar-filled glovebox were used for the preparation of photocathodes and for sensitive reagents. Operated at 15-20 mbar of overpressure, H_2O concentration was ~ 1 ppm and O_2 between 1 and 20 ppm.

Thermal evaporation. Al, LiF and C_{60} are thermally evaporated in a Joule evaporator. The evaporator top chamber is situated in a glovebox and allows the substrate transfer without seeing oxygen. Ti is evaporated in a Joule evaporator at a pressure smaller than 10^{-6} mbar. The samples are put in the substrate holder in the glovebox but have to be shortly in air for the transfer in the evaporator.

4. Experimental methods

4.1. Cleaning and etching of the substrates

DI water is provided by a Millipore Integral 3 water purification system and is generally used at 13 MΩ cm, and at 18 MΩ cm for electrochemical experiments.

Cleaning. ITO (indium tin oxide)-coated glass substrates (Xinyan Technology Ltd., XY20S, ITO thickness ca. 100 nm, < 20 Ω cm^{-2}), used as transparent electrode, are cleaned as follow:

- Sonication for 10 min in DI water with Decon (a few drops of pre-diluted commercial Decon in water) at 50 °C and max. power (9)
- 3 times rinsing with DI water,
- Sonication for 10 min in DI water (twice, in clean DI water each)
- Rinsing with ethanol
- Sonication for 10 min in acetone
- Sonication for 10 min in isopropanol
- Drying with N_2
- 15 min in UV-ozone cleaner
- Quick N_2 flux on the substrates after UV-ozone to remove dust
- Immediate transfer of the substrates in the glovebox

Once out of the UV-ozone cleaner, the substrates must be used immediately. If they are to be used later, they are stored in isopropanol after the step of sonication in isopropanol. Right before use, they are dried with N_2 and put 15 min in UV-ozone cleaner.

The UV-ozone treatment has several purposes. First, it removes organic pollution present on the ITO surface. It also turns the surface hydrophilic by creating hydroxyl functions. The hydrophilicity allows a good wettability of a solution on the substrate, making the spin-coating process easier. To evaluate the minimum time to make the surface hydrophilic, contact angle measurements were carried out after different times, and it turns out that only 5 min are necessary. However, the UV-ozone treatment also increase the work function of ITO, making it more suitable for hole collection in normal OSCs, and the treatment duration in use in our lab was 15 min.

Etching. ITO samples are aligned at the bottom of a plastic basin (with low edges) and a band of tape (Scotch® Magic™) is used to maintain them as well as to define the area which will be etched. The tape is gently pressed to avoid bubbles near the edge of the tape, in order to have a clean ITO border. It is important to have 1 L of DI water ready for just after the etching. Small amounts of fine zinc powder are deposited on the area of ITO which must be etched. With a cotton bud soaked in 37 % HCl, the ITO is removed: a brown color appears and must be entirely removed. With the other side of the cotton bud (and also soaked in HCl) the last traces of ITO are removed. This process must be very

fast to avoid damage to the tape. Then, the DI water is poured in the basin. The ITO samples are removed from the tape band and cleaned as described above.

4.2. Synthesis and deposition of MoS_3 sol and mixed MoS_3:TiO_2 suspension

Synthesis. MoS_3 particles were synthesized according to a procedure reported by Hu and coll.[1] In a typical preparation, molybdenum trioxide (Aldrich, MoO_3, 0.51 g, 3.48 mmol) was added to an aqueous solution of sodium sulfide (1.34 g, 17.37 mmol of anhydrous Na_2S in 125 mL of water). After dissolution, the solution should be light greenish yellow and the pH above 12. Fast addition of MoO_3 gives a darker solution and the synthesized particles are less stable.

This solution was then kept under vigorous stirring while 6.0 M aqueous HCl was added slowly (10 minutes) until the pH was below 4. It is however easier for the separation of particles to go under 2. At first, darkening of the solution was observed. After the addition of acid, the flask was covered with a water cooling column and refluxed for 30 min, resulting in an increase of the pH by 1 unit. After being cooled to ambient temperature, the suspension was centrifuged, the supernatant liquid was thrown away and particles were dispersed in DI water. This process was repeated twice to wash the particles. Then it was repeated twice in ethanol, and once in ether, to remove as much water as possible. Finally, without drying the precipitate, the particles were dispersed in acetone and sonicated for 10 minutes using an ultrasonic horn at 20 kHz. This sol can either be deposited by spin-coating or by spray-coating, depending on the substrate.

Storage. The suspension is stable for about 10 days in air, after which the particle aggregates and the solvent turns blue. For a long conservation, the suspension is placed in a protected atmosphere (e.g. Ar-filled glovebox), where it does not degrade during the period it is used (several months).

Concentration. The concentration is evaluated by drying a definite volume of the suspension in an oven or by TGA. A precise correlation between visible light absorption and concentration has been established and used to measure the concentration of the following syntheses of MoS_3.

Deposition. Spin-coating is carried out at 2000/5/60 (2000 rpm reached in 5 s and maintained for 60 s) in air or in the glovebox. The rotation was started approximately 2 s after deposition of the solution. The thickness can be controlled by the MoS_3 concentration (cf. section 2.3.3.1). As the sol is not viscous, changing the rotation speed does not impact the thickness. A part of the substrate was cleaned with a cotton bud soaked in acetone or ethanol or water, to improve the contact. Then, an electroplating tape mask is applied on the substrate by gently pressing with the tip of pliers. For spray, the samples are taken out of the glovebox, and the electroplating tape mask is applied with the tip of pliers. With Scotch® Magic™ tape, the samples are fixed on the heated sample holder (85 °C) and MoS_3 (~ 5 g L^{-1}) is deposited by spray-coating in air.

MoS_3:TiO_2. In some devices, MoS_3 was mixed with TiO_2 nanoparticles. This suspension was made by mixing the two suspensions to obtain different MoS_3:TiO_2 weight ratio (cf. section 2.3.5.2). The

suspension was sonicated for 30 min prior to deposition, and was deposited either by spin-coating or by spray-coating. Then the substrate was annealed at 120 °C for 30 min in air (or in the glovebox when deposited on P3HT:PCBM).

4.3. Platinum ink

The Pt/C ink was prepared by sonicating (1 h) 10 mg of commercial Pt/C (Alfa Aesar, 40 wt.% of Pt, HiSPEC 4000™) in 400 µL of ethanol, 100 µL of deionized water and 65 µL of a Nafion dispersion (D-520, 5 % w/w in water and isopropanol, from Alfa Aesar). The ink was diluted by 4 in ethanol, and deposited either by spin-coating (at 2000/5/60) or by drop-casting.

4.4. Synthesis and deposition of TiO_x thin films

Synthesis. TiO_x precursor was prepared as described in the literature.[2] 2 mL of titanium^{IV} isopropoxide $Ti[OCH(CH3)_2]_4$ (Aldrich>99.999% was mixed with 10 mL of 2-methoxyethanol ($C_3H_8O_2$, Aldrich) and 1 mL of ethanolamine (C_2H_7NO, Aldrich, >99%) were mixed in an Ar glovebox. Components were mixed in a hermetically sealed vial inside glove box and stirred for 3 h in a silicon oil bath at 100°C. The precursor was stored in a brown vial in the glovebox.

Deposition. Prior to deposition, it was diluted by 100 in anhydrous isopropanol in the glovebox. Deposition was carried out by spin-coating in air at 2000/5/60, followed by 1 min annealing at 110 °C. As the cleaning of a contact is difficult with solvents, a thin polyester film tape is used to mask an area before spin-coating, and is removed right after deposition. A thin film of approximately 7 nm was obtained. Afterwards, thermal treatment could be carried out in the glovebox (after MoS_3 deposition, in the case when TiO_x is deposited onto P3HT:PCBM) or in air (when MoS_3 is sprayed on TiO_x).

4.5. Synthesis and deposition of NiO_x thin films

Synthesis. NiO_x precursor was synthesized according to a reported procedure[3]. Nickel acetate (1.245 g, 5 mmol, 1.00 eq.) was dissolved in absolute ethanol (50 mL) with monoethanolamine (305 mg, 5 mmol, 1.00 eq.)). The solution was stirred for 4 h in a closed vial at 70 °C until complete dissolution. After cooling down, it was stored in a refrigerator (4 °C).

Deposition. Prior to deposition, the precursor was diluted by 4 in absolute ethanol in a 4 mL glass vial. It was then spin-coated at 4000/5/90 in air or in the glovebox using an Eppendorf pipette (80 µL) followed by immediate annealing at 110 °C for 10 s. Contacts were cleaned with a cotton bud with ethanol. The substrates were then annealed at 320 °C in air for 30 min. After removing the dust particles with N_2, they were submitted to UV-ozone treatment for 15 min, after which they had a grey color, disappearing quickly. Again, a short N_2 flux was used to remove dust. They were transferred as quickly as possible in the glovebox and immediately used for P3HT:PCBM deposition.

4.6. Graphene transfer

Monoloyers of graphene (G1L) are obtained by chemical vapor deposition (CVD) onto a copper catalyst (typically a copper foil). Right after synthesis, a thin layer of PMMA (2 µm thick) is spin-coated onto the foil to protect graphene. The G1L samples (with PMMA) were obtained from collaborators. For commercial graphene grown on a thin layer of nickel (300 nm) on SiO_2/Si substrates, 4 layers are obtained (G4L; 4 layers is an average value, but in reality it is comprised between 1 and 7 layers). The commercial sample has no protecting PMMA layer.

4.6.1 Wet transfer

PMMA-based transfer.

According to the standard procedure to transfer the monolayer without damage, the copper is etched in a solution containing $FeCl_3$ and HCl (prepared by dissolving 60 g of $FeCl_3$ in 132 g of DI water and 8 g of HCl 37 %). The resulting material is a soft floating piece of PMMA, with a graphene monolayer underneath (in contact with the etchant). With the help of a plastic foil (to pick up graphene without damage) and a toothpick (to move the floating substrate in water), the G1L/PMMA is picked up and put in DI water for 2 hours. With the same method, it is transferred into 0.5 M H_2SO_4 to remove traces

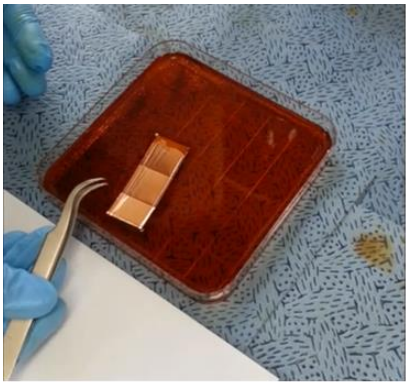


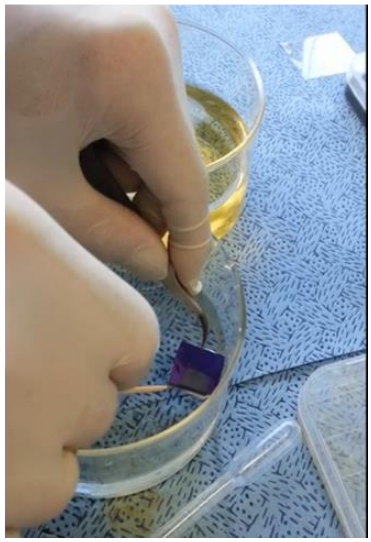

of iron. After 2 hours, it is transferred into DI water (and into fresh DI water after 2 hours). In each last step, the floating graphene is in contact with the aqueous media, and the PMMA layer is facing air. Pictures: Eric Moyen, Sungkyunkwan University, South Korea.

To deposit the graphene onto a target substrate, the substrate is plunged into the water in which the graphene is floating. It is gently removed from the water so that the graphene is adhering to the surface, the G1L is facing the substrate. When the graphene is entirely on the surface, the substrate is dried vertically for 30 min at room temperature, and then at 100 °C to remove water. Afterwards, the substrate is plunged into acetone to remove the PMMA. Depending on the later use, the time of soaking into acetone can be varied from minutes to several hours.

Graphene deposited by this procedure onto SiO_2/Si substrates is well preserved, as it can be seen on the MEB images before and after transfer. The graphene monolayer is made of continuous grains of hundreds of µm large.

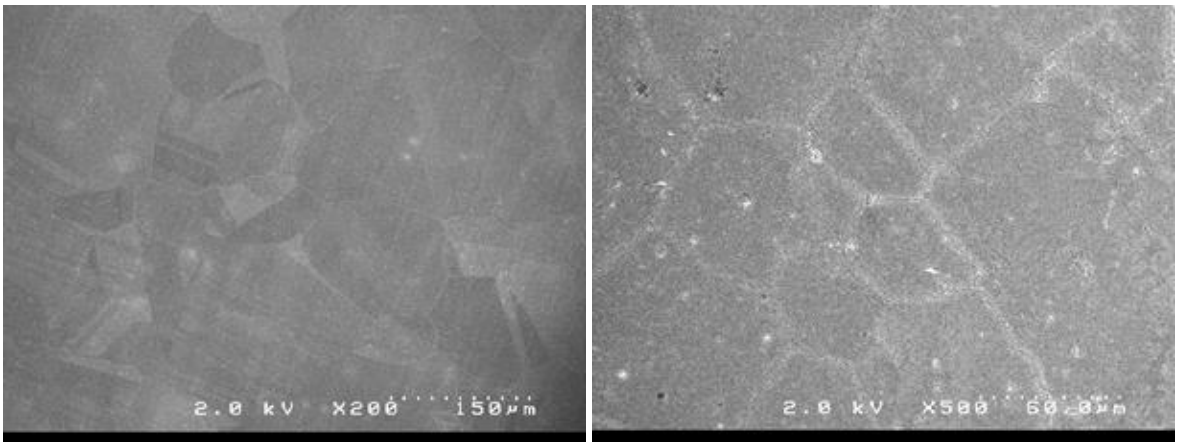

Fig. 105. Left: graphene on copper prior to transfer. Right: same sample after transfer on a SiO_2/Si substrate.

In our case, the target substrate is an organic solar cell. Thus, it cannot stand being soaked in water or acetone for a long time. First, we had to replace the PEDOT:PSS layer by NiO_x because PEDOT:PSS induced delamination of the whole device due to its hydrophilicity. A thin TiO_x layer was spin-coated onto P3HT:PCBM to prevent direct contact with water. Then, the procedure was adapted: the first steps were the same (etching, rinsing of PMMA\G1L), then the solar cell was plunged in water to pick up the G1L\PMMA (the G1L face in contact with the solar cell) and most of the water was removed with absorbing paper. The cell was immediately dried at 80°C. Quickly, it was plunged twice in acetone for 10 seconds, and dried, to remove the PMMA. It was then transferred back into the glovebox. The photocathodes made by this procedure were not efficient, it seems that short-circuits appeared between the anode and graphene (Fig. 106).

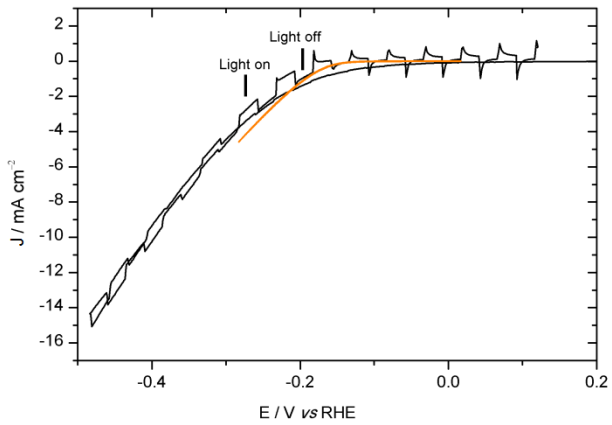

Fig. 106. Current density-voltage curve (50 mV s^{-1}) of an ITO\$NiO_x$\P3HT:PCBM\$TiO_x$\G1L\$MoS_3$ photocathode in N_2-saturated 0.5 M H_2SO_4 (black line). CV of ITO\$MoS_3$ in the same media for comparison.

It is probable that there is a short circuit. It has been observed on all similar cells, with the same inverted photocurrent and the same current-voltage curve as MoS_3 alone. It could be that the presence of graphene, which has a higher work function that the electrolyte, affects the whole device by allowing electrons to flow directly from ITO to MoS_3 as if there was no P3HT:PCBM.

For G4L, PMMA (Mw = 996 000, Aldrich) in solution in *ortho*-dichlorobenzene was spin-coated to form a 2 µm thick film, and was not annealed. Then, the same procedure than described for G1L was applied for this G4L. However, due to the etching of the sample only by the sides, one must be careful to remove any trace of PMMA on the sides of the SiO_2/Si substrate, so that the etchant can reach Ni.

PMMA-free transfer.

Graphene multilayers are obtained by CVD on a nickel catalyst. On a nickel foil, 30 to 60 layers can be obtained but the graphene is still partially mixed in the nickel foil, so that recovering it is complicated. On the contrary, G4L is easy to recover and contrary to G1L it is strong enough to float alone on water without PMMA support. The procedure to recover the graphene multilayers is the same as graphene monolayer on copper foil. However, there are some differences:

- The SiO_2/Si substrate is slightly floating when the graphene is still on it, but when the graphene starts to detach itself (due to the gradual dissolution of Ni), it weighs on the remaining attached graphene. Therefore, it is important not to put too much etchant (2-3 mm high in the container).

- When the graphene is detached, it cannot be transferred with a plastic foil as before. With 2 Pasteur pipettes, fresh DI water must be added while the etchant is removed, until no etchant is visible. Also, 0.5 M H_2SO_4 must be added and removed by the same method.
- The free-standing graphene is fragile. The transfer is a delicate process especially when it is transferred onto the organic solar cell (its hydrophobicity makes the water surface tension break the graphene layer). To limit the damage to the graphene layers, one must maintain the graphene layer with the plastic foil until the solar cell is moved out of the water.

After transfer, the trapped water is removed with absorbing paper and the substrate is dried.

G4L was transferred on ITO\$NiO_x$\P3HT:PCBM\$TiO_x$ to build a solar cell (Fig. 107). Photocathodes based on the same structure (ITO\$NiO_x$\P3HT:PCBM\$TiO_x$\G4L\$MoS_3$ produced only a few µA of photocurrent, probably due to the high work function of graphene.

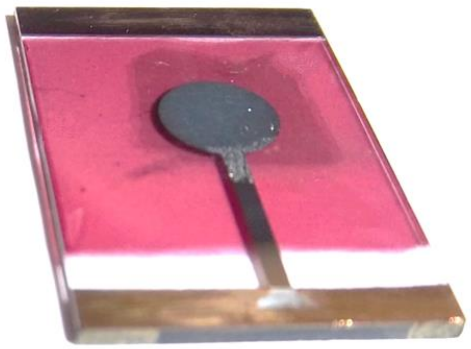

Fig. 107. Picture of an ITO\$NiO_x$\P3HT:PCBM\$TiO_x$\G4L\LiF\Al solar cell

4.6.1 Dry transfer

Thermal release tape. Thermal release tape (TRT) was purchased from Graphene Supermarket. To transfer G1L by thermal release tape, the PMMA is removed with acetone. The TRT is pasted on G1L/Cu. The copper foil is etched, and the TRT is picked up and washed in DI water and 0.5 M H_2SO_4. After drying at room temperature, it is applied on the substrate (for example SiO_2/Si) with pressure (a Pasteur pipette can be used to roll uniformly on the substrate). The substrate is then placed on a heating plate at 100 °C, until the TRT detached itself and leaves the graphene. Lower heating temperatures result in detachment of the TRT but traces of adhesive remains on the substrate. G4L and other multilayers are difficult to deposit in such a way because the G4L/TRT is not sticking to the target substrate.

With this deposition method, flakes of graphene are transferred onto SiO2 but the layer is not continuous, even when several transfers are made on the same substrate (Fig. 108). However, it seems that the transfer depends a lot on the target substrate, and that it does not occur onto P3HT:PCBM.

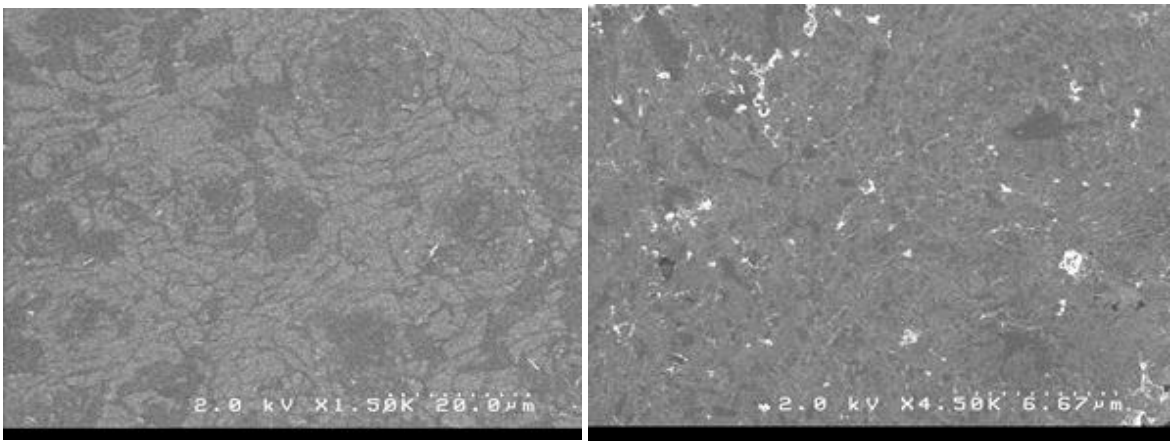

Fig. 108. Right: G1L transfer by TRT on SiO_2/Si. Left: 4 layers of G1L successively deposited with TRT on SiO_2/Si.

PDMS. PDMS stamping has been tested but graphene seems to stick to the PDMS surface, even when the latter has been silanized. Another technique was to put the G1L/PMMA on a 1 mm-thick PDMS stamp (the PMMA side in contact with PDMS), then to apply it on the graphene side onto the target substrate, and then to remove gently the PDMS while heating slightly (70 °C). Again, this technique is efficient on SiO_2/Si (the PMMA/graphene stays on the target substrate, and then PMMA is removed with acetone) but not on P3HT:PCBM.

4.6.1 Graphene oxide

GO was prepared using the standard Hummers[4,5] method followed by spontaneous exfoliation in water. The suspension was then centrifuged to remove unexfoliated graphite particles. GO flakes formed a gel in the supernatant. This gel was lyophilized and the dry GO was used to prepare a suspension in DI water (8 mg mL^{-1}). The GO suspension was then deposited by spin-coating, contacts were cleaned with a cotton bud and acetone, and the substrates were subsequently annealed at 150 °C for 15 min in air to recover some of the conducting properties of graphene. The film color changed from brown to gray due to this partial reduction.

4.7. Synthesis and deposition of MoO_x thin films

Synthesis. A solution of molybdenum tricarbonyl trispropionitrile $[Mo(CO)_3(EtCN)_3]$ was prepared in acetonitrile at a concentration of 0.05 M.[6] The solution was stirred for 24 h in a closed vial in the glovebox and was left to settle.

Deposition. The supernatant was taken with a syringe, and a PVDF filter (0.45 µm) was used to remove undissolved material. It was deposited by spin-coating in the glovebox at 5000/5/60. After contact cleaning (cotton bud with acetone), the samples were annealed in air at 150 °C for 20 min.

4.8. Fabrication of organic solar cells

Organic solar cells are prepared following procedures established at Orgatech (LPICM).

The typical device structure is the following:

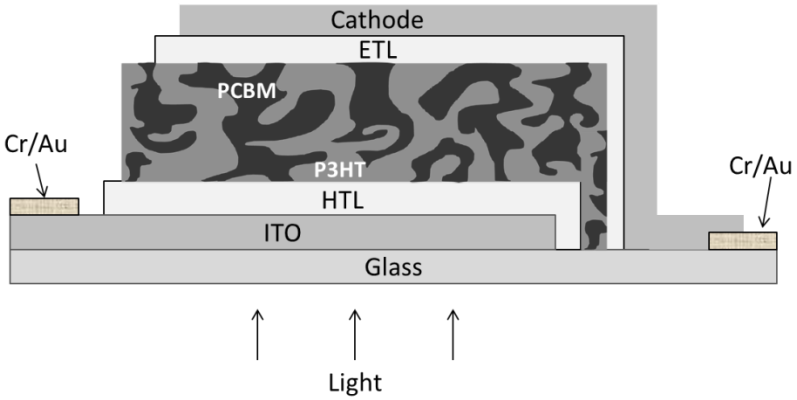

Fig. 109. OPV cell structure based on a P3HT:PCBM bulk heterojunction. The cathode is usually Al/LiF, and sometimes Ti. Other bulk heterojunction have been used during this PhD such as PCDTBT:$PC_{71}BM$ and P3HT:ICBA.

PEDOT:PSS. ITO-coated glass substrates are cleaned as described before, ending by 15min of UV-ozone. The substrates are kept in the UV-ozone cleaner and taken out one by one for the deposition of PEDOT:PSS. Right after being taken out, a short N_2 stream is applied to remove dust particles and PEDOT:PSS is deposited by spin-coating in air at 3000/5/30 + 5000/5/30 resulting in a 40 nm thick layer. A PVDF syringe filter (45 µm) is used to remove undesired particles from the PEDOT:PSS suspension. To avoid dust, which causes holes in the thin film, it is important to let 3-4 drops fall off from the filter before coating the first substrate of the batch, and one drop before each of the following substrate. Contacts are cleaned with a cotton bud and DI water.

PEDOT:PSS is then heated at 150°C for 10 min in air, and transferred immediately in the glovebox.

Deposition and heat treatment can be carried out in air or in a nitrogen-filled glovebox. It is mentioned with the data when needed.

P3HT:$PC_{60}BM$. Solutions are prepared by weighing P3HT (first) and $PC_{60}BM$ (second) in the same brown vial in air. The P3HT:$PC_{60}BM$ weight ratio used during the thesis was always 1:1 for a total concentration of 25 mg mL^{-1} of each material. The vial is transferred in a glovebox, where anhydrous *ortho*-dichlorobenzene added. The solution is stirred 2 h at 55 °C, then overnight at room temperature,

and 1 h at 55 °C prior to deposition. The solution is spin-coated in the glovebox at 1500/5/60 (unless otherwise mentioned). A PVDF filter (45 µm, 13 mm diameter) is used to remove particles, and similarly to PEDOT:PSS, it is better to let the first 3-4 drops fall off from the syringe before the first coating, and 1 drop before each following coating. It is better to coat the substrate entirely with solution before starting the rotation. Contacts are cleaned with a cotton bud and *ortho*-DCB. Annealing is carried out (for the fabrication of the photocathodes, it is carried out after the deposition of the catalyst).

Evaporation. The substrates are loaded on a sample holder. For Al, LiF, and C_{60}, the loading chamber is situated in a glovebox. Different masks can be used depending on the material and on the device architecture. Vacuum is always lower than 10^{-6} mbar. Evaporation of 1.2 nm LiF at 800 °C takes approx. 50 s (± 15 s). Evaporation of 100 nm Al at 1200 °C takes about 10 min (± 1 min). Evaporation of C_{60} starts at 480 °C but the temperature must be increased during the evaporation (typically, from 480 °C to 525 - 530 °C for a 50 nm thick layer in about 12 - 15 min.

Ti is evaporated in a Joule evaporator, at a rate of about 0.5 to 1 Å s^{-1}. It starts when the current is about 150 A, and finishes at about 175 A. Ti evaporation can begin at a fast pace, one must be careful not to increase the current to rapidly to give enough time for the metal to melt. The Joule evaporator is not in a glovebox. Thus, the devices were loaded in the sample holder inside the glovebox, transported to the evaporator in an air-tight plastic bag, and taken out just when the evaporator loading chamber was open.

4.9. Deposition of photocathodes

Many different combinations of materials have been used for the fabrication of photocathodes. Each layer has been deposited as described in the previous sections, but some processes have been slightly changed so that the processes of all successive depositions are compatible.

It is worth to note that during the first two years, the annealing of P3HT:PCBM (in the glovebox, 130 or 140 °C for 5 min, depending on the polymer) was performed right after deposition of the P3HT:PCBM layer. However, we noticed that better efficiencies were obtained when the annealing was performed after the deposition of MoS_3, i.e. as a final step of the device fabrication.

When the photocathode involves several evaporations of metals or C_{60}, the masks must be taken so that each evaporation will be carried out on a smaller area.

Also, a masking tape (electroplating tape) is used to define a precise electrochemical area (the disc area was made with a punch). This tape is chemically resistant and was applied onto the substrate before (or after) spray-coating (or spin-coating, respectively) MoS_3, with gentle pressing with pliers all around the disc to ensure the adhesion of the tape.

Finally, when the devices are ready (i.e. after MoS_3 deposition, and annealing if necessary), they are stored in the glovebox or preferably under vacuum in the glovebox airlock. They are taken out one by one for the photo-electrochemical testing.

ITO\PEDOT:PSS\P3HT:PCBM\MoS_3. PEDOT:PSS and P3HT:PCBM are deposited as described previously, without annealing. The electroplating tape is pasted and MoS_3 is deposited by spray-coating in air. The devices are finally annealed in the glovebox at 130 °C for 5 min.

ITO\PEDOT:PSS\P3HT:PCBM\MoS_3:TiO_2. PEDOT:PSS and P3HT:PCBM are deposited as described previously, without annealing. The electroplating tape is pasted and MoS_3:TiO_2 is deposited by spray-coating in air. The devices are finally annealed in the glovebox at 130 °C for 5 min.

ITO\PEDOT:PSS\P3HT:PCBM\$TiO_x$\$MoS_3$. PEDOT:PSS and P3HT:PCBM are deposited as described previously, without annealing, then TiO_x is deposited (as described previously). The electroplating tape is pasted and MoS_3 is deposited by spray-coating in air. The devices are finally annealed in the glovebox at 130 °C for 5 min.

ITO\$NiO_x$\P3HT:PCBM\$TiO_x$\$MoS_3$. NiO_x and P3HT:PCBM are deposited as described previously, without annealing, then TiO_x is deposited (as described previously). The electroplating tape is pasted and MoS_3 is deposited by spray-coating in air. The devices are finally annealed in the glovebox at 130 °C for 5 min.

ITO\$NiO_x$\P3HT:PCBM\$TiO_x$\G1L\$MoS_3$. NiO_x and P3HT:PCBM are deposited as described previously, without annealing, then TiO_x is deposited (as described previously). The annealing step was carried out for 5 min at 140 °C in the glovebox, and G1L was deposited by PMMA-based transfer, spray-coating of MoS_3 in air at 85 °C (temperature of the sample holder).

ITO\$NiO_x$\P3HT:PCBM\$TiO_x$\G4L\$MoS_3$. NiO_x as usual, P3HT:PCBM without the annealing step, TiO_x as usual + annealing step for 5 min at 140 °C in the glovebox, deposition of G4L by PMMA-free transfer, spray-coating of MoS3 in air at 85 °C (temperature of the sample holder).

ITO\PEDOT:PSS\P3HT:PCBM\LiF\Al\MoS_3. PEDOT:PSS to LiF\Al (1 x 0.8 mm²) as usual, MoS_3 by spin-coating in the glovebox (at 2000/5/30 followed immediately by 15 s drying at 70 °C to avoid damaging the Al with possible traces of water in MoS_3).

ITO\PEDOT:PSS\P3HT:PCBM\LiF\Al\Ti\MoS_3. PEDOT:PSS to P3HT:PCBM as usual, LiF\Al (1 x 0.8 mm² Ti as usual, MoS_3 by spin-coating in the glovebox (at 2000/5/30 followed immediately by 15 s drying at 70 °C to avoid damaging the Al with possible traces of water in MoS_3).

ITO\PEDOT:PSS\P3HT:PCBM\LiF\Ti\$MoS_3$ and ITO\PEDOT:PSS\P3HT:PCBMTi\$MoS_3$. PEDOT:PSS to LiF (or without LiF) as usual, transfer to the other evaporator for Ti. MoS3 by spray.

ITO\PEDOT:PSS\P3HT:PCBM\$C_{60}$\$MoS_3$ and ITO\PEDOT:PSS\P3HT:PCBM\LiF\$C_{60}$\$MoS_3$. PEDOT:PSS to P3HT:PCBM as usual, evaporation of LiF (or without LiF) and C_{60}. MoS_3 by spray.

ITO\NiO$_x$\P3HT:PCBM\MoS$_3$. NiO$_x$ as usual, P3HT:PCBM (without annealing), MoS$_3$ by spray in air, annealing 5 min at 140 °C. LiF\C$_{60}$ and C$_{60}$ can be evaporated prior to MoS$_3$ deposition.

ITO\GO\P3HT:PCBM\MoS$_3$. GO as described, P3HT:PCBM (without annealing), MoS$_3$ by spray in air, annealing 5 min at 140 °C.

ITO\MoO$_x$\P3HT:PCBM\MoS$_3$. MoO$_x$ as usual, P3HT:PCBM (without annealing), MoS$_3$ by spray in air, annealing 5 min at 140 °C. LiF\C$_{60}$ and C$_{60}$ can be evaporated prior to MoS$_3$ deposition.

References in the experimental section:

1 H. Vrubel, D. Merki and X. Hu, *Energy Environ. Sci.*, 2012, **5**, 6136–6144.

2 C. Meneses, J. Sanchez, M. Estrada, I. Pereyra, A. Avila-Garcia, A. Escobosa and M. Pavanello, *Microelectron. Technol. Devices (SBMicro), 2013 Symp.*, 2013, 1–4.

3 J. R. Manders, S.-W. Tsang, M. J. Hartel, T.-H. Lai, S. Chen, C. M. Amb, J. R. Reynolds and F. So, *Adv. Funct. Mater.*, 2013, **23**, 2993–3001.

4 J. William S. Hummers and R. E. Offeman, *J. Am. Chem. Soc*, 1958, **80**, 1339-.

5 J. Zhao, S. Pei, W. Ren, L. Gao and H. M. Cheng, *ACS Nano*, 2010, **4**, 5245–5252.

6 S. R. Hammond, J. Meyer, N. E. Widjonarko, P. F. Ndione, A. K. Sigdel, A. Garcia, A. Miedaner, M. T. Lloyd, A. Kahn, D. S. Ginley, J. J. Berry and D. C. Olson, *J. Mater. Chem.*, 2012, **22**, 3249–3254.

Appendix

Appendix 1. Tafel analysis of MoS_3

The mechanism of the HER at the electrode surface can be investigated by plotting the overpotential *vs* the current density. The resulting Tafel slope gives indication on the rate-determining step. An Ohmic-drop correction has been performed after the experiment, following a procedure described in ref.[1] (in the ESI). It consists of calculating a resistance value from the polarization curve. The overpotential η(V) observed during an experiment is given by Equ. 11:

$$\eta = a + b \ln j + jR \qquad \text{Equ. 11}$$

where a (V) is the Tafel constant, b (V dec^{-1}) is the Tafel slope, j (A cm^{-2}) is the current density and R (Ω cm²) is the total area-specific uncompensated resistance of the system, which is assumed to be constant over the range of overpotential in which the Tafel analysis is performed. The derivative of Equ. 11 with respect to current density gives Equ. 12 from which b and R can be easily obtained by plotting $d\eta/dj$ as a function of $1/j$.

$$\frac{d\eta}{dj} = \frac{b}{j} + R \qquad \text{Equ. 12}$$

The estimation of R allows correcting the experimental overpotential by subtracting the Ohmic drop jR according to Equ. 13:

$$\eta_{corr} = \eta - jR \qquad \text{Equ. 13}$$

During the calculation from a definite set of (η, j) experimental points, the derivative $d\eta/dj$ was replaced by their finite elements $\Delta\eta/\Delta j$ estimated from each pair of consecutive experimental points.

The second cycle of a CV of an ITO\MoS_3 substrate performed at 2 mV s^{-1} was used for the Tafel analysis. The resistance R was calculated in the range of –0.13 to –0.18 V *vs* RHE (i.e. in the beginning of the kinetic-controlled potential region) and was obtained at 0.05 Ω cm².

The Tafel plot is shown in Fig. A1:

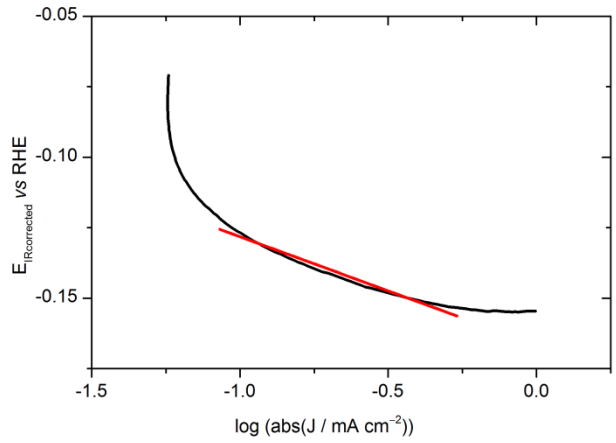

Fig. A1. Tafel plot and linear fit

The experimental Tafel plot after correction has a poor linearity. The Tafel plot obtained in the most linear region is 38 mV dec^{-1}, which is indicating that the rate-determining step is the electrochemical desorption, i.e. that the mechanism follows the Volmer-Heyrowski steps. The Tafel slope without IR-drop correction was 65 mV dec^{-1} but the linearity was better. 38 mV dec^{-1} is close to the Tafel slope that was obtained in ref.[1] for the smallest loading while 65 mV dec^{-1} was closer to the Tafel slope obtained with the highest loading. It was later shown by impedance spectroscopy that the chemically synthesized MoS_3 had a relatively slow electron transport, which increased the Tafel slope.[1]

A higher Tafel slope was found for spray-coated films (60 mV dec^{-1} after IR-drop correction), probably because of the higher thickness or less compact film.

Reference in Appendix 1

1 H. Vrubel, D. Merki and X. Hu, *Energy Environ. Sci.*, 2012, **5**, 6136–6144.

Appendix 2. XPS spectra

XPS survey, Mo 3d and S 2p spectra of MoO_3 are presented in Fig. A2 and Fig. A3.

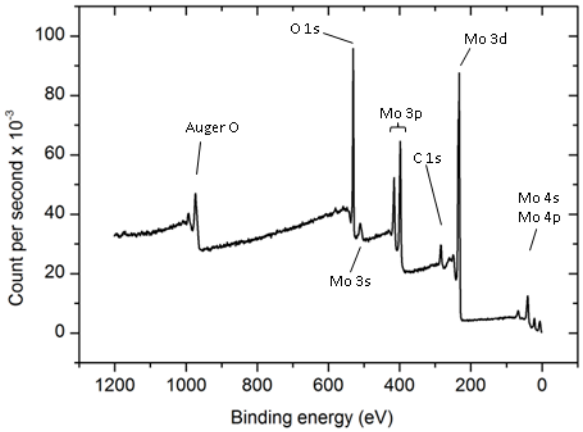

Fig. A2. Survey spectrum of MoO_3

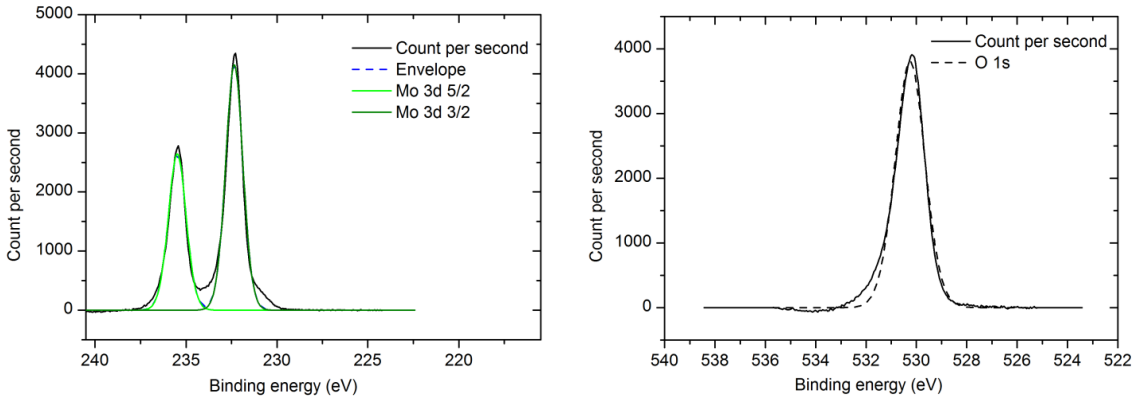

Fig. A3. Mo 3d and S 2p spectra of MoO_3

XPS survey, Mo 3d and S 2p spectra of MoS_2 are presented in Fig. A4 and Fig. A5.

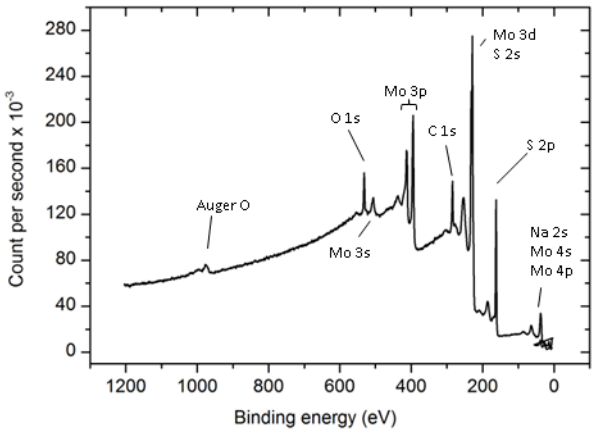

Fig. A4. Survey spectrum of MoS_2

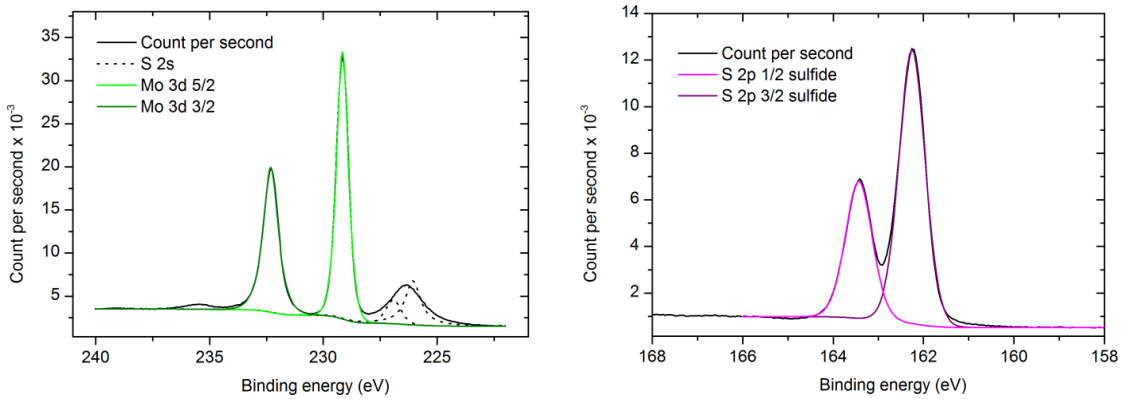

Fig. A5. Mo 3d and S 2p spectra of MoS_2

Appendix 3. TEM images

MoS_3 TEM pictures taken on the same sample as in Chapter 2. The particles are amorphous and with sizes ranging from 10 nm to 100 nm.

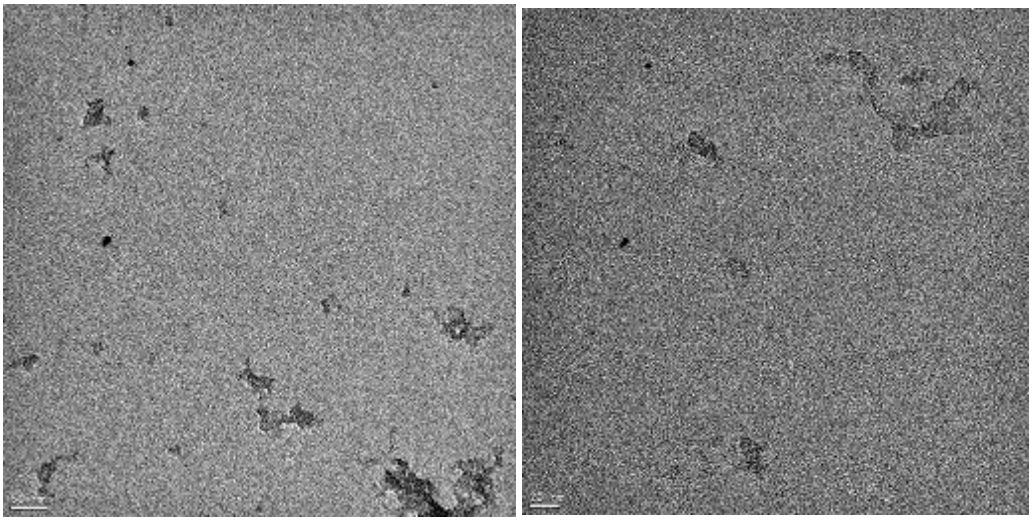

Fig. A6. Scale bar: 50 nm (left), 20 nm (right)

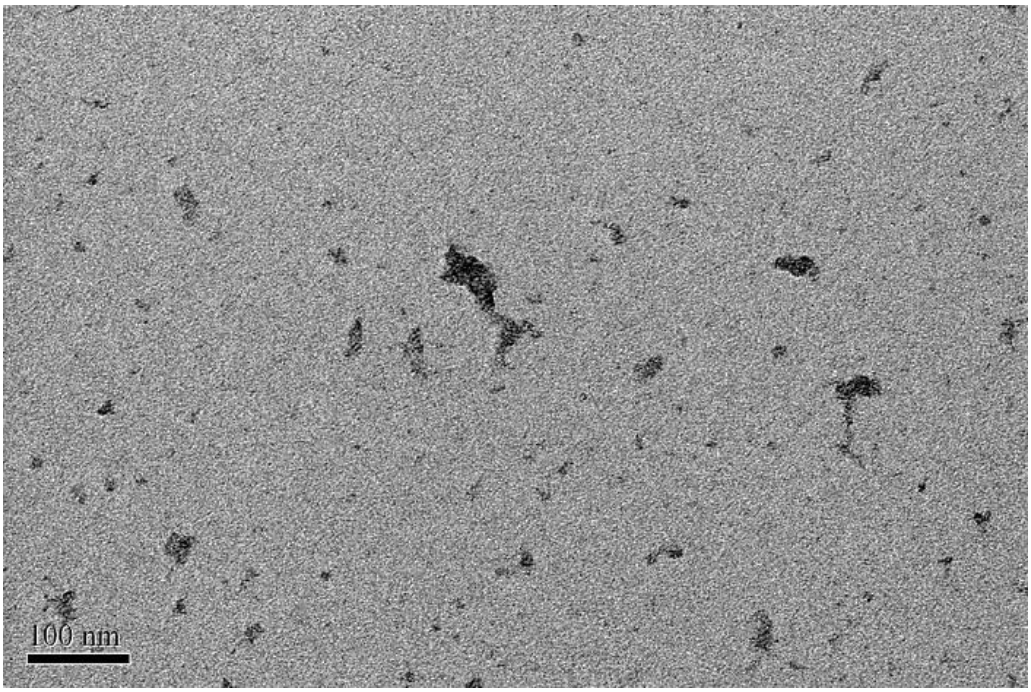

Fig. A7. Scale bar: 100 nm

Appendix 4. Table of all figures of merit

	$V_{0.1\ mA\ cm^{-2}}$	$J_{0\ V\ vs\ RHE}$	$\Phi_{saved,ideal}$	$\Phi_{saved,NPAC}$
ITO\PEDOT:PSS\P3HT:PCBM**MoS_3**	–0.15	50 µA cm^{-2}	0.004 % J_m = 29 µA cm^{-2}, V_m = 0.15 V	0.007 % $J_{photo,m}$ = 80 µA cm^{-2}, $V_{photo,m}$ = 0.09 V
ITO\PEDOT:PSS\P3HT:PCBM\LiF\Al\Ti**MoS_3**	0.48 V	8.5 mA cm^{-2}	0.64 % J_m = 5.1 mA cm^{-2}, V_m = 0.20 V	2.05 % $J_{photo,m}$ = 7.8 mA cm^{-2}, $V_{photo,m}$ = 0.41 V
ITO\PEDOT:PSS\P3HT:PCBM\LiF\Al\Ti**Pt/C**	0.67 V	7.9 mA cm^{-2}	1.42 % J_m = 6.0 mA cm^{-2}, V_m = 0.31 V	1.64 % $J_{photo,m}$ = 6.7 mA cm^{-2}, $V_{photo,m}$ = 0.39 V
ITO\PEDOT:PSS\P3HT:PCBM\Ti**MoS_3**	0.32 V	6.8 mA cm^{-2}	0.24 % J_m = 3.9 mA cm^{-2}, V_m = 0.11 V	1.30 % $J_{photo,m}$ = 7.7 mA cm^{-2}, $V_{photo,m}$ = 0.30 V
ITO\PEDOT:PSS\P3HT:PCBM\C_{60}**MoS_3**	0.24 V	0.9 mA cm^{-2}	0.03 % J_m = 0.4 mA cm^{-2}, V_m = 0.08 V	0.14 % $J_{photo,m}$ = 2.1 mA cm^{-2}, $V_{photo,m}$ = 0.30 V
ITO\NiO_x\P3HT:PCBM**MoS_3**	0.37 V	4.5 mA cm^{-2}	0.28 % J_m = 2.2 mA cm^{-2}, V_m = 0.13 V	1.23 % $J_{photo,m}$ = 5.1 mA cm^{-2}, $V_{photo,m}$ = 0.24 V
ITO\$NiO_x$\P3HT:PCBM\$C_{60}$**$MoS_3$**	0.45 V	1.5 mA cm^{-2}	0.17 % J_m = 0.7 mA cm^{-2}, V_m = 0.24 V	0.32 % $J_{photo,m}$ = 1.1 mA cm^{-2}, $V_{photo,m}$ = 0.30 V
ITO\GO\P3HT:PCBM**MoS_3**	0.22 V	1.8 mA cm^{-2}	0.13 % J_m = 0.8 mA cm^{-2}, V_m = 0.17 V	0.26 % $J_{photo,m}$ = 1.5 mA cm^{-2}, $V_{photo,m}$ = 0.17 V
ITO\MoO_x\P3HT:PCBM**MoS_3**	0.37 V	6.7 mA cm^{-2}	0.73 % J_m = 3.6 mA cm^{-2}, V_m = 0.20 V	2.10 % $J_{photo,m}$ = 6.2 mA cm^{-2}, $V_{photo,m}$ = 0.34 V
ITO\$MoO_x$\P3HT:PCBM\$C_{60}$**MoS3**	0.23 V	13.1mA cm^{-2}	0.62 % J_m = 6.4 mA cm^{-2}, V_m = 0.10 V	8.29 % $J_{photo,m}$ = 18.3 mA cm^{-2}, $V_{photo,m}$ = 0.45 V

Appendix 5. Experimental methodology

An experimental methodology approach was used in order to determine the influence of parameters of the synthesis, which were: rate of acid addition, final pH, time and temperature of heating, decantation before separation of the particles. Other parameters such as concentration and ratio of the precursors were not considered.

The response was the measurement of the current density of the HER during cyclic voltammetry when the potential was –0.6 V *vs* Ag/AgCl.

With 5 parameters, the closest matrix is H(8,8), therefore we can study five parameters and two interactions. We chose to study a first interaction between the time and temperature of heating, and the second between temperature of heating and decantation.

Parameter	Variable	Level X = –1	Level X = +1
Rate of acid addition	X_1	Slow (20 min)	Fast (5 min)
Final pH	X_2	3	4
Heating T	X_3	90 °C	Reflux
Heating time	X_4	20 min	40 min
Decantation	X_5	no	yes

Table 7. Parameters of the synthesis with their lower and upper boundaries

The matrix is H(8, 8) i.e. H(2^3, 2^3), and for five parameters, 3 = 5-2, therefore, p=2. The fractional factorial matrix will be constructed with $2^p - 1 = 2^2 - 1 = 3$ independent generators. The coefficients calculated with this matrix are: b_0, b_1, b_2, b_3, b_4, b_5, b_{34}, b_{35}. 8 experiments are needed to calculate 5 parameters and 2 interactions.

To choose the generators, they must have at least 3 terms so as not to aliase the principle coefficients, and they must not contains the studied interactions.

Among 123, 124, 125, 134, 135, 145, 234, 235, 245, and 345, we chose 123. Every generator containing 34 and 35 were eliminated. 124, 125, 145 and 245 remained. 124 and 125 were not independent from 123, therefore 245 and 145 remained. We chose 245.

Generators with 4 terms are: 1234, 1235, 1245, 1345, and 2345. 1234 and 1235 are not compatible with 123; and 1245 is not compatible with 245. 1345 and 2345 remained. We chose 1345.

Appendix

1345.245 ≡ 123 ; 1345.123 ≡ 245

The 3 independent generators are 123, 245 and 1345. The definition relationship is: I ≡ 123 ≡ 245 ≡ 1345

Inventory of the aliases:

$b_1 = b_1 + b_{23} + b_{245} + b_{345}$

$b_2 = b_2 + b_{13} + b_{25} + b_{1345}$

$b_3 = b_3 + b_{12} + b_{245} + b_{145}$

$b_4 = b_4 + b_{123} + b_{25} + b_{135}$

$b_5 = b_5 + b_{123} + b_{24} + b_{134}$

$b_{34} = b_{34} + b_{124} + b_{235} + b_{15}$

$b_{35} = b_{35} + b_{125} + b_{234} + b_{14}$

Construction of the matrix of experiments

The three independent columns are attributed to X_1, X_2, and X_4. X_3 is built as $X_1.X_2$. X_5 is built as $X_2.X_4$.

The matrix of experiments is:

X1	**X2**	**X4**	**X3**	**X5**
-	-	-	+	+
+	-	-	-	+
-	+	-	-	-
+	+	-	+	-
-	-	+	+	-
+	-	+	-	-
-	+	+	-	+
+	+	+	+	+

In real variables, the matrix is:

Rate of acid addition	Final pH	Heating time	Heating T	Decantation
Slow	3	20 min	Reflux	Yes
Fast	3	20 min	90 °C	Yes
Slow	4	20 min	90 °C	No
Fast	4	20 min	Reflux	No
Slow	3	40 min	Reflux	No
Fast	3	40 min	90 °C	No
Slow	4	40 min	90 °C	Yes
Fast	4	40 min	Reflux	Yes

The matrix of effects is:

b_0	b_1	b_2	b_4	b_3	b_5	b_{34} ($X_1.X_4$)	b_{35} ($X_1.X_2.X_4$)
+	-	-	-	+	+	+	-
+	+	-	-	-	+	-	+
+	-	+	-	-	-	+	+
+	+	+	-	+	-	-	-
+	-	-	+	+	-	-	+
+	+	-	+	-	-	+	-
+	-	+	+	-	+	-	-
+	+	+	+	+	+	+	+

Experimentally, the 8 experiments were carried out as 4 experiments and each batch was separated into 2 batches, each one treated differently.

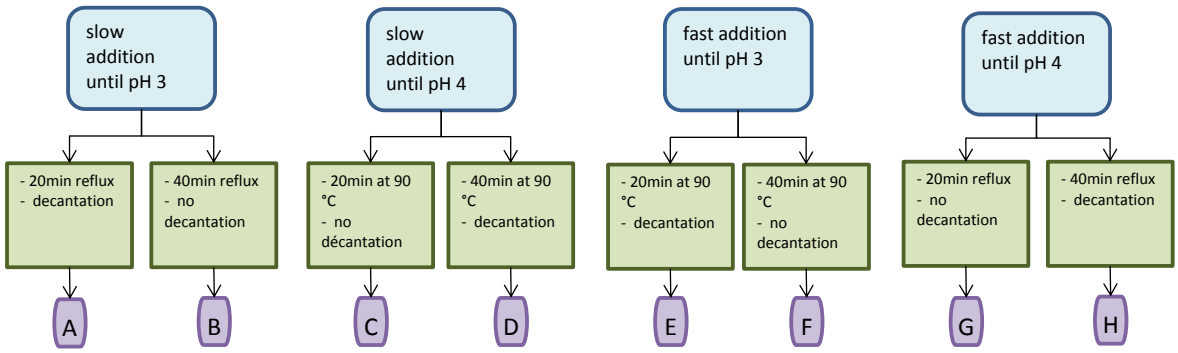

Fig. A8. Schematic view of the 8 batches prepared from 4 syntheses.

Electrochemical tests were carried out in H_2SO_4 0.5 M with a three-electrode setup.

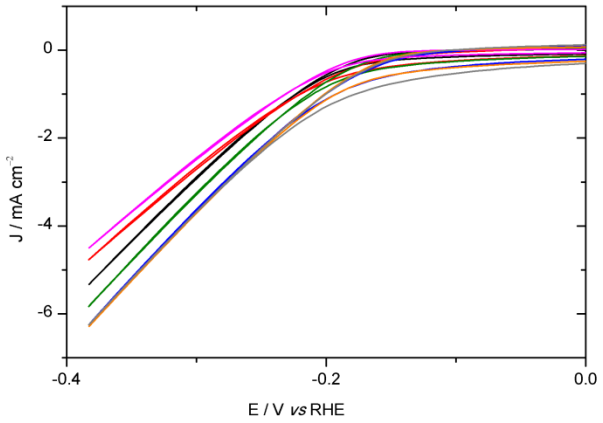

Fig. A9. Cyclic voltammetry experiments (50 mV s^{-1}) performed on the eight batches of MoS_3 (30 nm) deposited by spin-coating on ITO, in 0.5 M H_2SO_4 (black: A, red: B, green: C, blue: D, pink: F, orange: G, grey: H)

At -0.6 V vs. Ag/AgCl, the current densities (mA/cm²) are:

A	B	C	D	F	G	H
-4.8	-5.1	-5.7	-6.1	-4.4	-6.1	-5.9

Table 8: Current densities at -0.6V vs. Ag/AgCl

The electrochemical activity was similar for every batch and these experiments showed that no parameter was critical.